



Norwegian University of
Science and Technology

Spin Transport in a Finite-Depth Antiferromagnetic Insulator - Metallic Conductor Bilayer System with a Distinct Antiferromagnetic Surface Spin Exchange

Jonas Boym Flaten

MSc in Physics

Submission date: May 2018

Supervisor: Arne Brataas, IFY

Norwegian University of Science and Technology
Department of Physics

Abstract

A currently increasing interest in antiferromagnetic insulator spintronics, due to emergent attractive properties such as terahertz operation and spin transport enhancement, encourages theoretical investigation on the topic. In this thesis, a quantum-mechanical operator treatment of the spin transport between an antiferromagnetic insulator layer and a metallic conductor layer is presented. The antiferromagnetic layer has a distinct surface spin exchange, and both layers are of finite depth, as opposed to earlier work on similar systems.

In chapter 2, a simple cubic antiferromagnetic Heisenberg Hamiltonian with an easy-axis term is used to model the antiferromagnetic layer. The magnonic energy eigenstates are then calculated by bosonic diagonalisation of this Hamiltonian through a Holstein-Primakoff transformation, a Fourier transformation and an ansatz-based Bogoliubov transformation.

In chapter 3, a simple cubic tight-binding Hamiltonian with an antiferromagnetic interaction term is used to model the metallic layer. The electronic energy eigenstates are then calculated by fermionic diagonalisation of this Hamiltonian through a Fourier transformation and a canonical unitary transformation.

The antiferromagnetic and metallic diagonalisations are both shown to result in non-trivial trigonometric-hyperbolic systems of equations, which are solved numerically and compared to the results of direct numerical diagonalisations in their respective chapters. All numerical calculations are implemented and executed with a script provided in the appendix.

Finally in chapter 4, general expressions for the spin transport rates across the antiferromagnetic insulator-metallic conductor junction are derived by modelling the spin pumping/spin-transfer torque mechanism with an antiferromagnetic Heisenberg Hamiltonian and treating it as a small perturbation to invoke Fermi's golden rule.

The equations and expressions determining the magnons, electrons and spin transport of the bilayer system are concisely summed up in sections 2.16, 3.13 and 4.5. They provide the foundation for a variety of future work on spin transport phenomena, including the possibility of modelling trilayer systems with antiferromagnetic insulator interlayers to investigate theoretically the documented enhanced spin transport.

Sammendrag

En økende interesse for spintronikken rundt antiferromagnetiske isolatorer, som et resultat av stadig flere dokumenterte attraktive egenskaper, oppmuntrer til teoretisk arbeid innen feltet. Blant annet spås antiferromagnetiske isolatorer å operere med terahertz-frekvenser og å forsterke spinntransport. I denne oppgaven blir det presentert en kvantemekanisk operatortilnærming til spinntransporten mellom et antiferromagnetisk isolatorsjikt og et metallisk ledersjikt. Det antiferromagnetiske sjiktet har en distinkt spinnutveksling på overflatene, og begge sjikt har endelig dybde, i motsetning til tidligere arbeid på lignende systemer.

I kapittel 2 blir en antiferromagnetisk Heisenberg-modell på et vanlig kubisk gitter satt som Hamilton-operator for det antiferromagnetiske sjiktet. Modellen er modifisert med et hovedakseledd. Deretter blir de magnoniske energieigenstandene beregna ved å diagonalisere Hamilton-operatoren i bosoniske operatorer gjennom en Holstein-Primakoff-substitusjon, et Fourier-skifte og et prøveløsningsbasert Bogoliubov-skifte.

I kapittel 3 blir en tettbåndmodell på et vanlig kubisk gitter satt som Hamilton-operator for det metalliske sjiktet. Modellen er her modifisert med et ledd som beskriver vekselvirkninga til det antiferromagnetiske sjiktet. Deretter blir de elektroniske energieigenstandene beregna ved å diagonalisere Hamilton-operatoren i fermioniske operatorer gjennom et Fourier-skifte og et kanonisk, unitært skifte.

Både den antiferromagnetiske og den metalliske diagonaliseringa leder til ikke-trivielle trigonometrisk-hyperbolske ligningssystemer, som løses numerisk og sammenlignes med resultatene fra direkte numeriske diagonaliseringer i de respektive kapitlene. Alle numeriske kalkulasjoner er implementert og kjørt med skriptet som er lagt ved i appendiks.

Til slutt, i kapittel 4, blir generelle uttrykk for spinntransporten over skjøten mellom det antiferromagnetiske isolatorsjiktet og det metalliske ledersjiktet utleda. Mekanismen som driver spinnpumping og spinnoverføringsdreiemomenter over skjøten blir konkretisert i nok en antiferromagnetisk Heisenberg-modell. Den antas å være så svak at perturbasjons-teori – og dermed Fermis gygne regel – kan brukes.

Ligningene og uttrykkene som beskriver magnoner, elektroner og spinntransport i dobbeltsjiktssystemet er oppsummert konsist i seksjonene 2.16, 3.13 og 4.5. Disse legger grunnlaget for framtidig arbeid på mange ulike spinntransportfenomener. Blant annet kan trippeltsjiktssystemer med en antiferromagnetisk isolator i mellomsjiktet modelleres for å undersøke dokumentert forsterka spinntransport gjennom slike sjikt.

Preface

The thesis at hand was developed and written over the period of time from January 2017 to May 2018. Through my work I have come to know a branch of physics which is both complex and exciting. I hope to contribute more to the field of spintronics in the future.

For me, writing a Master's thesis has also been a lesson in prioritisation and time management. With such a large amount of time available to work, you require an equally large amount of some unearthly disciplinary power to pull it all through in due time. I have yet to possess this power. That said, I guess most Master's students experience the same, to some degree at least. I hope, and believe, that the lesson is well learned.

I want to thank my fellow students Even Thingstad and Ola Isaac Høgsen Mæhlen for valuable discussions on countless related (and often also unrelated) physical and mathematical topics over the duration of my work. Their insight into their respective fields of physics and mathematics are unmatched — at least among the people *I* know.

Of course my sincerest thanks also go to Niklas Rohling, who supervised this work to the first deadline and beyond. Thank you for your incredible patience and your deep dedication, both to the subject and to the thesis. Not all supervisors are so generous with their time as to arrange catch-up meetings twice a week. (Fellow students et al. [2017]) Indeed, without our continued e-mail correspondence over these last couple of months (not to mention these last couple of days), this thesis would probably never have been finished at all.



Jonas Boym Flaten
Trondheim, May 30th 2018

Notation

Much physical notation is used throughout the thesis. Most of it is commonly used in the field of quantum mechanics, while some of it is invented by the author. All choices are made to keep things as clear as consistent as possible.

Constants

i is the imaginary unit such that $i^2 = -1$.

\hbar is the reduced Planck constant.

\vec{e}_x , \vec{e}_y and \vec{e}_z are the unit vectors in the x-, y-, and z-directions of space respectively.

Formats

\vec{a} (arrow): Used to denote physical vector quantities that have a component in each of the x-, y- and z-directions of space. The components of the vector \vec{a} are denoted a_x , a_y and a_z respectively.

\bar{a} (bar): Used to denote mathematical vectors (1-tensors) of all dimensions. Row and column vectors are not distinguished.

\boxed{a} (box): Used to denote mathematical matrices (2-tensors) of all dimensions.

\mathbf{a} (boldface): Used to denote quantum mechanical operators. Quantum mechanical operators can also be vector quantities, such as the spin operator \vec{s} .

$[a]$ (brackets): Used to mark quantities and parameters from other articles and texts, as opposed to quantities and parameters from this thesis.

Symbols

• (bullet): Used to denote an unspecified letter, when it is only important to stress that there *is* a letter here.

* (asterisk): Used to denote the conjugate of a complex number.

† (dagger): Used to denote the adjoint of an operator, as well as the conjugate transpose of a matrix.

‡ (double dagger): Used to denote a summation of the following operator expression with its adjoint, hence making the total operator Hermitian.

: (colon): Used to denote a pair of nearest neighbours in a lattice. A sum $\sum_{\vec{q}:\vec{r}\in\mathbb{L}}$ is meant to run through every pair of nearest neighbour lattice points \vec{q} and \vec{r} in the lattice \mathbb{L} . Note that the nearest neighbour pairs are not ordered, so that the sum will only consider each pair once.

Introduction

Traditional electronic devices become smaller and smaller with each passing year. However, with the decreasing size new challenges arise. The latest International Technology Roadmap for Semiconductors from 2015 predicts electronic technology to hit a thermal ceiling in 2024. By then, the component density in electronic chips will have become so high that it is essentially impossible to cool them down by traditional means, due to finite heat dissipation. (Anthony [2016]) A completely new approach will be needed to push the component density even higher.

Spintronic devices, in which energy and information are carried by spin waves, or *magnons*, as well as electrons, could possibly resolve the problem. (Wolf et al. [2001], Kajiwara et al. [2010]) Since magnons move and interact through spin exchange in insulators, there is no ordinary Joule heating involved. Hence they could allow for even denser spintronic technology beyond the electronic thermal limit.

Only by thoroughly understanding how magnons behave, can one hope to design spintronic devices that are realistically manufacturable. Throughout this thesis, we will give a small contribution to this understanding by examining the interaction between magnons and electrons in a specific spintronic antiferromagnetic insulator–metallic conductor bilayer system. The system is extended from a similar system recently studied in Fjærbu et al. [2017] by the inclusion of a distinct surface spin exchange in the antiferromagnetic sublayer. In this introductory chapter we provide some background and motivation, brief summaries of the two most relevant pieces of earlier work as well as a presentation of the system in consideration and the structure of the thesis.

1.1 Motivation

With the long-term goal of using magnons to transport energy and information in spintronic devices, the mathematical aspects of magnons and their interaction with electrons are currently under investigation. A key concern used to be the fact that magnons tend to dissipate quickly, which makes them a poor candidate for transport. However in Demokritov et al. [2006] a *Bose-Einstein condensate* of magnons was observed in ferrimagnetic

yttrium iron garnet, $\text{Y}_3\text{Fe}_2(\text{FeO}_4)_3$, at room temperature. Essentially, in such a condensate there is only *one* bosonic state above vacuum which is thermally available. Since no other bosonic states are available, all particles in the condensate must occupy the same state, so there is no room for dissipation of energy into other states at all. Two following studies by the same group confirmed that the YIG condensate is indeed coherent (Demidov et al. [2008], Nowik-Boltyk et al. [2012]), and in Sun et al. [2016] it is further argued theoretically that the condensate is also superfluid. Such magnonic condensates could then possibly perform in spintronic devices to transport energy and information without dissipation and with outstanding speed.

Since the discovery of the YIG condensate in 2006, magnonic condensates have also been observed in antiferromagnetic cesium manganese fluoride, CsMnF_3 , and manganese carbonate, MnCO_3 . (Bunkov et al. [2011, 2012]) Clearly, magnonic condensates are obtainable in a variety of magnetic materials. However, the YIG condensate was excited by microwave pumping, and the two antiferromagnetic condensates were excited by nuclear magnetic resonance. Both these techniques would require relatively advanced components if they were to be used in spintronic devices. On the other hand, *electrically-driven* condensation is of great interest, as it would in comparison provide a simple route between traditional electric currents and the desired magnonic condensate currents. Magnons are known to leak energy and spin into adjacent metals in a process known as *spin pumping*. (Berger [1996], Cheng et al. [2014]) The reverse happens when electrons flip their spins to enhance or reduce the magnonic collective spin precession in adjacent magnetic insulators through the so-called *spin-transfer torque*. (Slonczewski [1996], Brataas et al. [2012]) These two phenomena are reciprocal phenomena, deeply connected to each other, and together they constitute the spin transfer mechanism between magnonic and electric currents. (Tserkovnyak et al. [2005]) If electrically-driven magnon condensation is to be explored quantitatively, a mathematical model which incorporates this mechanism must be invoked.

In Bender et al. [2012] and Bender et al. [2014], electrically-driven magnon condensation in a ferromagnetic insulator–metallic conductor bilayer system was investigated theoretically by Bender, Duine and Tserkovnyak. Here, it was shown that such condensation is theoretically achievable in a *ferromagnetic* insulator layer connected to a metallic conductor layer, provided that there is a certain temperature difference between the layers and a spin accumulation on the metallic side of the junction. The authors suggest that this spin accumulation can be introduced through the *spin Hall effect* (the spin analogue to the ordinary electric Hall effect), through which spin of opposite directions accumulate at the lateral surfaces of an electric current carrying conductor. (Dyakonov and Perel [1971], Hirsch [1999]) As the authors point out, the spin Hall effect was already demonstrated to generate magnonic currents in Kajiwara et al. [2010] and Liu et al. [2011], while the inverse spin Hall effect was used to detect magnonic currents in Sandweg et al. [2011].

More recently, electrically-driven magnon condensation in an *antiferromagnetic* insulator–metallic conductor bilayer system was investigated theoretically in Fjærbu et al. [2017]. As mentioned above, the model and approach of this paper is the foundation of this thesis and will be described in greater detail in section 1.2 below, but in essence it concludes that *two* magnonic condensates can appear in the antiferromagnetic insulator layer — one for each spin direction along the antiferromagnetic easy-axis. Fjærbu, Rohling and

Brataas predict the condensates to be reciprocally excitable even at room temperature by spin accumulation at the junction along their associated spin direction. In other words, magnon condensation could occur in the antiferromagnetic insulator layer for either sign of spin accumulation, and conversely spin pumping from the condensates could induce electric currents in both directions in the metallic conductor layer through the inverse spin Hall effect.

Fjærbu et al. [2017] contribute to the recently sparked interest in antiferromagnetic insulators as an alternative to ferromagnetic insulators in spintronic devices. This interest is justified by several attractive features of antiferromagnetic insulators. While ferromagnets create a magnetic stray field which could interfere with other magnetic components in a spintronic device, antiferromagnets are magnetically neutral in the sense that no such stray field is present outside the material. Furthermore, antiferromagnetic magnons have been demonstrated to operate at terahertz frequencies (Satoh et al. [2010]), which is much faster than ferromagnetic magnons. These properties makes antiferromagnetic insulators desirable for magnetic storage devices, in which fast switching of spin directions in one memory cell without interfering other cells is essential for good performance. (Gomonay and Loktev [2010]) The high operating frequencies also allow for more exotic devices such as spin Hall nano-oscillators, which produce electric AC currents from DC input, to deliver terahertz frequencies, as described in Cheng et al. [2016]. Finally in Wang et al. [2014] and Wang et al. [2015], antiferromagnetic insulator *interlayers* were demonstrated to significantly enhance spin pumping from a ferrimagnetic yttrium iron garnet layer, $\text{Y}_3\text{Fe}_2(\text{FeO}_4)_3$, to a metallic platinum layer, Pt. Among the antiferromagnetic insulators tested here is nickel oxide, NiO, which was further investigated in a multilayer system in Moriyama et al. [2015]. In Hahn et al. [2014] it was also compared to the non-magnetic insulator silica, SiO_2 , which contrarily blocked the spin pumping. All these experiments seem to suggest that antiferromagnetic insulators form interfaces (to both metallic conductors as well as other magnetic insulators) which transfer spin exceptionally well, thus making them ideal for enhancing interlayers.

Note that the theoretical approach used in Bender et al. [2012] and Fjærbu et al. [2017] is to express the interaction between the layers in terms of energy eigenstate creation and annihilation operators and then treat it as a small perturbation to the total Hamiltonian to invoke Fermi's golden rule and get transport rate expressions. Other theoretical approaches are also possible, such as the phenomenological Landau-Lifshitz-Gilbert (LLG) equations. These are equations of motion for the total magnetisation vector in ferromagnets, or the two sublattice magnetisation vectors in antiferromagnets. The equations describe modes of precession of the magnetisation vectors around an easy-axis, corresponding to different magnonic states. The precession is subject to a damping, known as the *Gilbert damping*, which was originally introduced phenomenologically, but it has later been shown to origin from spin pumping into adjacent materials among other mechanisms. (Tserkovnyak et al. [2002], Mizukami et al. [2002]) The LLG equations are often used to make relatively quick and accessible spin predictions. In Daniels et al. [2015], for example, LLG equations are used to calculate the excitation spectra of two types of antiferromagnetic insulators. Although we will not use this formalism in the calculations of this thesis, the LLG equations were used in Cheng et al. [2014] to argue that spin pumping from antiferromagnets should be as effective as spin pumping from ordinary ferromagnets. This

observation is the theoretical foundation for the introduction of an interaction across the antiferromagnetic-metallic junction in chapter 3. Hence, our transport calculations are actually indirectly justified by LLG calculations.

This section brought some insight into why antiferromagnetic insulators are well on their way to becoming a crucial component of spintronics. In the next section we move on to recap the model and approach in Fjærbu et al. [2017].

1.2 Earlier work: Semi-infinite-depth antiferromagnetic insulator–metallic conductor bilayer system with uniform antiferromagnetic spin exchange

In Fjærbu et al. [2017], Fjærbu, Rohling and Brataas consider a bilayer system consisting of a semi-infinite antiferromagnetic insulator on one side of the junction and a semi-infinite metallic conductor on the other side. They use a simple cubic antiferromagnetic Heisenberg model to describe the insulator, a simple cubic tight-binding model to describe the conductor and a Heisenberg spin exchange between static antiferromagnetic spins and itinerant electron spins at the interface to model the spin pumping/spin-transfer torque mechanism mentioned in section 1.1. The nearest-neighbour antiferromagnetic spin exchange $[J\hbar^2]$ is uniform throughout the antiferromagnetic insulator.

The energy eigenstates of the antiferromagnetic and metallic layers are calculated in the appendices of the paper. To simplify the resulting expressions, some key assumptions are made. First of all, the antiferromagnetic insulator temperature $[T_{\text{AF}}]$ is assumed to be much smaller than the Néel temperature. Then only magnons whose energy is much smaller than the spin exchange $[J\hbar^2]$ are thermally available, so only such low-energy magnons need to be considered. This is the *low-energy limit*. Furthermore, the anisotropy exchange $[K_z]$ associated with the antiferromagnetic easy-axis is also assumed to be much smaller than the spin exchange (which is usually the case, such as in rubidium manganese trifluoride, RbMnF_3 , as demonstrated in Windsor and Stevenson [1966], López Ortiz et al. [2014]). This is the *small-anisotropy limit*. Looking at the energy dispersion relation, the low-energy limit is then shown to be equivalent to the *long-wavelength limit*, for which the magnonic momentum $[|\mathbf{p}|d]$ is small. The exact expressions are then expanded in the small quantities $[|\mathbf{p}|d]$ and $[K_z/J]$ to get simpler approximate expressions for the amplitudes of the magnonic eigenstates.

In the long-wavelength and small-anisotropy limits, the *surface eigenstates* of the antiferromagnetic insulator — that is, the eigenstates with evanescent amplitudes that would normally be maximal at the interface and fade exponentially into the insulator — are shown to be approximately equal to uniform *delocalised eigenstates* with equal amplitudes along the direction perpendicular to the interface. This allows the authors to model the low-energy surface eigenstates by such uniform delocalised eigenstates, which simplifies the calculations further.

For the electronic eigenstates of the metallic conductor, *half-filling* is assumed, which means that exactly half of all the fermionic states are occupied by electrons. This determines the Fermi energy $[E_F]$ of the conductor. The Fermi energy, and hence the hopping

amplitude $[t]$, is also assumed to be large compared to the other energy scales of the system.

Finally, the interaction across the junction is treated as a perturbation, which allows for the usage of Fermi's golden rule to get transport rates. Magnon–phonon and magnon–magnon interactions are not included in the Hamiltonian, but introduced indirectly later when the two types of antiferromagnetic magnons and the metallic electrons are assumed to be driven into separate *quasi-equilibria*: The two magnon types are driven into Bose-Einstein distributions with temperatures $[T_{\pm}]$ and chemical potentials $[\mu_{\pm}]$, while the electrons are driven into a Fermi-Dirac distribution with temperature $[T_N]$. The electronic distribution is assumed to have different chemical potentials $[\mu_{\uparrow}]$ and $[\mu_{\downarrow}]$ for spin-up and spin-down electrons due to some spin polarising mechanism such as the spin Hall effect, resulting in the spin accumulation $[\Delta\mu = \mu_{\uparrow} - \mu_{\downarrow}]$. Two magnonic condensates are then shown to appear for large spin accumulations of opposite signs, as mentioned in the previous section.

1.3 Earlier work: Semi-infinite-depth antiferromagnetic insulator layer with a distinct surface spin exchange

Actually the effects of a distinct surface spin exchange in an antiferromagnetic insulator were *already* examined in 1969. In Wolfram and De Wames [1969], the model is a semi-infinite simple cubic Heisenberg model just as in Fjærbu et al. [2017], but instead of an easy-axis term proportional to the squares of the spin z-components, it has external magnetic field terms and anisotropy terms which are both proportional to simply the spin z-components instead. Using equations of motion for the lattice site spin operators, the random-phase approximation and a supermatrix inverse (referred to as a Green's function), a cubic equation is derived, and this is then solved to find the energy quanta of the antiferromagnet. The ratio of the surface spin exchange to the bulk spin exchange, $[\epsilon]$, is shown to directly control the energy spectrum of the antiferromagnet. There is always a magnonic *bulk continuum* of available states, but depending on the value of $[\epsilon]$ an additional doubly-degenerate magnonic *surface branch* may appear either below or above it. Within certain ranges of $[\epsilon]$, the surface branches are truncated and eventually absorbed by the bulk continuum. The threshold values of these ranges are derived in the second half of Wolfram and De Wames [1969] and should be viewed as the main results of the paper.

Even though the distinct surface spin exchange was already examined in Wolfram and De Wames [1969], note again that this was done for a *semi-infinite* antiferromagnetic layer. Our model is *finite* and hence more general. We will actually be able to reproduce some of the main results from Wolfram and De Wames' work in section 2.14.

1.4 System

The total system investigated in this thesis is shown qualitatively in figure 1.1. It is indeed an extension of the system investigated in Fjærbu et al. [2017] by the inclusion of a distinct surface spin exchange in the antiferromagnetic layer. However it is also different in that both layers are assumed to have a finite depth (in contrast to the semi-infinite layers in

Fjærbu et al. [2017]). This difference will lead to only a finite number of magnonic and electronic eigenstates for each planar wave vector \vec{k} in the Brillouin zone.

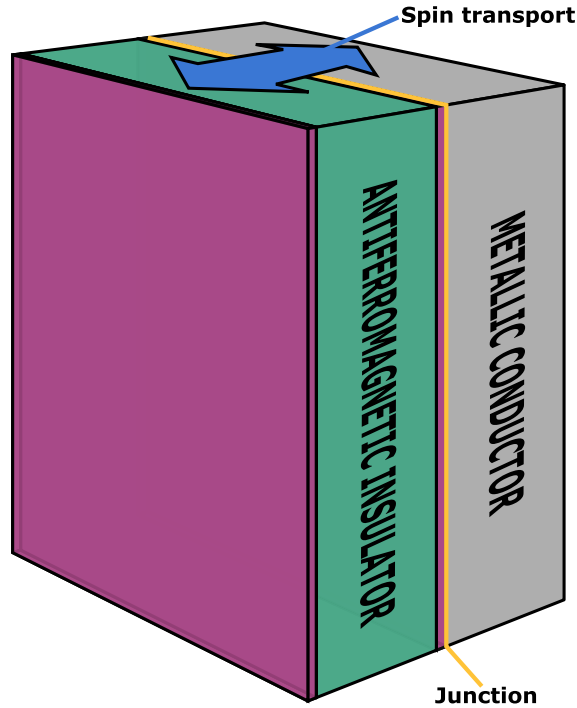


Figure 1.1: The total model investigated in this thesis. Spin is transported between a finite-depth antiferromagnetic insulator layer (indicated in teal) and a finite-depth metallic conductor layer (indicated in grey) across the junction between them (indicated in yellow). The antiferromagnetic layer has a distinct spin exchange parameter at its surfaces (indicated in purple). Note that the layers actually stretch into infinity in the directions parallel to the interface, though they look finite in this figure. The mathematical details of each layer are given in the figures 2.1 and 3.1 and their respective chapters.

1.5 Structure of thesis

We will first calculate the energy eigenstates of each layer in the chapters 2 and 3 and then treat the interaction across the junction as a small perturbation in chapter 4 to get expressions for the spin transport between the antiferromagnetic insulator and the metallic conductor layers. The results we derive are very general, in the sense that they can be used to describe various spin transport scenarios. Some prospects for future applications are suggested in chapter 5.

Antiferromagnetic Layer

The energy eigenstates of the finite antiferromagnetic insulator layer are calculated in this chapter. Our treatment begins with a proper description of the antiferromagnetic model.

2.1 Model

On the antiferromagnetic side of the junction, our model consists of a simple cubic lattice with lattice constant l . The lattice has N lattice planes in the x-direction, where N is an even number, while the planes stretch out into infinity in the y- and z-directions. In other words we are considering a layer of finite depth.

We label each lattice plane with \mathbb{P} and an index from 1 to N , so that the plane closest to the junction is called \mathbb{P}_1 and so on. The whole antiferromagnetic layer is labelled \mathbb{T} , so that $\mathbb{T} = \bigcup_n \mathbb{P}_n$. The lattice sites are given by the position vectors

$$\vec{r}_{pmn} = p\vec{l}_x + m\vec{l}_y + n\vec{l}_z \quad (2.1)$$

for any integer p between 1 and N , and any integers m and n . Here $\vec{l}_x = l\vec{e}_x$, $\vec{l}_y = l\vec{e}_y$ and $\vec{l}_z = l\vec{e}_z$ are the lattice basis vectors. On each lattice site there is a spin of quantum number s .

Our spin lattice is not very interesting without spin interactions of any kind. To describe these interactions we use a Heisenberg model with an easy-axis anisotropy along the z-axis. This model provides the following Hamiltonian:

$$\begin{aligned} \mathbf{H} = & \frac{S}{\hbar^2} \sum_{\vec{q}; \vec{r} \in \mathbb{P}_1} \vec{s}_{\vec{q}} \cdot \vec{s}_{\vec{r}} + \sum_{p=2}^{N-1} \frac{J}{\hbar^2} \sum_{\vec{q}; \vec{r} \in \mathbb{P}_p} \vec{s}_{\vec{q}} \cdot \vec{s}_{\vec{r}} + \frac{S}{\hbar^2} \sum_{\vec{q}; \vec{r} \in \mathbb{P}_N} \vec{s}_{\vec{q}} \cdot \vec{s}_{\vec{r}} \\ & + \sum_{p=1}^{N-1} \frac{J}{\hbar^2} \sum_{\vec{r} \in \mathbb{P}_p} \vec{s}_{\vec{r}} \cdot \vec{s}_{\vec{r}+\vec{l}_x} - \frac{K}{\hbar^2} \sum_{\vec{r} \in \mathbb{T}} s_{\vec{r}z}^2. \quad (2.2) \end{aligned}$$

Here \vec{s}_i are the spin operators on each lattice site, and the first three sums run over all pairs of nearest neighbour sites within each plane as described in the notation section.

S , J and K are important exchange parameters that are all positive. S sets the magnitude of spin exchange in each of the two surface planes \mathbb{P}_1 and \mathbb{P}_N , while J sets the magnitude of spin exchange in all the bulk planes, as well as between planes.

The fact that both S and J are positive is what makes the model antiferromagnetic. If the spins were classical vectors, the energetically favourable configurations for the spin lattice would be configurations of alternating neighbouring spins, since the dot products would be at their most negative. Spins are *not* classical vectors however, but rather vector operators, so such classical arguments should not be relied on. We will see in section 2.2 that the ground state of the system is not what one would expect classically.

The parameter K sets the magnitude of the easy-axis anisotropy along the z-direction, which is introduced through the last term. This anisotropy lowers the total energy with terms that are proportional to the squares of the spin z-components. In other words, the anisotropy makes it energetically favourable for the spin lattice to align its spins along the z-direction, and so it makes the z-axis the "easy-axis" of the system.

An overview of the antiferromagnetic layer model is given in figure 2.1.

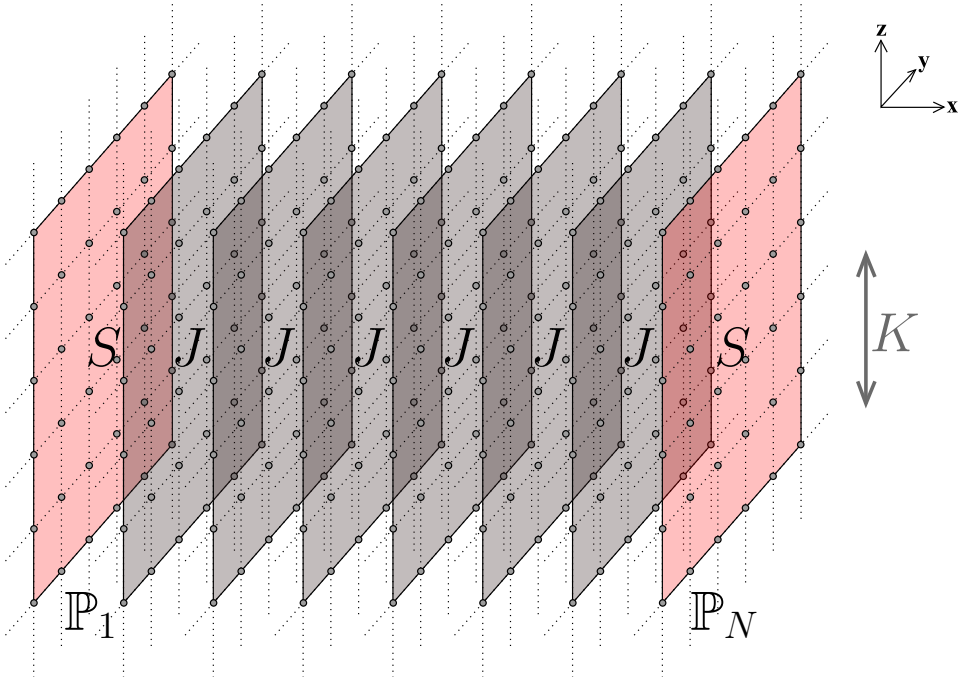


Figure 2.1: Our model for the antiferromagnetic side of the junction. (Here for 8 planes.) The surface planes \mathbb{P}_1 and \mathbb{P}_N have a distinct spin exchange parameter S compared to the bulk spin exchange parameter J . The easy-axis anisotropy is along the z-direction and controlled by the parameter K .

Note that the most important parameter is S , or rather the ratio $\frac{S}{J}$, as the distinct surface

exchange is one of the key features of this thesis. We will denote this ratio with a ρ ,

$$\rho = \frac{S}{J}. \quad (2.3)$$

Similarly, we will denote the ratio $\frac{K}{J}$ with a κ ,

$$\kappa = \frac{K}{J}. \quad (2.4)$$

If we set $\rho = 1$, then there is no distinct surface exchange, and the model reduces to the one considered in Fjærbu et al. [2017].

2.2 Néel state

Consider now a so-called *Néel state* $|N\rangle$ for our antiferromagnetic layer. This state is characterised by alternating maximal spins along the z-axis, so that the nearest neighbours of each spin site have spins in the opposite direction. Two sublattices can be defined: sublattice \mathbb{A} consisting of all sites with spin up and sublattice \mathbb{B} consisting of all sites with spin down. It is then clear that $\mathbb{T} = \mathbb{A} \cup \mathbb{B}$. Later on, we will also need to consider the part of the sublattices in each plane, so we define indexed \mathbb{A} and \mathbb{B} for this purpose: $\mathbb{A}_p = \mathbb{A} \cap \mathbb{P}_p$ and $\mathbb{B}_p = \mathbb{B} \cap \mathbb{P}_p$ for each plane index p between 1 and N .

A rough picture of one plane of the Néel state is shown in figure 2.2.

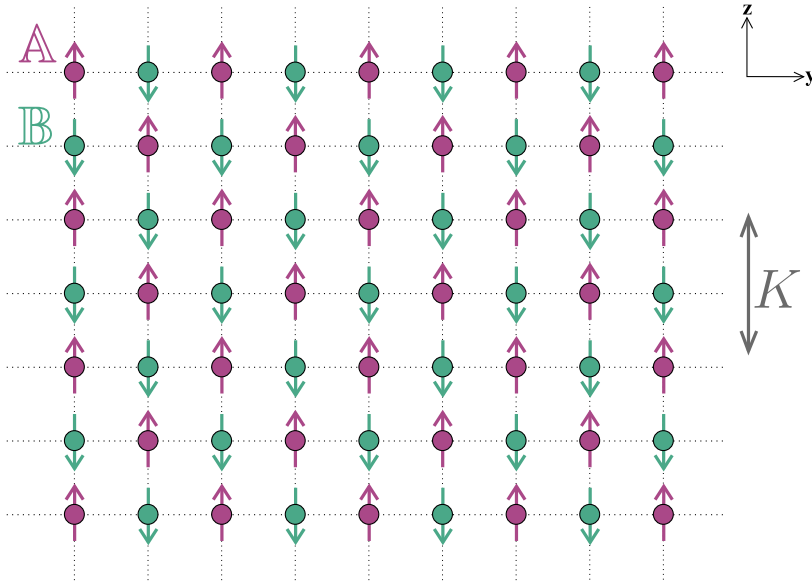


Figure 2.2: The Néel state of the antiferromagnetic layer has alternating maximal spins along the z-axis. Sublattice \mathbb{A} is the sublattice of spin up, while sublattice \mathbb{B} is the sublattice of spin down.

Note that the maximal value of each spin along the z-axis is $\pm\hbar s$, but the magnitude of each spin vector is always $\hbar\sqrt{s(s+1)}$ and so actually a little larger. Thus although the spins are said to be "along the z-axis", there is always a small perpendicular component. This perpendicular component can be shown to have the magnitude $\hbar\sqrt{s}$, but the expected value of the component in any perpendicular direction is zero due to symmetry.

The Néel state seems like a sensible ground state for our antiferromagnetic layer, since the alternating spins along the z-axis would classically minimize both the dot product terms and the easy-axis term of the Hamiltonian (2.2). However quantum-mechanically it is *not* the exact ground state of the model. This can be shown by considering what the spin dot product terms do mathematically to the Néel state.

Each dot product is taken between nearest neighbour spins, and so we know that one of the spins lies in the up sublattice \mathbb{A} , while the other lies in the down sublattice \mathbb{B} . Therefore we can look at a general dot product between an up spin on a site $\vec{a} \in \mathbb{A}$ and a down spin on a site $\vec{b} \in \mathbb{B}$. Writing out the spin dot product we see that

$$\vec{S}_{\vec{a}} \cdot \vec{S}_{\vec{b}} = S_{\vec{a}x}S_{\vec{b}x} + S_{\vec{a}y}S_{\vec{b}y} + S_{\vec{a}z}S_{\vec{b}z}, \quad (2.5)$$

so each dot product term actually corresponds to three operator terms. Note next that

$$S_{\vec{a}\pm}S_{\vec{b}\mp} = (S_{\vec{a}x} \pm iS_{\vec{a}y})(S_{\vec{b}x} \mp iS_{\vec{b}y}) = S_{\vec{a}x}S_{\vec{b}x} + S_{\vec{a}y}S_{\vec{b}y} \pm i(S_{\vec{a}y}S_{\vec{b}x} - S_{\vec{a}x}S_{\vec{b}y}), \quad (2.6)$$

and so

$$S_{\vec{a}x}S_{\vec{b}x} + S_{\vec{a}y}S_{\vec{b}y} = \frac{1}{2}(S_{\vec{a}+}S_{\vec{b}-} + S_{\vec{a}-}S_{\vec{b}+}). \quad (2.7)$$

Now let the operator (2.7) work on the Néel state $|N\rangle$. Since the spins at the sites \vec{a} and \vec{b} are already up and down, the first term will vanish; it is not possible to raise the up spin or lower the down spin further. The second term, however, will shift the z-components of the two spins one step down and one step up, respectively. Because the total spin magnitude is constant, this shift can be viewed as "tilting the spins one step away from the z-axis". (Imagining the spins as classical vectors, their x- and y-components have to grow when their z-components shrink.) The resulting state is thus a new state where the two spins at \vec{a} and \vec{b} have been tilted.

Since the Hamiltonian (2.2) contains one operator (2.7) for each pair of neighbouring sites, the effect of this part of \mathbf{H} on $|N\rangle$ is to create a superposition of different tilt states. But the other part of \mathbf{H} consists of z-component spin terms, which simply scale $|N\rangle$ because it is an eigenstate. In total then, the Hamiltonian creates a superposition of $|N\rangle$ and different tilt states when acting on $|N\rangle$. This new superposition is not a multiple of the original state, and so the Néel state $|N\rangle$ is not even an eigenstate of \mathbf{H} . Because it is not an eigenstate, it is certainly not the ground state.

Even though the Néel state $|N\rangle$ is not the actual ground state of our antiferromagnetic layer, it is common to assume that the actual ground state $|G\rangle$ is very close,

$$|G\rangle \approx |N\rangle. \quad (2.8)$$

In fact it is common to assume that *all* low energy states of the magnet are very close to the Néel state. This assumption is solely based on qualitative arguments such as the ones made above, but it is verified further if it leads to results that make sense and match the results from other models. The assumption greatly simplifies the problem, as it allows us to introduce so-called Holstein-Primakoff bosons. We will do this in the next section.

2.3 Holstein-Primakoff transformation

The spin operators in the Hamiltonian (2.2), while quite easy to grasp conceptually, are not ideal if we are to find the energy eigenstates of our antiferromagnetic layer. The goal is then to transform the various operators of the Hamiltonian into bosonic operators \mathbf{b}_\bullet with the simple commutation relation

$$\mathbf{b}_i \mathbf{b}_j^\dagger = \mathbf{b}_j^\dagger \mathbf{b}_i + \delta_{ij} \quad (2.9)$$

for all integers i and j , in such a way that the Hamiltonian takes on a diagonal form

$$\mathbf{H} = \sum_i \varepsilon_i \mathbf{b}_i^\dagger \mathbf{b}_i. \quad (2.10)$$

When the Hamiltonian has this form, the energy quanta of the system can be extracted directly from (2.10) as ε_\bullet .

They first step is to transform the spin operators $\vec{\mathbf{s}}_\bullet$ into bosonic operators through the so-called Holstein-Primakoff transformation. This transformation utilises the quantised nature of the spin ladder operators $\mathbf{s}_{\bullet\pm}$ by associating a boson type to each of them. An important difference between ordinary bosons and spin ladders is that while there is no restriction to the number of bosons a system can have, there is a fixed number of steps on the spin ladder. However, the Holstein-Primakoff transformation also incorporates this by collapsing the bosonic Fock space at the end of the ladder.

The full Holstein-Primakoff transformation for each spin site \vec{r} is

$$\begin{aligned} \mathbf{s}_{\vec{r}+} &= \begin{cases} \hbar \sqrt{2s - \mathbf{a}_{\vec{r}}^\dagger \mathbf{a}_{\vec{r}}} \mathbf{a}_{\vec{r}} & \text{if } \vec{r} \in \mathbb{A} \\ \hbar \mathbf{b}_{\vec{r}}^\dagger \sqrt{2s - \mathbf{b}_{\vec{r}}^\dagger \mathbf{b}_{\vec{r}}} & \text{if } \vec{r} \in \mathbb{B} \end{cases}, \\ \mathbf{s}_{\vec{r}-} &= \begin{cases} \mathbf{a}_{\vec{r}}^\dagger \sqrt{2s - \mathbf{a}_{\vec{r}}^\dagger \mathbf{a}_{\vec{r}}} & \text{if } \vec{r} \in \mathbb{A} \\ \hbar \sqrt{2s - \mathbf{b}_{\vec{r}}^\dagger \mathbf{b}_{\vec{r}}} \mathbf{b}_{\vec{r}} & \text{if } \vec{r} \in \mathbb{B} \end{cases}, \\ \mathbf{s}_{\vec{r}z} &= \begin{cases} \hbar(s - \mathbf{a}_{\vec{r}}^\dagger \mathbf{a}_{\vec{r}}) & \text{if } \vec{r} \in \mathbb{A} \\ -\hbar(s - \mathbf{b}_{\vec{r}}^\dagger \mathbf{b}_{\vec{r}}) & \text{if } \vec{r} \in \mathbb{B} \end{cases}, \end{aligned} \quad (2.11)$$

where \mathbf{a}_\bullet and \mathbf{b}_\bullet are bosonic operators that commute with each other and satisfy bosonic commutation relations similar to (2.9).

The transformation is defined differently for sites on sublattice \mathbb{A} and on sublattice \mathbb{B} , because we would like to consider the Néel state as the vacuum state with no bosons. Then, each Holstein-Primakoff boson tilts the spin of the Néel state one step away from the z -axis as described in section 2.2; the \mathbf{a}_\bullet bosons tilt one up spin on sublattice \mathbb{A} downwards, and the \mathbf{b}_\bullet bosons tilt one down spin on sublattice \mathbb{B} upwards. The effect of a Holstein-Primakoff boson on the Néel state is illustrated in figure 2.3.

The transformation (2.11) allows for a maximum number of $2s$ bosons, which corresponds to the end of the spin ladder where the spin have been tilted all the way around to the opposite direction. It is also pretty straightforward to show that the transformation is consistent with the commutation relations of the original spin operators.

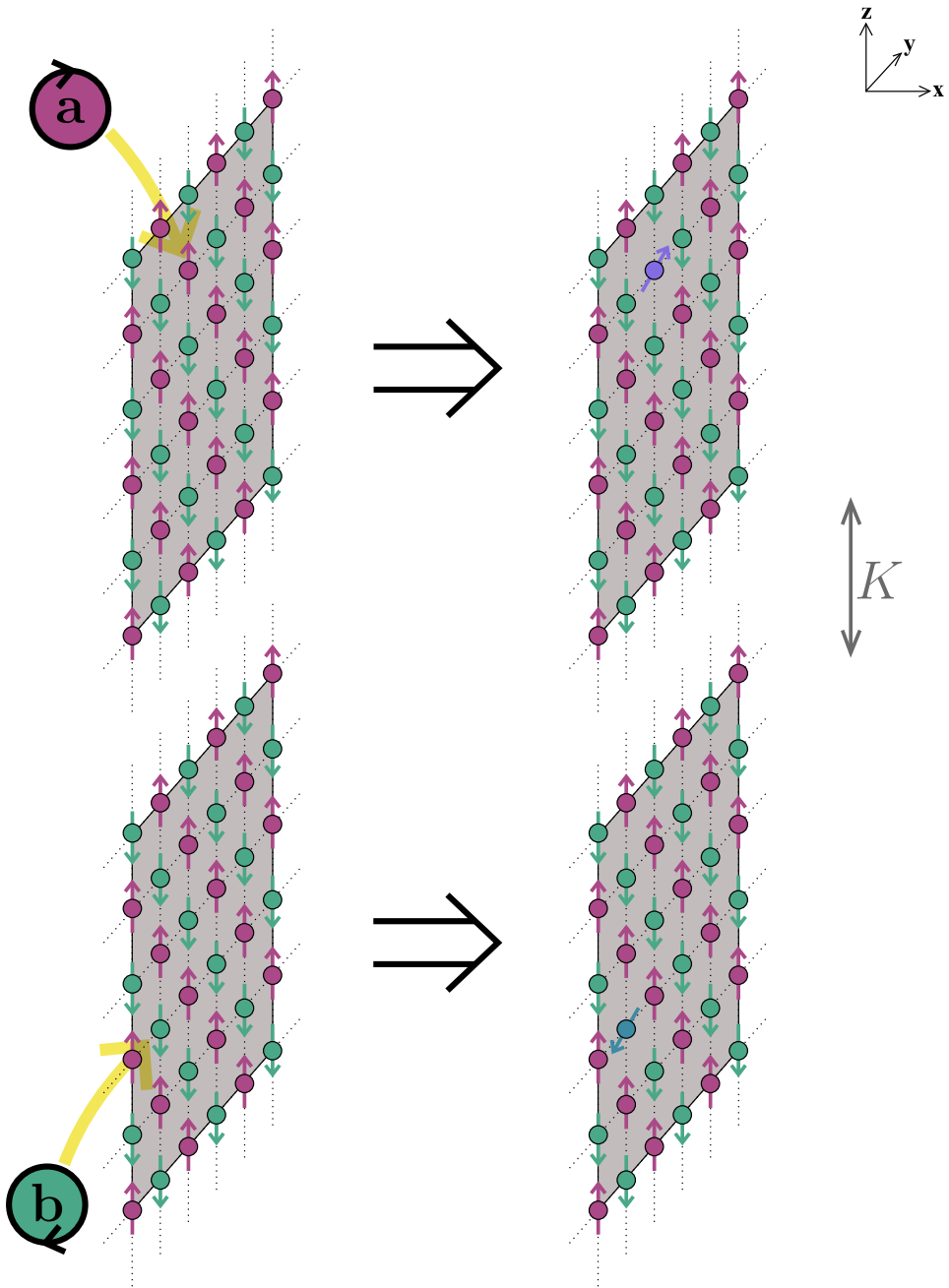


Figure 2.3: The Holstein-Primakoff bosons $a_{\vec{r}}$ and $b_{\vec{r}}$ tilt the spin of a given lattice site one step away from the z-axis. (Note that it is the operators $a_{\vec{r}}^\dagger$ and $b_{\vec{r}}^\dagger$ that actually create the bosons.)

As discussed in section 2.2, although the Néel state $|N\rangle$ is not the actual ground state of the system, it is qualitatively reasonable to assume that the low energy states of the magnet are very close to the Néel state. In terms of Holstein-Primakoff bosons, this corresponds to a very small number of bosons, as each boson represents a small deviation from the Néel state. If we assume that the number of Holstein-Primakoff bosons is very small, the transformation (2.11) can be simplified, because we only need to consider the lowest order bosonic terms in the Hamiltonian. Keeping in mind that each term in the Hamiltonian (2.2) contains exactly two spin operators, we see that the terms will have zero, two or four bosonic operators. Keeping only the zeroth order terms would give us a constant Hamiltonian, so we decide to also keep the second order terms while neglecting the fourth order terms. The Holstein-Primakoff transformation can then be approximated by

$$\begin{aligned} \mathbf{s}_{\vec{r}+} &\approx \begin{cases} \hbar\sqrt{2s} \mathbf{a}_{\vec{r}} & \text{if } \vec{r} \in \mathbb{A} \\ \hbar\sqrt{2s} \mathbf{b}_{\vec{r}}^\dagger & \text{if } \vec{r} \in \mathbb{B} \end{cases}, \\ \mathbf{s}_{\vec{r}-} &\approx \begin{cases} \hbar\sqrt{2s} \mathbf{a}_{\vec{r}}^\dagger & \text{if } \vec{r} \in \mathbb{A} \\ \hbar\sqrt{2s} \mathbf{b}_{\vec{r}} & \text{if } \vec{r} \in \mathbb{B} \end{cases}, \\ \mathbf{s}_{\vec{r}z} &= \begin{cases} \hbar(s - \mathbf{a}_{\vec{r}}^\dagger \mathbf{a}_{\vec{r}}) & \text{if } \vec{r} \in \mathbb{A} \\ -\hbar(s - \mathbf{b}_{\vec{r}}^\dagger \mathbf{b}_{\vec{r}}) & \text{if } \vec{r} \in \mathbb{B} \end{cases} \end{aligned} \quad (2.12)$$

for each spin site \vec{r} . Here the number operator terms in the square roots have been neglected because in the Hamiltonian they only give rise to terms of order higher than two. The z-component transformation is still kept exact because the number operator terms here give rise to terms of order two as well as terms of order four. Thus some additional fourth order terms will have to be neglected later.

Before we apply the transformation, we introduce a planar site number M to our model. Even though this number is meant to be infinite as the planes stretch out to infinity, it will help us keep track of some important aspects of the antiferromagnetic layer such as the ground state energy and the number of allowed wave vectors. The total number of lattice sites is then MN , while the number of neighbour site pairs in each plane is about $2M$. (Two pairs for each site — an approximation that is exact if we consider M to be infinite.)

The stage is set for us to consider the different spin products of the Hamiltonian (2.2) and transform them using (2.12). In all the following equations, spin sites \vec{a} and \vec{b} are assumed to be in sublattice \mathbb{A} and \mathbb{B} respectively. From equation (2.7) it follows that

$$\mathbf{s}_{\vec{a}x} \mathbf{s}_{\vec{b}x} + \mathbf{s}_{\vec{a}y} \mathbf{s}_{\vec{b}y} \approx \hbar^2 s (\mathbf{a}_{\vec{a}} \mathbf{b}_{\vec{b}} + \mathbf{a}_{\vec{a}}^\dagger \mathbf{b}_{\vec{b}}^\dagger) \quad (2.13)$$

when the transformation is applied. Furthermore, neglecting terms of fourth order, we see that

$$\mathbf{s}_{\vec{a}z} \mathbf{s}_{\vec{b}z} \approx -\hbar^2 s^2 + \hbar^2 s (\mathbf{a}_{\vec{a}}^\dagger \mathbf{a}_{\vec{a}} + \mathbf{b}_{\vec{b}}^\dagger \mathbf{b}_{\vec{b}}). \quad (2.14)$$

The last spin products that need to be considered are the ones in the easy-axis term. They are

$$\mathbf{s}_{\vec{a}z}^2 = \hbar^2 (s - \mathbf{a}_{\vec{a}}^\dagger \mathbf{a}_{\vec{a}})^2 \approx \hbar^2 s^2 - 2\hbar^2 s \mathbf{a}_{\vec{a}}^\dagger \mathbf{a}_{\vec{a}} \quad (2.15)$$

and

$$s_{bz}^2 = \hbar^2 (s - \mathbf{b}_b^\dagger \mathbf{b}_b)^2 \approx \hbar^2 s^2 - 2\hbar^2 s \mathbf{b}_b^\dagger \mathbf{b}_b, \quad (2.16)$$

again neglecting terms of fourth order.

With the spin products (2.13)–(2.16) calculated, we can finally transform the Hamiltonian (2.2) into its new form. Writing out every spin product and summing over all neighbour site pairs and all sites where possible, we end up with the following expression:

$$\begin{aligned} \mathbf{H} = & - \left(4S + (3N - 5)J + NK \right) Ms(s + 1) \\ & + Ss \sum_{\vec{a}:\vec{b} \in \mathbb{P}_1} (\mathbf{a}_{\vec{a}} \mathbf{b}_{\vec{b}} + \mathbf{a}_{\vec{a}}^\dagger \mathbf{b}_{\vec{b}}^\dagger + \mathbf{a}_{\vec{a}}^\dagger \mathbf{a}_{\vec{a}} + \mathbf{b}_{\vec{b}} \mathbf{b}_{\vec{b}}^\dagger) \\ & + \sum_{p=2}^{N-1} Js \sum_{\vec{a}:\vec{b} \in \mathbb{P}_p} (\mathbf{a}_{\vec{a}} \mathbf{b}_{\vec{b}} + \mathbf{a}_{\vec{a}}^\dagger \mathbf{b}_{\vec{b}}^\dagger + \mathbf{a}_{\vec{a}}^\dagger \mathbf{a}_{\vec{a}} + \mathbf{b}_{\vec{b}} \mathbf{b}_{\vec{b}}^\dagger) \\ & + Ss \sum_{\vec{a}:\vec{b} \in \mathbb{P}_N} (\mathbf{a}_{\vec{a}} \mathbf{b}_{\vec{b}} + \mathbf{a}_{\vec{a}}^\dagger \mathbf{b}_{\vec{b}}^\dagger + \mathbf{a}_{\vec{a}}^\dagger \mathbf{a}_{\vec{a}} + \mathbf{b}_{\vec{b}} \mathbf{b}_{\vec{b}}^\dagger) \\ & + \sum_{p=1}^{N-1} Js \left(\sum_{\vec{a} \in \mathbb{A}_p} (\mathbf{a}_{\vec{a}} \mathbf{b}_{\vec{a}+\vec{l}_x} + \mathbf{a}_{\vec{a}}^\dagger \mathbf{b}_{\vec{a}+\vec{l}_x}^\dagger + \mathbf{a}_{\vec{a}}^\dagger \mathbf{a}_{\vec{a}} + \mathbf{b}_{\vec{a}+\vec{l}_x} \mathbf{b}_{\vec{a}+\vec{l}_x}^\dagger) \right. \\ & \left. + \sum_{\vec{b} \in \mathbb{B}_p} (\mathbf{a}_{\vec{b}+\vec{l}_x} \mathbf{b}_{\vec{b}} + \mathbf{a}_{\vec{b}+\vec{l}_x}^\dagger \mathbf{b}_{\vec{b}}^\dagger + \mathbf{a}_{\vec{b}+\vec{l}_x}^\dagger \mathbf{a}_{\vec{b}+\vec{l}_x} + \mathbf{b}_{\vec{b}} \mathbf{b}_{\vec{b}}^\dagger) \right) \\ & + 2Ks \left(\sum_{\vec{a} \in \mathbb{A}} \mathbf{a}_{\vec{a}}^\dagger \mathbf{a}_{\vec{a}} + \sum_{\vec{b} \in \mathbb{B}} \mathbf{b}_{\vec{b}} \mathbf{b}_{\vec{b}}^\dagger \right). \quad (2.17) \end{aligned}$$

The first constant term is the classical ground state energy of the antiferromagnetic layer for spin vectors of magnitude $\hbar\sqrt{s(s+1)}$:

$$E_G = - \left(4S + (3N - 5)J + NK \right) Ms(s + 1). \quad (2.18)$$

This will also be the quantum ground state energy as long as no more constant terms drop out later on.

The second, third and fourth terms of the Holstein-Primakoff transformed Hamiltonian (2.17) all represent *intraplanar* spin interactions (within each plane), while the fifth term represents *interplanar* spin interactions (between planes). The sixth and last term stems from the easy-axis anisotropy.

2.4 Fourier transformation

Now that the Hamiltonian is expressed in terms of bosonic operators $\mathbf{a}_{\vec{a}}$ and $\mathbf{b}_{\vec{b}}$, the next step is to transform it further until it ends up in a diagonal form such as (2.10). To this

end we introduce bosonic *operator waves* through a Fourier transformation in the yz -plane. This transformation will greatly simplify the intraplanar interactions, as the Fourier bosons are delocalised over the planes.

Before we can introduce Fourier bosons however, we will have to look at the lattice to find allowed wave vectors. Define first the *planar lattice* with lattice vectors

$$\begin{aligned}\vec{l}_1 &= \vec{l}_y + \vec{l}_z = l(\vec{e}_y + \vec{e}_z), \\ \vec{l}_2 &= \vec{l}_y - \vec{l}_z = l(\vec{e}_y - \vec{e}_z)\end{aligned}\quad (2.19)$$

and lattice sites given through

$$\vec{r}_{mn} = m\vec{l}_1 + n\vec{l}_2 \quad (2.20)$$

for integers m and n between $-G$ and $(G + 1)$. If we let G be infinitely large, this lattice spans over all lattice sites of sublattice \mathbb{A} or sublattice \mathbb{B} in any plane, depending on where we place the origin. There are $(2G + 2)^2$ sites in the lattice, so the relation to the total planar site number M is

$$M = 2(2G + 2)^2. \quad (2.21)$$

The planar lattice is illustrated in figure 2.4. Note that the lattice constant for the planar lattice is $\sqrt{2}l$.

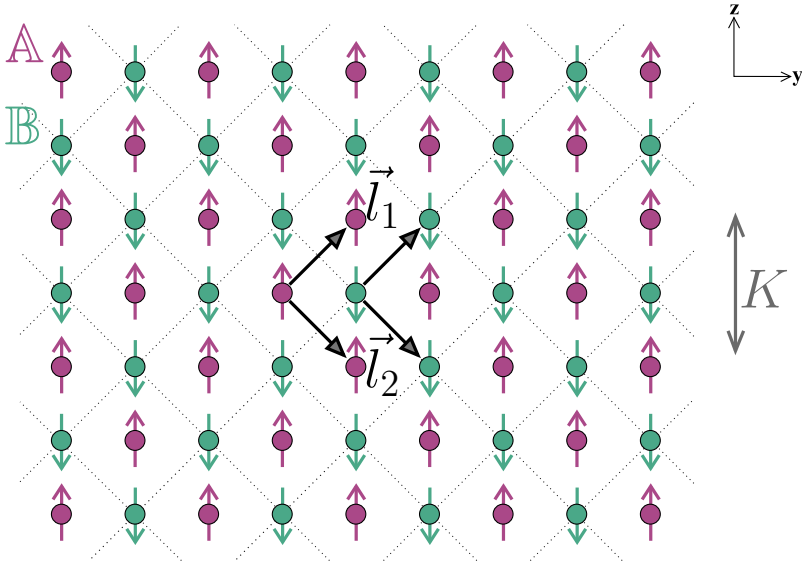


Figure 2.4: The planar lattice, with lattice vectors \vec{l}_1 and \vec{l}_2 , describes both sublattice \mathbb{A} and sublattice \mathbb{B} for any plane, depending on where the origin is placed. The lattice constant for the planar lattice is $\sqrt{2}l$.

Next, let us construct the reciprocal planar lattice. This lattice has lattice vectors

$$\begin{aligned}\vec{g}_1 &= \frac{\pi}{l}(\vec{e}_y + \vec{e}_z), \\ \vec{g}_2 &= \frac{\pi}{l}(\vec{e}_y - \vec{e}_z),\end{aligned}\tag{2.22}$$

as can be easily constructed from the relation

$$\vec{l}_i \cdot \vec{g}_j = 2\pi\delta_{ij}.\tag{2.23}$$

With this reciprocal planar lattice defined, we move on to construct a *wave lattice* of allowed wave vectors. This wave lattice lies within the Brillouin zone of the reciprocal planar lattice and is given by

$$\vec{k}_{mn} = \frac{m}{2G+2}\vec{g}_1 + \frac{n}{2G+2}\vec{g}_2 = \frac{\pi}{l}\frac{m+n}{2G+2}\vec{e}_y + \frac{\pi}{l}\frac{m-n}{2G+2}\vec{e}_z\tag{2.24}$$

for all integers m and n between $-G$ and $(G+1)$. There are $(2G+2)^2$ wave vectors in the wave lattice, which is the same as the number of sites in the planar lattice. The wave lattice is discrete, but it essentially becomes continuous and fills up the Brillouin zone in the limit when M (and thus G) tend to infinity. The Brillouin zone is depicted in figure 2.5.

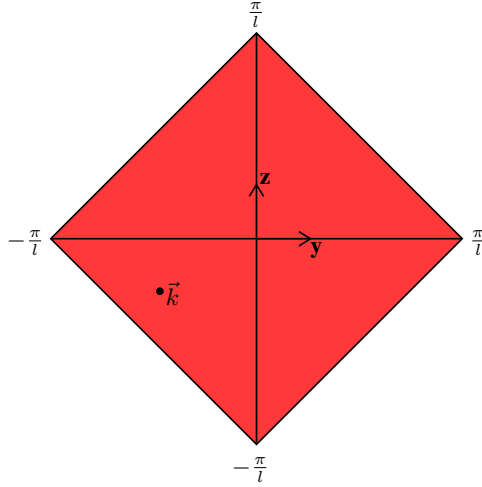


Figure 2.5: The Brillouin zone of the antiferromagnetic layer (indicated in red). Because the planar lattice size G is taken to be infinite, all planar wave vectors \vec{k} within the Brillouin zone are possible.

Define at last the operator waves

$$\begin{aligned}\mathbf{a}_{\vec{k},p} &= \frac{1}{2G+2} \sum_{\vec{r}} e^{i\vec{k}\cdot\vec{r}} \mathbf{a}_{p,\vec{r}}, \\ \mathbf{b}_{\vec{k},p} &= \frac{1}{2G+2} \sum_{\vec{r}} e^{i\vec{k}\cdot\vec{r}} \mathbf{b}_{p,\vec{r}}\end{aligned}\tag{2.25}$$

for all wave vectors \vec{k} in the wave lattice (2.24). Here the Holstein-Primakoff operators \mathbf{a}_{\bullet} and \mathbf{b}_{\bullet} are subscripted with the plane index p and the planar position vector \vec{r} instead of the regular position vector. The sums run through every planar lattice site.

From here on, we will need the useful sums

$$\sum_{\vec{r}} e^{i(\vec{k}' - \vec{k}'') \cdot \vec{r}} = (2G + 2)^2 \delta_{\vec{k}', \vec{k}''}, \quad (2.26)$$

$$\sum_{\vec{k}} e^{i\vec{k} \cdot (\vec{r}' - \vec{r}'')} = (2G + 2)^2 \delta_{\vec{r}', \vec{r}''}. \quad (2.27)$$

These hold for all pairs of wave vectors \vec{k}' and \vec{k}'' , and all pairs of planar lattice sites \vec{r}' and \vec{r}'' , respectively. It is fairly easy to prove that they follow from the definitions above. Among other things, the sums can be used to prove that the operator waves (2.25) are in fact bosonic operators with commutation relations similar to (2.9). Such a transformation that preserves the bosonic commutation relations is called a *canonical* transformation.

The sums (2.26) and (2.27) can also be used to prove the back transformation

$$\begin{aligned} \mathbf{a}_{p, \vec{r}} &= \frac{1}{2G + 2} \sum_{\vec{k}} e^{-i\vec{k} \cdot \vec{r}} \mathbf{a}_{\vec{k}, p}, \\ \mathbf{b}_{p, \vec{r}} &= \frac{1}{2G + 2} \sum_{\vec{k}} e^{-i\vec{k} \cdot \vec{r}} \mathbf{b}_{\vec{k}, p}, \end{aligned} \quad (2.28)$$

which is remarkably simple. To summarise, the transformation (2.25) is both canonical and neat, and it is known as the *Fourier transformation*.

Each Fourier operator (2.25) is a sum of Holstein-Primakoff operators within one plane, with a complex plane wave distribution of amplitudes. The effect of such an operator on the Néel state $|N\rangle$ is to create a superposition of states in which exactly one spin has been tilted away from the z-axis. The probability of each state is equal, because the modulus of each amplitude is the same. Thus, one can visualize a Fourier boson as *one* spin tilt spread randomly across the given plane. Figure 2.6 illustrates this.

Using the Fourier back transformation (2.28) as well as the sums (2.26) and (2.27), we can start transforming the Hamiltonian (2.17). There are eight types of operator product sums involved that we need to consider. The first one is $\sum_{\vec{a}, \vec{b} \in \mathbb{P}_p} \mathbf{a}_{\vec{a}} \mathbf{b}_{\vec{b}}$. Introducing the planar neighbour vector $\vec{\delta}$, we can rewrite this sum over neighbouring pairs to a double sum as follows:

$$\sum_{\vec{a}, \vec{b} \in \mathbb{P}_p} \mathbf{a}_{\vec{a}} \mathbf{b}_{\vec{b}} = \sum_{\vec{r}} \sum_{\vec{\delta}} \mathbf{a}_{p, \vec{r}} \mathbf{b}_{p, \vec{r} + \vec{\delta}}.$$

The sum over $\vec{\delta}$ runs through each of the four planar neighbour vectors \vec{l}_y , $-\vec{l}_y$, \vec{l}_z and $-\vec{l}_z$. Transforming to Fourier operators we end up with

$$\sum_{\vec{a}, \vec{b} \in \mathbb{P}_p} \mathbf{a}_{\vec{a}} \mathbf{b}_{\vec{b}} = \sum_{\vec{k}} \omega_{\vec{k}} \mathbf{a}_{\vec{k}, p} \mathbf{b}_{-\vec{k}, p} \quad (2.29)$$

after some algebra. Here, the important *wave parameter*

$$\omega_{\vec{k}} = 2(\cos(lk_y) + \cos(lk_z)) \quad (2.30)$$

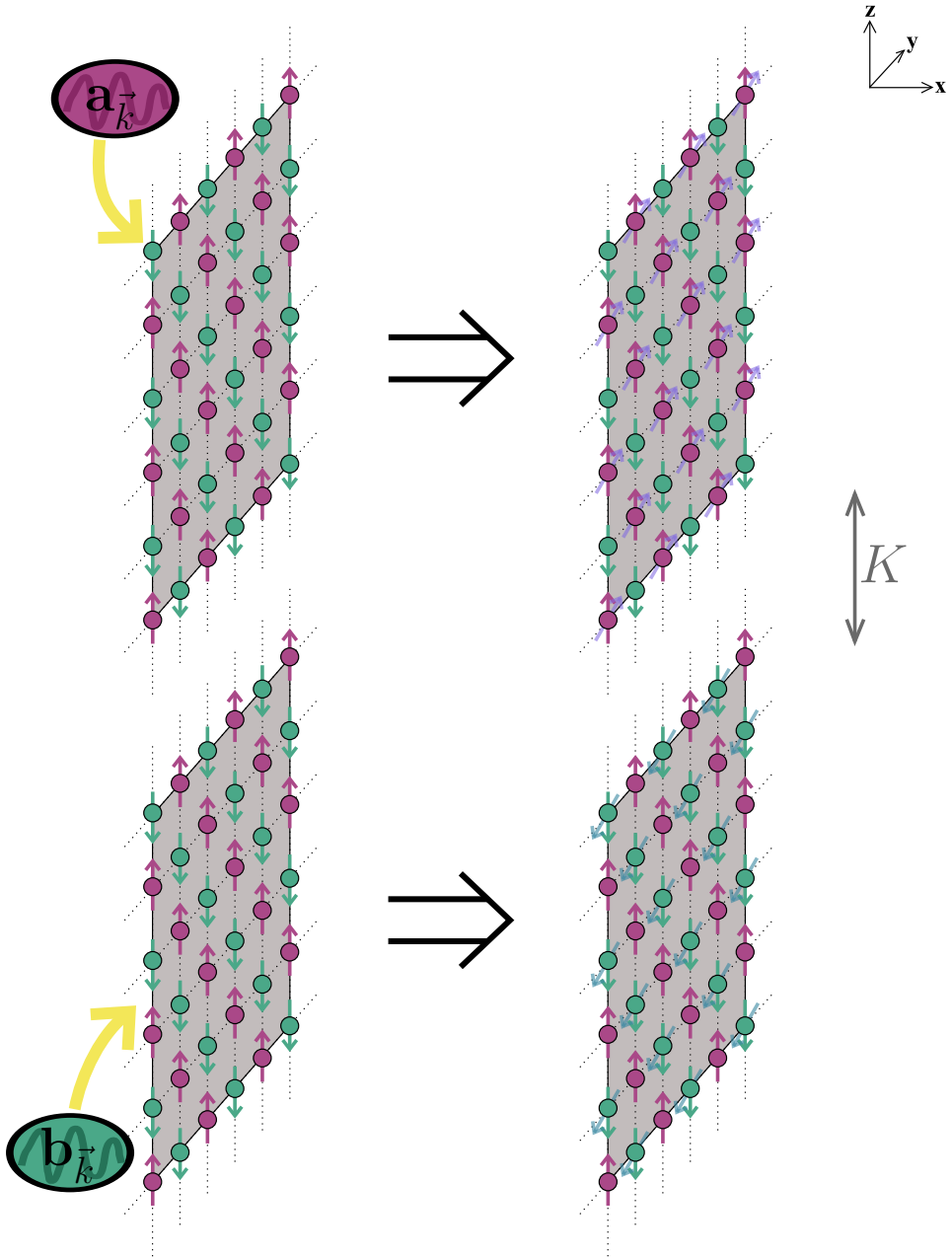


Figure 2.6: The Fourier bosons $a_{\vec{k},p}$ and $b_{\vec{k},p}$ tilt one spin in the plane \mathbb{P}_p , but the exact position of the spin tilt is randomly spread across the plane. (Note that it is the operators $a_{\vec{k},p}^\dagger$ and $b_{\vec{k},p}^\dagger$ that actually create the bosons.)

has been defined. The next sum, $\sum_{\vec{a}, \vec{b} \in \mathbb{P}_p} \mathbf{a}_{\vec{a}}^\dagger \mathbf{b}_{\vec{b}}^\dagger$, is just the adjoint of (2.29), and since $\omega_{\vec{k}}$ is real it follows straightforwardly that

$$\sum_{\vec{a}, \vec{b} \in \mathbb{P}_p} \mathbf{a}_{\vec{a}}^\dagger \mathbf{b}_{\vec{b}}^\dagger = \sum_{\vec{k}} \omega_{\vec{k}} \mathbf{a}_{\vec{k}, p}^\dagger \mathbf{b}_{-\vec{k}, p}^\dagger. \quad (2.31)$$

The operator $\mathbf{b}_{-\vec{k}, p}$ in the equations above seems ill-defined in the special case of a wave vector \vec{k} on the edge of the Brillouin zone, that is when m or n is equal to $(G + 1)$ in (2.24), because m and n is only allowed to run to $-G$ in the negative direction. However, any wave vector *outside* the Brillouin zone corresponds to a wave vector *in* the Brillouin zone by adding or subtracting an appropriate amount of reciprocal lattice vectors (2.22), as can be seen from the definition of the Fourier operators (2.25) using the dot product relation (2.23). In the case of a wave vector \vec{k} on the edge of the Brillouin zone, it turns out that $\mathbf{b}_{-\vec{k}, p} = \mathbf{b}_{\vec{k}, p}$, so there is no problem with summing over the negative of \vec{k} in the equations.

Considering now the third sum $\sum_{\vec{a} \in \mathbb{A}_p} \mathbf{a}_{\vec{a}}^\dagger \mathbf{a}_{\vec{a}}$, we rewrite the sum to

$$\sum_{\vec{a} \in \mathbb{A}_p} \mathbf{a}_{\vec{a}}^\dagger \mathbf{a}_{\vec{a}} = \sum_{\vec{r}} \mathbf{a}_{p, \vec{r}}^\dagger \mathbf{a}_{p, \vec{r}}$$

and transform it to get the simple result

$$\sum_{\vec{a} \in \mathbb{A}_p} \mathbf{a}_{\vec{a}}^\dagger \mathbf{a}_{\vec{a}} = \sum_{\vec{k}} \mathbf{a}_{\vec{k}, p}^\dagger \mathbf{a}_{\vec{k}, p}. \quad (2.32)$$

A similar calculation for the fourth sum $\sum_{\vec{b} \in \mathbb{B}_p} \mathbf{b}_{\vec{b}} \mathbf{b}_{\vec{b}}^\dagger$ provides

$$\sum_{\vec{b} \in \mathbb{B}_p} \mathbf{b}_{\vec{b}} \mathbf{b}_{\vec{b}}^\dagger = \sum_{\vec{k}} \mathbf{b}_{-\vec{k}, p} \mathbf{b}_{-\vec{k}, p}^\dagger. \quad (2.33)$$

Here we used the fact that summing over the negative of \vec{k} is identical to summing over the positive of \vec{k} , which follows straightforwardly from the discussion above.

For the interplanar sum $\sum_{\vec{a} \in \mathbb{A}_p} \mathbf{a}_{\vec{a}} \mathbf{b}_{\vec{a} + \vec{l}_x}$ we rewrite

$$\sum_{\vec{a} \in \mathbb{A}_p} \mathbf{a}_{\vec{a}} \mathbf{b}_{\vec{a} + \vec{l}_x} = \sum_{\vec{r}} \mathbf{a}_{p, \vec{r}} \mathbf{b}_{p+1, \vec{r}}$$

and get

$$\begin{aligned} \sum_{\vec{a} \in \mathbb{A}_p} \mathbf{a}_{\vec{a}} \mathbf{b}_{\vec{a} + \vec{l}_x} &= \sum_{\vec{k}} \mathbf{a}_{\vec{k}, p} \mathbf{b}_{-\vec{k}, p+1}, \\ \sum_{\vec{a} \in \mathbb{A}_p} \mathbf{a}_{\vec{a}}^\dagger \mathbf{b}_{\vec{a} + \vec{l}_x}^\dagger &= \sum_{\vec{k}} \mathbf{a}_{\vec{k}, p}^\dagger \mathbf{b}_{-\vec{k}, p+1}^\dagger. \end{aligned} \quad (2.34)$$

Similarly, for $\sum_{\vec{b} \in \mathbb{B}_p} \mathbf{a}_{\vec{b}+\vec{l}_x} \mathbf{b}_{\vec{b}}$ we get

$$\begin{aligned} \sum_{\vec{b} \in \mathbb{B}_p} \mathbf{a}_{\vec{b}+\vec{l}_x} \mathbf{b}_{\vec{b}} &= \sum_{\vec{k}} \mathbf{a}_{\vec{k},p+1} \mathbf{b}_{-\vec{k},p}, \\ \sum_{\vec{b} \in \mathbb{B}_p} \mathbf{a}_{\vec{b}+\vec{l}_x}^\dagger \mathbf{b}_{\vec{b}}^\dagger &= \sum_{\vec{k}} \mathbf{a}_{\vec{k},p+1}^\dagger \mathbf{b}_{-\vec{k},p}^\dagger. \end{aligned} \quad (2.35)$$

With the eight operator product sums (2.29)–(2.35) calculated, only insertion into the Hamiltonian (2.17) remains. This is fairly straightforward and results in the following operator:

$$\begin{aligned} \mathbf{H} &= -\left(4S + (3N - 5)J + NK\right)Ms(s + 1) \\ &\quad + Ss \sum_{\vec{k}} \left(\omega_{\vec{k}} (\mathbf{a}_{\vec{k},1} \mathbf{b}_{-\vec{k},1} + \mathbf{a}_{\vec{k},1}^\dagger \mathbf{b}_{-\vec{k},1}^\dagger) + 4(\mathbf{a}_{\vec{k},1}^\dagger \mathbf{a}_{\vec{k},1} + \mathbf{b}_{-\vec{k},1} \mathbf{b}_{-\vec{k},1}^\dagger) \right) \\ &\quad + \sum_{p=2}^{N-1} Js \sum_{\vec{k}} \left(\omega_{\vec{k}} (\mathbf{a}_{\vec{k},p} \mathbf{b}_{-\vec{k},p} + \mathbf{a}_{\vec{k},p}^\dagger \mathbf{b}_{-\vec{k},p}^\dagger) + 4(\mathbf{a}_{\vec{k},p}^\dagger \mathbf{a}_{\vec{k},p} + \mathbf{b}_{-\vec{k},p} \mathbf{b}_{-\vec{k},p}^\dagger) \right) \\ &\quad + Ss \sum_{\vec{k}} \left(\omega_{\vec{k}} (\mathbf{a}_{\vec{k},N} \mathbf{b}_{-\vec{k},N} + \mathbf{a}_{\vec{k},N}^\dagger \mathbf{b}_{-\vec{k},N}^\dagger) + 4(\mathbf{a}_{\vec{k},N}^\dagger \mathbf{a}_{\vec{k},N} + \mathbf{b}_{-\vec{k},N} \mathbf{b}_{-\vec{k},N}^\dagger) \right) \\ &\quad + \sum_{p=1}^{N-1} Js \sum_{\vec{k}} \left(\mathbf{a}_{\vec{k},p} \mathbf{b}_{-\vec{k},p+1} + \mathbf{a}_{\vec{k},p}^\dagger \mathbf{b}_{-\vec{k},p+1}^\dagger + \mathbf{a}_{\vec{k},p}^\dagger \mathbf{a}_{\vec{k},p} + \mathbf{b}_{-\vec{k},p+1} \mathbf{b}_{-\vec{k},p+1}^\dagger \right. \\ &\quad \left. + \mathbf{a}_{\vec{k},p+1} \mathbf{b}_{-\vec{k},p} + \mathbf{a}_{\vec{k},p+1}^\dagger \mathbf{b}_{-\vec{k},p}^\dagger + \mathbf{a}_{\vec{k},p+1}^\dagger \mathbf{a}_{\vec{k},p+1} + \mathbf{b}_{-\vec{k},p} \mathbf{b}_{-\vec{k},p}^\dagger \right) \\ &\quad + \sum_{p=1}^N 2Ks \sum_{\vec{k}} \left(\mathbf{a}_{\vec{k},p}^\dagger \mathbf{a}_{\vec{k},p} + \mathbf{b}_{-\vec{k},p} \mathbf{b}_{-\vec{k},p}^\dagger \right). \end{aligned} \quad (2.36)$$

This long operator can be rewritten to

$$\mathbf{H} = E_G + Js \sum_{\vec{k}} \mathbf{h}_{\vec{k}} \quad (2.37)$$

if we use the ground state energy E_G defined in (2.18) and introduce the dimensionless

partial Hamiltonian operators $\mathbf{h}_{\vec{k}}$, defined as

$$\begin{aligned}
 \mathbf{h}_{\vec{k}} = & \rho \left(\omega_{\vec{k}} (\mathbf{a}_{\vec{k},1} \mathbf{b}_{-\vec{k},1} + \mathbf{a}_{\vec{k},1}^\dagger \mathbf{b}_{-\vec{k},1}^\dagger) + 4(\mathbf{a}_{\vec{k},1}^\dagger \mathbf{a}_{\vec{k},1} + \mathbf{b}_{-\vec{k},1} \mathbf{b}_{-\vec{k},1}^\dagger) \right) \\
 & + \sum_{p=2}^{N-1} \left(\omega_{\vec{k}} (\mathbf{a}_{\vec{k},p} \mathbf{b}_{-\vec{k},p} + \mathbf{a}_{\vec{k},p}^\dagger \mathbf{b}_{-\vec{k},p}^\dagger) + 4(\mathbf{a}_{\vec{k},p}^\dagger \mathbf{a}_{\vec{k},p} + \mathbf{b}_{-\vec{k},p} \mathbf{b}_{-\vec{k},p}^\dagger) \right) \\
 & + \rho \left(\omega_{\vec{k}} (\mathbf{a}_{\vec{k},N} \mathbf{b}_{-\vec{k},N} + \mathbf{a}_{\vec{k},N}^\dagger \mathbf{b}_{-\vec{k},N}^\dagger) + 4(\mathbf{a}_{\vec{k},N}^\dagger \mathbf{a}_{\vec{k},N} + \mathbf{b}_{-\vec{k},N} \mathbf{b}_{-\vec{k},N}^\dagger) \right) \\
 & + \sum_{p=1}^{N-1} \left(\mathbf{a}_{\vec{k},p} \mathbf{b}_{-\vec{k},p+1} + \mathbf{a}_{\vec{k},p}^\dagger \mathbf{b}_{-\vec{k},p+1}^\dagger + \mathbf{a}_{\vec{k},p}^\dagger \mathbf{a}_{\vec{k},p} + \mathbf{b}_{-\vec{k},p+1} \mathbf{b}_{-\vec{k},p+1}^\dagger \right. \\
 & \left. + \mathbf{a}_{\vec{k},p+1} \mathbf{b}_{-\vec{k},p} + \mathbf{a}_{\vec{k},p+1}^\dagger \mathbf{b}_{-\vec{k},p}^\dagger + \mathbf{a}_{\vec{k},p+1}^\dagger \mathbf{a}_{\vec{k},p+1} + \mathbf{b}_{-\vec{k},p} \mathbf{b}_{-\vec{k},p}^\dagger \right) \\
 & + \sum_{p=1}^N 2\kappa \left(\mathbf{a}_{\vec{k},p}^\dagger \mathbf{a}_{\vec{k},p} + \mathbf{b}_{-\vec{k},p} \mathbf{b}_{-\vec{k},p}^\dagger \right) \quad (2.38)
 \end{aligned}$$

for all wave vectors \vec{k} in the wave lattice (2.24). We see that our Hamiltonian in (2.37) is beginning to approach the diagonal form of equation (2.10). If the operators $\mathbf{h}_{\vec{k}}$ could just be rewritten to a diagonal form in some bosonic operators, the problem would be solved. To this end, we omit the wave vector subscript from here on and focus on the diagonalisation of a general partial Hamiltonian \mathbf{h} . Note however that \mathbf{a}_p corresponds to $\mathbf{a}_{\vec{k},p}$, \mathbf{b}_p corresponds to $\mathbf{b}_{-\vec{k},p}$ and ω corresponds to $\omega_{\vec{k}}$ in all the following calculations.

The general partial Hamiltonian \mathbf{h} can be expressed quite neatly in block matrix form as

$$\mathbf{h} = \begin{bmatrix} \bar{\mathbf{a}}^\dagger & \bar{\mathbf{b}} \end{bmatrix} \begin{bmatrix} \boxed{D} & \boxed{C} \\ \boxed{C} & \boxed{D} \end{bmatrix} \begin{bmatrix} \bar{\mathbf{a}} \\ \bar{\mathbf{b}}^\dagger \end{bmatrix}, \quad (2.39)$$

where the vectors on each side have dimension $2N$ and contain one of each operator \mathbf{a}_\bullet and \mathbf{b}_\bullet (or their adjoints where denoted). The $N \times N$ submatrices \boxed{C} and \boxed{D} are defined as

$$\boxed{C} = \begin{bmatrix} \omega\rho & 1 & & & & & \\ 1 & \omega & 1 & & & & \\ & 1 & \omega & 1 & & & \\ & & \ddots & \ddots & \ddots & & \\ & & & 1 & \omega & 1 & \\ & & & & 1 & \omega\rho & \end{bmatrix} \quad (2.40)$$

and

$$\boxed{D} = \begin{bmatrix} d_S & & & & & & \\ & d_B & & & & & \\ & & d_B & & & & \\ & & & \ddots & & & \\ & & & & d_B & & \\ & & & & & d_S & \end{bmatrix}, \quad (2.41)$$

where the coefficients d_S and d_B have been introduced as

$$\begin{aligned} d_S &= 4\rho + 1 + 2\kappa, \\ d_B &= 6 + 2\kappa. \end{aligned} \quad (2.42)$$

The subscripts "S" and "B" denote "surface" and "bulk" respectively, as the coefficients are associated with spin exchange in those parts of the antiferromagnetic layer.

Before we move on, let us find the possible values for the wave parameter ω , which was defined in (2.30). From the wave vector expression (2.24) we see that the involved cosine phases are

$$\begin{aligned} lk_y &= \frac{m+n}{2G+2}\pi, \\ lk_z &= \frac{m-n}{2G+2}\pi \end{aligned} \quad (2.43)$$

for integer values m and n between $-G$ and $(G+1)$. Using the trigonometric identity

$$2 \cos \alpha \cos \beta = \cos(\alpha + \beta) + \cos(\alpha - \beta), \quad (2.44)$$

which is valid for all phases α and β in \mathbb{R} , ω can then be rewritten to

$$\omega = 4 \cos\left(\frac{m}{2G+2}\pi\right) \cos\left(\frac{n}{2G+2}\pi\right). \quad (2.45)$$

Since the cosine arguments are both in the interval $\langle -\frac{\pi}{2}, \frac{\pi}{2} \rangle$, it is now clear that

$$0 \leq \omega \leq 4., \quad (2.46)$$

ω takes its maximal value of 4 only for $m = n = 0$ (which corresponds to the center of the Brillouin zone) and its minimal value of 0 for $m = (G+1)$ or $n = (G+1)$ (which correspond to the edges of the Brillouin zone). In figure 2.7 the wave parameter is plotted as a function of the ratios $\mu = \frac{m}{2G+2}$ and $\nu = \frac{n}{2G+2}$.

2.5 Symmetries of the Hamiltonian

To do the last transformation we need an ansatz, and so we pause to look at some symmetries of our Hamiltonian. Looking at the partial Hamiltonian operators \mathbf{h} defined in (2.38), note first of all that all intraplanar and easy-axis terms are of the form $\mathbf{a}_p \mathbf{b}_p + \mathbf{a}_p^\dagger \mathbf{b}_p^\dagger$ or $\mathbf{a}_p^\dagger \mathbf{a}_p + \mathbf{b}_p \mathbf{b}_p^\dagger$ for different plane indices p . Since \mathbf{a}_\bullet and \mathbf{b}_\bullet commute, the first type of term can be rewritten to

$$\mathbf{a}_p \mathbf{b}_p + \mathbf{a}_p^\dagger \mathbf{b}_p^\dagger = \mathbf{b}_p \mathbf{a}_p + \mathbf{b}_p^\dagger \mathbf{a}_p^\dagger, \quad (2.47)$$

and utilising the bosonic commutation relations, the second type of term can be rewritten to

$$\mathbf{a}_p^\dagger \mathbf{a}_p + \mathbf{b}_p \mathbf{b}_p^\dagger = \mathbf{a}_p \mathbf{a}_p^\dagger - 1 + \mathbf{b}_p^\dagger \mathbf{b}_p + 1 = \mathbf{b}_p^\dagger \mathbf{b}_p + \mathbf{a}_p \mathbf{a}_p^\dagger. \quad (2.48)$$

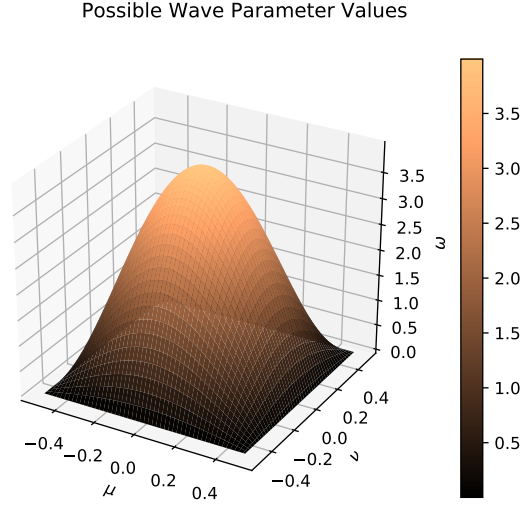


Figure 2.7: The wave parameter ω plotted for the possible values of μ and ν , corresponding to the Brillouin zone depicted in figure 2.5. The wave parameter takes values between 0 and 4.

A similar calculation for the interplanar terms results in

$$\begin{aligned}
 & \mathbf{a}_p \mathbf{b}_{p+1} + \mathbf{a}_p^\dagger \mathbf{b}_{p+1}^\dagger + \mathbf{a}_p^\dagger \mathbf{a}_p + \mathbf{b}_{p+1} \mathbf{b}_{p+1}^\dagger + \mathbf{a}_{p+1} \mathbf{b}_p + \mathbf{a}_{p+1}^\dagger \mathbf{b}_p^\dagger + \mathbf{a}_{p+1}^\dagger \mathbf{a}_{p+1} + \mathbf{b}_p \mathbf{b}_p^\dagger \\
 = & \mathbf{b}_p \mathbf{a}_{p+1} + \mathbf{b}_p^\dagger \mathbf{a}_{p+1}^\dagger + \mathbf{b}_p^\dagger \mathbf{b}_p + \mathbf{a}_{p+1} \mathbf{a}_{p+1}^\dagger + \mathbf{b}_{p+1} \mathbf{a}_p + \mathbf{b}_{p+1}^\dagger \mathbf{a}_p^\dagger + \mathbf{b}_{p+1}^\dagger \mathbf{b}_{p+1} + \mathbf{a}_p \mathbf{a}_p^\dagger.
 \end{aligned} \tag{2.49}$$

The three types of terms above look intriguingly symmetric with respect to a swap $\mathbf{a} \leftrightarrow \mathbf{b}$. Remember however that the \mathbf{a}_p and \mathbf{b}_p operators above have opposite signs on their wave vector \vec{k} . But fortunately, as discussed in section 2.4, the sum over positive \vec{k} in the total Hamiltonian (2.36) can be swapped with a sum over negative \vec{k} . In other words, while each partial operator \mathbf{h} is *not* symmetric with respect to the swap, the total Hamiltonian \mathbf{H} actually *is* symmetric with respect to the swap $\mathbf{a} \leftrightarrow \mathbf{b}$.

Note furthermore that the intraplanar and easy-axis terms are also symmetric with respect to a swap $p \leftrightarrow (N + 1 - p)$ for all plane indices p , as every pair of planes then swapped has the same coefficients. The interplanar term runs through every interplanar interaction, and is thus also symmetric through the swap. This means that the swap $p \leftrightarrow (N + 1 - p)$, which corresponds to a reflection over the middle plane, is another symmetry of the Hamiltonian. (Because the number of planes N is even, the middle plane is not an actual lattice plane.)

Both of the symmetries discussed above are of course also present in the original Hamiltonian (2.2). However, the Holstein-Primakoff and Fourier transformations made them easier to spot. A symmetry in the Hamiltonian causes an energy quantum degeneracy in the following sense. Assume that the magnons of the system have been found —

that is, the MN bosonic operators \mathbf{m}_\bullet that render the Hamiltonian in the diagonal form (2.10). Then we know that the following commutation relation holds for all indices n from 1 to MN :

$$\mathbf{H}\mathbf{m}_n^\dagger = \mathbf{m}_n^\dagger\mathbf{H} + \varepsilon_n\mathbf{m}_n^\dagger. \quad (2.50)$$

It is this commutation relation that ensures that the states $|m_n\rangle = \mathbf{m}_n^\dagger|\rangle$, where $|\rangle$ denotes the vacuum state, are in fact eigenstates of the Hamiltonian, because the diagonal Hamiltonian annihilates the vacuum state. But the magnons \mathbf{m}_\bullet must be sums of the Fourier operators (2.25) and their adjoints. If the magnon state \mathbf{m}_n fulfils the commutation relation (2.50), then so must the magnon \mathbf{m}'_n , which was constructed by performing the symmetry swap on \mathbf{m}_n . In other words, there seems to be two magnonic states with the same energy, but there are two possibilities:

The first possibility is that \mathbf{m}'_n is not a new operator, but simply $\pm\mathbf{m}_n$. Then the magnon state \mathbf{m}_n is said to have a definite *parity* with respect to the symmetry swap — either symmetric (+) or antisymmetric (−).

The second possibility is that \mathbf{m}'_n is a new operator. Then there are two magnon states corresponding to the same energy quantum ε_n , and so ε_n is said to be *degenerate*. From these two states it is however possible to construct a set of magnons that have definite parity with respect to the symmetry swap. This is done by defining the new operators

$$\mathbf{m}_{S_n} = R_S(\mathbf{m}_n + \mathbf{m}'_n), \quad (2.51)$$

$$\mathbf{m}_{A_n} = R_A(\mathbf{m}_n - \mathbf{m}'_n), \quad (2.52)$$

which are also magnons of the same energy because they are linear combinations of the old ones. (R_S and R_A are rescaling factors that keep the bosonic commutation relations properly normalised.)

To summarise, a symmetry in the Hamiltonian ensures that for each non-degenerate energy quantum, the magnons must have definite parity with respect to the symmetry swap, and for each degenerate energy quantum, magnons of definite parity can be constructed.

In our case, we will assume that all the magnons are non-degenerate and have definite parity with respect to a reflection over the middle plane. However, we will assume that the magnons *are* degenerate with respect to a swap of the sublattices. This assumption will allow us to concentrate on one half of the magnons, as the other half can then be constructed by swapping \mathbf{a}_\bullet and \mathbf{b}_\bullet .

2.6 Bogoliubov transformation

The partial Hamiltonian (2.38) contains terms that have the form $\mathbf{a}_p\mathbf{b}_q + \mathbf{a}_p^\dagger\mathbf{b}_q^\dagger$ for plane indices p and q and keep us from attaining a diagonal form. To remove these terms, a transformation based on linear combinations of the old operators is not enough — we will need to introduce linear combinations of the old operators and their adjoints. A so-called *Bogoliubov transformation* is in order.

Contrary to the two previous transformations, the Bogoliubov transformation does not have an explicit expression which is the same for all systems. Rather, we demand it to diagonalise the Hamiltonian while being injective and canonical, and then work out the

equations to satisfy this. The Hamiltonian to be diagonalised is

$$\mathbf{h} = [\bar{\mathbf{a}}^\dagger \quad \bar{\mathbf{b}}] \boxed{A} \begin{bmatrix} \bar{\mathbf{a}} \\ \bar{\mathbf{b}}^\dagger \end{bmatrix}, \quad (2.53)$$

where the $2N \times 2N$ block matrix \boxed{A} was defined as

$$\boxed{A} = \begin{bmatrix} \boxed{D} & \boxed{C} \\ \boxed{C} & \boxed{D} \end{bmatrix}. \quad (2.54)$$

Introduce now the Bogoliubov operators α_\bullet and β_\bullet defined through the equation

$$\begin{bmatrix} \bar{\alpha} \\ \bar{\beta}^\dagger \end{bmatrix} = \boxed{B} \begin{bmatrix} \bar{\mathbf{a}} \\ \bar{\mathbf{b}}^\dagger \end{bmatrix}. \quad (2.55)$$

There are N operators α_\bullet and N operators β_\bullet , and the dimension of the Bogoliubov matrix \boxed{B} is $2N \times 2N$ — the same as \boxed{A} . Because we demand the Bogoliubov transformation to be injective, we assume that the inverse of \boxed{B} exists, so we can write

$$\begin{bmatrix} \bar{\mathbf{a}} \\ \bar{\mathbf{b}}^\dagger \end{bmatrix} = \boxed{B}^{-1} \begin{bmatrix} \bar{\alpha} \\ \bar{\beta}^\dagger \end{bmatrix} \quad (2.56)$$

and

$$[\bar{\mathbf{a}}^\dagger \quad \bar{\mathbf{b}}] = [\bar{\alpha}^\dagger \quad \bar{\beta}] \boxed{B}^{-1\dagger}. \quad (2.57)$$

Performing the transformation on (2.53), we get

$$\mathbf{h} = [\bar{\alpha}^\dagger \quad \bar{\beta}] \boxed{B}^{-1\dagger} \boxed{A} \boxed{B}^{-1} \begin{bmatrix} \bar{\alpha} \\ \bar{\beta}^\dagger \end{bmatrix}, \quad (2.58)$$

and so the problem of diagonalising the Hamiltonian reduces to the problem of diagonalising the block matrix \boxed{A} in the sense that

$$\boxed{B}^{-1\dagger} \boxed{A} \boxed{B}^{-1} = \boxed{E} \quad (2.59)$$

for some diagonal energy matrix \boxed{E} .

An obvious concern of ours is that \boxed{E} might have negative elements, which would result in an unphysical model with infinitely stacking negative energy magnons. However, utilising the Gershgorin disc theorem, we can prove that this is not the case. The matrix \boxed{A} has only two eigendiscs:

1. \mathbb{D}_I that is centered in $d_S = 4\rho + 1 + 2\kappa$ with radius $\omega\rho + 1$.
2. \mathbb{D}_B that is centered in $d_B = 6 + 2\kappa$ with radius $\omega + 2$.

But using the possible range of the wave parameter (2.46) we see that

$$\begin{aligned} \omega\rho + 1 &< 4\rho + 1 + 2\kappa, \\ \omega + 2 &< 6 + 2\kappa \end{aligned} \quad (2.60)$$

as long as κ is positive, so both eigendiscs, and hence all eigenvalues, lie entirely within the positive half-plane. Furthermore \boxed{A} is a real symmetric matrix, so the eigenvalues are all real. Then in total, the eigenvalues have to be real and positive, and so \boxed{A} is positive-definite.

It can be shown that if a matrix \boxed{M} is positive-definite, all diagonalisations $\boxed{T}^\dagger \boxed{M} \boxed{T}$ for any transformation matrix \boxed{T} are also positive-definite. This completes our proof that the elements of \boxed{E} have to be positive, because the eigenvalues of a diagonal matrix are the same as its elements.

Calmed by the fact that our model is physically consistent (at least for now), we define the $N \times N$ submatrices \boxed{u} and \boxed{v} of \boxed{B} as follows:

$$\boxed{B} = \begin{bmatrix} \boxed{u} & \boxed{v} \\ \boxed{v}^* & \boxed{u}^* \end{bmatrix}. \quad (2.61)$$

Here we utilised the sublattice symmetry discussed in section 2.5: We see that with this definition the Bogoliubov operators take on the forms

$$\begin{aligned} \alpha_n &= u_{np} \mathbf{a}_p + v_{np} \mathbf{b}_p^\dagger, \\ \beta_n &= u_{np} \mathbf{b}_p + v_{np} \mathbf{a}_p^\dagger \end{aligned} \quad (2.62)$$

for all indices n between 1 and N . Then the β_\bullet operators are the same as the α_\bullet operators, just with \mathbf{a}_\bullet and \mathbf{b}_\bullet swapped. (In the equation above, the Einstein summation convention is used.) When creating an α_\bullet or β_\bullet boson we see that the amplitudes u_p are associated with the creation of \mathbf{a}_\bullet or \mathbf{b}_\bullet bosons, respectively. Meanwhile the amplitudes v_p are associated with the annihilation of the opposite type of bosons. Due to this, we will refer to the u_p amplitudes as *creation amplitudes* and the v_p amplitudes as *annihilation amplitudes*.

Ordering the Bogoliubov matrix \boxed{B} in the way (2.61) also imposes the following form on the energy matrix \boxed{E} :

$$\boxed{E} = \begin{bmatrix} \boxed{\varepsilon} & \\ & \boxed{\varepsilon} \end{bmatrix}. \quad (2.63)$$

Here, $\boxed{\varepsilon}$ is a diagonal energy submatrix containing all the energy quanta of the system along its diagonal. The quantities left to determine are then the energy submatrix $\boxed{\varepsilon}$ and the amplitude matrices \boxed{u} and \boxed{v} .

Using the expressions in (2.62), we can calculate the four commutators

$$[\alpha_{n'}, \alpha_{n''}^\dagger] = u_{n'p} u_{n''p}^* - v_{n'p} v_{n''p}^*, \quad (2.64)$$

$$[\beta_{n'}, \beta_{n''}^\dagger] = u_{n'p} u_{n''p}^* - v_{n'p} v_{n''p}^*, \quad (2.65)$$

$$[\alpha_{n'}, \beta_{n''}] = u_{n'p} v_{n''p}^* - v_{n'p} u_{n''p}^*, \quad (2.66)$$

$$[\alpha_{n'}, \beta_{n''}^\dagger] = 0. \quad (2.67)$$

For the Bogoliubov transformation to be canonical, the first two commutators have to be $\delta_{n',n''}$ while the two last commutators have to be zero. Hence canonicity provides us

with the following matrix equations for $\begin{bmatrix} u \\ v \end{bmatrix}$ and $\begin{bmatrix} v \\ u \end{bmatrix}$:

$$\begin{aligned} \begin{bmatrix} u & u^\dagger \\ v & v^\dagger \end{bmatrix} - \begin{bmatrix} v & v^\dagger \\ u & u^\dagger \end{bmatrix} &= \begin{bmatrix} I \\ 0 \end{bmatrix}, \\ \begin{bmatrix} u & v^\dagger \\ v & u^\dagger \end{bmatrix} - \begin{bmatrix} v & u^\dagger \\ u & v^\dagger \end{bmatrix} &= \begin{bmatrix} 0 \\ I \end{bmatrix}. \end{aligned} \quad (2.68)$$

These two equations can be further rewritten to the block matrix equation

$$\begin{bmatrix} \begin{bmatrix} u & v \\ v & u \end{bmatrix} & \begin{bmatrix} u^\dagger & -v^\dagger \\ -v^\dagger & u^\dagger \end{bmatrix} \end{bmatrix} = \begin{bmatrix} I & \\ & I \end{bmatrix}. \quad (2.69)$$

It now becomes clear that the inverse of $\begin{bmatrix} B \end{bmatrix}$ is given by

$$\begin{bmatrix} B \end{bmatrix}^{-1} = \begin{bmatrix} \begin{bmatrix} u^\dagger & -v^\dagger \\ -v^\dagger & u^\dagger \end{bmatrix} \end{bmatrix}, \quad (2.70)$$

and by introducing the negation block matrix

$$\begin{bmatrix} N \end{bmatrix} = \begin{bmatrix} I & \\ & -I \end{bmatrix}, \quad (2.71)$$

this inverse can be concisely written as the matrix product

$$\begin{bmatrix} B \end{bmatrix}^{-1} = \begin{bmatrix} N & B^\dagger & N \end{bmatrix}. \quad (2.72)$$

To summarise, the demand that the Bogoliubov transformation be canonical reduced to the equation (2.72) for the inverse of $\begin{bmatrix} B \end{bmatrix}$. A final way of expressing this is

$$\begin{bmatrix} B & N & B^\dagger \end{bmatrix} = \begin{bmatrix} B^\dagger & N & B \end{bmatrix} = \begin{bmatrix} N \end{bmatrix}, \quad (2.73)$$

where the fact that $\begin{bmatrix} N \end{bmatrix}^2 = \begin{bmatrix} I \end{bmatrix}$ has been used.

The diagonalisation condition (2.59) can be combined with the expression for the inverse (2.72) to give the equation

$$\begin{bmatrix} N & B & N & A & N & B^\dagger \end{bmatrix} \begin{bmatrix} N \end{bmatrix} = \begin{bmatrix} E \end{bmatrix}.$$

Multiplying this from the left by $\begin{bmatrix} B^\dagger \end{bmatrix}$ and from the right by $\begin{bmatrix} N \end{bmatrix}$, and then using the canonicity condition (2.73), we end up with

$$\left(\begin{bmatrix} A & N \end{bmatrix} \right) \begin{bmatrix} B^\dagger \end{bmatrix} = \begin{bmatrix} B^\dagger \end{bmatrix} \left(\begin{bmatrix} E & N \end{bmatrix} \right). \quad (2.74)$$

This is nothing else than an eigenequation, saying that the columns of $\begin{bmatrix} B^\dagger \end{bmatrix}$ must be eigenvectors of $\begin{bmatrix} A & N \end{bmatrix}$ with eigenvalues given along the diagonal of $\begin{bmatrix} E & N \end{bmatrix}$. Since both matrices $\begin{bmatrix} A & N \end{bmatrix}$ and $\begin{bmatrix} E & N \end{bmatrix}$ are real, the eigenvectors can be chosen to be real, and so the form of the Bogoliubov matrix reduces to

$$\begin{bmatrix} B \end{bmatrix} = \begin{bmatrix} \begin{bmatrix} u & v \\ v & u \end{bmatrix} \end{bmatrix}. \quad (2.75)$$

The problem of diagonalising the partial Hamiltonian (2.38) has turned into the problem of finding the eigenvectors of the coefficient matrix $\begin{bmatrix} A & N \end{bmatrix}$. From here, there are two possible ways to continue:

1. We can find the eigenvectors of $\begin{bmatrix} A & N \end{bmatrix}$ numerically and rescale them to fulfil the canonicity condition (2.73).
2. We can try to find the eigenvectors of $\begin{bmatrix} A & N \end{bmatrix}$ analytically by introducing an ansatz for $\begin{bmatrix} u \end{bmatrix}$ and $\begin{bmatrix} v \end{bmatrix}$ and solving the resulting equations.

The two possibilities will be explored further in the next sections. While the first approach is more straightforward, the second approach will provide a deeper insight into the energy spectrum and other aspects of the antiferromagnetic layer.

2.7 Numerical diagonalisation

The eigenequation (2.74) can be solved numerically. For this thesis, the Python language was used to write a suitable solver using the versatile NumPy library. This library relies on BLAS and LAPACK, which are standard routines for efficient numerical calculations of linear algebra problems. The code is included in Appendix A.

The solver was implemented as a class `MagnetSolver` which takes in the parameters N , ρ , κ and ω . For the numerical approach to work, we should make sure that the eigenvectors found numerically actually *can* be rescaled to fulfil the canonicity condition (2.73). After all, it is not entirely obvious from the eigenequation (2.74) that the eigenvectors in $\begin{bmatrix} B \end{bmatrix}^\dagger$ are able to do this in all cases.

The proof of this is similar to the proof that eigenvectors of a Hermitian matrix are orthogonal if they correspond to distinct eigenvalues. Assume that \bar{b}' and \bar{b}'' are eigenvectors of $\begin{bmatrix} A & N \end{bmatrix}$ with the distinct eigenvalues ε' and ε'' , respectively. Then

$$\begin{aligned} \begin{bmatrix} A & N \end{bmatrix} \bar{b}' &= \varepsilon' \bar{b}', \\ \begin{bmatrix} A & N \end{bmatrix} \bar{b}'' &= \varepsilon'' \bar{b}'', \end{aligned} \tag{2.76}$$

and if we transpose the first of these equations, we get

$$\bar{b}' \begin{bmatrix} N & A \end{bmatrix} = \varepsilon' \bar{b}', \tag{2.77}$$

because the eigenvalue ε' is known to be real. Now look at the scalar matrix product $\bar{b}' \begin{bmatrix} N & A & N \end{bmatrix} \bar{b}''$. Using equation (2.77) and (2.76) this product can be expressed in two different ways:

$$\begin{aligned} \bar{b}' \begin{bmatrix} N & A & N \end{bmatrix} \bar{b}'' &= \varepsilon' \bar{b}' \begin{bmatrix} N \end{bmatrix} \bar{b}'', \\ \bar{b}' \begin{bmatrix} N & A & N \end{bmatrix} \bar{b}'' &= \varepsilon'' \bar{b}' \begin{bmatrix} N \end{bmatrix} \bar{b}''. \end{aligned}$$

Subtracting these two equations, we see that

$$(\varepsilon' - \varepsilon'') \bar{b}' \begin{bmatrix} N \end{bmatrix} \bar{b}'' = 0,$$

which means that

$$\bar{b}' \boxed{N} \bar{b}'' = 0, \quad (2.78)$$

since the eigenvalues ε' and ε'' are distinct from one another.

In our case, we assume that all the eigenvalues in $\boxed{E} \boxed{N}$ are distinct, because we assumed in section 2.5 that the only degeneracy of the system is the degeneracy with respect to the lattice swap, and this degeneracy is lifted by the negation matrix \boxed{N} in the eigenequation (2.74). Thus, if we denote the columns of \boxed{B}^\dagger (or equivalently the rows of \boxed{B}) with \bar{b}_n for all indices n between 1 and $2N$, and write out the matrix product $\boxed{B} \boxed{N} \boxed{B}^\dagger$, we see that

$$\begin{aligned} \boxed{B} \boxed{N} \boxed{B}^\dagger &= \begin{bmatrix} \bar{b}_1 \boxed{N} \bar{b}_1 & \bar{b}_1 \boxed{N} \bar{b}_2 & \dots & \bar{b}_1 \boxed{N} \bar{b}_{2N} \\ \bar{b}_2 \boxed{N} \bar{b}_1 & \bar{b}_2 \boxed{N} \bar{b}_2 & \dots & \bar{b}_2 \boxed{N} \bar{b}_{2N} \\ \vdots & \vdots & \ddots & \vdots \\ \bar{b}_{2N} \boxed{N} \bar{b}_1 & \bar{b}_{2N} \boxed{N} \bar{b}_2 & \dots & \bar{b}_{2N} \boxed{N} \bar{b}_{2N} \end{bmatrix} \\ &= \begin{bmatrix} \bar{b}_1 \boxed{N} \bar{b}_1 & & & \\ & \ddots & & \\ & & \bar{b}_{2N} \boxed{N} \bar{b}_{2N} & \end{bmatrix}, \end{aligned} \quad (2.79)$$

because all the vectors \bar{b}_\bullet are eigenvectors corresponding to distinct eigenvalues. Hence we see that the matrix product at least have a diagonal form, and it remains to ensure that each product

$$P_n = \bar{b}_n \boxed{N} \bar{b}_n = \sum_p (u_{np}^2 - v_{np}^2) \quad (2.80)$$

for all indices n between 1 and N is equal to 1. Then the products in the lower half of the matrix product (2.79) are automatically equal to -1 , because u_p and v_p are swapped here.

As long as P_n is positive, this normalisation is easily achieved by rescaling each eigenvector pair \bar{b}_n and \bar{b}_{N+n} by $\sqrt{\frac{1}{P_n}}$. But note that

$$\bar{b}_n \boxed{N} \boxed{A} \boxed{N} \bar{b}_n = \varepsilon_n \bar{b}_n \boxed{N} \bar{b}_n,$$

which means that P_n can be written

$$P_n = \frac{\bar{b}_n \boxed{N} \boxed{A} \boxed{N} \bar{b}_n}{\varepsilon_n}. \quad (2.81)$$

Since \boxed{A} is positive-definite as was shown in section 2.6, the product in the nominator is positive. (This is one of the properties of positive-definite matrices.) Then, since ε_n is also positive, it follows that P_n is always positive, and our normalisation is ensured.

To summarise, the procedure for our numerical solver should be:

1. Define the coefficient matrix $\boxed{A} \boxed{N}$.

2. Calculate the eigenvectors and eigenvalues of $\begin{bmatrix} A & N \end{bmatrix}$ numerically.
3. Store the eigenvectors as rows in the eigenmatrix $\begin{bmatrix} B \end{bmatrix}$.
4. Sort the eigenmatrix $\begin{bmatrix} B \end{bmatrix}$ so that the eigenvectors corresponding to negative eigenvalues are in the lower half of the matrix.
5. Sort each half of the eigenmatrix by increasing absolute value (or in some other sensible way).
6. Calculate the positive normalisation factor P_n given in (2.80) for each eigenvector \bar{b}_n in the upper half of $\begin{bmatrix} B \end{bmatrix}$.
7. Rescale each eigenvector pair \bar{b}_n and \bar{b}_{N+n} by the factor $\sqrt{\frac{1}{P_n}}$.

The procedure above was implemented in the `MagnetSolver` class as the class method `calcNumMagnons`. Here the eigenequation itself is solved by the `eig` method from NumPy's `linalg` module. In the figures 2.8 and 2.9, the magnon amplitudes of a 12-plane antiferromagnetic layer are plotted. The values of ρ , κ and ω are specified in the plots. The magnons have an increasing amount of nodes with increasing energy, as is typical for quantum systems. We will get an explanation to this in section 2.13.

2.8 Analytical equations

The eigenequation (2.74) is mathematically quite structured, so it is reasonable to think that it might possibly be solved analytically. To this end, we write it out blockwise,

$$\begin{aligned}
 \begin{bmatrix} D \end{bmatrix} \begin{bmatrix} u \end{bmatrix}^\dagger - \begin{bmatrix} C \end{bmatrix} \begin{bmatrix} v \end{bmatrix}^\dagger &= \begin{bmatrix} u \end{bmatrix}^\dagger \begin{bmatrix} \varepsilon \end{bmatrix}, \\
 \begin{bmatrix} D \end{bmatrix} \begin{bmatrix} v \end{bmatrix}^\dagger - \begin{bmatrix} C \end{bmatrix} \begin{bmatrix} u \end{bmatrix}^\dagger &= -\begin{bmatrix} v \end{bmatrix}^\dagger \begin{bmatrix} \varepsilon \end{bmatrix}, \\
 \begin{bmatrix} C \end{bmatrix} \begin{bmatrix} u \end{bmatrix}^\dagger - \begin{bmatrix} D \end{bmatrix} \begin{bmatrix} v \end{bmatrix}^\dagger &= \begin{bmatrix} v \end{bmatrix}^\dagger \begin{bmatrix} \varepsilon \end{bmatrix}, \\
 \begin{bmatrix} C \end{bmatrix} \begin{bmatrix} v \end{bmatrix}^\dagger - \begin{bmatrix} D \end{bmatrix} \begin{bmatrix} u \end{bmatrix}^\dagger &= -\begin{bmatrix} u \end{bmatrix}^\dagger \begin{bmatrix} \varepsilon \end{bmatrix}.
 \end{aligned}$$

These four submatrix equations are degenerate as a consequence of the sublattice symmetry, and so they can be reduced to the two equations

$$\begin{aligned}
 \begin{bmatrix} D \end{bmatrix} \begin{bmatrix} u \end{bmatrix}^\dagger - \begin{bmatrix} C \end{bmatrix} \begin{bmatrix} v \end{bmatrix}^\dagger &= \begin{bmatrix} u \end{bmatrix}^\dagger \begin{bmatrix} \varepsilon \end{bmatrix}, \\
 \begin{bmatrix} D \end{bmatrix} \begin{bmatrix} v \end{bmatrix}^\dagger - \begin{bmatrix} C \end{bmatrix} \begin{bmatrix} u \end{bmatrix}^\dagger &= -\begin{bmatrix} v \end{bmatrix}^\dagger \begin{bmatrix} \varepsilon \end{bmatrix}.
 \end{aligned} \tag{2.82}$$

These equations correspond to the eigenequation (2.74), and it was proven in section 2.7 that the eigenvectors always fulfil the canonicity condition (2.73) after a normalisation, as long as the energy quanta are only doubly degenerate.

Let us then focus on a single column n of equation (2.82), corresponding to one specific magnon of the antiferromagnetic layer. We will omit n from here on, but keep in mind

Low Energy Magnons of the Antiferromagnetic Layer
 ($N = 12$, $\rho = 0.80$, $\kappa = 0.002$, $\omega = 4.00$)

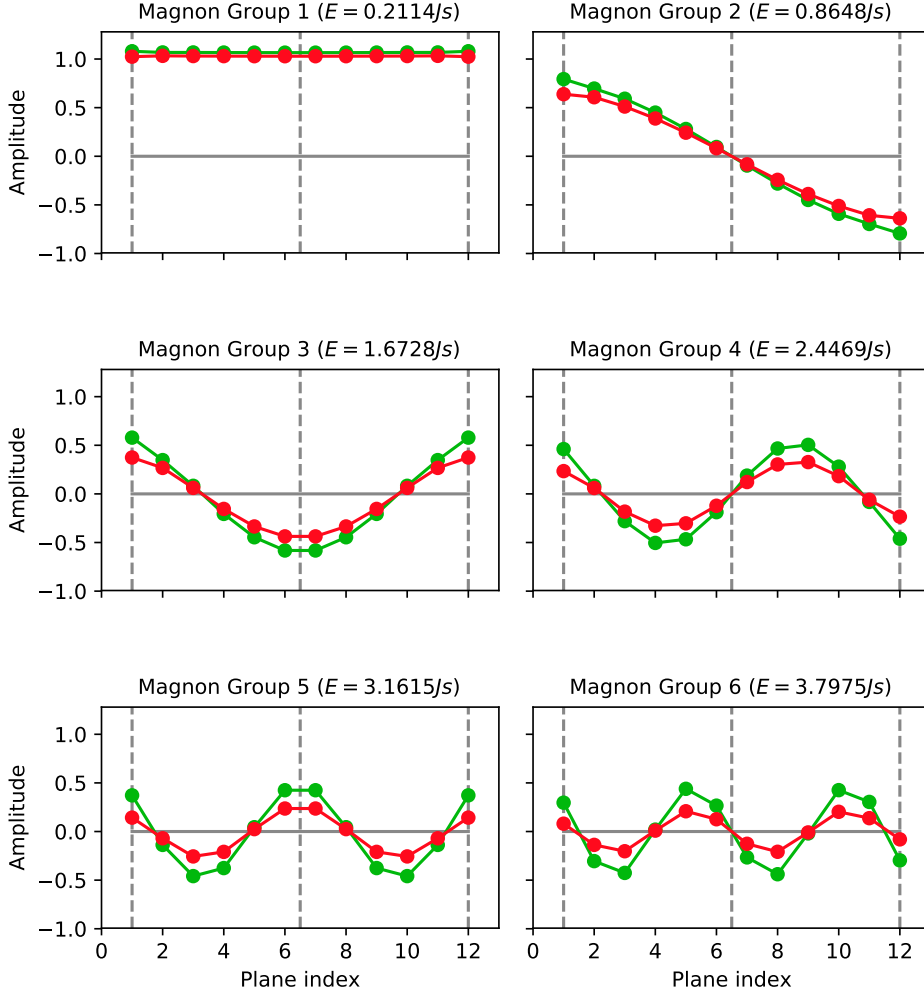


Figure 2.8: The low energy magnons of a 12-plane antiferromagnetic layer for the given parameters. The creation amplitudes u_p and the annihilation amplitudes v_p are plotted in green and red, respectively. The surface planes and the middle plane are indicated by the dotted lines. Note that each plot represents two magnons — one of type α_\bullet and one of type β_\bullet .

High Energy Magnons of the Antiferromagnetic Layer
 ($N = 12, \rho = 0.80, \kappa = 0.002, \omega = 4.00$)

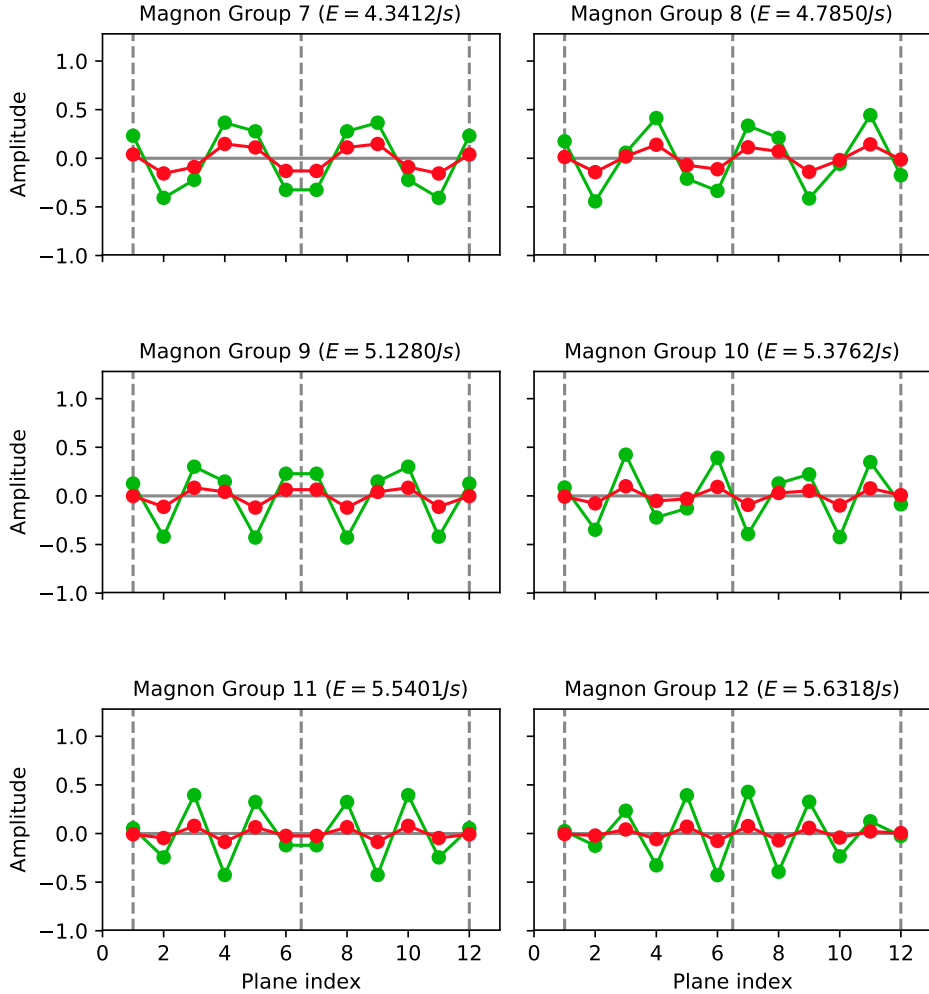


Figure 2.9: The high energy magnons of a 12-plane antiferromagnetic layer for the given parameters. The creation amplitudes u_p and the annihilation amplitudes v_p are plotted in green and red, respectively. The surface planes and the middle plane are indicated by the dotted lines. Note that each plot represents two magnons — one of type α_\bullet and one of type β_\bullet .

that there should be exactly N solutions to our equations. Picking any row p that is not the first (1) or last (N), the corresponding element equation is

$$\begin{aligned}(d_B - \varepsilon)u_p &= v_{p-1} + \omega v_p + v_{p+1}, \\ (d_B + \varepsilon)v_p &= u_{p-1} + \omega u_p + u_{p+1}.\end{aligned}\tag{2.83}$$

Here, ε is defined as the corresponding diagonal element of $\boxed{\varepsilon}$, and thus the energy quantum of the magnon. As these equations do not involve the surface exchange parameter S , we will call them the *bulk equations* of the system. Picking the first row, we get the *surface equations*

$$\begin{aligned}(d_S - \varepsilon)u_1 &= \omega \rho v_1 + v_2, \\ (d_S + \varepsilon)v_1 &= \omega \rho u_1 + u_2.\end{aligned}\tag{2.84}$$

Picking the last row will give us another set of equations, but because the amplitudes u_p and v_p have a definite parity with respect to reflection, these equations do not add anything new and need not be considered.

If we can find an ansatz that solves the bulk equations (2.83) and is also defined for *all* integers p (not only the integers corresponding to actual planes), the surface equations above can be simplified by writing out the bulk equations for the integer $p = 1$,

$$\begin{aligned}(d_B - \varepsilon)u_1 &= v_0 + \omega v_1 + v_2, \\ (d_B + \varepsilon)v_1 &= u_0 + \omega u_1 + u_2.\end{aligned}$$

These equations can be subtracted from the surface equations (2.84) to yield the new surface equations

$$\begin{aligned}(d_S - d_B)u_1 &= \omega(\rho - 1)v_1 - v_0, \\ (d_S - d_B)v_1 &= \omega(\rho - 1)u_1 - u_0,\end{aligned}\tag{2.85}$$

which provide exactly the same information as the original ones when coupled with the bulk equations. (Note that the terms u_0 and v_0 have no physical meaning, but they are mathematically well defined as long as the ansatz holds for all integers p .)

The new surface equations (2.85) look very similar to the original ones, but they do not include the unknown energy quantum ε , and are therefore easier to work with. They will also prove to be more symmetric for our ansatz. We can introduce some new parameters to make the algebra even cleaner. The definitions of d_S and d_B back in the equation (2.42) tell us that $(d_S - d_B) = (4\rho - 5)$, so by introducing the coefficients

$$\begin{aligned}\zeta &= 4\rho - 5, \\ \eta &= \omega(\rho - 1),\end{aligned}\tag{2.86}$$

the surface equations take the final concise form

$$\begin{aligned}\zeta u_1 &= \eta v_1 - v_0, \\ \zeta v_1 &= \eta u_1 - u_0.\end{aligned}\tag{2.87}$$

2.9 Parity ansatz

With the bulk and surface equations worked out, we are in position to make an ansatz for the amplitudes u_p and v_p . To summarise our results so far, the amplitudes must be real and of definite reflection parity, and they must satisfy both the bulk equations (2.83) and the surface equations (2.87). A reasonable ansatz with definite parity would be a wave ansatz with trigonometric or hyperbolic functions. Such wave functions appear all over in physics, and we will show that they can indeed solve this system too.

The exact ansatz we will use is inspired by Wolfram and De Wames [1969]. Define first the *middle plane index* as

$$p_m = \frac{N + 1}{2}. \quad (2.88)$$

(Note that this index is not an integer, nor does it index an actual lattice plane, but it *does* give us the x-position of the center of the layer.) Our ansatz then takes the following form for all indices p between 1 and N :

$$\begin{aligned} u_p &= U(-1)^p \frac{\sinh}{\cosh}(\vartheta(p - p_m)) + X \frac{\cosh}{\sinh}(\varphi(p - p_m)), \\ v_p &= V(-1)^p \frac{\sinh}{\cosh}(\vartheta(p - p_m)) + W \frac{\cosh}{\sinh}(\varphi(p - p_m)). \end{aligned} \quad (2.89)$$

Here, U , X , V and W are amplitudes while ϑ and φ are frequencies that can be real or purely imaginary. The upper functions correspond to magnons that are reflection symmetric over the middle plane index p_m , while the lower functions correspond to magnons that are reflection antisymmetric. (While the first terms seem to have the opposite parity of the second terms, this is not true because the factor $(-1)^p$ will have opposite signs on each side of the middle plane as long as there is an even number of planes N , as was specified back in section 2.1.)

We will distinguish between three main types of magnons based on the frequencies ϑ and φ :

- *surface magnons* with two real frequencies,
- *bulk magnons* with two imaginary frequencies,
- *mixed magnons* with one real and one imaginary frequency.

The terms above were chosen because real frequencies give rise to hyperbolic amplitudes that rise exponentially and take maximal values at the surfaces, while imaginary frequencies give rise to trigonometric amplitudes that oscillate throughout the layer and hence are not localised at any particular place.

Before we plug the ansatz (2.89) into our equations from 2.8, we will look at the ranges of interest for the frequencies ϑ and φ . First, note that for negative values of ϑ or φ , the sine terms in (2.89) will switch sign. But this corresponds to the exact same ansatz after another small redefinition of the corresponding amplitudes. Thus we can restrict ourselves to only considering positive real or imaginary values of ϑ and φ , including zero.

In the case of imaginary frequencies the ranges of interest are truncated further because of aliasing. Let us first consider the case of an imaginary ϑ . Pulling the imaginary unit i

out of ϑ , the involved trigonometric functions in the ansatz (2.89) are then $\sin(\vartheta(p - p_m))$ and $\cos(\vartheta(p - p_m))$ for some real-valued ϑ , since

$$\begin{aligned}\sinh(\iota\alpha) &= \iota \sin \alpha, \\ \cosh(\iota\alpha) &= \cos \alpha,\end{aligned}\tag{2.90}$$

for all phases $\alpha \in \mathbb{R}$. But note that

$$(p - p_m) = \frac{2p - N - 1}{2}.\tag{2.91}$$

If we add an even integer of π to ϑ , we then see that

$$\begin{aligned}\sin((\vartheta + 2z\pi)(p - p_m)) &= (-1)^z \sin(\vartheta(p - p_m)), \\ \cos((\vartheta + 2z\pi)(p - p_m)) &= (-1)^z \cos(\vartheta(p - p_m))\end{aligned}\tag{2.92}$$

for all integers $z \in \mathbb{Z}$. This is because the integer product $z(2p - N - 1)$ has the same type (even or odd) as the integer z . The terms in the ansatz involving ϑ will hence pick up a factor of $(-1)^z$ after this shift. But as in the case of negative values, this corresponds to the exact same ansatz with just a redefinition of the amplitudes.

Since the ansatz is the same for ϑ and $\vartheta + 2z\pi$, we can restrict ourselves to only considering a period of 2π for the frequency ϑ . But furthermore, since values between π and 2π can be translated to negative values between $-\pi$ and 0 , which can then be translated to their corresponding positive values between 0 and π , then in fact only the interval 0 to π is interesting.

The reasoning above of course also applies to the case of an imaginary φ . To summarise then, our ranges of interest are

- positive real values of ϑ and φ above 0 ,
- positive imaginary values of ϑ and φ in the interval $[0, \iota\pi]$.

We will restrict the ranges further later.

Plugging the general parity ansatz (2.89) into the bulk equations (2.83) yields four parametric bulk equations:

$$\begin{aligned}(d_B - \varepsilon)U &= (\omega - 2 \cosh \vartheta)V, \\ (d_B - \varepsilon)X &= (\omega + 2 \cosh \varphi)W, \\ (d_B + \varepsilon)V &= (\omega - 2 \cosh \vartheta)U, \\ (d_B + \varepsilon)W &= (\omega + 2 \cosh \varphi)X.\end{aligned}\tag{2.93}$$

These turn out to be the same for symmetric and antisymmetric magnons. Multiply now the two first ones by $(d_B + \varepsilon)$ and the two second ones by $(d_B - \varepsilon)$ to obtain the equations

$$\begin{aligned}(d_B^2 - \varepsilon^2)U &= (\omega - 2 \cosh \vartheta)^2 U, \\ (d_B^2 - \varepsilon^2)V &= (\omega - 2 \cosh \vartheta)^2 V, \\ (d_B^2 - \varepsilon^2)X &= (\omega + 2 \cosh \varphi)^2 X, \\ (d_B^2 - \varepsilon^2)W &= (\omega + 2 \cosh \varphi)^2 W,\end{aligned}\tag{2.94}$$

which tell us that either $U = V = 0$ or $d_B^2 - \varepsilon^2 = (\omega - 2 \cosh \vartheta)^2$, and similarly either $X = W = 0$ or $d_B^2 - \varepsilon^2 = (\omega + 2 \cosh \varphi)^2$. But if $U = V = 0$ or $X = W = 0$, then the respective frequency ϑ or φ have no impact on the ansatz (2.89), so it can be set to satisfy the above relations in all cases. In total then, we get the quadratic relation

$$d_B^2 - \varepsilon^2 = (\omega - 2 \cosh \vartheta)^2 = (\omega + 2 \cosh \varphi)^2 \quad (2.95)$$

between the energy quantum ε and the frequencies ϑ and φ . We will dissect this relation into two equations shortly, but note already that it provides a maximum threshold quantum for all the energy quanta of the antiferromagnetic layer,

$$\varepsilon \leq d_B = 6 + 2\kappa = \varepsilon_\wedge, \quad (2.96)$$

and so we will use the more fitting name ε_\wedge for d_B from now on.

The quadratic relation (2.95) contains two equations. From the original equations (2.93) we get two more equations

$$\begin{aligned} V &= QU, \\ W &= RX, \end{aligned} \quad (2.97)$$

where the ratios

$$\begin{aligned} Q &= \frac{\omega - 2 \cosh \vartheta}{\varepsilon_\wedge + \varepsilon}, \\ R &= \frac{\omega + 2 \cosh \varphi}{\varepsilon_\wedge + \varepsilon} \end{aligned} \quad (2.98)$$

were defined. With these definitions we can rewrite one of the equations in (2.95) to

$$Q^2 = R^2 = \frac{\varepsilon_\wedge - \varepsilon}{\varepsilon_\wedge + \varepsilon} < 1. \quad (2.99)$$

This equation seems to give rise to two solution branches $Q = R$ or $Q = -R$. However, we will prove next that only the second solution branch needs to be considered.

Assuming $Q = R$, the definitions (2.98) provide the link equation

$$\cosh \vartheta + \cosh \varphi = 0 \quad (2.100)$$

between the frequencies ϑ and φ . It is immediately clear that no surface magnons of this type can exist, because both terms are strictly positive in that case. Furthermore, no mixed magnons can exist either — the real frequency would then be forced to be 0, but this value is considered imaginary and not in our range of interest for real frequencies.

In other words, only bulk magnons of the type $Q = -R$ can exist. Pulling out imaginary units i , the link equation above becomes

$$\cos \vartheta + \cos \varphi = 0, \quad (2.101)$$

which has the solution

$$\vartheta = \pi - \varphi \quad (2.102)$$

within the range of interest. Looking at the ϑ terms in the ansatz, their argument is then

$$(\pi - \varphi)(p - p_m) = p\pi - (N + 1)\frac{\pi}{2} - \varphi(p - p_m), \quad (2.103)$$

so the trigonometric functions simplify to

$$\begin{aligned} \sin(\vartheta(p - p_m)) &= -(-1)^p \sin\left(\varphi(p - p_m) + (N + 1)\frac{\pi}{2}\right), \\ \cos(\vartheta(p - p_m)) &= (-1)^p \cos\left(\varphi(p - p_m) + (N + 1)\frac{\pi}{2}\right). \end{aligned}$$

They can be simplified even further by using the fact that adding an odd integer of $\frac{\pi}{2}$ to the argument of a trigonometric function has the impact

$$\begin{aligned} \sin\left(\alpha + (2z + 1)\frac{\pi}{2}\right) &= (-1)^z \cos \alpha, \\ \cos\left(\alpha + (2z + 1)\frac{\pi}{2}\right) &= -(-1)^z \sin \alpha \end{aligned} \quad (2.104)$$

for all phases $\alpha \in \mathbb{R}$ and all integers $z \in \mathbb{Z}$. Using this, we see that

$$\begin{aligned} \sin(\vartheta(p - p_m)) &= -(-1)^{p+\frac{N}{2}} \cos(\varphi(p - p_m)), \\ \cos(\vartheta(p - p_m)) &= -(-1)^{p+\frac{N}{2}} \sin(\varphi(p - p_m)) \end{aligned} \quad (2.105)$$

in the case $Q = R$. But this means that the ansatz (2.89) reduces to

$$\begin{aligned} u_p &= X \frac{\cos}{\sin}(\varphi(p - p_m)), \\ v_p &= W \frac{\cos}{\sin}(\varphi(p - p_m)) \end{aligned} \quad (2.106)$$

with a redefinition of the amplitudes, since the alternating factor $(-1)^p$ is squared and disappears. In other words, the case $Q = R$ corresponds to setting $U = V = 0$ in the ansatz (2.89). But this can also be done in the case $Q = -R$, and so we can actually neglect the case $Q = R$ entirely without loss of solutions.

Consider then the case $Q = -R$. The ratio definitions (2.98) now provide the link equation

$$\cosh \vartheta = \cosh \varphi + \omega, \quad (2.107)$$

between ϑ and φ . The amplitude relations (2.97) simplify to

$$\begin{aligned} V &= -RU, \\ W &= RX, \end{aligned} \quad (2.108)$$

for the common ratio

$$R = \frac{\omega + 2 \cosh \varphi}{\varepsilon_\wedge + \varepsilon}. \quad (2.109)$$

The last equation in (2.95) can finally be rewritten to the dispersion relation

$$\varepsilon = \sqrt{\varepsilon_\wedge^2 - (\omega + 2 \cosh \varphi)^2}. \quad (2.110)$$

To summarise then, the parametric bulk equations (2.93) have resulted in four equations (as they should): the link equation (2.107), the two amplitude relations (2.108) with the ratio R defined in (2.109) and the energy dispersion relation (2.110).

We now move on to find parametric surface equations. Plugging the general parity ansatz (2.89) into the surface equations (2.87) and substituting $V = -RU$ and $W = RX$, we end up with a matrix equation

$$\boxed{M} \begin{bmatrix} U \\ X \end{bmatrix} = \begin{bmatrix} 0 \\ 0 \end{bmatrix}, \quad (2.111)$$

for the amplitudes U and X , where the big coefficient matrix \boxed{M} has the following elements:

$$\begin{aligned} M_{11} &= R \frac{\sinh\left(\frac{N+1}{2}\vartheta\right)}{\cosh\left(\frac{N+1}{2}\vartheta\right)} + (\zeta + \eta R) \frac{\sinh\left(\frac{N-1}{2}\vartheta\right)}{\cosh\left(\frac{N-1}{2}\vartheta\right)}, \\ M_{12} &= R \frac{\cosh\left(\frac{N+1}{2}\varphi\right)}{\sinh\left(\frac{N+1}{2}\varphi\right)} + (\zeta - \eta R) \frac{\cosh\left(\frac{N-1}{2}\varphi\right)}{\sinh\left(\frac{N-1}{2}\varphi\right)}, \\ M_{21} &= \frac{\sinh\left(\frac{N+1}{2}\vartheta\right)}{\cosh\left(\frac{N+1}{2}\vartheta\right)} + (\zeta R + \eta) \frac{\sinh\left(\frac{N-1}{2}\vartheta\right)}{\cosh\left(\frac{N-1}{2}\vartheta\right)}, \\ M_{22} &= -\frac{\cosh\left(\frac{N+1}{2}\varphi\right)}{\sinh\left(\frac{N+1}{2}\varphi\right)} - (\zeta R - \eta) \frac{\cosh\left(\frac{N-1}{2}\varphi\right)}{\sinh\left(\frac{N-1}{2}\varphi\right)}. \end{aligned} \quad (2.112)$$

Here again, the upper functions correspond to symmetric magnons while the lower functions correspond to antisymmetric magnons. To ensure that the matrix equation (2.111) has other solutions for U and X than the trivial solution $U = X = 0$, we demand that the determinant of \boxed{M} be zero. After some algebra, this results in the long equation

$$\begin{aligned} &\frac{2R}{1+R^2} \frac{\sinh\left(\frac{N+1}{2}\vartheta\right)}{\cosh\left(\frac{N+1}{2}\vartheta\right)} \frac{\cosh\left(\frac{N+1}{2}\varphi\right)}{\sinh\left(\frac{N+1}{2}\varphi\right)} \\ &+ \left(\zeta - \frac{2R}{1+R^2}\eta\right) \frac{\sinh\left(\frac{N+1}{2}\vartheta\right)}{\cosh\left(\frac{N+1}{2}\vartheta\right)} \frac{\cosh\left(\frac{N-1}{2}\varphi\right)}{\sinh\left(\frac{N-1}{2}\varphi\right)} \\ &+ \left(\zeta + \frac{2R}{1+R^2}\eta\right) \frac{\sinh\left(\frac{N-1}{2}\vartheta\right)}{\cosh\left(\frac{N-1}{2}\vartheta\right)} \frac{\cosh\left(\frac{N+1}{2}\varphi\right)}{\sinh\left(\frac{N+1}{2}\varphi\right)} \\ &+ \frac{2R}{1+R^2}(\zeta^2 - \eta^2) \frac{\sinh\left(\frac{N-1}{2}\vartheta\right)}{\cosh\left(\frac{N-1}{2}\vartheta\right)} \frac{\cosh\left(\frac{N-1}{2}\varphi\right)}{\sinh\left(\frac{N-1}{2}\varphi\right)} = 0. \end{aligned}$$

Note however that

$$\frac{2R}{1+R^2} = \frac{2R(\varepsilon_\Lambda + \varepsilon)}{(\varepsilon_\Lambda + \varepsilon) + (\varepsilon_\Lambda - \varepsilon)} = \frac{\omega + 2 \cosh \varphi}{\varepsilon_\Lambda} \quad (2.113)$$

using (2.99), so the equation above simplifies to

$$\begin{aligned}
 & (\omega + 2 \cosh \varphi) \frac{\sinh \left(\frac{N+1}{2} \vartheta \right)}{\cosh \left(\frac{N+1}{2} \vartheta \right)} \frac{\cosh \left(\frac{N+1}{2} \varphi \right)}{\sinh \left(\frac{N+1}{2} \varphi \right)} \\
 & + (\varepsilon_{\wedge} \zeta - (\omega + 2 \cosh \varphi) \eta) \frac{\sinh \left(\frac{N+1}{2} \vartheta \right)}{\cosh \left(\frac{N+1}{2} \vartheta \right)} \frac{\cosh \left(\frac{N-1}{2} \varphi \right)}{\sinh \left(\frac{N-1}{2} \varphi \right)} \\
 & + (\varepsilon_{\wedge} \zeta + (\omega + 2 \cosh \varphi) \eta) \frac{\sinh \left(\frac{N-1}{2} \vartheta \right)}{\cosh \left(\frac{N-1}{2} \vartheta \right)} \frac{\cosh \left(\frac{N+1}{2} \varphi \right)}{\sinh \left(\frac{N+1}{2} \varphi \right)} \\
 & + (\omega + 2 \cosh \varphi) (\zeta^2 - \eta^2) \frac{\sinh \left(\frac{N-1}{2} \vartheta \right)}{\cosh \left(\frac{N-1}{2} \vartheta \right)} \frac{\cosh \left(\frac{N-1}{2} \varphi \right)}{\sinh \left(\frac{N-1}{2} \varphi \right)} = 0, \quad (2.114)
 \end{aligned}$$

which will serve as our first parametric surface equation. Since this equation can be solved with the link equation (2.107) to find the possible values of the frequencies ϑ and φ , we will call it the *condition equation* of our problem. The last parametric surface equation relating the amplitudes U and X drops out from the matrix equation (2.111) as

$$\begin{aligned}
 & \left(\frac{\sinh \left(\frac{N+1}{2} \vartheta \right)}{\cosh \left(\frac{N+1}{2} \vartheta \right)} + (\zeta R + \eta) \frac{\sinh \left(\frac{N-1}{2} \vartheta \right)}{\cosh \left(\frac{N-1}{2} \vartheta \right)} \right) U \\
 & = \left(\frac{\cosh \left(\frac{N+1}{2} \varphi \right)}{\sinh \left(\frac{N+1}{2} \varphi \right)} + (\zeta R - \eta) \frac{\cosh \left(\frac{N-1}{2} \varphi \right)}{\sinh \left(\frac{N-1}{2} \varphi \right)} \right) X. \quad (2.115)
 \end{aligned}$$

Having worked out both the parametric bulk equations (2.107)–(2.110) and the parametric surface equations (2.114)–(2.115), we are in principle able to solve them to obtain all magnons of the antiferromagnetic layer. Note however that the condition equation (2.114) is a trigonometric or hyperbolic equation that cannot be solved explicitly. We then have to solve it numerically, so there seems to be no purely analytical solution for this system after all — at least not in the general case. Nevertheless, we will still use our analytical results to gain further insight into the antiferromagnetic layer. In the next section we take a closer look at the link (2.107) between the frequencies ϑ and φ .

2.10 Threshold frequencies

From the previous section, we know that the interesting values of ϑ and φ are real values above 0 and imaginary values between 0 and $i\pi$. But the link equation (2.107) relates $\cosh \vartheta$ and $\cosh \varphi$, and so it can be used to get the frequency ϑ for any given value of φ . In this section, we will introduce a visualisation to make this relationship clearer.

In figure 2.10, the function $\cosh \vartheta$ or $\cosh \varphi$ is plotted on the range of interest. The black branch corresponds to real values and hence a hyperbolic cosine function, while the red branch corresponds to imaginary values and a trigonometric cosine function.

The link equation (2.107) tells us that the value of $\cosh \vartheta$ should be a distance ω above $\cosh \varphi$. If we plot φ as a point on one the branches in figure 2.10, we can imagine an “omega layer” of height ω above φ and pinpoint ϑ in the intersection between the top of the ω layer and the graph. In figure 2.11 we give three examples, corresponding to the three main branches of surface magnons, bulk magnons and mixed magnons.

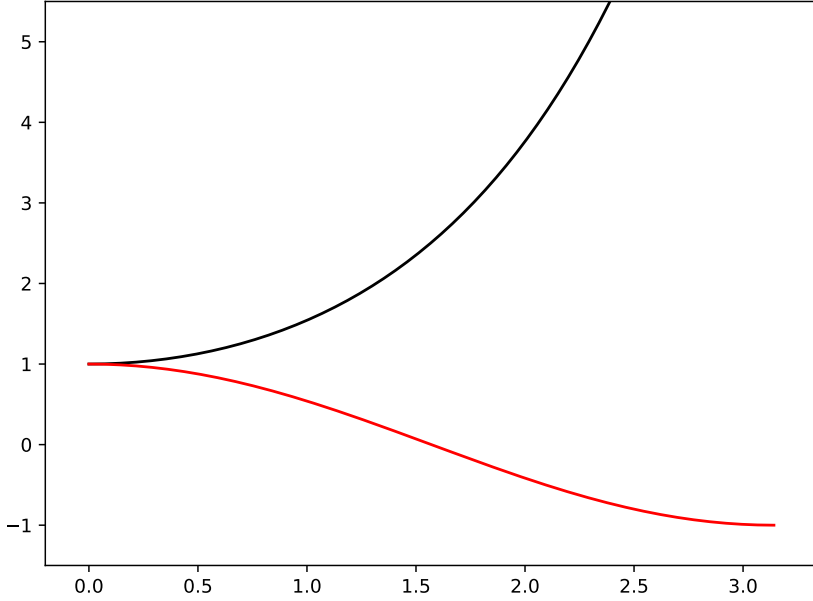


Figure 2.10: Frequency chart for our antiferromagnetic layer. The black branch corresponds to real values of ϑ or φ , while the red branch corresponds to imaginary values. The frequency value (real or imaginary) is on the x-axis, against the cosine value (hyperbolic or trigonometric) on the y-axis.

The visualisation in figure 2.11 makes several things clear about the relation between the frequencies ϑ and φ and their corresponding magnons. First of all, mixed magnons with imaginary ϑ and real φ cannot exist. All real values of φ above 0 correspond to surface magnons. The *surface threshold frequency*

$$\varphi_S = 0, \quad (2.116)$$

separates surface magnons and mixed magnons. We see from the dispersion relation (2.110) that the corresponding *surface threshold quantum* is

$$\varepsilon_S = \sqrt{\varepsilon_\Lambda^2 - (\omega + 2)^2}. \quad (2.117)$$

Using the dispersion relation and the fact from back in section 2.6 that all the energy quanta of the antiferromagnetic layer have to be larger than zero, we also find the threshold frequency

$$\varphi_V = \operatorname{arcosh} \left(\frac{\varepsilon_\Lambda - \omega}{2} \right) \quad (2.118)$$

as the upper limit for real values of φ . The corresponding threshold quantum is $\varepsilon_V = 0$.

It is also clear from the visualisation in figure 2.11 that bulk magnons only exist for $\omega \leq 2$, because ϑ is pushed onto the real branch for higher ω values. We can identify the

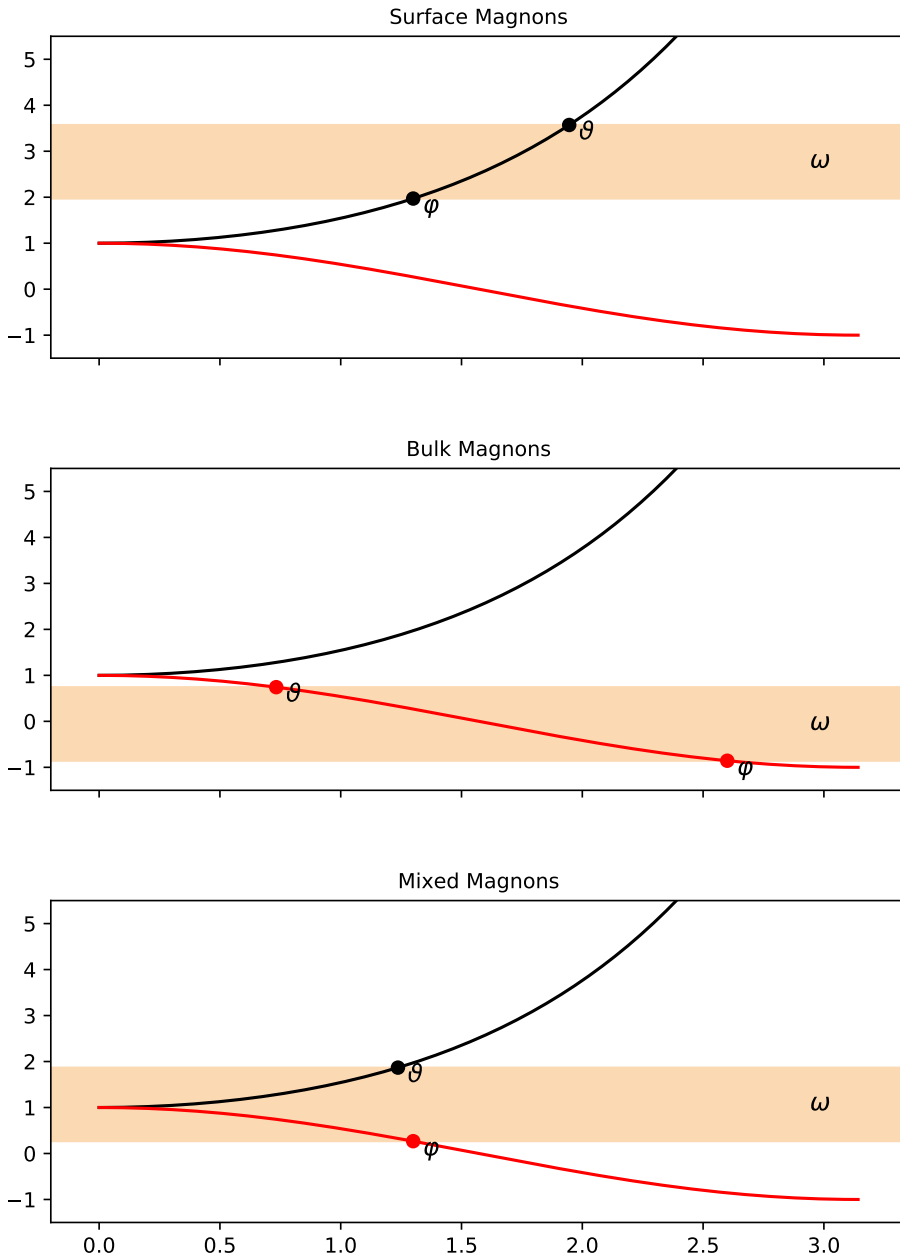


Figure 2.11: Frequency charts for the three types of magnons in the antiferromagnetic layer. Surface magnons have two real (black) frequencies, bulk magnons have two imaginary (red) frequencies, while mixed magnons have one frequency of each kind.

bulk threshold frequency

$$\varphi_B = \iota \arccos(1 - \omega) \quad (2.119)$$

as the lowest imaginary value of φ corresponding to a bulk magnon. For imaginary values of φ below this, ϑ is pushed onto the real branch, so the magnon is mixed. The corresponding *bulk threshold energy quantum* is

$$\varepsilon_B = \sqrt{\varepsilon_\lambda^2 - (\omega - 2)^2}. \quad (2.120)$$

We move on to uncover a degeneracy in the case of bulk magnons that will allow us to reduce the range of interest further. Pulling out the imaginary unit ι from ϑ and φ , the link equation (2.107) for bulk magnons becomes

$$\cos \vartheta = \cos \varphi + \omega \quad (2.121)$$

and the dispersion relation (2.110) for bulk magnons becomes

$$\varepsilon = \sqrt{\varepsilon_\lambda^2 - (\omega + 2 \cos \varphi)^2}. \quad (2.122)$$

In both these equations φ lies in the interval $[\arccos(1 - \omega), \pi]$. But we see from (2.122) that the energy quantum ε only depends on the square of the quantity $(\omega + 2 \cos \varphi)$, which in the given interval of φ runs from $(2 - \omega)$ to $(\omega - 2)$. In other words, for each bulk magnon with frequency φ , there is another bulk magnon with the same energy but *another* frequency φ' . The relation between φ and φ' is

$$2 \cos \varphi' + \omega = -2 \cos \varphi - \omega. \quad (2.123)$$

Using (2.121) this equation can be rewritten to the relations

$$\begin{aligned} \cos \varphi' &= -\cos \vartheta, \\ \cos \vartheta' &= -\cos \varphi, \end{aligned}$$

which mean that

$$\begin{aligned} \varphi' &= \pi - \vartheta, \\ \vartheta' &= \pi - \varphi \end{aligned} \quad (2.124)$$

within the interval of interest. Using the equation (2.104) that was found back in section 2.9 when considering the case $Q = R$, we obtain equations similar to (2.105) for the ansatz terms involving ϑ' and φ' . It then becomes clear that the primed frequencies lead to the exact same magnon as the unprimed ones, just that in this case the φ' term takes on the role as the alternating term while the ϑ' term takes on the role as non-alternating. In other words, we do not need to consider imaginary values of φ over the full interval $[\iota \arccos(1 - \omega), \iota\pi]$, but rather $[\iota \arccos(1 - \omega), \iota \arccos(-\frac{\omega}{2})]$. The *maximum threshold frequency*

$$\varphi_\lambda = \iota \arccos\left(-\frac{\omega}{2}\right) \quad (2.125)$$

corresponds to $(\omega + 2 \cosh \varphi) = 0$ and hence the maximum threshold quantum ε_λ .

This concludes our discussion of the frequency ranges of interest. Since ϑ is determined by the link equation (2.107), only φ needs to be considered. The ranges of interest for φ are

- real values in the interval $\langle 0, \operatorname{arcosh}\left(\frac{\varepsilon_\wedge - \omega}{2}\right)\rangle$ for surface magnons,
- imaginary values in the interval $[0, \iota \arccos(1 - \omega)]$ for mixed magnons,
- imaginary values in the interval $[\iota \arccos(1 - \omega), \iota \arccos(-\frac{\omega}{2})]$ for bulk magnons.

For the special value $\omega = 0$, ϑ and φ coincide, so there exist no mixed magnons. For values $\omega > 2$ on the other hand, bulk magnons cannot exist. The range of interest for mixed magnons is then the whole interval $[0, \iota\pi]$.

We will spend the remainder of this section to take a closer look at magnons at the different threshold frequencies.

Consider first a magnon at the maximum threshold frequency φ_\wedge . In this case $\varepsilon = \varepsilon_\wedge$ and we see from (2.109) that $R = 0$. Pulling out the imaginary unit ι from the frequencies ϑ and φ , we also see that

$$\begin{aligned}\cos \varphi &= -\frac{\omega}{2}, \\ \cos \vartheta &= \frac{\omega}{2},\end{aligned}$$

which means that $\cos \vartheta + \cos \varphi = 0$ and $\vartheta = \pi - \varphi$. This relation between ϑ and φ is exactly what we considered in section 2.9, so we can use (2.105) to reduce the ansatz (2.89) to

$$\begin{aligned}u_p &= \left(X - U(-1)^{\frac{N}{2}}\right) \frac{\cos(\varphi(p - p_m))}{\sin(\varphi(p - p_m))}, \\ v_p &= 0.\end{aligned}\tag{2.126}$$

Meanwhile, the condition equation (2.114) reduces to

$$\zeta \left(\frac{\sin\left(\frac{N+1}{2}\vartheta\right)}{\cos\left(\frac{N+1}{2}\vartheta\right)} \frac{\cos\left(\frac{N-1}{2}\varphi\right)}{\sin\left(\frac{N-1}{2}\varphi\right)} + \frac{\sin\left(\frac{N-1}{2}\vartheta\right)}{\cos\left(\frac{N-1}{2}\vartheta\right)} \frac{\cos\left(\frac{N+1}{2}\varphi\right)}{\sin\left(\frac{N+1}{2}\varphi\right)} \right) = 0.\tag{2.127}$$

But using (2.104), we obtain the identities

$$\begin{aligned}\frac{\sin\left(\frac{N+1}{2}\vartheta\right)}{\cos\left(\frac{N+1}{2}\vartheta\right)} &= (-1)^{\frac{N}{2}} \frac{\cos\left(\frac{N+1}{2}\varphi\right)}{\sin\left(\frac{N+1}{2}\varphi\right)}, \\ \frac{\sin\left(\frac{N-1}{2}\vartheta\right)}{\cos\left(\frac{N-1}{2}\vartheta\right)} &= -(-1)^{\frac{N}{2}} \frac{\cos\left(\frac{N-1}{2}\varphi\right)}{\sin\left(\frac{N-1}{2}\varphi\right)},\end{aligned}\tag{2.128}$$

and so it turns out that the condition equation above is solved automatically for all ω values. This apparently universal maximum threshold solution is eliminated by considering the other surface equations that drop out from the matrix equation (2.111). They reduce to

$$\begin{aligned}\zeta \frac{\sin\left(\frac{N-1}{2}\vartheta\right)}{\cos\left(\frac{N-1}{2}\vartheta\right)} U &= -\zeta \frac{\cos\left(\frac{N-1}{2}\varphi\right)}{\sin\left(\frac{N-1}{2}\varphi\right)} X, \\ \left(\frac{\sin\left(\frac{N+1}{2}\vartheta\right)}{\cos\left(\frac{N+1}{2}\vartheta\right)} + \eta \frac{\sin\left(\frac{N-1}{2}\vartheta\right)}{\cos\left(\frac{N-1}{2}\vartheta\right)} \right) U & \\ = \left(\frac{\cos\left(\frac{N+1}{2}\varphi\right)}{\sin\left(\frac{N+1}{2}\varphi\right)} - \eta \frac{\cos\left(\frac{N-1}{2}\varphi\right)}{\sin\left(\frac{N-1}{2}\varphi\right)} \right) X,\end{aligned}$$

and with the identities above they reduce further to

$$\begin{aligned} \zeta (-1)^{\frac{N}{2}} \frac{\cos \left(\frac{N-1}{2} \varphi \right)}{\sin \left(\frac{N-1}{2} \varphi \right)} U &= \zeta \frac{\cos \left(\frac{N-1}{2} \varphi \right)}{\sin \left(\frac{N-1}{2} \varphi \right)} X, \\ (-1)^{\frac{N}{2}} \left(\frac{\cos \left(\frac{N+1}{2} \varphi \right)}{\sin \left(\frac{N+1}{2} \varphi \right)} - \eta \frac{\cos \left(\frac{N-1}{2} \varphi \right)}{\sin \left(\frac{N-1}{2} \varphi \right)} \right) U \\ &= \left(\frac{\cos \left(\frac{N+1}{2} \varphi \right)}{\sin \left(\frac{N+1}{2} \varphi \right)} - \eta \frac{\cos \left(\frac{N-1}{2} \varphi \right)}{\sin \left(\frac{N-1}{2} \varphi \right)} \right) X. \end{aligned} \quad (2.129)$$

From these equations, it is clear that X is given by

$$X = U (-1)^{\frac{N}{2}}, \quad (2.130)$$

but when plugged into the reduced ansatz (2.126), it leads to a trivial solution which is zero everywhere. The only exception to this is when

$$\begin{aligned} \zeta \frac{\cos \left(\frac{N-1}{2} \varphi \right)}{\sin \left(\frac{N-1}{2} \varphi \right)} &= 0, \\ \frac{\cos \left(\frac{N+1}{2} \varphi \right)}{\sin \left(\frac{N+1}{2} \varphi \right)} &= \eta \frac{\cos \left(\frac{N-1}{2} \varphi \right)}{\sin \left(\frac{N-1}{2} \varphi \right)}, \end{aligned}$$

so that all the matrix elements of (2.111) vanish and the amplitudes U and X are free. $\frac{\cos \left(\frac{N-1}{2} \varphi \right)}{\sin \left(\frac{N-1}{2} \varphi \right)} = 0$ and $\frac{\cos \left(\frac{N+1}{2} \varphi \right)}{\sin \left(\frac{N+1}{2} \varphi \right)} = 0$ also lead to trivial solutions, so the only option turns out to be

$$\begin{aligned} \zeta &= 0, \\ \frac{\cos \left(\frac{N+1}{2} \varphi \right)}{\sin \left(\frac{N+1}{2} \varphi \right)} &= \eta \frac{\cos \left(\frac{N-1}{2} \varphi \right)}{\sin \left(\frac{N-1}{2} \varphi \right)}. \end{aligned}$$

From the definition of ζ and η in (2.86), we see that $\zeta = 0$ corresponds to $\rho = \frac{5}{4}$ and $\eta = \frac{\omega}{4}$. To summarise, maximum threshold solutions exist only in the special case

$$\begin{aligned} \rho &= \frac{5}{4}, \\ 4 \frac{\cos \left(\frac{N+1}{2} \arccos \left(-\frac{\omega}{2} \right) \right)}{\sin \left(\frac{N+1}{2} \arccos \left(-\frac{\omega}{2} \right) \right)} &= \omega \frac{\cos \left(\frac{N-1}{2} \arccos \left(-\frac{\omega}{2} \right) \right)}{\sin \left(\frac{N-1}{2} \arccos \left(-\frac{\omega}{2} \right) \right)}. \end{aligned} \quad (2.131)$$

Here the upper functions correspond to symmetric magnons and the lower functions correspond to antisymmetric magnons as usual.

Consider now a symmetric magnon at the bulk threshold frequency φ_B given in (2.119). At this threshold, ϑ is zero, and so all sine factors involving ϑ vanish. This means that the first terms in the ansatz (2.89) disappear. The condition equation (2.114) is also automatically solved, so it appears to be a valid solution. But looking at the other surface equation (2.115), we see that in this case X , and so also W , is forced to be zero, so actually *both* terms in the ansatz vanish. Hence the apparent solution is a trivial solution after all.

A similar argument holds in the case of a symmetric magnon at the threshold frequency $\varphi = \iota\pi$, in which all cosine factors involving φ disappear, as well as in the case of an

antisymmetric magnon at the surface threshold frequency $\varphi_S = 0$, in which all sine factors involving φ disappear. In total then, the bulk threshold frequency $\varphi_B = \iota \arccos(1 - \omega)$ and the threshold frequency $\varphi = \iota\pi$ (which only appears for $\omega \geq 2$) should be excluded when considering symmetric magnons, and the surface threshold frequency $\varphi_S = 0$ should be excluded when considering antisymmetric magnons.

The considerations above apply in all cases except the subtle special case in which all the matrix elements of the matrix equation (2.111) vanish. We will not inspect this special case further. Instead, we will move on to normalise our analytical solutions.

2.11 Normalisation

The link equation (2.107) and the condition equation (2.114) can be solved together to get all the possible values of ϑ and φ . With these values known, we obtain the energy quantum ε from the dispersion relation (2.110), the ratio R determining V and W in terms of U and X from equation (2.109) and the last relation between U and X from equation (2.115). The final value of U can then be determined from the normalisation

$$\sum_p (u_p^2 - v_p^2) = 1 \quad (2.132)$$

as explained in section 2.7. In this section, we will find an explicit analytical expression for U .

Plugging our ansatz (2.89) into the normalisation equation above, we get

$$\begin{aligned} \sum_p \left(U^2 \frac{\sinh^2}{\cosh^2}(\vartheta(p - p_m)) + X^2 \frac{\cosh^2}{\sinh^2}(\varphi(p - p_m)) \right. \\ \left. + 2UX \frac{1 + R^2}{1 - R^2} (-1)^p \frac{\sinh}{\cosh}(\vartheta(p - p_m)) \frac{\cosh}{\sinh}(\varphi(p - p_m)) \right) = \frac{1}{1 - R^2}, \end{aligned}$$

where $V = -RU$ and $W = RX$ were used to eliminate V and W . Introduce now the ratio O as

$$O = \frac{\frac{\sinh}{\cosh}\left(\frac{N+1}{2}\vartheta\right) + (\zeta R + \eta) \frac{\sinh}{\cosh}\left(\frac{N-1}{2}\vartheta\right)}{\frac{\sinh}{\cosh}\left(\frac{N+1}{2}\varphi\right) + (\zeta R - \eta) \frac{\sinh}{\cosh}\left(\frac{N-1}{2}\varphi\right)}, \quad (2.133)$$

and rewrite (2.115) to the simple relation

$$X = OU. \quad (2.134)$$

Then the normalisation simplifies to

$$\begin{aligned} \frac{1}{(1 - R^2)U^2} = \sum_p \left(\frac{\sinh^2}{\cosh^2}(\vartheta(p - p_m)) + O^2 \frac{\cosh^2}{\sinh^2}(\varphi(p - p_m)) \right. \\ \left. + 2O \frac{1 + R^2}{1 - R^2} (-1)^p \frac{\sinh}{\cosh}(\vartheta(p - p_m)) \frac{\cosh}{\sinh}(\varphi(p - p_m)) \right), \end{aligned}$$

and using the hyperbolic identities

$$\begin{aligned} 2 \sinh^2 \alpha &= \cosh(2\alpha) - 1, \\ 2 \cosh^2 \alpha &= \cosh(2\alpha) + 1, \\ 2 \sinh \alpha \cosh \beta &= \sinh(\alpha + \beta) + \sinh(\alpha - \beta), \end{aligned} \quad (2.135)$$

which apply to all phases α and β , it reduces further to

$$\begin{aligned} \frac{2}{(1-R^2)U^2} &= \sum_p \left(\cosh(2\vartheta(p-p_m)) + O^2 \cosh(2\varphi(p-p_m)) \mp (1-O^2) \right. \\ &\left. + 2O \frac{1+R^2}{1-R^2} (-1)^p \left(\sinh((\vartheta+\varphi)(p-p_m)) \pm \sinh((\vartheta-\varphi)(p-p_m)) \right) \right). \end{aligned} \quad (2.136)$$

There are four hyperbolic terms in this equation that we need to sum over all p from 1 to N . To this end, we first look at the sum $\sum_p e^{\pm\alpha(p-p_m)}$, which can be rewritten to

$$\sum_{p=1}^N e^{\pm\alpha(p-p_m)} = e^{\mp\alpha p_m} \left(\sum_{p=0}^N e^{\pm\alpha p} - 1 \right).$$

As long as the phase α is not $\iota 2z\pi$ for some integer $z \in \mathbb{Z}$, this can be summed as a finite geometric sum to

$$\sum_{p=1}^N e^{\pm\alpha(p-p_m)} = e^{\mp\alpha p_m} \left(\frac{e^{\pm(N+1)\alpha} - 1}{e^{\pm\alpha} - 1} - 1 \right), \quad (2.137)$$

and with the definition (2.88) for p_m , this yields

$$\sum_{p=1}^N e^{\pm\alpha(p-p_m)} = \frac{\sinh\left(\frac{N+1}{2}\alpha\right)}{\sinh\left(\frac{\alpha}{2}\right)} e^{\mp\frac{\alpha}{2}} - e^{\mp\frac{N+1}{2}\alpha}. \quad (2.138)$$

Adding then $e^{\alpha(p-p_m)}$ and $e^{-\alpha(p-p_m)}$ to get $\cosh(\alpha(p-p_m))$, we end up with

$$\sum_p \cosh(\alpha(p-p_m)) = \frac{\sinh\left(\frac{N+1}{2}\alpha\right)}{\sinh\left(\frac{\alpha}{2}\right)} \cosh\left(\frac{\alpha}{2}\right) - \cosh\left(\frac{N+1}{2}\alpha\right).$$

But this can be simplified even further by using the identity

$$\sinh \alpha \cosh \beta - \cosh \alpha \sinh \beta = \sinh(\alpha - \beta), \quad (2.139)$$

which is applicable to all phases α and β . With this, we finally obtain

$$\sum_p \cosh(\alpha(p-p_m)) = \frac{\sinh\left(N\frac{\alpha}{2}\right)}{\sinh\left(\frac{\alpha}{2}\right)}. \quad (2.140)$$

As mentioned, this formula applies to all phases α except $\iota 2z\pi$ for some integer $z \in \mathbb{Z}$. In that special case, the sum is simply N (which is also the limit of the formula above).

To sum the hyperbolic sine terms of (2.136), note first that these are multiplied by the alternating factor $(-1)^p$. The corresponding exponential sums are then $\sum_p (-1)^p e^{\pm\alpha(p-p_m)}$, which yield

$$\sum_{p=1}^N (-1)^p e^{\pm\alpha(p-p_m)} = e^{\mp\alpha p_m} \left(\frac{e^{\pm(N+1)\alpha} + 1}{e^{\pm\alpha} + 1} - 1 \right)$$

(as long as the phase α is not $\iota(2z+1)\pi$ for some integer $z \in \mathbb{Z}$), and so

$$\sum_{p=1}^N (-1)^p e^{\pm\alpha(p-p_m)} = \frac{\cosh\left(\frac{N+1}{2}\alpha\right)}{\cosh\left(\frac{\alpha}{2}\right)} e^{\mp\frac{\alpha}{2}} - e^{\mp\frac{N+1}{2}\alpha}. \quad (2.141)$$

Subtracting then $(-1)^p e^{\alpha(p-p_m)}$ and $(-1)^p e^{-\alpha(p-p_m)}$ to get $(-1)^p \sinh(\alpha(p-p_m))$, we end up with

$$\sum_p (-1)^p \sinh(\alpha(p-p_m)) = -\frac{\cosh\left(\frac{N+1}{2}\alpha\right)}{\cosh\left(\frac{\alpha}{2}\right)} \sinh\left(\frac{\alpha}{2}\right) + \sinh\left(\frac{N+1}{2}\alpha\right).$$

Now again using the identity (2.139), we get

$$\sum_p (-1)^p \sinh(\alpha(p-p_m)) = \frac{\sinh\left(N\frac{\alpha}{2}\right)}{\cosh\left(\frac{\alpha}{2}\right)}. \quad (2.142)$$

This formula applies to all phases α except $\iota(2z+1)\pi$ for some integer $z \in \mathbb{Z}$, in which case the sum is simply $-N(-1)^{\frac{N}{2}}$ (which is also the limit of the formula).

Moving back to the normalisation (2.136) we see that the relevant phases are 2ϑ , 2φ , $(\vartheta + \varphi)$ and $(\vartheta - \varphi)$. Using first our cosine sum formula (2.140), we get that

$$\begin{aligned} \sum_p \cosh(2\vartheta(p-p_m)) &= \frac{\sinh(N\vartheta)}{\sinh\vartheta}, \\ \sum_p \cosh(2\varphi(p-p_m)) &= \frac{\sinh(N\varphi)}{\sinh\varphi}. \end{aligned} \quad (2.143)$$

Using next our sine sum formula (2.142), we get that

$$\begin{aligned} \sum_p (-1)^p \left(\sinh((\vartheta + \varphi)(p-p_m)) \pm \sinh((\vartheta - \varphi)(p-p_m)) \right) \\ = \frac{\sinh\left(N\frac{\vartheta+\varphi}{2}\right)}{\cosh\left(\frac{\vartheta+\varphi}{2}\right)} \pm \frac{\sinh\left(N\frac{\vartheta-\varphi}{2}\right)}{\cosh\left(\frac{\vartheta-\varphi}{2}\right)}, \end{aligned}$$

which can be rewritten using the hyperbolic identity

$$2 \cosh \alpha \cosh \beta = \cosh(\alpha + \beta) + \cosh(\alpha - \beta) \quad (2.144)$$

as well as the last identity in (2.135) to

$$\begin{aligned} & \sum_p (-1)^p \left(\sinh((\vartheta + \varphi)(p - p_m)) \pm \sinh((\vartheta - \varphi)(p - p_m)) \right) \\ &= 2 \frac{\sinh\left(\frac{N+1}{2}\vartheta\right) \cosh\left(\frac{N-1}{2}\varphi\right) + \sinh\left(\frac{N-1}{2}\vartheta\right) \cosh\left(\frac{N+1}{2}\varphi\right)}{\omega + 2 \cosh \varphi}, \end{aligned} \quad (2.145)$$

after some algebra. We recognise the terms in the nominator and the denominator from other equations.

Plugging the results (2.143) and (2.145) into the normalisation (2.136), we end up with the final equation

$$\begin{aligned} \frac{2}{(1 - R^2)U^2} &= \frac{\sinh(N\vartheta)}{\sinh \vartheta} + O^2 \frac{\sinh(N\varphi)}{\sinh \varphi} \mp N(1 - O^2) \\ &+ 4O \frac{1 + R^2}{1 - R^2} \frac{\sinh\left(\frac{N+1}{2}\vartheta\right) \cosh\left(\frac{N-1}{2}\varphi\right) + \sinh\left(\frac{N-1}{2}\vartheta\right) \cosh\left(\frac{N+1}{2}\varphi\right)}{\omega + 2 \cosh \varphi}, \end{aligned} \quad (2.146)$$

which can be used to get properly normalised magnons. This normalisation equation concludes our analytical work for the general case.

2.12 Magnon plots

To make sure that the analytical equations found in sections 2.8–2.11 are correct, we will solve the link equation (2.107) and the condition equation (2.114) numerically to get the possible frequencies ϑ and φ and check that our analytical solutions are consistent with the figures 2.8 and 2.9, which were found by numerical diagonalisation in section 2.7.

To this end, define the *condition function* as the left hand side of the condition equation (2.114). The condition function is then supposed to be zero for all the possible values of ϑ and φ , and using the link equation (2.107) to eliminate ϑ , the solutions can be found numerically by Newton’s method.

In the magnon solver script introduced in section 2.7, a class method `findMagnons` was added to the class `MagnetSolver`. This method takes in a parity (symmetric or antisymmetric) and a type (surface, bulk or mixed) and calculates the corresponding condition function within the range of interest for the frequency parameter φ . It then finds the roots of the function using Newton’s method and proceeds to calculate the other magnon quantities following the procedure described in the beginning of section 2.11. The value of U is given by the normalisation equation (2.146), and finally the results are plotted in the same fashion as the results from numerical diagonalisation. There is also an option to plot the condition function over the range of interest.

An umbrella method `calcAnaMagnons` was also implemented, which runs multiple executions of `findMagnons` — one for each specification. The implementation of Newton’s method used in the script is the method `newton` from the `optimize` module of the SciPy library. The SciPy library is a specialised Python library that works with the NumPy library, but provides additional scientific calculus functionality such as numerical optimisation and integration.

Note that for imaginary frequencies ϑ or φ , the corresponding hyperbolic terms in the ansatz (2.89) become trigonometric. However in the case of hyperbolic sine functions, the imaginary unit ι does not disappear when pulled out of the frequency, but instead stays as shown in (2.90). With a small redefinition of the corresponding amplitude by absorbing the imaginary unit into the amplitude, most of the equations stay the same when switching affected hyperbolic functions with their trigonometric counterparts. The only exception is the ratio O given in (2.133) and the normalisation equation (2.146). For imaginary ϑ or φ , O becomes imaginary. This does not affect the relation $X = OU$ with redefined amplitudes, but the normalisation equation, in which squares of both O and the amplitude U appear, the signs must be adjusted in some cases. All this is done in the magnon solver script, whose code can be found in appendix A.

For comparison, the "analytical" method `calcAnaMagnons` was executed for the same parameters as the ones used back in the figures 2.8 and 2.9. One symmetric surface magnon pair, five symmetric mixed magnon pairs and six antisymmetric mixed magnon pairs were found. In other words, no antisymmetric surface magnon pair exists for these parameters, and the second magnon pair in figure 2.8 is actually a mixed magnon pair. This makes sense, as the graphs look more like bounded trigonometric graphs than exponentially growing hyperbolic graphs.

Figures 2.12–2.17 show the resulting plots from the analytical approach as well as the condition function in each case. Both the energy quanta and the amplitude graphs match the results from the numerical diagonalisation approach exactly.

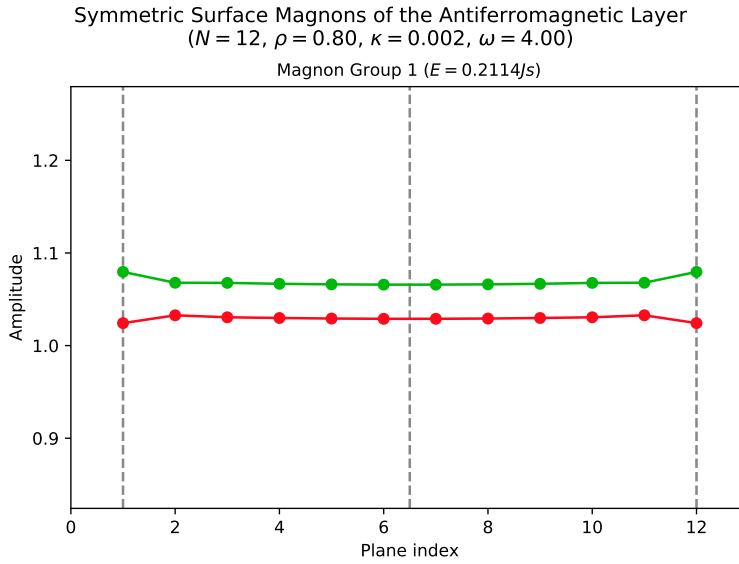


Figure 2.12: The symmetric surface magnons of a 12-plane antiferromagnetic layer for the given parameters.

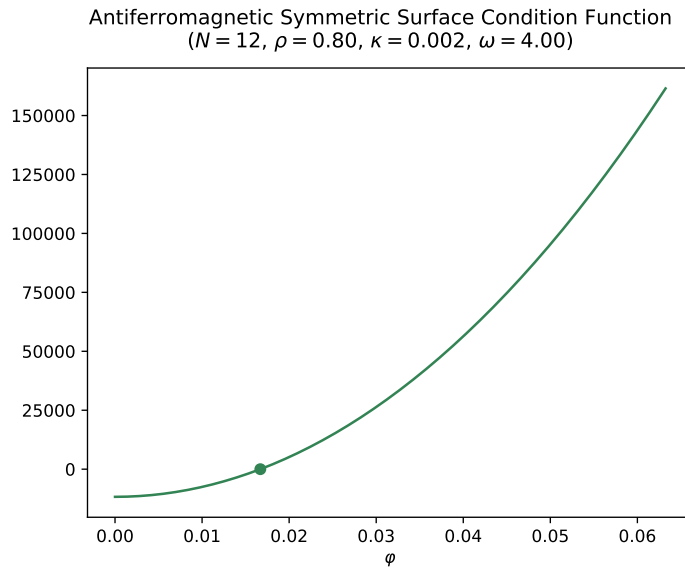


Figure 2.13: Condition function for the symmetric surface magnons of a 12-plane antiferromagnetic layer for the given parameters. The found root is marked with a point.

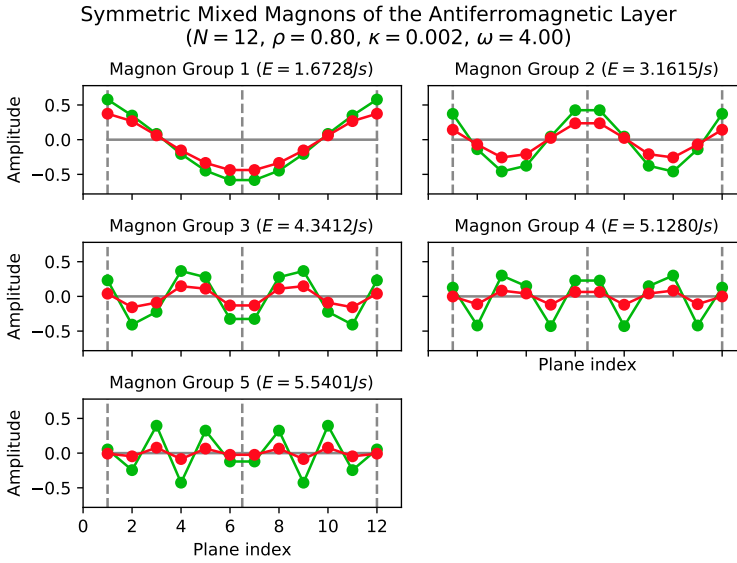


Figure 2.14: The symmetric mixed magnons of a 12-plane antiferromagnetic layer for the given parameters.

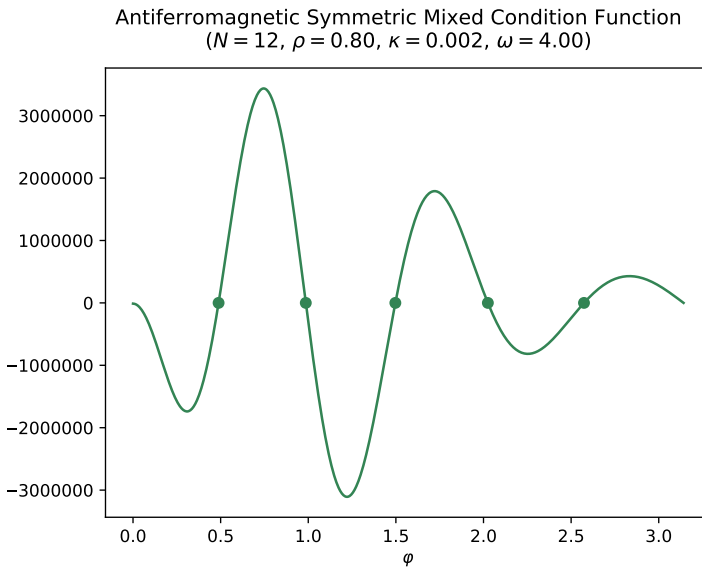


Figure 2.15: Condition function for the symmetric mixed magnons of a 12-plane antiferromagnetic layer for the given parameters. The found roots are marked with points.

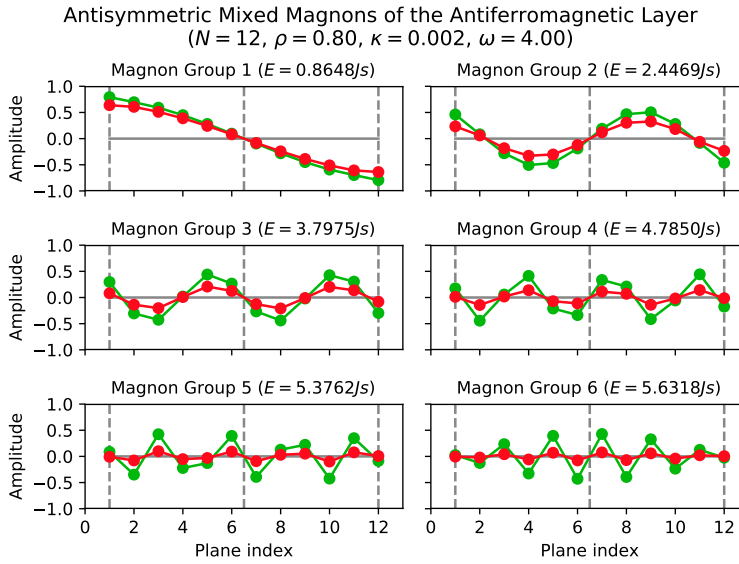


Figure 2.16: The antisymmetric mixed magnons of a 12-plane antiferromagnetic layer for the given parameters.

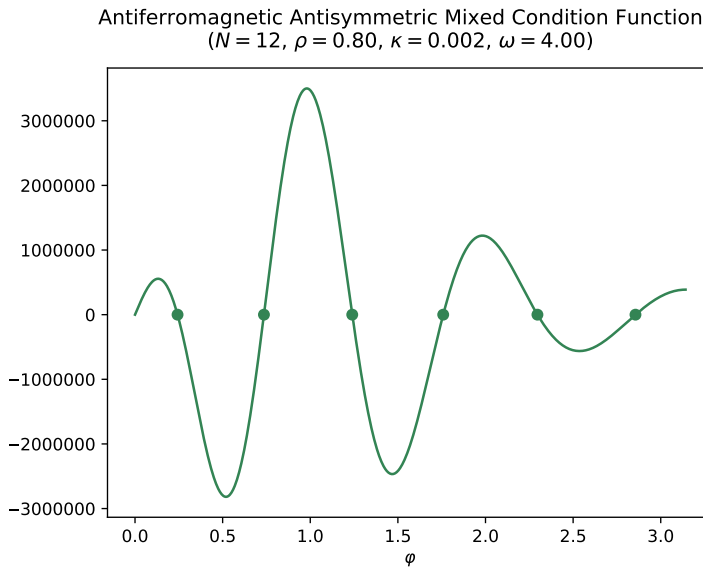


Figure 2.17: Condition function for the antisymmetric mixed magnons of a 12-plane antiferromagnetic layer for the given parameters. The found roots are marked with points.

The condition function for antisymmetric surface magnons is shown in figure 2.18. The function appears to be strictly increasing from its initial value of zero, which explains why there are no antisymmetric surface magnons in this case.

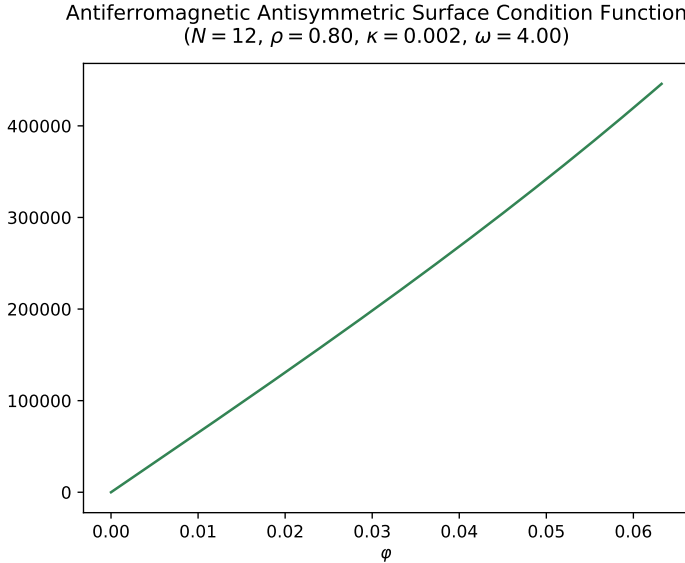


Figure 2.18: Condition function for the antisymmetric surface magnons of a 12-plane antiferromagnetic layer for the given parameters. As there are no roots on the range of interest, no antisymmetric surface magnons exist for this set of parameters.

So far all our magnon plots have been for the maximal wave parameter value $\omega = 4$, which corresponds to the special case of a zero planar wave vector. We now plot magnons for the wave parameter value $\omega = 1.7$, which corresponds to a non-zero planar wave vector. This case is a little more interesting, as it allows for bulk magnons, and we see from the plots in figures 2.19–2.24 that bulk magnons indeed appear. In this case, antisymmetric surface magnons also make their debut.

An interesting observation is that the symmetric surface magnons are strongly localised at the surfaces in this case compared to the almost uniform magnons in the case $\omega = 4$. Apparently, magnons that have a planar direction tend to localise more than magnons of no planar direction. Some more experimentation with the parameters justified this. Another observation that seems to be general is that the surface magnons have much higher amplitude values at the surfaces than the other magnons.

Ever since we split up the Hamiltonian (2.36) into partial Hamiltonians (2.38) back in section 2.4, we have concentrated on one specific value of the wave parameter ω at a time. However, now that we have our results, we should stand back and emphasise that our antiferromagnetic layer has magnons for *every* value of ω between 0 and 4. The total energy spectrum will be investigated in the next section.

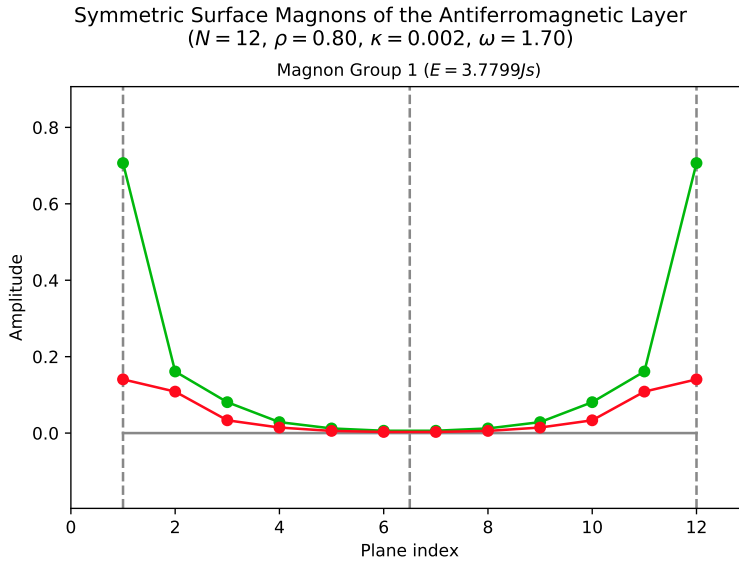


Figure 2.19: The symmetric surface magnons of a 12-plane antiferromagnetic layer for the given parameters. These magnons are much more strongly localised at the surfaces than the symmetric surface magnons for $\omega = 4$.

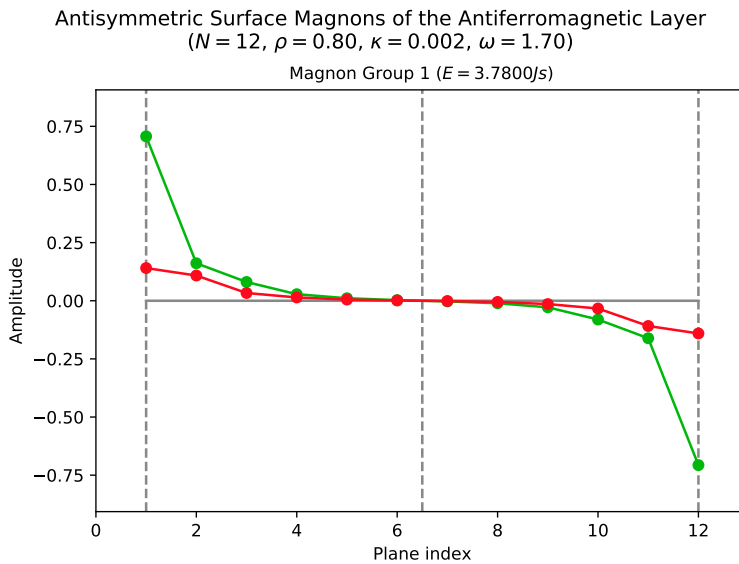


Figure 2.20: The antisymmetric surface magnons of a 12-plane antiferromagnetic layer for the given parameters.

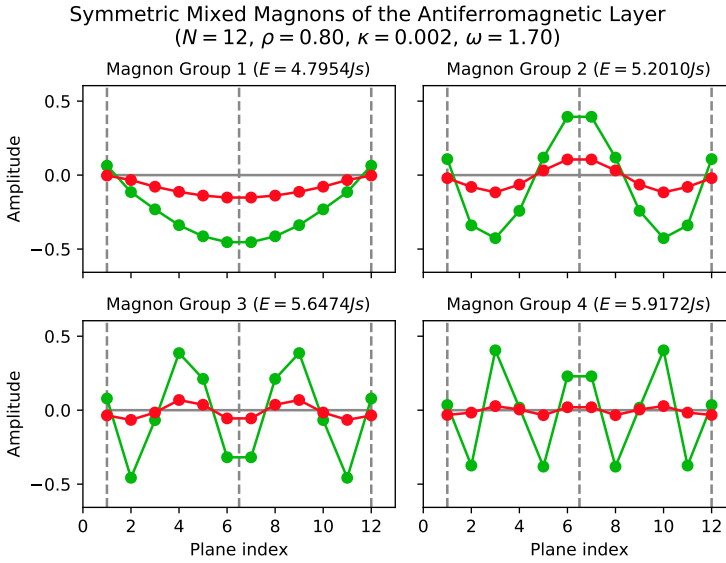


Figure 2.21: The symmetric mixed magnons of a 12-plane antiferromagnetic layer for the given parameters.

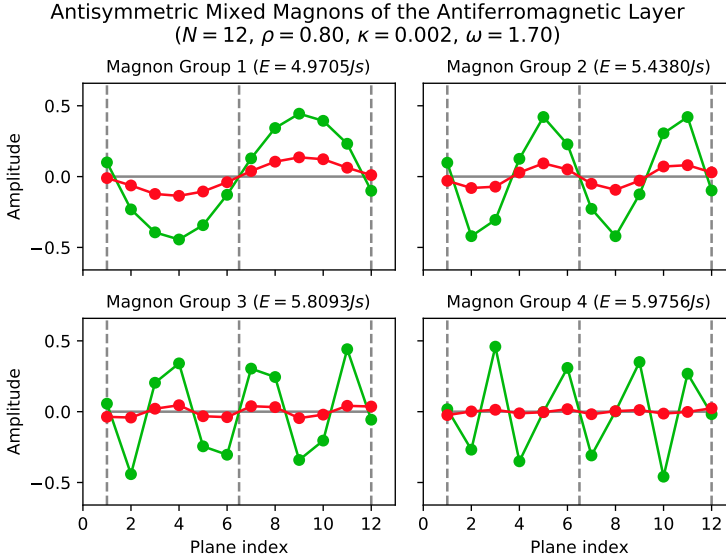


Figure 2.22: The antisymmetric mixed magnons of a 12-plane antiferromagnetic layer for the given parameters.

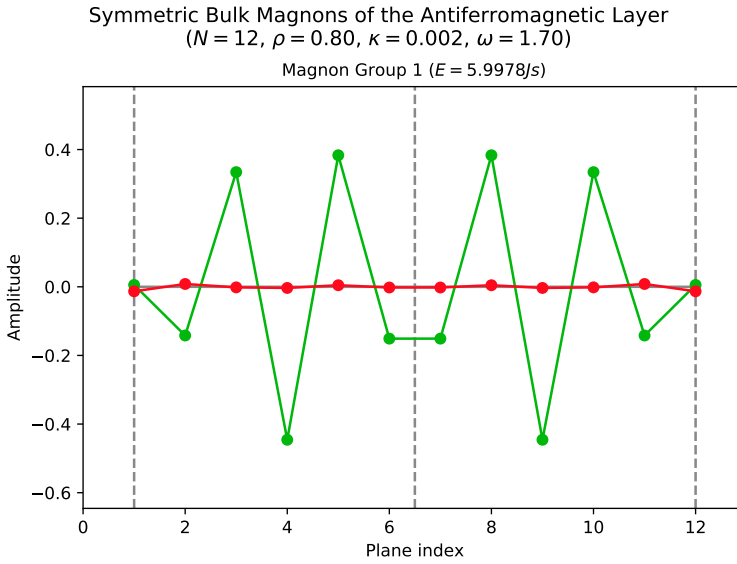


Figure 2.23: The symmetric bulk magnons of a 12-plane antiferromagnetic layer for the given parameters.

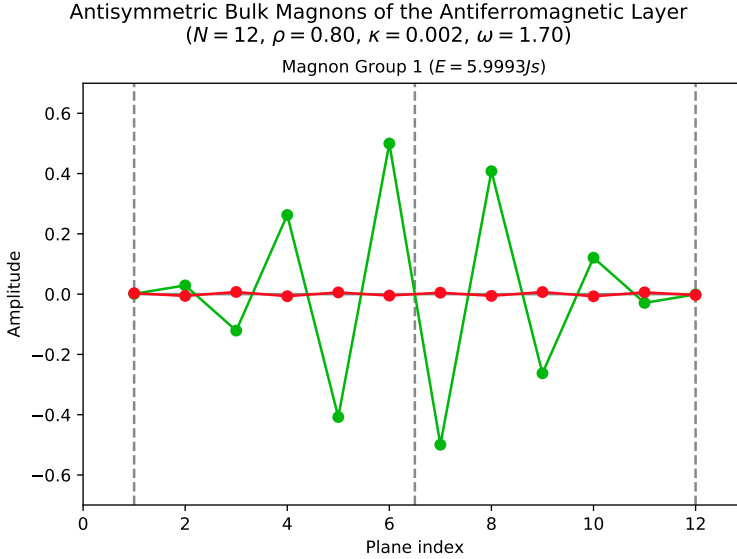


Figure 2.24: The antisymmetric bulk magnons of a 12-plane antiferromagnetic layer for the given parameters.

2.13 Energy spectrum

The energy spectrum of our antiferromagnetic layer should be plotted over all values of the wave parameter ω . Section 2.10 already gave us many important results about energy thresholds that we will use.

The surface threshold energy ε_S given in (2.117) separates surface magnons and mixed magnons. Surface magnons have energy quanta below ε_S , and we see from the dispersion relation (2.110) that the higher the real frequency φ is, the lower the energy quantum.

The bulk threshold energy ε_B given in (2.120) separates mixed magnons and bulk magnons. Mixed magnons have energy quanta between ε_S and ε_B , but this time the higher the imaginary frequency φ is, the higher the energy quantum too. This explains why the number of nodes increase with increasing energy, as was noted back in section 2.7, because a high frequency corresponds to a high number of nodes.

For $\omega \leq 2$ there exist bulk magnons that have energies from the bulk threshold energy ε_B and up to the maximum threshold energy $\varepsilon_\Lambda = 6 + 2\kappa$. Also here the energy increases with the imaginary frequency φ . For $\omega > 2$, there are no bulk magnons and the bulk threshold energy is the maximum threshold for *all* magnons.

Before we plot the energy spectrum, we look at the special case $\omega = 0$, corresponding to planar wave vectors at the edge of the Brillouin zone. In this case, ϑ and φ are actually forced to be equal. This is apparent using the visualisation introduced in section 2.10 with an omega layer of height zero. But now it follows that the symmetric and antisymmetric versions of the condition equation (2.114) simplify to the same condition equation,

$$\begin{aligned}
 & 2 \cosh \varphi \sinh \left(\frac{N+1}{2} \varphi \right) \cosh \left(\frac{N+1}{2} \varphi \right) \\
 & + \varepsilon_\Lambda \zeta \left(\sinh \left(\frac{N+1}{2} \varphi \right) \cosh \left(\frac{N-1}{2} \varphi \right) + \sinh \left(\frac{N-1}{2} \varphi \right) \cosh \left(\frac{N+1}{2} \varphi \right) \right) \\
 & + 2\zeta^2 \cosh \varphi \sinh \left(\frac{N-1}{2} \varphi \right) \cosh \left(\frac{N-1}{2} \varphi \right) = 0, \quad (2.147)
 \end{aligned}$$

because η vanishes and the frequencies coincide. This means that each energy quantum in this case corresponds to one symmetric and one antisymmetric magnon branch. The symmetric and antisymmetric branches split for higher values of ω .

In the magnon solver script a method `plotMagSpectrum` was added to plot the energy spectrum of our antiferromagnetic layer. This method takes in the parameters N , ρ and κ and creates one instance of the `MagnetSolver` class for each value of ω . Each class instance runs a numerical diagonalisation to get the allowed energy quanta, and the energy quanta, as well as the threshold energies ε_S , ε_B and ε_Λ are plotted over the range of ω .

The energy spectrum of a 12-plane antiferromagnetic layer with $\rho = 0.8$ and $\kappa = 0.002$ is shown in figure 2.25. Zooming in on parts of the spectrum in figures 2.26, 2.27 and 2.28, we see that the spectrum is consistent with our results from section 2.12. The magnon branches appear in pairs that coincide at $\omega = 0$. One of these branches is then symmetric, while the other one is antisymmetric, as discussed above. Finally we see that one of the surface branches is truncated for ω values above 3.75, where it becomes a mixed branch. This is why no antisymmetric surface magnon appeared in the case of $\omega = 4.0$.

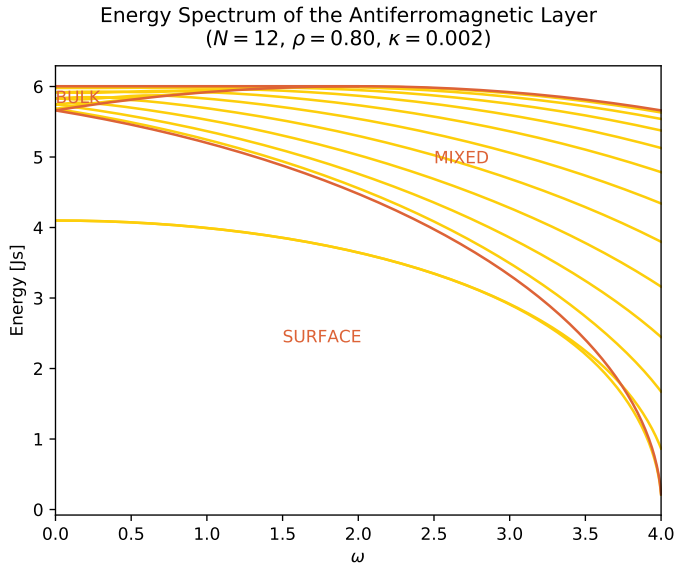


Figure 2.25: The energy spectrum of a 12-plane antiferromagnetic layer for the given parameters. The actual energy branches are plotted in yellow, while the threshold energies are plotted in brown.

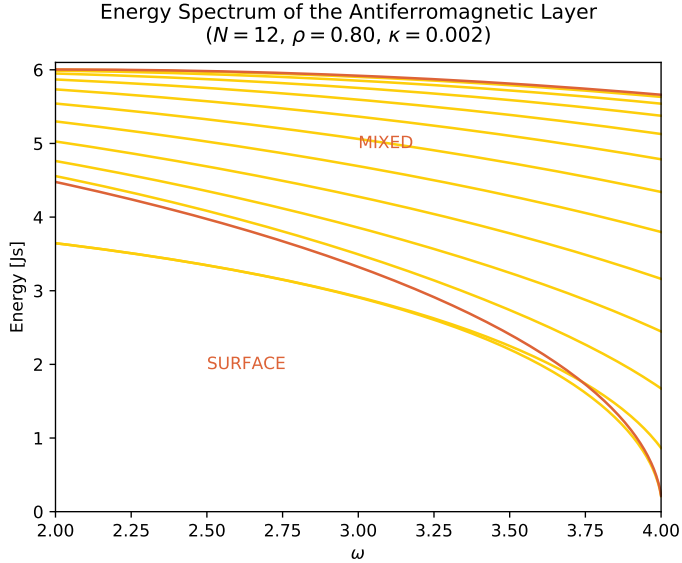


Figure 2.26: Zooming in on the right part of the spectrum, we see that there are eleven mixed magnons and one surface magnon for $\omega = 4.0$.

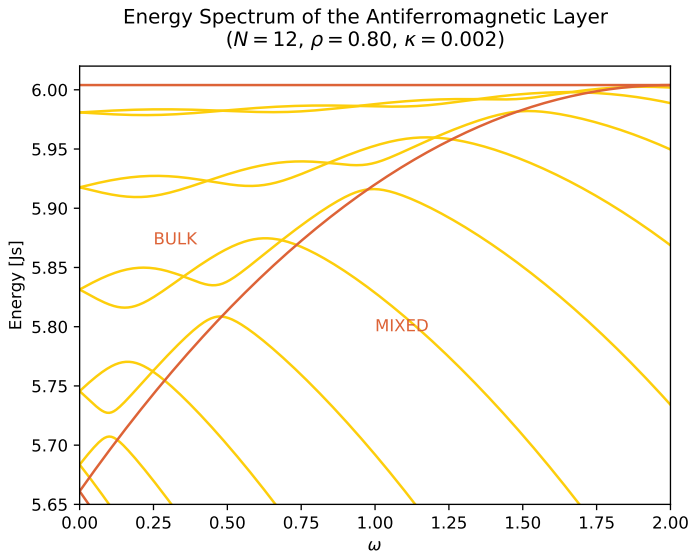


Figure 2.27: Zooming in on the bulk part of the spectrum, we see that there are two bulk magnons and eight mixed magnons for the $\omega = 1.7$. Here we also see that the magnon branches appear in pairs at $\omega = 0$.

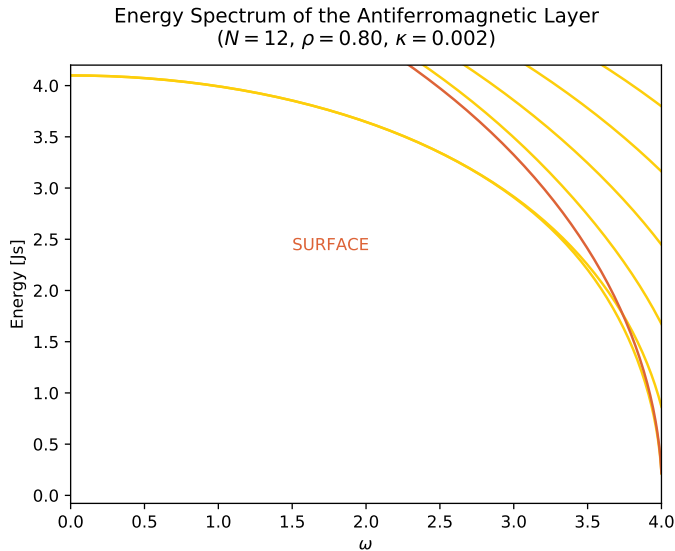


Figure 2.28: Zooming in on the lower part of the spectrum, we see that there are two surface magnons for $\omega = 1.7$ and one surface magnon for $\omega = 4$. The antisymmetric surface branch is truncated at high values, which is why no antisymmetric surface magnons appear in the last case.

In the figures 2.25–2.28, we see that there are never more than two surface magnons for each value of the wave parameter ω . This makes sense from the hyperbolic nature of the surface condition equation (2.114). Since all terms grow exponentially, there should be one solution at most where the positive and negative terms catch up with each other. However we know that the number of magnon branches should correspond to the plane number N . For a higher plane number then, all additional magnon branches have to be bulk/mixed branches. We plot the energy spectrum for the same parameters but 40 planes in figure 2.29. Apparently, the bulk/mixed branches are going towards an energy continuum for higher plane numbers. We will call this continuum the *bulk continuum* of the antiferromagnetic layer. Even though most of the magnons within this continuum are actually mixed magnons, they all share the delocalised nature of the trigonometric functions, in contrast to the surface localised nature of the hyperbolic functions.

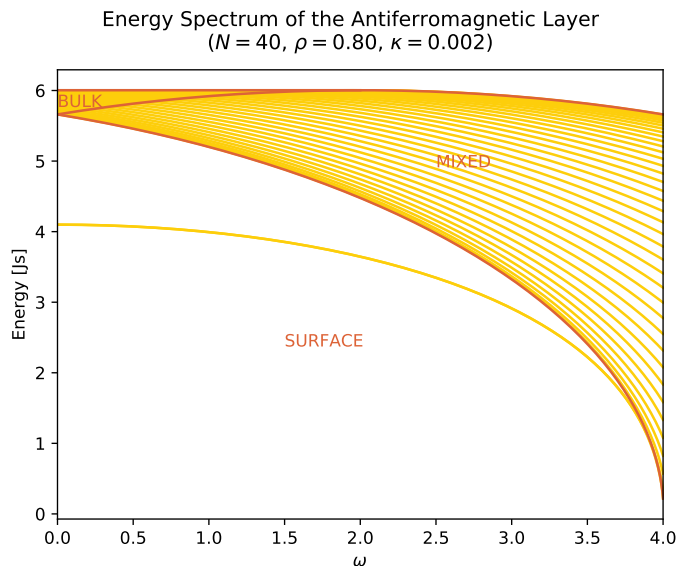


Figure 2.29: The energy spectrum of a 40-plane antiferromagnetic layer for the given parameters.

We are very soon in a position to compare our results to the main results from Wolfram and De Wames [1969]. To do this, we have to go to the *semi-infinite limit* for which the number of planes in the layer N approaches infinity.

2.14 Semi-infinite limit

As described in section 1.3, Wolfram and De Wames [1969] also studied an antiferromagnetic Heisenberg model on a simple cubic lattice with a distinct surface spin exchange. But there are two key differences between their model and the model of this thesis. The first difference is the number of planes in the x -direction, which is *semi-infinite* in their case. That is, there is only one surface in their model, as their antiferromagnetic layer stretches

into infinity, in contrast to our finite antiferromagnetic layer with two surfaces.

The second difference is the easy-axis term in our Hamiltonian (2.2), which is replaced in Wolfram and De Wames' treatment with an anisotropy term involving simply the spin z-components instead of their squares. This anisotropy term is controlled by an external magnetic field through the parameter $[\omega_H]$ and an anisotropy field through the parameter $[\omega_A(i)]$. The anisotropy field carries opposite signs on each of the two sublattices, so it enhances alternating spins along the z-axis similar to the parameter K in our treatment. However, it is distinct at the surface, where it takes the value $[\omega_{A1}]$, while in the bulk it takes the uniform value $[\omega_A]$.

The fundamental difference between our squared easy-axis term and the non-squared anisotropy term of Wolfram and De Wames is a problem when it comes to comparing results. Fortunately, their main results, which are the threshold values of the surface spin exchange ratio $[\epsilon]$, were derived in the special case of a vanishing anisotropy field, $[\omega_A] = [\omega_{A1}] = 0$. The remaining external magnetic field term only results in a well-known energy shift which can be eliminated by introducing the "effective" energy quanta $[\omega - \omega_H]$ instead of the actual energy quanta $[\omega]$. With this redefined energy, the results looks similar to the case of no external magnetic field.

To compare our results to the results of Wolfram and De Wames [1969] then, we only need to take the limits $N \rightarrow \infty$ and $\kappa \rightarrow 0$. Looking at the condition equation (2.114), the factors involving N and φ are $\cosh\left(\frac{N \pm 1}{2}\varphi\right)$ and $\sinh\left(\frac{N \pm 1}{2}\varphi\right)$. In the case bulk and mixed magnons with an imaginary frequency φ , these factors get an increasing amount of nodes with increasing N , so in the limit $N \rightarrow \infty$, the condition equation is virtually solved for *all* possible values of φ on the range of interest. This means that there is an infinite amount of magnons within the bulk continuum introduced in the previous section, justifying the name "continuum".

In the case of surface magnons with real frequencies ϑ and φ , the factors involving N and φ can be approximated to

$$\begin{aligned}\cosh\left(\frac{N \pm 1}{2}\varphi\right) &\approx \frac{e^{\frac{N \pm 1}{2}\varphi}}{2}, \\ \sinh\left(\frac{N \pm 1}{2}\varphi\right) &\approx \frac{e^{\frac{N \pm 1}{2}\varphi}}{2}\end{aligned}\quad (2.148)$$

in the limit $N \rightarrow \infty$. A similar approximation applies to the factors involving N and ϑ . Using this, the condition equation (2.114) can now be reduced to

$$\begin{aligned}(\omega + 2 \cosh \varphi)e^{\frac{\vartheta + \varphi}{2}} + (\varepsilon_\Lambda \zeta - (\omega + 2 \cosh \varphi)\eta)e^{\frac{\vartheta - \varphi}{2}} + \\ (\varepsilon_\Lambda \zeta + (\omega + 2 \cosh \varphi)\eta)e^{-\frac{\vartheta - \varphi}{2}} + (\omega + 2 \cosh \varphi)(\zeta^2 - \eta^2)e^{-\frac{\vartheta + \varphi}{2}} = 0,\end{aligned}$$

where the factors involving N was divided out. Multiplying through by $e^{\frac{\vartheta + \varphi}{2}}$ and refactoring the terms, this equation becomes simply

$$(\omega + 2 \cosh \varphi) \left((e^\vartheta + \eta) (e^\varphi - \eta) + \zeta^2 \right) + \varepsilon_\Lambda \zeta (e^\vartheta + e^\varphi) = 0. \quad (2.149)$$

Both in the symmetric and the antisymmetric case the condition equation reduced to (2.149). This means that the frequencies ϑ and φ , and hence also the energy quanta ε , of

the symmetric and antisymmetric surface magnons actually coincide in the limit $N \rightarrow \infty$. Looking back at the figures 2.25 and 2.29, we see that this indeed seems to be the case, as the symmetric and antisymmetric surface branches are nearly indistinguishable already at 40 planes.

Taking now the limit $\kappa \rightarrow 0$, the maximum threshold energy ε_Λ becomes 6, so the condition equation (2.149) reduces further to

$$(\omega + 2 \cosh \varphi) \left((e^\vartheta + \eta) (e^\varphi - \eta) + \zeta^2 \right) + 6\zeta (e^\vartheta + e^\varphi) = 0.$$

We proceed to look at surface magnons at the surface threshold energy ε_S given in (2.117), corresponding to $\varphi = 0$ and $\vartheta = \operatorname{arcosh}(1 + \omega)$. This is where the surface magnon branch gets truncated by the bulk continuum as described in Wolfram and De Wames [1969]. Solving the resulting equation

$$(\omega + 2) \left((1 - \eta) \left(e^{\operatorname{arcosh}(1+\omega)} + \eta \right) + \zeta^2 \right) + 6\zeta \left(e^{\operatorname{arcosh}(1+\omega)} + 1 \right) = 0 \quad (2.150)$$

for ω , we find the values of ω at which the surface branch crosses into the bulk continuum. Note that for $\omega = 4$, the equation is always solved. This can be seen by noting that in this case $\eta = 4(\rho - 1) = \zeta + 1$. In other words, the surface branch always intersects the surface threshold at $\omega = 4$. Based on the value of ρ , the equation might have one additional solution, corresponding to a surface branch truncation.

An important threshold is the value of ρ for which $\omega = 0$ is a solution of (2.150). At this threshold, the entire surface branch disappears into the bulk continuum, and it can be shown that no surface branch exists for higher values of ρ . But $\omega = 0$ corresponds to $\eta = 0$, and substituting these values into the truncation condition (2.150), we end up with the simple quadratic equation

$$\zeta^2 + 6\zeta + 1 = 0,$$

which has the solution $\zeta = -3 \pm 2\sqrt{2}$ corresponding to

$$\rho = \frac{1 + \sqrt{2}}{2} \approx 1.207. \quad (2.151)$$

This is the exact threshold value found in Wolfram and De Wames [1969] section IV.

It can also be shown that equation (2.150) has a solution other than $\omega = 4$ only at values above the threshold $\rho \approx 1.107$. The calculation of this is a little more involved and will not be done here, but in figure 2.30, the left side of the truncation condition has been plotted for three different values of ρ to illustrate this. For values of ρ below 1.107, the surface branch is not truncated at all. In the figures 2.31– 2.33 the energy spectrum of a 100-plane antiferromagnetic layer is plotted for three different values of ρ to illustrate the truncation of the surface branch.

Surface Truncation Condition of the Semi-Infinite Antiferromagnetic Layer

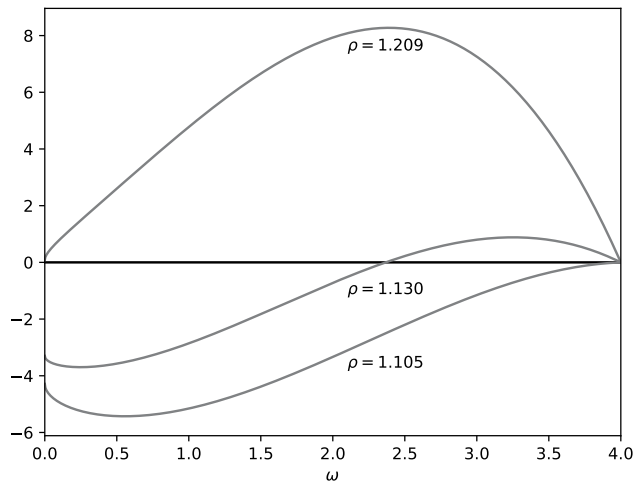


Figure 2.30: The left side of the surface truncation condition (2.150) plotted for three different values of ρ . Only between the threshold values $\rho \approx 1.107$ and $\rho \approx 1.207$ does the equation have another solution than $\omega = 4$.

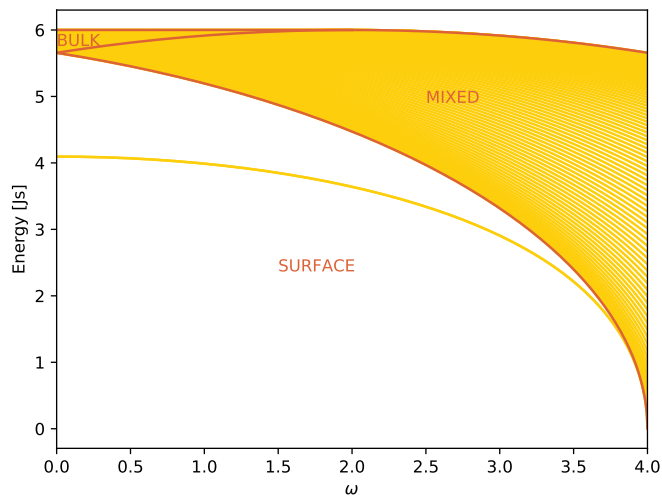
Energy Spectrum of the Antiferromagnetic Layer
($N = 100$, $\rho = 0.800$, $\kappa = 0.000$)

Figure 2.31: The energy spectrum of a 100-plane antiferromagnetic layer below the truncation threshold $\rho \approx 1.107$. The surface branch is full in this case, and only intersects the bulk continuum at $\omega = 4$ where both tend towards zero.

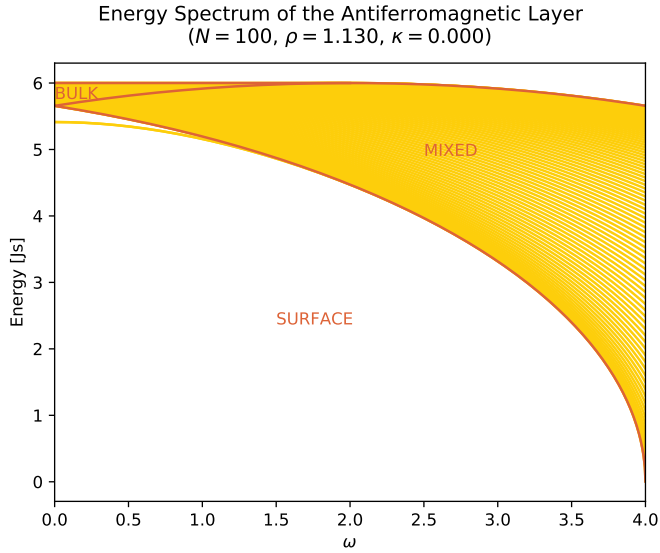


Figure 2.32: The energy spectrum of a 100-plane antiferromagnetic layer in the truncation range between $\rho \approx 1.107$ and $\rho \approx 1.207$. The surface branch is truncated at around $\omega \approx 2.0$, which matches the root of the corresponding truncation condition in figure 2.30.

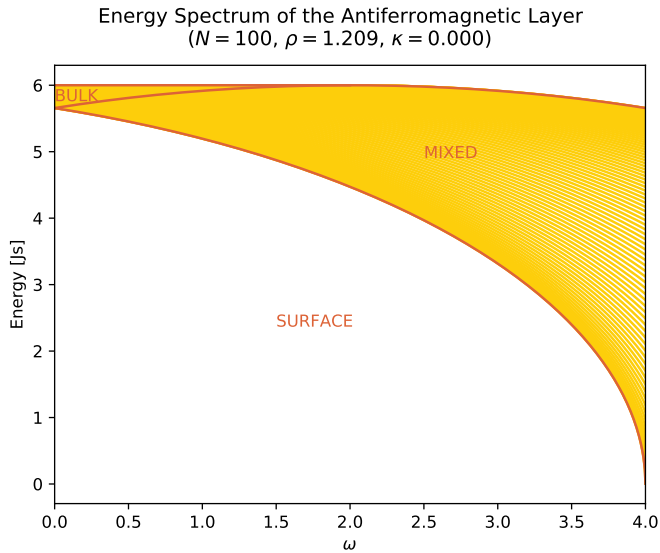


Figure 2.33: The energy spectrum of a 100-plane antiferromagnetic layer above the truncation threshold $\rho \approx 1.207$. The surface branch is completely absorbed by the bulk continuum in this case.

For the observant reader, one remark has to be made before we turn our attention away from Wolfram and De Wames [1969]. Our surface magnons correspond to the acoustical branches discussed in that article, but so far we have ignored the so-called "optical branches" that are also treated. They appear for values ρ above 1.25 and have energy quanta *above* the bulk continuum, and hence above ε_\wedge . Such magnons exist for our model as well, even in the finite case as shown in figure 2.34. Obviously then, our parity ansatz (2.89) does not cover all possible solutions of the problem. However when discussing spin transport across the junction, we are typically only interested in low energy magnons with energy quanta $\varepsilon \ll 1$. Therefore, we will continue to neglect the optical magnons. If we consider values of ρ below 1.25 only, these magnons will not appear anyway.

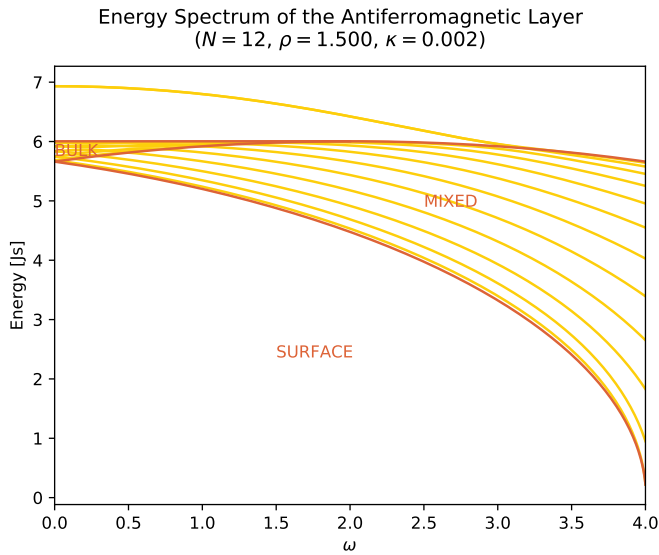


Figure 2.34: The energy spectrum of a 12-plane antiferromagnetic layer above the optical threshold $\rho = 1.25$ discussed in Wolfram and De Wames [1969]. The upper branch is an optical branch with energy quanta above ε_\wedge . Because only low-energy magnons contribute to spin transport, we neglect such magnons in this thesis.

2.15 Surface amplitudes

As seen at the end of section 2.12, for small values of ω surface magnons tend to have much higher amplitudes at the surfaces than other magnons. It will turn out later that it is these *surface amplitudes* that contribute to spin transport across the junction. While the explicit expression for the spin transport will have to wait until chapter 4, we here plot some surface amplitudes over different values of ρ to get a feeling of how the surface exchange parameter S affects them.

In figures 2.35 and 2.36, the surface amplitudes of the three lowest-energy magnons are plotted for the cases $\omega = 4$ and $\omega = 1.7$. We see that there is a clear qualitative difference between the case in which there are antisymmetric surface magnons and the case where there are none. Another feature of the plots is that in the special case $\omega = 4$, the first and second surface amplitudes seem to have maximal values for ρ values close to one, while in the case $\omega = 1.7$, the first and second surface amplitudes stay pretty constant. The amplitudes are always larger for $\omega = 4$ than for $\omega = 1.7$. This would indicate that the $\omega = 4$ magnons contribute more to spin transport than the magnons with a planar direction like the $\omega = 1.7$ magnons. However, for low ρ values, the $\omega = 4$ magnons are not as dominant as for ρ values close to one.

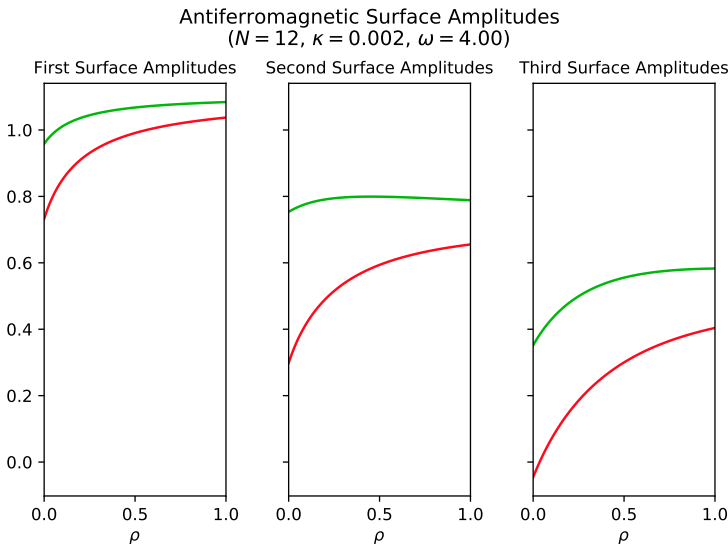


Figure 2.35: Surface amplitudes of the antiferromagnetic layer as a function of the ratio $\rho = \frac{S}{J}$ for the given parameters. Since there are no antisymmetric surface magnons in this case, the second surface amplitudes are smaller than the first surface amplitudes.

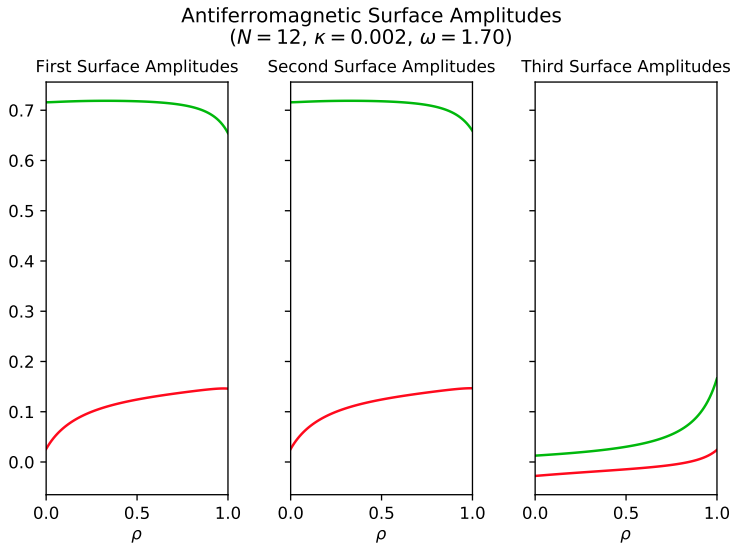


Figure 2.36: Surface amplitudes of the antiferromagnetic layer as a function of the ratio $\rho = \frac{S}{J}$ for the given parameters. In this case the antisymmetric surface magnons match the symmetric surface magnons in surface amplitude size, and even exceeds them when ρ gets close to one.

2.16 Summary

The key results for the finite-depth antiferromagnetic insulator layer with a distinct surface spin exchange are concisely summed up here. For more details, please consult the rest of the chapter.

The N -plane antiferromagnetic layer with Hamiltonian

$$\mathbf{H} = \frac{S}{\hbar^2} \sum_{\vec{q}, \vec{r} \in \mathbb{P}_1} \vec{s}_{\vec{q}} \cdot \vec{s}_{\vec{r}} + \sum_{p=2}^{N-1} \frac{J}{\hbar^2} \sum_{\vec{q}, \vec{r} \in \mathbb{P}_p} \vec{s}_{\vec{q}} \cdot \vec{s}_{\vec{r}} + \frac{S}{\hbar^2} \sum_{\vec{q}, \vec{r} \in \mathbb{P}_N} \vec{s}_{\vec{q}} \cdot \vec{s}_{\vec{r}} \\ + \sum_{p=1}^{N-1} \frac{J}{\hbar^2} \sum_{\vec{r} \in \mathbb{P}_p} \vec{s}_{\vec{r}} \cdot \vec{s}_{\vec{r} + \vec{l}_x} - \frac{K}{\hbar^2} \sum_{\vec{r} \in \mathbb{T}} s_{\vec{r}z}^2$$

has an energy spectrum given by

$$E = \varepsilon J S, \\ \varepsilon = \sqrt{(6 + 2\kappa)^2 - (\omega + 2 \cosh \varphi)^2},$$

where φ is given implicitly through the system of equations

$$\cosh \vartheta = \cosh \varphi + \omega$$

and

$$(\omega + 2 \cosh \varphi) \frac{\sinh \left(\frac{N+1}{2} \vartheta \right) \cosh \left(\frac{N+1}{2} \varphi \right)}{\cosh \left(\frac{N+1}{2} \vartheta \right) \sinh \left(\frac{N+1}{2} \varphi \right)} \\ + \left((6 + 2\kappa)(4\rho - 5) - \omega(\omega + 2 \cosh \varphi)(\rho - 1) \right) \frac{\sinh \left(\frac{N+1}{2} \vartheta \right) \cosh \left(\frac{N-1}{2} \varphi \right)}{\cosh \left(\frac{N+1}{2} \vartheta \right) \sinh \left(\frac{N-1}{2} \varphi \right)} \\ + \left((6 + 2\kappa)(4\rho - 5) + \omega(\omega + 2 \cosh \varphi)(\rho - 1) \right) \frac{\sinh \left(\frac{N-1}{2} \vartheta \right) \cosh \left(\frac{N+1}{2} \varphi \right)}{\cosh \left(\frac{N-1}{2} \vartheta \right) \sinh \left(\frac{N+1}{2} \varphi \right)} \\ + (\omega + 2 \cosh \varphi) \left((4\rho - 5)^2 - \omega^2(\rho - 1)^2 \right) \frac{\sinh \left(\frac{N-1}{2} \vartheta \right) \cosh \left(\frac{N-1}{2} \varphi \right)}{\cosh \left(\frac{N-1}{2} \vartheta \right) \sinh \left(\frac{N-1}{2} \varphi \right)} = 0.$$

Here,

$$\rho = \frac{S}{J}, \\ \kappa = \frac{K}{J}, \tag{2.152}$$

and

$$\omega = 2(\cos(lk_y) + \cos(lk_z))$$

for all planar wave vectors \vec{k} within the Brillouin zone depicted in figure 2.37. l is the lattice parameter of the simple cubic antiferromagnetic lattice.

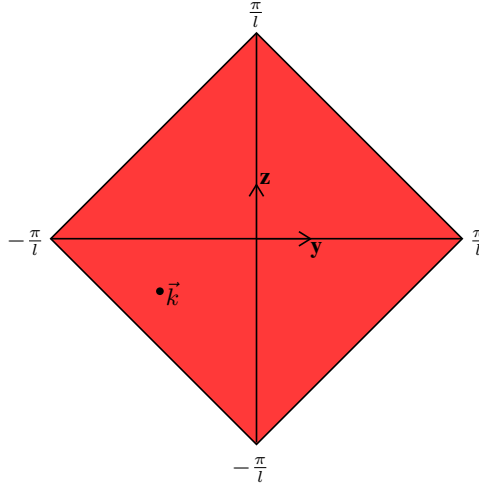


Figure 2.37: The Brillouin zone of the finite antiferromagnetic layer.

The dual magnonic eigenstates are generated by the bosonic operators

$$\alpha = \sum_{p=1}^N \left(u_p \mathbf{a}_{\vec{k},p} + v_p \mathbf{b}_{-\vec{k},p}^\dagger \right),$$

$$\beta = \sum_{p=1}^N \left(u_p \mathbf{b}_{-\vec{k},p} + v_p \mathbf{a}_{\vec{k},p}^\dagger \right),$$

where the amplitudes are given by

$$u_p = U(-1)^p \frac{\sinh \left(\vartheta \left(p - \frac{N+1}{2} \right) \right)}{\cosh \left(\vartheta \left(p - \frac{N+1}{2} \right) \right)} + OU \frac{\cosh \left(\varphi \left(p - \frac{N+1}{2} \right) \right)}{\sinh \left(\varphi \left(p - \frac{N+1}{2} \right) \right)},$$

$$v_p = -RU(-1)^p \frac{\sinh \left(\vartheta \left(p - \frac{N+1}{2} \right) \right)}{\cosh \left(\vartheta \left(p - \frac{N+1}{2} \right) \right)} + ROU \frac{\cosh \left(\varphi \left(p - \frac{N+1}{2} \right) \right)}{\sinh \left(\varphi \left(p - \frac{N+1}{2} \right) \right)},$$

with the ratios

$$R = \frac{\omega + 2 \cosh \varphi}{(6 + 2\kappa) + \varepsilon},$$

$$O = \frac{\frac{\sinh \left(\frac{N+1}{2} \vartheta \right)}{\cosh \left(\frac{N+1}{2} \vartheta \right)} + ((4\rho - 5)R + \omega(\rho - 1)) \frac{\sinh \left(\frac{N-1}{2} \vartheta \right)}{\cosh \left(\frac{N-1}{2} \vartheta \right)}}{\frac{\cosh \left(\frac{N+1}{2} \varphi \right)}{\sinh \left(\frac{N+1}{2} \varphi \right)} ((4\rho - 5)R - \omega(\rho - 1)) \frac{\cosh \left(\frac{N-1}{2} \varphi \right)}{\sinh \left(\frac{N-1}{2} \varphi \right)}},$$

and the normalisation

$$\frac{2}{(1 - R^2)U^2} = \frac{\sinh(N\vartheta)}{\sinh \vartheta} + O^2 \frac{\sinh(N\varphi)}{\sinh \varphi} \mp N(1 - O^2)$$

$$+ 4O \frac{1 + R^2}{1 - R^2} \frac{\frac{\sinh \left(\frac{N+1}{2} \vartheta \right)}{\cosh \left(\frac{N+1}{2} \vartheta \right)} \frac{\cosh \left(\frac{N-1}{2} \varphi \right)}{\sinh \left(\frac{N-1}{2} \varphi \right)} + \frac{\sinh \left(\frac{N-1}{2} \vartheta \right)}{\cosh \left(\frac{N-1}{2} \vartheta \right)} \frac{\cosh \left(\frac{N+1}{2} \varphi \right)}{\sinh \left(\frac{N+1}{2} \varphi \right)}}{\omega + 2 \cosh \varphi}.$$

Finally, the operators $\mathbf{a}_{\vec{k},p}$ and $\mathbf{b}_{-\vec{k},p}$ are planar sublattice spin flip waves given by

$$\mathbf{a}_{\vec{k},p} = \frac{1}{2G+2} \sum_{\vec{r}} e^{i\vec{k}\cdot\vec{r}} \mathbf{a}_{p,\vec{r}},$$

$$\mathbf{b}_{-\vec{k},p} = \frac{1}{2G+2} \sum_{\vec{r}} e^{-i\vec{k}\cdot\vec{r}} \mathbf{b}_{p,\vec{r}},$$

in which the operators $\mathbf{a}_{p,\vec{r}}$ and $\mathbf{b}_{p,\vec{r}}$ are Holstein-Primakoff operators associated with spin flips at each lattice site in the spin-up and spin-down sublattices, respectively.

Normally, there are N solutions to the frequencies ϑ and φ , and hence N magnon pairs, for each planar wave vector \vec{k} in the Brillouin zone. All these magnons have energy quanta that lie within a bulk/mixed continuum similar to the one shown in figure 2.38, except possibly one or two surface magnon branches which lie below.

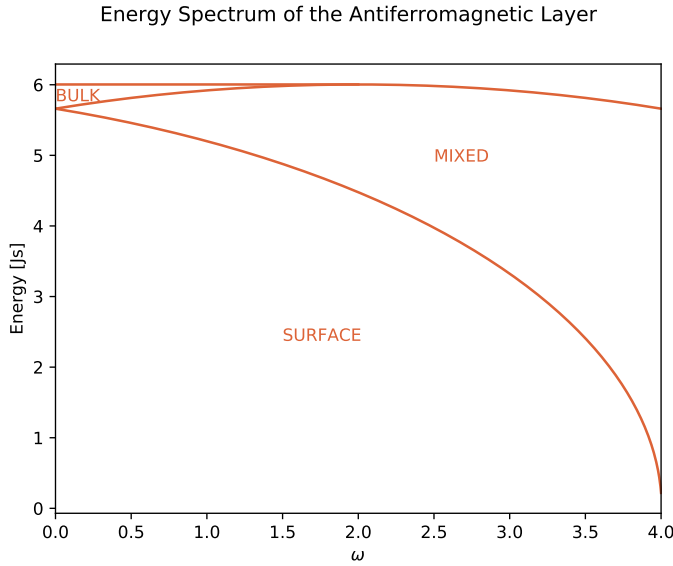


Figure 2.38: The energy spectrum of the finite antiferromagnetic layer for $\kappa = 0.002$.

Note however that our solutions do not comprise magnons with an energy quantum ε larger than $(6 + 2\kappa)$, as discussed in section 2.14.

Chapter 3

Metallic Layer

With the magnonic eigenstates calculated, we move on to calculating the energy eigenstates of the finite metallic conductor layer. We follow a similar approach as in chapter 2, and begin our treatment with a proper description of the metallic model.

3.1 Model

On the metallic side of the junction, our model is initially quite similar to the model on the antiferromagnetic side. Here too is a simple cubic lattice with the same lattice constant l . Furthermore, the lattice has N lattice planes in the x-direction which stretch out into infinity in the y- and z-directions, so we are again considering a layer of finite depth. While the lattice constant l is the same on both sides of the junction, we allow for a different number of x-planes on this side. Hence, the N in this chapter is not necessarily the same as the N in chapter 2.

For clarity, the notation throughout this chapter will mostly be similar to the notation in chapter 2 whenever the situation is analogous. Hence we label each lattice plane with \mathbb{P} and an index from 1 to N , so that the plane closest to the junction is called \mathbb{P}_1 and so on. (Note that the coordinate system has been rotated 180 degrees compared to the coordinate system used in chapter 2.) The whole metallic layer is labelled \mathbb{M} , so that $\mathbb{M} = \bigcup_n \mathbb{P}_n$. Finally the lattice sites are given by an equation identical to (2.1) for all integers p between 1 and N , and all integers m and n .

Because of the interaction with the antiferromagnetic layer, we will need two sublattices \mathbb{A} and \mathbb{B} in the metallic layer as well. Define \mathbb{A}_1 and \mathbb{B}_1 to be the sublattices of \mathbb{P}_1 next to antiferromagnetic up and down spins, respectively. Then the two sublattices can be extended to the rest of the metallic layer so that each site in sublattice \mathbb{A} is the nearest neighbour of four sites in sublattice \mathbb{B} and vice versa (in analogy to the sublattices in chapter 2). Of course, the Néel order is not present in the metallic layer in the same sense as in the antiferromagnetic layer, but we will see that in some sense, the order spreads into the metallic layer as well.

The metallic lattice is not a spin lattice like in the antiferromagnetic case. Instead, it is a hopping lattice in which electrons can hop between orbitals localised on each lattice site. We use a modified tight-binding model to describe the electronic interactions. In addition to the usual hopping term, our tight-binding model has a spin interaction term that couples electrons in the surface plane \mathbb{P}_1 to the antiferromagnetic spins on the other side of the junction. More specifically, the Hamiltonian operator is

$$\mathbf{H} = \frac{Is}{2} \sum_{\vec{a} \in \mathbb{A}_1} (\mathbf{c}_{\uparrow\vec{a}}^\dagger \mathbf{c}_{\uparrow\vec{a}} - \mathbf{c}_{\downarrow\vec{a}}^\dagger \mathbf{c}_{\downarrow\vec{a}}) - \frac{Is}{2} \sum_{\vec{b} \in \mathbb{B}_1} (\mathbf{c}_{\uparrow\vec{b}}^\dagger \mathbf{c}_{\uparrow\vec{b}} - \mathbf{c}_{\downarrow\vec{b}}^\dagger \mathbf{c}_{\downarrow\vec{b}}) - H \sum_{m, \vec{q}; \vec{r} \in \mathbb{M}} (\mathbf{c}_{m\vec{q}}^\dagger \mathbf{c}_{m\vec{r}} + \mathbf{c}_{m\vec{r}}^\dagger \mathbf{c}_{m\vec{q}}), \quad (3.1)$$

where I is the spin exchange parameter across the interface, s is the spin quantum number of the antiferromagnetic spins, H is the metallic hopping parameter and $\mathbf{c}_{m\vec{r}}^\dagger$ are fermionic operators creating an electron of spin m (\uparrow or \downarrow) on the lattice site \vec{r} . An overview of the metallic layer model is given in figure 3.1.

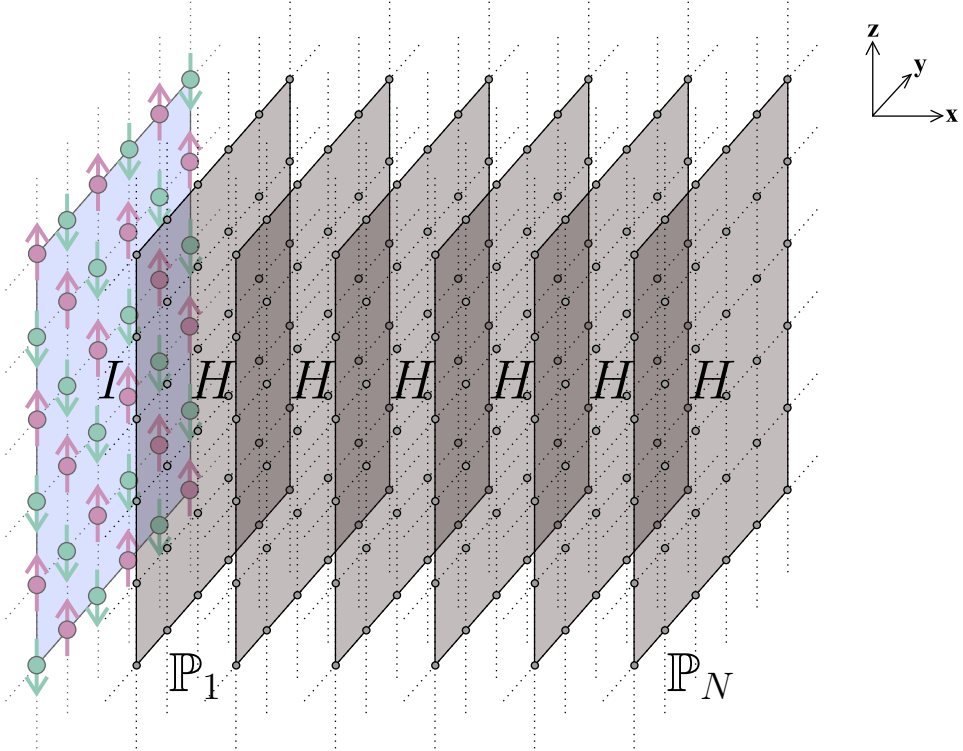


Figure 3.1: Our model for the metallic side of the junction. (Here for 6 planes.) The hopping parameter H is the same throughout the metal. The surface plane \mathbb{P}_1 is coupled with spin exchange parameter I to the antiferromagnetic layer, which is taken to be in the Néel state.

From our thorough discussion in chapter 2, we know all too well that the antiferromagnetic layer can be in other states than the Néel state. The Néel state corresponds to magnonic vacuum, but any number of magnons could be added to the system. However, the Néel state is the state of the antiferromagnetic layer *to the zeroth order* in the magnon operators α_\bullet and β_\bullet . Correspondingly, the interaction term in (3.1) is the spin interaction across the junction to the zeroth order in the same magnon operators. A small number of magnons was the assumption that let us introduce the approximate Holstein-Primakoff transformation (2.12) back in chapter 2 in the first place, so this simplification makes sense. We will consider the spin interaction across the junction to the *first* order in magnon operators as a small perturbation in chapter 4. This perturbation will then give rise to spin transport across the junction.

As in the case of the antiferromagnetic layer, our goal is to transform the Hamiltonian (3.1) into the simple diagonal form

$$\mathbf{H} = \sum_n \epsilon_n \mathbf{c}_n^\dagger \mathbf{c}_n, \quad (3.2)$$

this time for *fermionic* operators \mathbf{c}_\bullet that satisfy the simple anticommutation relation

$$\mathbf{c}_i \mathbf{c}_j^\dagger = -\mathbf{c}_j^\dagger \mathbf{c}_i + \delta_{ij} \quad (3.3)$$

for all integers i and j . Then the energy quanta of the system can be extracted as ϵ_\bullet . We will use a somewhat similar approach to chapter 2, starting with a sublattice Fourier transformation in the next section.

3.2 Fourier transformation

To do a Fourier transformation on the metal Hamiltonian (3.1), we must introduce various planar lattices analogous to the ones described in detail back in chapter 2 section 2.4. Introduce first the planar sublattice vectors \vec{l}_1 and \vec{l}_2 given in (2.19) that span the sublattices \mathbb{A}_p and \mathbb{B}_p of each plane \mathbb{P}_p , and then their reciprocal lattice vectors \vec{g}_1 and \vec{g}_2 given in (2.22). If we assume (as on the antiferromagnetic side) that these planar sublattices have G sites in each negative direction and $(G + 1)$ sites in each positive direction, a planar wave lattice identical to the one given in (2.24) can be defined for the metallic layer. Finally, the useful sums (2.26) and (2.27) come with this lattice.

Two types of planar electronic operator waves can now be defined:

$$\begin{aligned} \mathbf{a}_{m\vec{k},p} &= \frac{1}{2G+2} \sum_{\vec{a} \in \mathbb{A}_p} e^{i\vec{k} \cdot \vec{a}} \mathbf{c}_{m\vec{a}}, \\ \mathbf{b}_{m\vec{k},p} &= \frac{1}{2G+2} \sum_{\vec{b} \in \mathbb{B}_p} e^{i\vec{k} \cdot \vec{b}} \mathbf{c}_{m\vec{b}}. \end{aligned} \quad (3.4)$$

Each operator wave has a defined spin m (\uparrow or \downarrow), a defined planar wave vector \vec{k} and a defined plane index p . Using the sum identity (2.27), these operators can be shown to be

fermionic with the normal anticommutation relation and the back transformation

$$\begin{aligned} \mathbf{c}_{m\vec{a}} &= \frac{1}{2G+2} \sum_{\vec{k}} e^{-i\vec{k}\cdot\vec{a}} \mathbf{a}_{m\vec{k},p} \quad \text{for } \vec{a} \in \mathbb{A}_p, \\ \mathbf{c}_{m\vec{b}} &= \frac{1}{2G+2} \sum_{\vec{k}} e^{-i\vec{k}\cdot\vec{b}} \mathbf{b}_{m\vec{k},p} \quad \text{for } \vec{b} \in \mathbb{B}_p. \end{aligned} \quad (3.5)$$

Splitting up the hopping term of the Hamiltonian (3.1) in intraplanar and interplanar terms,

$$\begin{aligned} \sum_{m,\vec{q};\vec{r} \in \mathbb{M}} (\mathbf{c}_{m\vec{q}}^\dagger \mathbf{c}_{m\vec{r}} + \mathbf{c}_{m\vec{r}}^\dagger \mathbf{c}_{m\vec{q}}) &= \sum_{p=1}^N \left(\sum_{m,\vec{a} \in \mathbb{A}_p} \sum_{\vec{\delta}} (\mathbf{c}_{m\vec{a}}^\dagger \mathbf{c}_{m\vec{a}+\vec{\delta}} + \mathbf{c}_{m\vec{a}+\vec{\delta}}^\dagger \mathbf{c}_{m\vec{a}}) \right) \\ + \sum_{p=1}^{N-1} \left(\sum_{m,\vec{a} \in \mathbb{A}_p} (\mathbf{c}_{m\vec{a}}^\dagger \mathbf{c}_{m\vec{a}+\vec{l}_x} + \mathbf{c}_{m\vec{a}+\vec{l}_x}^\dagger \mathbf{c}_{m\vec{a}}) + \sum_{m,\vec{b} \in \mathbb{B}_p} (\mathbf{c}_{m\vec{b}}^\dagger \mathbf{c}_{m\vec{b}+\vec{l}_x} + \mathbf{c}_{m\vec{b}+\vec{l}_x}^\dagger \mathbf{c}_{m\vec{b}}) \right), \end{aligned} \quad (3.6)$$

we can then substitute in the back transformations (3.5) to get

$$\begin{aligned} \sum_{m,\vec{q};\vec{r} \in \mathbb{M}} (\mathbf{c}_{m\vec{q}}^\dagger \mathbf{c}_{m\vec{r}} + \mathbf{c}_{m\vec{r}}^\dagger \mathbf{c}_{m\vec{q}}) &= \sum_{p=1}^N \sum_{m\vec{k}} \omega_{\vec{k}} \left(\mathbf{a}_{m\vec{k},p}^\dagger \mathbf{b}_{m\vec{k},p} + \mathbf{b}_{m\vec{k},p}^\dagger \mathbf{a}_{m\vec{k},p} \right) \\ + \sum_{p=1}^{N-1} \sum_{m\vec{k}} \left(\mathbf{a}_{m\vec{k},p}^\dagger \mathbf{b}_{m\vec{k},p+1} + \mathbf{b}_{m\vec{k},p+1}^\dagger \mathbf{a}_{m\vec{k},p} + \mathbf{b}_{m\vec{k},p}^\dagger \mathbf{a}_{m\vec{k},p+1} + \mathbf{a}_{m\vec{k},p+1}^\dagger \mathbf{b}_{m\vec{k},p} \right), \end{aligned} \quad (3.7)$$

where the wave parameter $\omega_{\vec{k}}$ was introduced just as in chapter 2 as (2.30). The diagonal terms stay diagonal,

$$\sum_{\vec{a} \in \mathbb{A}_1} \mathbf{c}_{m\vec{a}}^\dagger \mathbf{c}_{m\vec{a}} = \sum_{\vec{k}} \mathbf{a}_{m\vec{k},1}^\dagger \mathbf{a}_{m\vec{k},1}, \quad (3.8)$$

$$\sum_{\vec{b} \in \mathbb{B}_1} \mathbf{c}_{m\vec{b}}^\dagger \mathbf{c}_{m\vec{b}} = \sum_{\vec{k}} \mathbf{b}_{m\vec{k},1}^\dagger \mathbf{b}_{m\vec{k},1}, \quad (3.9)$$

and so the total Hamiltonian (3.1) can be split up as

$$\begin{aligned} \mathbf{H} &= \frac{Is}{2} \sum_{\vec{k}} \left(\mathbf{a}_{\uparrow\vec{k},1}^\dagger \mathbf{a}_{\uparrow\vec{k},1} - \mathbf{a}_{\downarrow\vec{k},1}^\dagger \mathbf{a}_{\downarrow\vec{k},1} \right) - \frac{Is}{2} \sum_{\vec{k}} \left(\mathbf{b}_{\uparrow\vec{k},1}^\dagger \mathbf{b}_{\uparrow\vec{k},1} - \mathbf{b}_{\downarrow\vec{k},1}^\dagger \mathbf{b}_{\downarrow\vec{k},1} \right) \\ &\quad - H \sum_{m\vec{k}} \left(\sum_{p=1}^N \omega_{\vec{k}} \left(\mathbf{a}_{m\vec{k},p}^\dagger \mathbf{b}_{m\vec{k},p} + \mathbf{b}_{m\vec{k},p}^\dagger \mathbf{a}_{m\vec{k},p} \right) \right. \\ &\quad \left. + \sum_{p=1}^{N-1} \left(\mathbf{a}_{m\vec{k},p}^\dagger \mathbf{b}_{m\vec{k},p+1} + \mathbf{b}_{m\vec{k},p+1}^\dagger \mathbf{a}_{m\vec{k},p} + \mathbf{b}_{m\vec{k},p}^\dagger \mathbf{a}_{m\vec{k},p+1} + \mathbf{a}_{m\vec{k},p+1}^\dagger \mathbf{b}_{m\vec{k},p} \right) \right). \end{aligned} \quad (3.10)$$

Through the Fourier transformation, the metallic Hamiltonian has been separated over different cases of spin m and planar wave vector \vec{k} . This is made clear by introducing partial Hamiltonians $\mathbf{h}_{m\vec{k}}$ as

$$\mathbf{h}_{m\vec{k}} = \begin{bmatrix} \bar{\mathbf{a}}_{m\vec{k}}^\dagger & \bar{\mathbf{b}}_{m\vec{k}}^\dagger \end{bmatrix} \begin{bmatrix} \pm \boxed{D} & \boxed{C} \\ \boxed{C} & \mp \boxed{D} \end{bmatrix} \begin{bmatrix} \bar{\mathbf{a}}_{m\vec{k}} \\ \bar{\mathbf{b}}_{m\vec{k}} \end{bmatrix} \quad (3.11)$$

and recasting the Hamiltonian (3.10) to

$$\mathbf{H} = H \sum_{m\vec{k}} \mathbf{h}_{m\vec{k}}. \quad (3.12)$$

In the expression for $\mathbf{h}_{m\vec{k}}$ above, the split signs refer to the two possible spin values of m — the upper sign is for \uparrow and the lower sign is for \downarrow . The vectors $\bar{\mathbf{a}}_{m\vec{k}}$ and $\bar{\mathbf{b}}_{m\vec{k}}$ run through all operators $\mathbf{a}_{m\vec{k},p}$ and $\mathbf{b}_{m\vec{k},p}$ respectively, for all indices p from 1 to N . Thus they are column vectors of length N , and their adjoints $\bar{\mathbf{a}}_{m\vec{k}}^\dagger$ and $\bar{\mathbf{b}}_{m\vec{k}}^\dagger$ are row vectors of the same length running through all the adjoint operators.

The $N \times N$ matrices \boxed{D} and \boxed{C} are named in analogy to chapter 2, but in this case, \boxed{D} is not centrosymmetric,

$$\boxed{D} = \begin{bmatrix} \lambda & & & \\ & 0 & & \\ & & \ddots & \\ & & & 0 \end{bmatrix}, \quad (3.13)$$

with its lone element λ defined as the ratio

$$\lambda = \frac{Is}{2H}, \quad (3.14)$$

and \boxed{C} is tridiagonal,

$$\boxed{C} = \begin{bmatrix} -\omega_{\vec{k}} & -1 & & & \\ -1 & -\omega_{\vec{k}} & -1 & & \\ & -1 & \omega_{\vec{k}} & \ddots & \\ & & \ddots & \ddots & -1 \\ & & & -1 & -\omega_{\vec{k}} \end{bmatrix}. \quad (3.15)$$

Our task is then to diagonalise each partial Hamiltonian $\mathbf{h}_{m\vec{k}}$. From here on we omit the spin value m and the planar wave vector \vec{k} and concentrate on this task for a given case of parameters.

3.3 Unitary transformation

To do the next and final transformation, we look at symmetries of the Hamiltonian (3.10), just as we did in chapter 2. In this case they include a symmetry with respect to a "sub-lattice swap/spin flip" $\mathbf{a} \leftrightarrow \mathbf{b} / \uparrow \leftrightarrow \downarrow$ (in which the two sublattices and the two spin values

are interchanged simultaneously), and an antisymmetry with respect to a "sublattice anti-swap" $\mathbf{a} \rightarrow -\mathbf{b}/\mathbf{b} \rightarrow \mathbf{a}$ (in which the \mathbf{b} operators are swapped with the \mathbf{a} operators while the \mathbf{a} operators are swapped with the negative of the \mathbf{b} operators). Both symmetries are apparent in the matrix expression (3.11) for the partial Hamiltonian.

The first symmetry lets us concentrate on one particular spin value, say spin up, and then construct the spin down eigenstates by the sublattice swap/spin flip. Hence we will focus on the spin up case from here on.

The second antisymmetry provides a clue for the form of the transformation matrix in the following. Omit the index $\uparrow \vec{k}$ and introduce the new electron operators $\bar{\gamma}$ by the transformation

$$\bar{\gamma} = \boxed{B} \begin{bmatrix} \bar{\mathbf{a}} \\ \bar{\mathbf{b}} \end{bmatrix}. \quad (3.16)$$

In other words, there are $2N$ operators γ_{\bullet} , all linear combinations of the old wave operators \mathbf{a}_{\bullet} and \mathbf{b}_{\bullet} , with coefficients given in the rows of the transformation matrix \boxed{B} . Using the antisymmetry explained above, the form of \boxed{B} can be chosen to be

$$\boxed{B} = \begin{bmatrix} \boxed{o} & \boxed{w} \\ \boxed{w} & -\boxed{o} \end{bmatrix}, \quad (3.17)$$

because the lower half of \boxed{B} then corresponds to the "antiswapped" eigenstates. Since the Hamiltonian is antisymmetric with respect to this swap, the energy quanta of these lower states will have the negative value of their upper counterparts. Ordering then all positive energy eigenstates in the upper half, we can split the vector $\bar{\gamma}$ as follows:

$$\bar{\gamma} = \begin{bmatrix} \bar{\gamma}^+ \\ \bar{\gamma}^- \end{bmatrix} \quad (3.18)$$

Enforcing canonicity of the transformation so that all the new operators γ_{\bullet} are also fermionic, we end up with the following constraints on the submatrices \boxed{o} and \boxed{w} :

$$\begin{aligned} \boxed{o} \boxed{o}^\dagger + \boxed{w} \boxed{w}^\dagger &= \boxed{I}, \\ \boxed{o} \boxed{w}^\dagger - \boxed{w} \boxed{o}^\dagger &= \boxed{0}. \end{aligned} \quad (3.19)$$

From these we can construct the inverse of \boxed{B} by noting that

$$\begin{bmatrix} \boxed{o} & \boxed{w} \\ \boxed{w} & -\boxed{o} \end{bmatrix} \begin{bmatrix} \boxed{o}^\dagger & \boxed{w}^\dagger \\ \boxed{w}^\dagger & -\boxed{o}^\dagger \end{bmatrix} = \begin{bmatrix} \boxed{I} & \\ & \boxed{I} \end{bmatrix}, \quad (3.20)$$

which means that

$$\boxed{B}^{-1} = \begin{bmatrix} \boxed{o}^\dagger & \boxed{w}^\dagger \\ \boxed{w}^\dagger & -\boxed{o}^\dagger \end{bmatrix} = \boxed{B}^\dagger, \quad (3.21)$$

and so the canonicity condition for \boxed{B} in this case is that it be unitary. The back transformation is then simply

$$\begin{bmatrix} \bar{\mathbf{a}} \\ \bar{\mathbf{b}} \end{bmatrix} = \boxed{B}^\dagger \bar{\gamma}. \quad (3.22)$$

Since we concentrate on the case of spin up, we can define the coefficient matrix \boxed{A} as

$$\boxed{A} = \begin{bmatrix} \boxed{D} & \boxed{C} \\ \boxed{C} & -\boxed{D} \end{bmatrix}. \quad (3.23)$$

Diagonalisation of the spin up partial Hamiltonian in (3.11) through the transformation (3.16) then means that

$$\boxed{B} \boxed{A} \boxed{B}^\dagger = \boxed{E}, \quad (3.24)$$

where the diagonal energy matrix \boxed{E} has the form

$$\boxed{E} = \begin{bmatrix} \boxed{\epsilon} & \\ & -\boxed{\epsilon} \end{bmatrix} \quad (3.25)$$

for some diagonal submatrix $\boxed{\epsilon}$ with positive entries. (As explained above, the lower half of the energy quanta then have negative values due to the antisymmetry.) By the unitarity of \boxed{B} , the diagonalisation turns into an eigenequation

$$\boxed{A} \boxed{B}^\dagger = \boxed{B}^\dagger \boxed{E}, \quad (3.26)$$

which shows that the columns of \boxed{B}^\dagger must be the eigenvectors of the coefficient matrix \boxed{A} . Because \boxed{A} is real and symmetric, its eigenvalues (that is, the energy quanta) are real, as they should be. Furthermore, since both \boxed{A} and its eigenvalues are real, the eigenvectors can also be chosen to be real, so we do not need to consider complex candidates for the submatrices \boxed{o} and \boxed{w} .

3.4 Numerical diagonalisation

The eigenequation (3.26) can be solved numerically to find the eigenstates γ_\bullet and energy quanta ϵ_\bullet of the metallic layer. The eigenstates are fermionic, so we will call them simply *electrons* from here on.

Since the coefficient matrix \boxed{A} is real and symmetric, eigenvectors corresponding to different eigenvalues are always orthogonal. Thus after finding numerically the eigenvectors of \boxed{A} , the matrix of eigenvectors can be made unitary by normalisation of each eigenvector pair \bar{b}_n and \bar{b}_{N+n} for all indices n between 1 and N . This is achieved easily by calculating the quantity

$$P_n = \sum_p (o_{np}^2 + w_{np}^2), \quad (3.27)$$

which is always positive, and rescaling the two eigenvectors by $\sqrt{\frac{1}{P_n}}$.

The solver script introduced in chapter 2 was extended with a new class `MetalSolver`, based on the `MagnetSolver` class but adjusted to find the eigenstates of the metallic layer instead of the antiferromagnetic layer. In figure 3.2, the electrons of a 6-plane metallic layer are plotted for the specified values of λ and ω . The plots were found by numerical diagonalisation in the class method `calcNumElectrons`.

Electrons of the Metallic Layer
 $(N = 6, \lambda = 0.80, \omega = 4.00)$

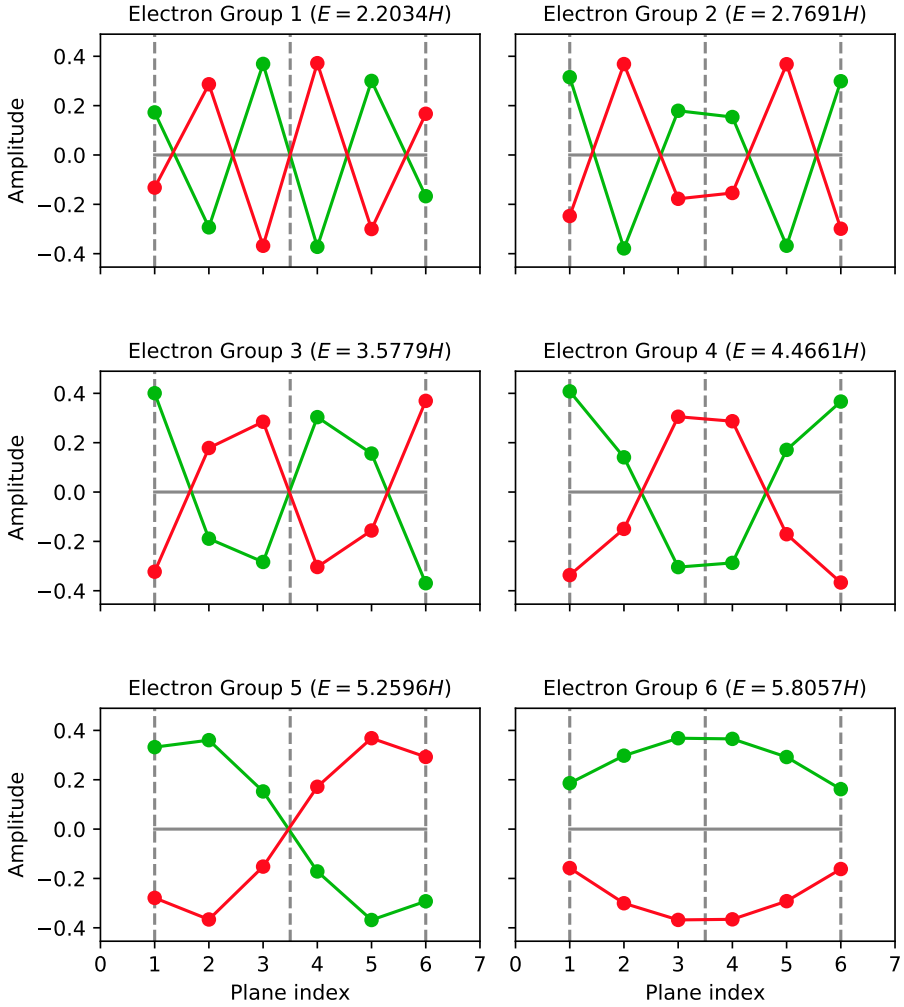


Figure 3.2: The electrons of a 6-plane metallic layer for the given parameters. The amplitudes o_p and w_p are plotted in green and red, respectively. Note that each plot represents two electrons — one with spin up and one with spin down.

We see that there is no parity over the middle plane in the metallic case. This makes sense because our metallic model is asymmetric. Each plot in the figure represents two electrons with opposite spin values. However, further two electrons with negative energy quanta can be read out of the same plots by antiswapping the amplitudes o_p and w_p (swapping the amplitudes and negating one of them). In this sense, each plot actually represents *four* electrons.

3.5 Analytical equations

Having plotted numerical results in the previous section, we write out the element equations of the matrix eigenequation (3.26) to an analytical end. Writing it out blockwise, we get

$$\boxed{D} \boxed{o}^\dagger + \boxed{C} \boxed{w}^\dagger = \boxed{o}^\dagger \boxed{\epsilon}, \quad (3.28)$$

$$\boxed{C} \boxed{o}^\dagger - \boxed{D} \boxed{w}^\dagger = \boxed{w}^\dagger \boxed{\epsilon}, \quad (3.29)$$

and looking at a bulk element of these matrix equations we end up with the *bulk equations*

$$\begin{aligned} \epsilon o_p &= -w_{p-1} - \omega w_p - w_{p+1}, \\ \epsilon w_p &= -o_{p-1} - \omega o_p - o_{p+1} \end{aligned} \quad (3.30)$$

for all plane indices p from 2 to $N - 1$, while looking at the upper and lower elements we get the four *surface equations*

$$\begin{aligned} (\epsilon - \lambda)o_1 &= -\omega w_1 - w_2, \\ (\epsilon + \lambda)w_1 &= -\omega o_1 - o_2, \\ \epsilon o_N &= -\omega w_N - w_{N-1}, \\ \epsilon w_N &= -\omega o_N - o_{N-1}. \end{aligned} \quad (3.31)$$

In these equations, the index n labelling the different eigenstates is omitted, but keep in mind that there are N such eigenstates, and then N more by doing the sublattice antiswap, and finally $2N$ more by doing the sublattice swap/spin flip on these. Thus in total, there are $4N$ different eigenstates for each value of the wave parameter ω .

If we can find an analytical solution for o_p and w_p which is valid for *all* integers p (not only 1 to N) and solves the bulk equations (3.30) for all p , we can use the bulk equations for $p = 1$ and $p = N$ to simplify the surface equations (3.31) to

$$\begin{aligned} o_0 &= \lambda w_1, \\ w_0 &= -\lambda o_1, \\ o_{N+1} &= 0, \\ w_{N+1} &= 0. \end{aligned} \quad (3.32)$$

The two last of these extended surface equations tell us that such an analytical solution should have nodes at o_{N+1} and w_{N+1} .

To find the analytical solutions, we will not use an ansatz like in chapter 2, but instead decouple the bulk equations and solve the resulting recurrence relations. The bulk equations (3.30) can be decoupled by introducing the two combinations

$$x_p = o_p + w_p, \quad (3.33)$$

$$y_p = o_p - w_p, \quad (3.34)$$

and respectively add and subtract the two bulk equations to get

$$\epsilon x_p = -x_{p-1} - \omega x_p - x_{p+1}, \quad (3.35)$$

$$\epsilon y_p = y_{p-1} + \omega y_p + y_{p+1}. \quad (3.36)$$

These equations can then be recast to the second order recurrence relations

$$x_{p+1} = -(\omega + \epsilon)x_p - x_{p-1}, \quad (3.37)$$

$$y_{p+1} = -(\omega - \epsilon)y_p - y_{p-1}. \quad (3.38)$$

Similarly the surface equations (3.32) can be added and subtracted to get

$$x_0 = -\lambda y_1,$$

$$y_0 = \lambda x_1,$$

$$x_{N+1} = 0,$$

$$y_{N+1} = 0. \quad (3.39)$$

To find solutions for x_p and y_p , we have to solve the characteristic polynomials of the recurrence relations (3.37) and (3.38). These have the respective roots

$$\chi_{\pm} = -\frac{\omega + \epsilon}{2} \pm \sqrt{\left(\frac{\omega + \epsilon}{2}\right)^2 - 1}, \quad (3.40)$$

$$v_{\pm} = -\frac{\omega - \epsilon}{2} \pm \sqrt{\left(\frac{\omega - \epsilon}{2}\right)^2 - 1}. \quad (3.41)$$

Note already that neither χ_{\pm} nor v_{\pm} can be zero, but

$$\chi_+ \chi_- = 1, \quad (3.42)$$

$$v_+ v_- = 1, \quad (3.43)$$

which means that χ_- is the inverse of χ_+ and v_- is the inverse of v_+ .

Let us define some ranges of energy based on the roots above. We will say that

- the energy is *within the lower continuum* if $\left(\frac{\omega + \epsilon}{2}\right)^2 \leq 1$,
- the energy is *within the upper continuum* if $\left(\frac{\omega - \epsilon}{2}\right)^2 \leq 1$.

The lower continuum then corresponds to energy quanta ϵ between $(-\omega - 2)$ and $(-\omega + 2)$, while the upper continuum corresponds to energy quanta ϵ between $(\omega - 2)$ and $(\omega + 2)$.

Note that when $\omega = 2$ the two continua touch, and when $\omega < 2$ they overlap. When $\omega > 2$ however, there is a gap between the two continua. It may seem arbitrary to call the two ranges "continua" now, but this will make sense by the end of the chapter. With the given terminology in mind, it is clear from (3.40) that χ_{\pm} is complex for energy quanta within the lower continuum, and real for energy quanta outside the lower continuum. In the special case of an electron on the edge of the lower continuum ($(\frac{\omega+\epsilon}{2})^2 = 1$), the two roots χ_{\pm} coincide and become the degenerate root

$$\chi = -\frac{\omega + \epsilon}{2}. \quad (3.44)$$

Similarly, it is clear from (3.41) that v_{\pm} is complex for energy quanta within the upper continuum and real for energy quanta outside the upper continuum. In the special case of an electron on the edge of the upper continuum ($(\frac{\omega-\epsilon}{2})^2 = 1$), the two roots v_{\pm} coincide and become the degenerate root

$$v = -\frac{\omega - \epsilon}{2}. \quad (3.45)$$

Solutions to the recurrence relations (3.37) and (3.38) normally take the general form

$$x_p = X\chi_+^p + U\chi_-^p, \quad (3.46)$$

$$y_p = Yv_+^p + Vv_-^p, \quad (3.47)$$

for some amplitudes X, U, Y and V . But in the special case of an electron on the edge of the lower continuum, x_p instead takes the form

$$x_p = (Xp + U)\chi^p, \quad (3.48)$$

and in the case of an electron on the edge of the upper continuum, y_p takes the form

$$y_p = (Yp + V)v^p. \quad (3.49)$$

(These are all well known results for second order recurrence relations which are also fairly easy to prove.) The four unknown amplitudes X, U, Y and V and the energy quantum ϵ can be determined from the four surface equations (3.39) and the normalisation

$$\sum_{p=1}^N (o_p^2 + w_p^2) = 1 \quad (3.50)$$

which comes from the canonicity condition (3.19). In terms of x_p and y_p , this normalisation is

$$\sum_{p=1}^N \frac{x_p^2 + y_p^2}{2} = 1. \quad (3.51)$$

The two last of the surface equations (3.39) can be used to eliminate the amplitudes U and V already. Substituting the general solutions (3.46) and (3.47) into them provides

$$X\chi_+^{N+1} + U\chi_-^{N+1} = 0,$$

$$Yv_+^{N+1} + Vv_-^{N+1} = 0$$

which can be rewritten using $\chi_+\chi_- = 1$ and $v_+v_- = 1$ to

$$U = -\chi_+^{2(N+1)}X, \quad (3.52)$$

$$V = -v_+^{2(N+1)}Y, \quad (3.53)$$

and entered back into the general solutions to get

$$x_p = X\chi_+^{N+1} \left(\chi_+^{p-(N+1)} - \chi_-^{p-(N+1)} \right), \quad (3.54)$$

$$y_p = Yv_+^{N+1} \left(v_+^{p-(N+1)} - v_-^{p-(N+1)} \right). \quad (3.55)$$

In the case of electrons on the edge of the lower continuum, the general solution (3.48) for x_p has to be used instead, whose substitution into the third surface equation in (3.39) yields

$$(N+1)X + U = 0,$$

which can be rewritten to

$$U = -(N+1)X \quad (3.56)$$

and entered back into the general solution to get

$$x_p = X(p - (N+1))\chi^p. \quad (3.57)$$

Similarly, in the case of electrons on the edge of the upper continuum, the general solution (3.49) for y_p has to be used instead, and this in combination with the fourth surface equation in (3.39) yields

$$V = -(N+1)Y \quad (3.58)$$

and thus

$$y_p = Y(p - (N+1))v^p. \quad (3.59)$$

Recall from section 3.3 that for any allowed energy quantum ϵ , the energy quantum of opposite sign is also allowed, and the corresponding electron can be constructed simply by antismapping the amplitudes o_p and w_p . This allows us to concentrate only on the allowed *positive* energy quanta, as the allowed negative energy quanta can then be found by the antiswap.

First we restrict our focus to positive energy quanta in the upper continuum and above. For $\omega \leq 2$, all these satisfy $-\frac{\omega-\epsilon}{2} \geq -\frac{\omega}{2}$, which allows us to write

$$-\frac{\omega-\epsilon}{2} = \cosh \psi \quad (3.60)$$

for some frequency ψ . If ψ is taken to be either purely imaginary between 0 and $i \arccos(-\frac{\omega}{2})$ or real above 0, then every value can be taken with a suitable choice of ψ . For $\omega > 2$, the quanta instead satisfy $-\frac{\omega-\epsilon}{2} \geq -1$, so in this case ψ should instead take imaginary values between 0 and $i\pi$ or real values above 0. The imaginary values $\psi = 0$ and $\psi = i\pi$ correspond to electrons at the top and bottom of the upper continuum, respectively. Other imaginary values of ψ correspond to electrons within the upper continuum, while real values of ψ correspond to electrons above the upper continuum.

Note now that

$$-\frac{\omega + \epsilon}{2} = \frac{\omega - \epsilon}{2} - \omega = -\cosh \psi - \omega, \quad (3.61)$$

which means that $-\frac{\omega + \epsilon}{2}$ takes on values from $(1 - \omega)$ and down. If we write

$$-\frac{\omega + \epsilon}{2} = -\cosh \xi, \quad (3.62)$$

for some purely imaginary frequency ξ between 0 and $\iota\pi$ or some real frequency ξ above 0, every value from 1 and down can be taken with a suitable choice of ξ . Like in the case of ψ , the imaginary values $\xi = 0$ and $\xi = \iota\pi$ correspond to electrons at the top and bottom of the *lower* continuum, respectively, while other imaginary values of ξ correspond to electrons within the lower continuum and real values of ξ correspond to electrons below the lower continuum. However, the frequencies ξ and ψ are related through

$$\cosh \xi = \cosh \psi + \omega \quad (3.63)$$

so ξ is actually restricted by ψ . Furthermore, we recognise this link between the frequencies ψ and ξ as the exact same relation as we had between the frequencies φ and ϑ back in chapter 2. Then the visualisation introduced in section 2.10 applies, and all threshold frequencies carry over.

Before we look at these threshold frequencies, we move on to see another analogy to the antiferromagnetic layer. With the given defining equations (3.60) and (3.62) for ψ and ξ , the characteristic roots χ_{\pm} and v_{\pm} take the simple forms

$$\chi_{\pm} = -\cosh \xi \pm \sqrt{\cosh^2 \xi - 1} = -(\cosh \xi \mp \sinh \xi) = -e^{\mp \xi}, \quad (3.64)$$

$$v_{\pm} = \cosh \psi \pm \sqrt{\cosh^2 \psi - 1} = \cosh \psi \pm \sinh \psi = e^{\pm \psi}, \quad (3.65)$$

and so the general solutions become, after absorbing all constant factors into X and Y ,

$$x_p = X(-1)^p \sinh(\xi(p - (N + 1))), \quad (3.66)$$

$$y_p = Y \sinh(\psi(p - (N + 1))), \quad (3.67)$$

with x_p replaced by

$$x_p = X(-1)^p (p - (N + 1)) e^{p\xi} \quad (3.68)$$

in the special case of solutions on the edge of the lower continuum (ξ equal to 0 or $\iota\pi$), and y_p replaced by

$$y_p = Y(p - (N + 1)) e^{p\psi} \quad (3.69)$$

in the special case of solutions on the edge of the upper continuum (ψ equal to 0 or $\iota\pi$). The sine functions in (3.66) and (3.67) can be either hyperbolic or trigonometric based on the frequencies ξ and ψ . Inspired by the terminology for magnons in chapter 2, we will then distinguish between three main types of electrons:

- *surface electrons* with two real frequencies,
- *bulk electrons* with two imaginary frequencies,

- *mixed electrons* with one real and one imaginary frequency.

For bulk electrons and mixed electrons, ψ is imaginary, so their energy quanta lie within the upper continuum. Surface electrons on the other hand have real values of ψ and energy quanta above the upper continuum. By antisymmetry there is always another electron with energy quantum on the opposite side of zero, so there are also corresponding bulk electrons and mixed electrons within the lower continuum, and corresponding surface electrons below.

From the defining equation (3.60), we get the metallic dispersion relation

$$\epsilon = \omega + 2 \cosh \psi, \quad (3.70)$$

which allows us to study the threshold frequencies of the metallic layer and the corresponding threshold energies. The threshold frequency

$$\psi_0 = \iota \arccos\left(-\frac{\omega}{2}\right) \quad (3.71)$$

for $\omega \leq 2$ corresponds to the energy quantum $\epsilon = 0$, while the *bottom threshold frequency*

$$\psi_V = \iota\pi \quad (3.72)$$

for $\omega > 2$ corresponds to the *bottom threshold energy*

$$\epsilon_V = (\omega - 2). \quad (3.73)$$

The *bulk threshold frequency*

$$\psi_B = \iota \arccos(1 - \omega) \quad (3.74)$$

for $\omega \leq 2$ corresponds to the *bulk threshold energy*

$$\epsilon_B = 2 - \omega \quad (3.75)$$

at the top edge of the lower continuum (but still within the upper continuum). For imaginary ψ values below this, ξ is pushed onto the real frequency branch and the electrons become mixed electrons with energy quanta above ϵ_B . Finally, the *surface threshold frequency*

$$\psi_S = 0 \quad (3.76)$$

corresponds to the *surface threshold energy*

$$\epsilon_S = \omega + 2 \quad (3.77)$$

at the top edge of the upper continuum. Electrons with real values of ψ are surface electrons with energy quanta above ϵ_S .

The general solutions in equations (3.66)–(3.69) satisfy both the bulk recurrence relations (3.37) and (3.38), as well as the two last surface equations in (3.39). Now we will make sure that they also satisfy the two first surface equations. In the next section we look at bulk electrons, mixed electrons and surface electrons, which are not at any threshold, but within or above the upper continuum. Then in section 3.7 we look at the threshold electrons for which the special edge solutions (3.68) and (3.69) must be used.

3.6 Bulk, mixed and surface electrons

Consider electrons which are not on any threshold at all — that is, the frequencies ξ and ψ are either real above 0 or imaginary between 0 and $\iota\pi$, but not any of the threshold frequencies specified in the previous section. The two first surface equations in (3.39) then become

$$\begin{aligned} -X \sinh((N+1)\xi) &= \lambda Y \sinh(N\psi), \\ -Y \sinh((N+1)\psi) &= \lambda X \sinh(N\xi) \end{aligned} \quad (3.78)$$

when plugging in the general solutions (3.66) and (3.67). Note that $\sinh((N+1)\psi)$ and $\sinh(N\psi)$ cannot be zero at the same time, because this would imply that $\psi = \iota \frac{m}{N+1} \pi = \iota \frac{n}{N} \pi$ for two integers m and n , which is only possible if ψ is 0 or $\iota\pi$, corresponding to threshold electrons. The same goes for $\sinh((N+1)\xi)$ and $\sinh(N\xi)$. From the equations above it is then clear that neither X nor Y can be set to zero without also forcing the other one to be zero. (This argument fails when $\lambda = 0$, but we will consider this special case later, in section 3.12.)

Multiply the first of the surface equations (3.78) with $-\sinh((N+1)\psi)$ and use the last equation to get

$$\sinh((N+1)\xi) \sinh((N+1)\psi) - \lambda^2 \sinh(N\xi) \sinh(N\psi) = 0 \quad (3.79)$$

after dividing away X . This equation provides the second connection between ξ and ψ , much like the condition equation (2.114) in the case of magnons. Together with the link equation (3.63), it can be used to determine the allowed frequencies ψ and ξ , and hence also the energy quanta ϵ through the dispersion relation (3.70). When all these quantities are known, the first of the surface equations (3.78) can be rewritten to

$$X = -\lambda Y \frac{\sinh(N\psi)}{\sinh((N+1)\xi)}, \quad (3.80)$$

The final form of the general solution is then

$$\begin{aligned} x_p &= -\lambda Y \sinh(N\psi) \frac{(-1)^p \sinh(\xi(p - (N+1)))}{\sinh((N+1)\xi)}, \\ y_p &= Y \sinh(\psi(p - (N+1))). \end{aligned} \quad (3.81)$$

Before we move on to threshold electrons in the next section, we take a closer look at the condition equation (3.79) to find the exact number of surface solutions that are possible. To this end we rewrite it to

$$\lambda^2 = \frac{\sinh((N+1)\xi)}{\sinh(N\xi)} \frac{\sinh((N+1)\psi)}{\sinh(N\psi)} \quad (3.82)$$

and consider the hyperbolic sine ratio function

$$\text{sinh}_a x = \frac{\sinh(ax)}{\sinh x} \quad (3.83)$$

for some $a > 1 \in \mathbb{R}$. Using the Taylor expansion of the hyperbolic sine function, it is clear that $\text{sinh}_a 0 = a$. Furthermore, the derivative of $\text{sinh}_a x$ is

$$\frac{d}{dx} \text{sinh}_a x = \frac{a \sinh x \cosh(ax) - \cosh x \sinh(ax)}{\sinh^2 x}, \quad (3.84)$$

which is 0 for $x = 0$. The sign of this derivative is necessarily the same as the sign of its nominator. But taking the derivative of the nominator, we see that

$$\frac{d}{dx} (a \sinh x \cosh(ax) - \cosh x \sinh(ax)) = (a^2 - 1) \sinh x \sinh(ax), \quad (3.85)$$

and this is positive for all $x > 0$. In other words, the nominator of the derivative (3.84) is zero for $x = 0$ and then strictly increasing for all $x > 0$, so the derivative itself is positive for all $x > 0$. Then the function $\text{sinh}_a x$ as defined in (3.83) is a strictly increasing function for $x > 0$.

This result about $\text{sinh}_a x$ is what we need to prove that there can be a maximum of one surface solution to the condition equation (3.79). For surface electrons, we obtain the expression

$$\xi = \text{arcosh}(\omega + \cosh \psi) \quad (3.86)$$

from the link equation (3.63), and since both the hyperbolic cosine function and the area hyperbolic cosine function are strictly increasing functions for positive arguments, ξ is a strictly increasing function of ψ . Rewriting equation (3.82) to

$$\lambda^2 = \text{sinh}_{\frac{N+1}{N}}(N\xi) \text{sinh}_{\frac{N+1}{N}}(N\psi), \quad (3.87)$$

we see that the right hand side is a strictly increasing function of ψ for all real $\psi > 0$. Then the equation can only have a single surface solution.

There are no solutions at all to equation (3.87) if λ^2 is less than or equal to the minimal value of the right hand side, which is its value at $\psi = 0$. Thus the condition for surface electrons to appear is

$$\frac{N+1}{N} \frac{\sinh((N+1) \text{arcosh}(1+\omega))}{\sinh(N \text{arcosh}(1+\omega))} < \lambda^2. \quad (3.88)$$

The left hand side of this condition is also a strictly increasing function of ω . If λ is less than its overall minimum value, then no surface electrons appear for any values of the wave parameter ω . Since the minimum value is $(\frac{N+1}{N})^2$ at $\omega = 0$, the threshold value of λ for surface electrons to appear at all is

$$\lambda_S = \frac{N+1}{N}. \quad (3.89)$$

We have found the condition equation (3.79) and the general solution (3.81) for the electrons of the metallic layer. Furthermore, we have found a condition (3.88) for surface electrons to appear for any specific value of ω , and an overall threshold λ_S for surface electrons to appear at all. In the next section, we move on to threshold electrons.

3.7 Threshold electrons

At some of the threshold frequencies specified in the previous section, the electronic solutions take special forms of x_p and y_p given in (3.68) and (3.69). More specifically, (3.68) replaces the general solution (3.66) at the bulk threshold frequency ψ_B given in (3.74) (which corresponds to the top of the lower continuum), while (3.69) replaces the general solution (3.67) at the bottom threshold frequency ψ_V given in (3.72) or the surface threshold frequency ψ_S given in (3.76)

For very special values of the wave parameter ω , electrons can actually be at *two* of these thresholds simultaneously. In the case $\omega = 0$, the bulk and surface threshold energies coincide at $\psi = \xi = 0$, so there could be a threshold electron at the top of both continua. In this case the two continua completely overlap. In the case $\omega = 2$, the bulk and bottom threshold energies coincide at $\psi = \iota\pi$ and $\xi = 0$, which corresponds to a threshold electron at the bottom of the upper continuum which is simultaneously at the top of the lower continuum. In this case the two energy continua just touch each other.

Such *double-threshold electrons* have the general solutions for x_p and y_p given in (3.68) and (3.69). Substituting these into the two first surface equations in (3.39) however, the equations become

$$\begin{aligned} -(N+1)X &= \lambda NY e^\psi, \\ -(N+1)Y &= \lambda NX e^\xi, \end{aligned} \quad (3.90)$$

and multiplying the first equation by $-(N+1)$ and then using the last equation it turns out that

$$(N+1)^2 - \lambda^2 N^2 e^{\psi+\xi} = 0.$$

This is not possible in the case $\omega = 2$ when $e^{\psi+\xi} = -1$, while in the case $\omega = 0$ when $e^{\psi+\xi} = 1$, it means that

$$\lambda = \frac{N+1}{N}, \quad (3.91)$$

which we recognise as the threshold value λ_S defined in (3.89). Then, from the first equation above it follows that

$$X = -\lambda \frac{N}{N+1} Y e^\psi = -Y$$

To summarise, double-threshold electrons are only possible in the special case of $\omega = 0$ and $\lambda = \lambda_S$. In this case, the energy quantum is $\epsilon = 2$ and the corresponding amplitudes turn out to be

$$\begin{aligned} x_p &= -Y(p - (N+1))(-1)^p, \\ y_p &= Y(p - (N+1)). \end{aligned} \quad (3.92)$$

Next, we look at the possibility of *bulk threshold electrons* which lie only at the top of the lower continuum. In this case the two first surface equations in (3.39) become

$$\begin{aligned} -(N+1)X &= \lambda Y \sinh(N\psi), \\ -Y \sinh((N+1)\psi) &= \lambda NX e^\xi. \end{aligned} \quad (3.93)$$

Multiply the last equation by $-(N + 1)$ and then use the first equation to get

$$(N + 1) \sinh((N + 1)\psi) - \lambda^2 N e^\xi \sinh(N\psi) = 0.$$

But in this case, $\psi = \iota \arccos(1 - \omega)$ and $\xi = 0$, so the condition equation above turns into

$$\frac{N + 1}{N} \frac{\sin((N + 1) \arccos(1 - \omega))}{\sin(N \arccos(1 - \omega))} = \lambda^2 \quad (3.94)$$

Whenever this condition is fulfilled, the last surface equation above becomes

$$Y = -\lambda X \frac{N}{\sin((N + 1) \arccos(1 - \omega))},$$

so the general solution for such electrons becomes

$$\begin{aligned} x_p &= X(p - (N + 1))(-1)^p, \\ y_p &= -\lambda X N \frac{\sin((p - (N + 1)) \arccos(1 - \omega))}{\sin((N + 1) \arccos(1 - \omega))}, \end{aligned} \quad (3.95)$$

with the bulk threshold energy $\epsilon = (2 - \omega)$.

Bottom threshold electrons at ψ_v for $\omega > 2$ lie only at the bottom of the upper continuum. In this case the surface equations become

$$\begin{aligned} -X \sinh((N + 1)\xi) &= \lambda N Y e^\psi, \\ -(N + 1)Y &= \lambda X \sinh(N\xi). \end{aligned} \quad (3.96)$$

Multiply the first equation by $-(N + 1)$ and then use the last equation to get

$$(N + 1) \sinh((N + 1)\xi) - \lambda^2 N e^\psi \sinh(N\xi) = 0, \quad (3.97)$$

But since $\psi = \iota\pi$ and $\xi = \operatorname{arcosh}(\omega - 1)$ in this case, this equation reduces to

$$(N + 1) \sinh((N + 1) \operatorname{arcosh}(\omega - 1)) + \lambda^2 N \sinh(N \operatorname{arcosh}(\omega - 1)) = 0. \quad (3.98)$$

Since both terms in the above equation are positive, we conclude that bottom threshold electrons at the bottom of the upper continuum for $\omega > 2$ are never possible.

Finally we look at *surface threshold electrons* at the top of the upper continuum. The general solutions and the surface equations initially are the same as for the bottom threshold electrons considered above, so the surface equations become (3.96) and the corresponding condition equation becomes (3.97). However in this case, $\psi = 0$ and $\xi = \operatorname{arcosh}(1 + \omega)$, so the condition equation reduces to

$$\frac{N + 1}{N} \frac{\sinh((N + 1) \operatorname{arcosh}(1 + \omega))}{\sinh(N \operatorname{arcosh}(1 + \omega))} = \lambda^2 \quad (3.99)$$

which is solvable as long as λ is above the threshold λ_S . We recognise this condition as the threshold of the condition (3.88) for surface electrons to appear. When this condition holds, the first of the surface equations in (3.96) can be rewritten to

$$X = -\lambda Y \frac{N}{\sinh((N + 1) \operatorname{arcosh}(1 + \omega))},$$

and the general solution becomes

$$\begin{aligned} x_p &= -\lambda Y N \frac{(-1)^p \sinh((p - (N + 1)) \operatorname{arcosh}(1 + \omega))}{\sinh((N + 1) \operatorname{arcosh}(1 + \omega))}, \\ y_p &= Y(p - (N + 1)) \end{aligned} \quad (3.100)$$

with the surface threshold energy $\epsilon = (\omega + 2)$.

To summarise, the conditions (3.94) and (3.99) must be satisfied for bulk or surface threshold electrons to appear in the metallic layer. Hence, such threshold electrons only appear at specific values of the wave parameter ω . While the bulk threshold condition is satisfied for many values of ω , the surface threshold condition can only be satisfied for one value of ω at most. For ω values below this threshold, proper surface electrons appear, while for ω values above this threshold, only bulk and mixed electrons are possible.

3.8 Gap electrons

There is one type of electron which we have neglected so far, and that is electrons whose positive energy quanta lie within the gap mentioned back in section 3.5. The gap energy quanta fulfil $-\frac{\omega + \epsilon}{2} < -\frac{\omega}{2}$ and $-\frac{\omega - \epsilon}{2} < -1$ for $\omega > 2$. Write then

$$\begin{aligned} -\frac{\omega + \epsilon}{2} &= -\cosh \xi, \\ -\frac{\omega - \epsilon}{2} &= -\cosh \psi \end{aligned}$$

for some real frequency parameters ξ and ψ . From this it is clear that

$$\epsilon = \omega - 2 \cosh \psi, \quad (3.101)$$

while ξ and ψ are related through

$$\cosh \xi = \omega - \cosh \psi. \quad (3.102)$$

Since we only consider gap electrons with positive energy quanta ϵ between 0 and $(\omega - 2)$, only ψ values between 0 and $\operatorname{arcosh}(\frac{\omega}{2})$ need to be considered.

With the definitions above, the characteristic roots χ_{\pm} and v_{\pm} defined in (3.40) and (3.41) become

$$\chi_{\pm} = -\cosh \xi \pm \sqrt{\cosh^2 \xi - 1} = -(\cosh \xi \mp \sinh \xi) = -e^{\mp \xi}, \quad (3.103)$$

$$v_{\pm} = -\cosh \psi \pm \sqrt{\cosh^2 \psi - 1} = -(\cosh \psi \mp \sinh \psi) = -e^{\mp \psi}, \quad (3.104)$$

and so the general solutions have the form

$$x_p = X(-1)^p \sinh((p - (N + 1))\xi), \quad (3.105)$$

$$y_p = Y(-1)^p \sinh((p - (N + 1))\psi) \quad (3.106)$$

after absorbing all constant factors into X and Y . Substituting these into the two first surface equations in (3.39), however, we get

$$-X \sinh((N+1)\xi) = -\lambda Y \sinh(N\psi), \quad (3.107)$$

$$-Y \sinh((N+1)\psi) = \lambda X \sinh(N\xi), \quad (3.108)$$

and multiplying the first of these equations with $\sinh((N+1)\psi)$ we end up with the condition equation

$$\sinh((N+1)\xi) \sinh((N+1)\psi) + \lambda^2 \sinh(N\xi) \sinh(N\psi) = 0, \quad (3.109)$$

which has no solutions for *any* real values of ξ and ψ above 0. We conclude that gap electrons do not exist, and so the region between the two energy continua is a proper energy vacuum.

Having considered all the possible energy quanta of the metallic layer as well as found the corresponding equations, we proceed to normalise our solutions in the next section.

3.9 Normalisation

With the general solutions worked out for all the possible types of electrons, it is time to normalise them. We start by looking at bulk, mixed and surface electrons, whose general solution is given in (3.81). Plugging these into the normalisation (3.51), we get the equation

$$\sum_{p=1}^N \left(\lambda^2 Y^2 \sinh^2(N\psi) \frac{\sinh^2(\xi(p-(N+1)))}{\sinh^2((N+1)\xi)} + Y^2 \sinh^2(\psi(p-(N+1))) \right) = 2.$$

Using the first identity in (2.135) this equation turns into

$$\begin{aligned} \sum_{p=1}^N \left(\lambda^2 \sinh^2(N\psi) \frac{\cosh(2\xi(p-(N+1))) - 1}{\sinh^2((N+1)\xi)} + (\cosh(2\psi(p-(N+1))) - 1) \right) \\ = \frac{4}{Y^2}. \end{aligned} \quad (3.110)$$

To sum up the hyperbolic cosine terms, we use equation (2.137) from section 2.11 with $(N+1)$ instead of p_m to obtain

$$\sum_{p=1}^N e^{\pm\alpha(p-(N+1))} = \frac{\sinh(\frac{N+1}{2}\alpha)}{\sinh(\frac{\alpha}{2})} e^{\mp(\frac{N}{2}+1)\alpha} - e^{\mp(N+1)\alpha},$$

which yields the summation

$$\sum_{p=1}^N \cosh(\alpha(p-(N+1))) = \frac{\sinh(\frac{N+1}{2}\alpha)}{\sinh(\frac{\alpha}{2})} \cosh\left(\left(\frac{N}{2}+1\right)\alpha\right) - \cosh((N+1)\alpha). \quad (3.111)$$

This equation applies to all phases α . Then the normalisation above becomes

$$\lambda^2 \frac{\sinh^2(N\psi)}{\sinh^2((N+1)\xi)} \left(\frac{\sinh((N+1)\xi)}{\sinh \xi} \cosh((N+2)\xi) - \cosh(2(N+1)\xi) - N \right) + \left(\frac{\sinh((N+1)\psi)}{\sinh \psi} \cosh((N+2)\psi) - \cosh(2(N+1)\psi) - N \right) = \frac{4}{Y^2} \quad (3.112)$$

for bulk, mixed and surface electrons.

Next we look at double threshold electrons. The general solution (3.92) provides the normalisation equation

$$\sum_{p=1}^N Y^2 (p - (N+1))^2 = 1,$$

which can be rewritten to

$$\sum_{p=1}^N p^2 = \frac{1}{Y^2}.$$

Using the pyramid number formula

$$\sum_{p=1}^N p^2 = \frac{N(N+1)(2N+1)}{6}, \quad (3.113)$$

the normalisation for double threshold electrons then becomes

$$\frac{2N(N+1)(2N+1)}{3} = \frac{4}{Y^2}. \quad (3.114)$$

For bulk threshold electrons, the general solution (3.95) provides the normalisation equation

$$\sum_{p=1}^N \left(X^2 (p - (N+1))^2 + \lambda^2 X^2 N^2 \frac{\sin^2((p - (N+1)) \arccos(1 - \omega))}{\sin^2((N+1) \arccos(1 - \omega))} \right) = 2,$$

which can be rewritten to

$$\frac{\lambda^2 N^2}{\sin^2((N+1) \arccos(1 - \omega))} \sum_{p=1}^N (1 - \cos(2(p - (N+1)) \arccos(1 - \omega))) + 2 \sum_{p=1}^N p^2 = \frac{4}{X^2}$$

and then summed using (3.113) and (3.111) to give

$$\begin{aligned} & \frac{\lambda^2 N^2}{\sin^2((N+1)\arccos(1-\omega))} \left(N + \cos(2(N+1)\arccos(1-\omega)) \right. \\ & \quad \left. - \frac{\sin((N+1)\arccos(1-\omega))}{\sin\arccos(1-\omega)} \cos((N+2)\arccos(1-\omega)) \right) \\ & \quad + \frac{N(N+1)(2N+1)}{3} = \frac{4}{X^2}. \end{aligned} \quad (3.115)$$

Similarly for surface threshold electrons, the general solution (3.100) provides the normalisation equation

$$\sum_{p=1}^N \left(\lambda^2 Y^2 N^2 \frac{\sinh^2((p-(N+1))\operatorname{arcosh}(1+\omega))}{\sinh^2((N+1)\operatorname{arcosh}(1+\omega))} + Y^2 (p-(N+1))^2 \right) = 2,$$

which can be rewritten and summed using (3.113) and (3.111) to give

$$\begin{aligned} & - \frac{\lambda^2 N^2}{\sinh^2((N+1)\operatorname{arcosh}(1+\omega))} \left(N + \cosh(2(N+1)\operatorname{arcosh}(1+\omega)) \right. \\ & \quad \left. - \frac{\sinh((N+1)\operatorname{arcosh}(1+\omega))}{\sinh\operatorname{arcosh}(1+\omega)} \cosh((N+2)\operatorname{arcosh}(1+\omega)) \right) \\ & \quad + \frac{N(N+1)(2N+1)}{3} = \frac{4}{Y^2}. \end{aligned} \quad (3.116)$$

The normalisation equations (3.112), (3.114), (3.115) and (3.116) conclude our analytical work on the electronic solutions.

3.10 Electron plots

The class `MetalSolver` was now extended with a class method `calcAnaElectrons` similar to the `calcAnaMagnons` of the `MagnetSolver` class. This class method uses the results from sections 3.5–3.9 to find specific types of electrons by rooting the corresponding condition functions and calculating the electronic parameters. In figure 3.3 the electronic eigenstates of a 6-plane metallic layer are plotted for the specified values of λ and ω , which are the same as the ones used back in section 3.4. These plots were found by rooting the condition function shown in figure 3.4. We see that both the energy quanta and the amplitudes match exactly, so our analytical calculations in the sections 3.5–3.9 seem correct. In the figures 3.5, 3.6 and 3.7, the electronic eigenstates for other parametric values are plotted. In this case, both surface electrons, mixed electrons and bulk electrons appear. Because λ (and thus the spin exchange across the junction) is set larger here, the electrons are even more asymmetric over the middle plane in this second case than in the first case.

Mixed Electrons of the Metallic Layer
 ($N = 6, \lambda = 0.80, \omega = 4.00$)

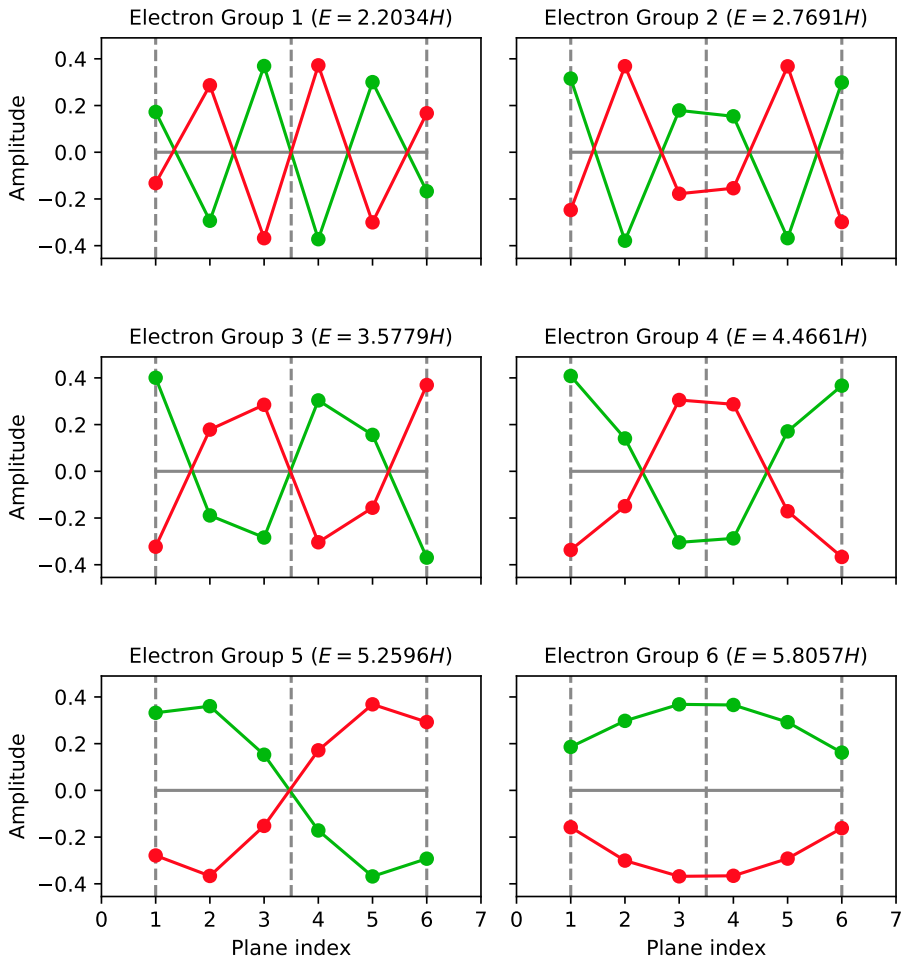


Figure 3.3: The mixed electrons of a 6-plane metallic layer for the given parameters. The energy quanta as well as the amplitudes match exactly to the electrons in figure 3.2.

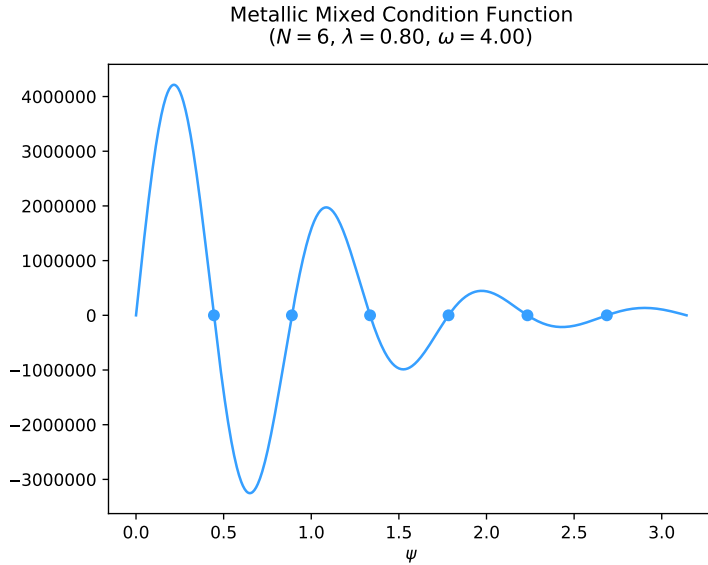


Figure 3.4: Condition function for mixed electrons in a 6-plane metallic layer for the given parameters. The found roots are marked with points.

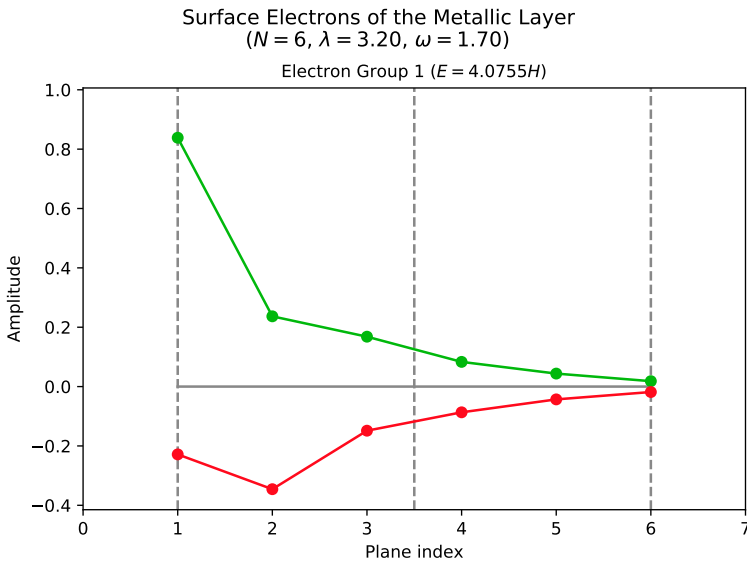


Figure 3.5: The surface electrons of a 6-plane metallic layer for the given parameters.

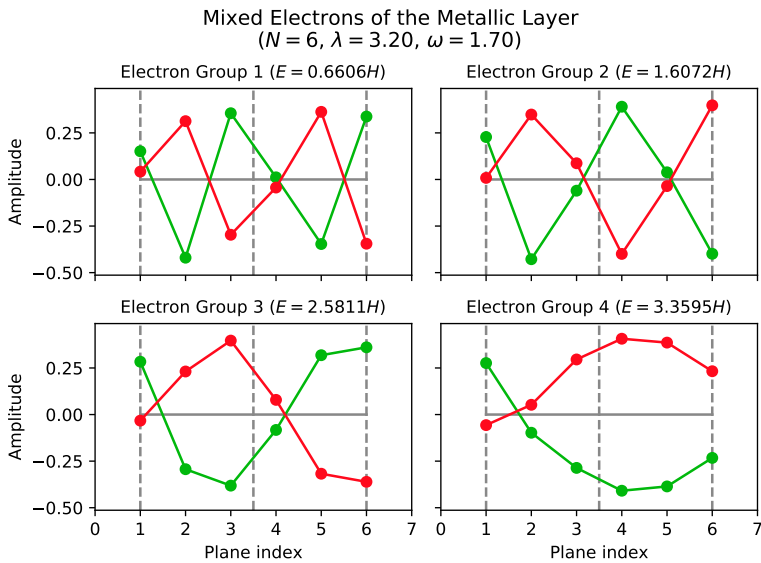


Figure 3.6: The mixed electrons of a 6-plane metallic layer for the given parameters.

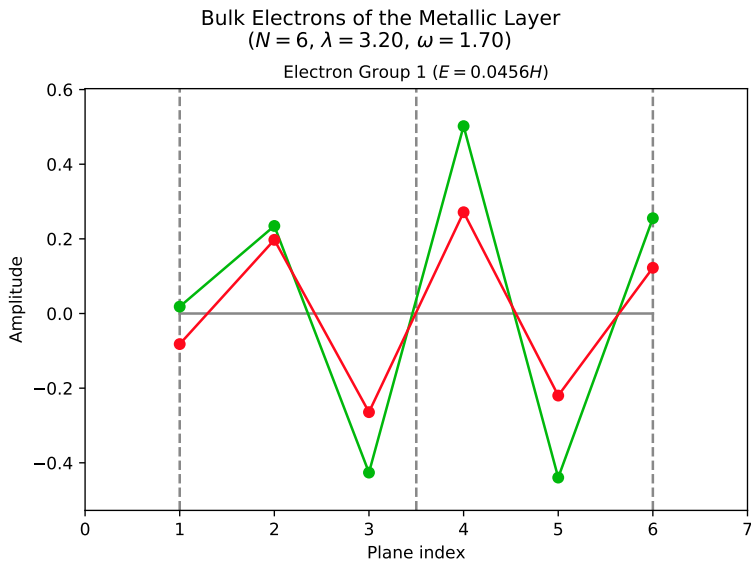


Figure 3.7: The bulk electrons of a 6-plane metallic layer for the given parameters.

3.11 Energy spectrum

We will summarise what we found about the energy spectrum of the metallic layer in this section. As in the previous sections we consider only positive energy electrons, but remember that for each such electron, there is a corresponding electron with negative energy, and furthermore two corresponding electrons of opposite spin. Therefore, we actually talk about electron *groups* rather than single electrons in the following discussion, and the energy spectrum plots can be mirrored over the x-axis to include all possible energy quanta.

A method `plotMetSpectrum` was added to the solver script, which takes in the parameters N and λ and creates one instance of `MetalSolver` for each value of the wave parameter ω , runs a numerical diagonalisation to get the allowed energy quanta and plots the energy quanta over the range of ω . In section 3.5, we found the threshold frequencies that separate the different types of electrons. The corresponding threshold energies separate them in the energy spectrum plots.

The energy spectra of 6-plane metallic layers with $\lambda = 0.8$ and $\lambda = 3.2$ are shown in figures 3.8 and 3.9. Since 3.2 is greater than the threshold value $\lambda_S = \frac{7}{6} \approx 1.17$ found in section 3.6, we see that a surface electron branch is present in the last plot. The points where the allowed quanta cross the threshold energies are where threshold electrons appear. We see that there are many values of ω for which bulk threshold electrons appear, while there is at most one value of ω for which a surface threshold electron appears. This is consistent with the threshold conditions (3.94) and (3.99) found in section 3.7. In figure 3.10 the spectrum of a 40-plane metallic layer is shown.

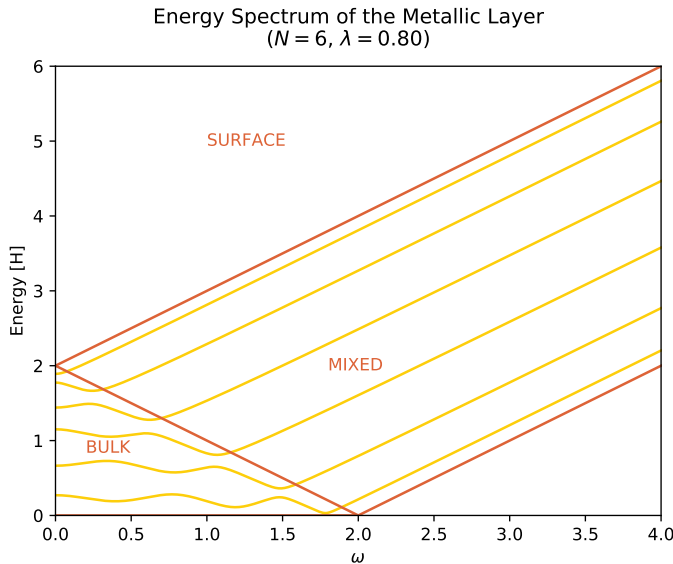


Figure 3.8: The energy spectrum of a 6-plane metallic layer for the given parameters. The actual energy branches are plotted in yellow, while the threshold energies are plotted in brown. Note that for each positive energy branch in this plot, there is also an allowed negative energy branch.

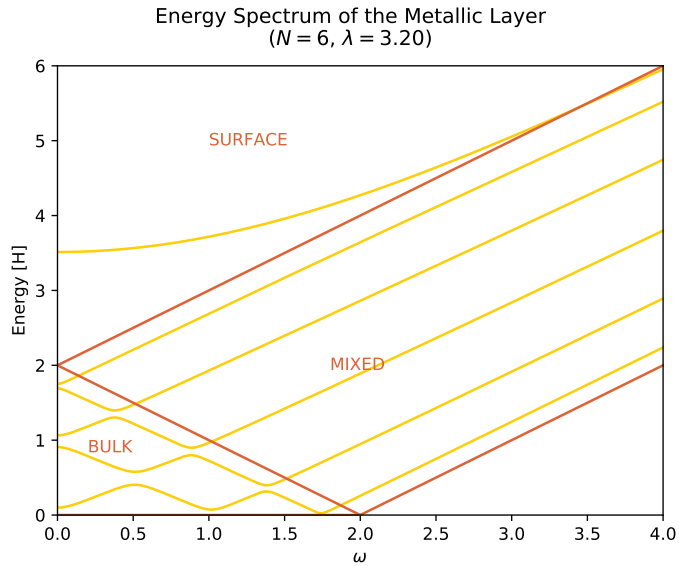


Figure 3.9: The energy spectrum of a 6-plane metallic layer for the given parameters. Here, a surface electron branch is present for most values of the wave parameter ω .

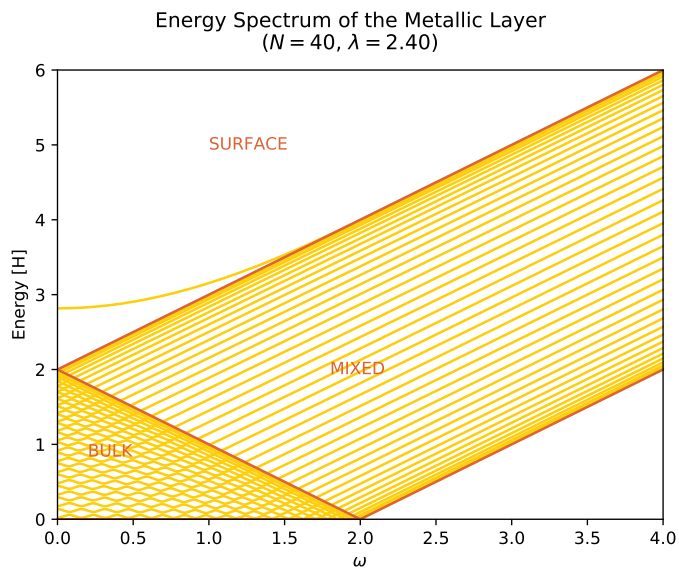


Figure 3.10: The energy spectrum of a 40-plane metallic layer for the given parameters. All branches except one surface branch lie within the bulk continuum.

We found in section 3.5 that the condition (3.79) has at most one surface solution for each value of ω . In other words, only one surface electron branch can exist no matter how many planes there are in the metallic layer. Like in the case of the antiferromagnetic layer then, this explains why all the additional electron branches for higher plane numbers lie within the upper continuum, as is apparent in the 40-plane metallic layer spectrum. Hence the name "continuum" is finally justified, and we will simply call it the *bulk continuum* from here on to stress the delocalised nature of the bulk and mixed electrons within.

3.12 Non-interacting limit

So far we have considered $\lambda \neq 0$, so that there is an interaction across the junction between the antiferromagnetic and metallic layers. Consider now the *non-interacting limit* of $\lambda \rightarrow 0$. Without any interaction between the layers, the metallic model reduces to a simple tight-binding model, so the distinction between the sublattices \mathbb{A} and \mathbb{B} should turn out to be superfluous. To see that this is indeed the case, we look to the equations. The surface equations in (3.78) reduce to

$$X \sinh((N+1)\xi) = 0, \quad (3.117)$$

$$Y \sinh((N+1)\psi) = 0, \quad (3.118)$$

which force the frequencies ξ and ψ to be imaginary and quantised in bits of $\iota \frac{\pi}{N+1}$, or their associated amplitudes X and Y to vanish. The amplitudes x_p and y_p become

$$x_p = X(-1)^p \sin\left((p - (N+1))\frac{m}{N+1}\pi\right), \quad (3.119)$$

$$y_p = Y \sin\left((p - (N+1))\frac{n}{N+1}\pi\right), \quad (3.120)$$

where m and n are integers between 1 and N . However note that

$$\sin\left((p - (N+1))\frac{m}{N+1}\pi\right) = \sin\left(\frac{m}{N+1}\pi p - m\pi\right) = (-1)^m \sin\left(\frac{m}{N+1}\pi p\right), \quad (3.121)$$

and similarly

$$(-1)^p \sin\left(\frac{m}{N+1}\pi p\right) = \sin\left(\frac{m}{N+1}\pi p - p\pi\right) = -\sin\left(\frac{(N+1) - m}{N+1}\pi p\right) \quad (3.122)$$

for any integer m . Using these two identities and absorbing all constant factors into X and Y , the amplitudes above reduce to

$$x_p = X \sin\left(\frac{(N+1) - m}{N+1}\pi p\right), \quad (3.123)$$

$$y_p = Y \sin\left(\frac{n}{N+1}\pi p\right), \quad (3.124)$$

so we see that they actually have a very similar form. Normally only one of these amplitudes are non-zero. To see this, remember that there is a link equation (3.63) between the frequencies ξ and ψ . This link equation is only satisfied for very special values of the wave parameter ω given by

$$\omega = \cos\left(\frac{m}{N+1}\pi\right) - \cos\left(\frac{n}{N+1}\pi\right). \quad (3.125)$$

For all other values, both frequencies cannot be quantised at the same time, so one of the amplitudes X or Y has to be zero. The resulting electron either lies within the lower continuum (for $\xi = \iota\frac{m}{N+1}\pi$ and $Y = 0$) or in the upper continuum (for $\psi = \iota\frac{n}{N+1}\pi$ and $X = 0$). These two cases are related by the antisymmetry, so really only the upper continuum electron needs to be considered. The electronic solutions in the non-interacting limit are then

$$x_p = 0, \quad (3.126)$$

$$y_p = Y \sin\left(\frac{n}{N+1}\pi p\right) \quad (3.127)$$

with the corresponding energy quanta

$$\epsilon = \omega + 2 \cos\left(\frac{n}{N+1}\pi\right) \quad (3.128)$$

for all integers n between 1 and N . A quick normalisation using some results from section 3.9 provides the equation

$$(N+1) = \frac{4}{Y^2} \quad (3.129)$$

to determine the amplitude Y .

Note that since the amplitudes x_p disappear, the original amplitudes $o_p = \frac{x_p + y_p}{2}$ and $w_p = \frac{x_p - y_p}{2}$ are simply negatives of each other. Similarly, for electrons in the lower continuum the amplitudes y_p disappear so that o_p and w_p are equal. To see why this makes the sublattices \mathbb{A} and \mathbb{B} superfluous, we look at the original Hamiltonian (3.1). Without the first two interaction terms, the model can be solved by a single Fourier transformation followed by a unitary transformation, instead of the two sublattice Fourier transformations given in (3.4). The planar lattice used for this Fourier transformation is spanned by \vec{l}_y and \vec{l}_z , and the corresponding Brillouin zone is twice the size of the normal Brillouin zone. The wave vectors \vec{k}' in the extended part of the Brillouin zone correspond to the wave vectors \vec{k} within the normal Brillouin zone through the shift $\frac{\pi}{t}(\vec{e}_y + \vec{e}_z)$. But this shift makes the Fourier amplitude $e^{\iota\vec{k}'\cdot\vec{r}}$ the opposite sign of the Fourier amplitude $e^{\iota\vec{k}\cdot\vec{r}}$ at exactly the lattice sites in sublattice \mathbb{B} , and the corresponding energy quantum also has the opposite sign. In other words, electrons within the lower continuum (which have the same amplitude throughout each plane) correspond to electrons within the normal Brillouin zone, while electrons within the upper continuum (which have alternating amplitudes in each plane) correspond to electrons within the extended part of the Brillouin zone. With the single Fourier transformation and the extended Brillouin zone, the distinction between the sublattices \mathbb{A} and \mathbb{B} is indeed superfluous.

In figure 3.11, the electrons of a non-interacting 6-plane metallic layer are shown for the specific value $\omega = 1.7$. The first electron group belongs to the lower continuum, which explains why the amplitudes are equal in this case. Figure 3.12 shows the energy spectrum. The up and down going electron branches cross each other at specific points, corresponding to the special values of ω given above in (3.125).

In figure 3.13, the normal and extended Brillouin zones are illustrated.

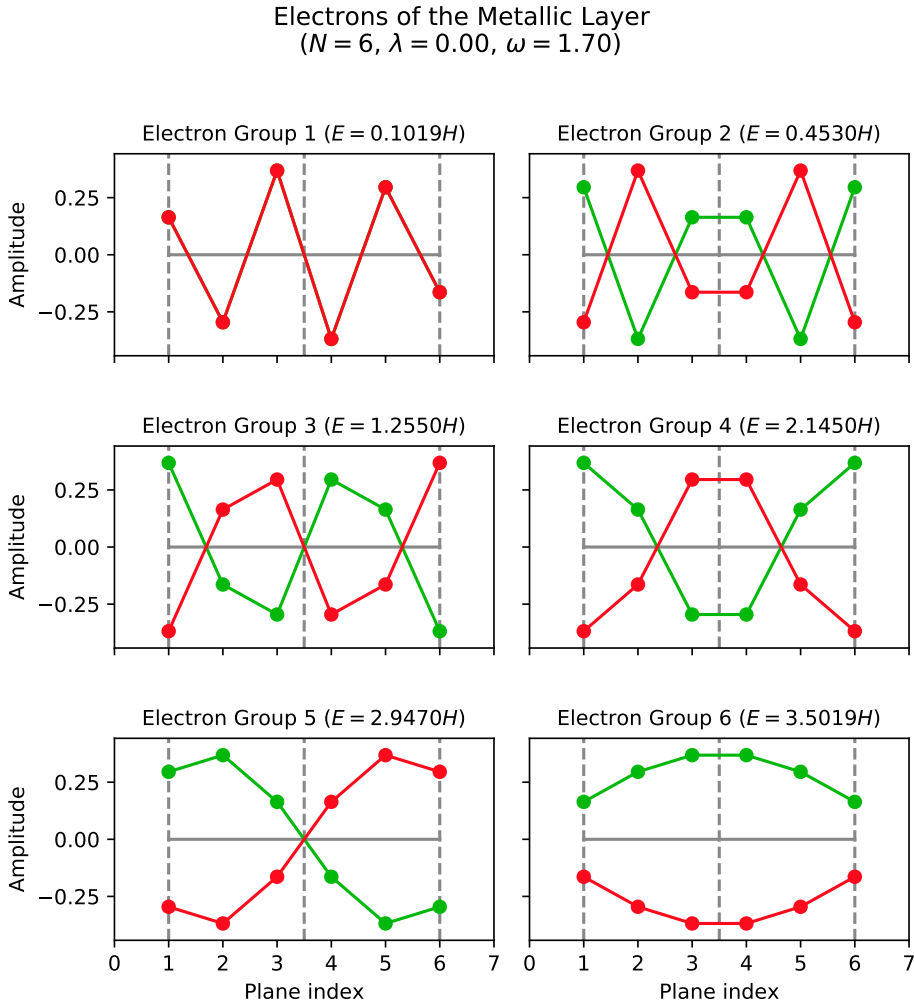


Figure 3.11: The electrons of a non-interacting 6-plane metallic layer for the given parameters. In the non-interacting limit $\lambda \rightarrow 0$, the amplitudes o_p and w_p are simply equal or negatives of each other, corresponding to wave vectors in the normal and extended regions of the Brillouin zone, respectively.

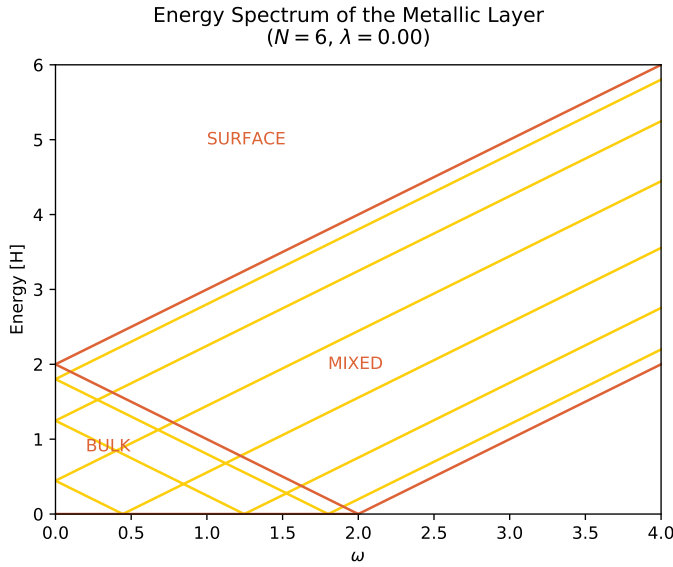


Figure 3.12: The energy spectrum of a non-interacting 6-plane metallic layer. The electron branches of the upper and lower bulk continua cross at certain values of ω .

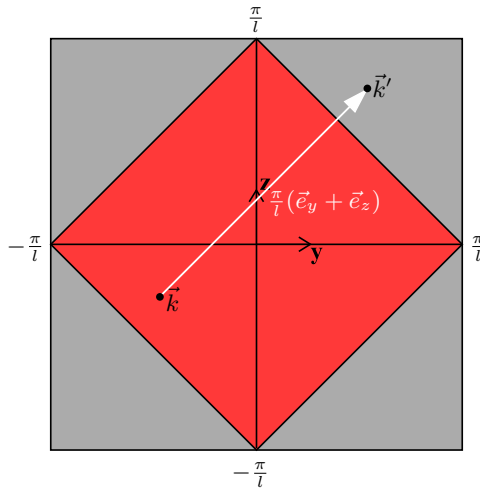


Figure 3.13: The extended Brillouin zone, which appears in the non-interacting limit. The normal Brillouin zone (red) corresponds to electrons in the lower continuum, while the extended region (grey) corresponds to electrons in the upper continuum. The lower continuum electron with wave vector \vec{k} and the upper continuum electron with wave vector \vec{k}' have equal amplitudes on each planar sublattice \mathbb{A}_p , but because of the shift $\frac{\pi}{l}(\vec{e}_y + \vec{e}_z)$, the amplitudes of the latter has the opposite sign on each planar sublattice \mathbb{B}_p and also the opposite sign on its energy quantum.

3.13 Summary

The key results for the finite-depth metallic conductor layer are concisely summed up here. For more details, please consult the rest of the chapter.

The N -plane metallic layer with Hamiltonian

$$\mathbf{H} = \frac{Is}{2} \sum_{\vec{a} \in \mathbb{A}_1} (\mathbf{c}_{\uparrow\vec{a}}^\dagger \mathbf{c}_{\uparrow\vec{a}} - \mathbf{c}_{\downarrow\vec{a}}^\dagger \mathbf{c}_{\downarrow\vec{a}}) - \frac{Is}{2} \sum_{\vec{b} \in \mathbb{B}_1} (\mathbf{c}_{\uparrow\vec{b}}^\dagger \mathbf{c}_{\uparrow\vec{b}} - \mathbf{c}_{\downarrow\vec{b}}^\dagger \mathbf{c}_{\downarrow\vec{b}}) - H \sum_{m, \vec{q}; \vec{r} \in \mathbb{M}} (\mathbf{c}_{m\vec{q}}^\dagger \mathbf{c}_{m\vec{r}} + \mathbf{c}_{m\vec{r}}^\dagger \mathbf{c}_{m\vec{q}})$$

has an energy spectrum given by

$$E = \epsilon H, \\ \epsilon = \pm(\omega + 2 \cosh \psi),$$

where ψ is given implicitly through the system of equations

$$\cosh \xi = \cosh \psi + \omega$$

and

$$\sinh((N+1)\xi) \sinh((N+1)\psi) - \lambda^2 \sinh(N\xi) \sinh(N\psi) = 0.$$

Here,

$$\lambda = \frac{Is}{2H}$$

and

$$\omega = 2(\cos(lk_y) + \cos(lk_z))$$

for all planar wave vectors \vec{k} within the Brillouin zone depicted in figure 2.5. l is the lattice parameter of the simple cubic metallic lattice.

The electronic eigenstates are generated by the fermionic operators

$$\gamma_{\uparrow\vec{k}}^+ = \sum_{p=1}^N (o_p \mathbf{a}_{\uparrow\vec{k},p} + w_p \mathbf{b}_{\uparrow\vec{k},p}), \\ \gamma_{\uparrow\vec{k}}^- = \sum_{p=1}^N (w_p \mathbf{a}_{\uparrow\vec{k},p} o_p \mathbf{b}_{\uparrow\vec{k},p}), \\ \gamma_{\downarrow\vec{k}}^+ = \sum_{p=1}^N (o_p \mathbf{b}_{\downarrow\vec{k},p} + w_p \mathbf{a}_{\downarrow\vec{k},p}), \\ \gamma_{\downarrow\vec{k}}^- = \sum_{p=1}^N (w_p \mathbf{b}_{\downarrow\vec{k},p} - o_p \mathbf{a}_{\downarrow\vec{k},p}),$$

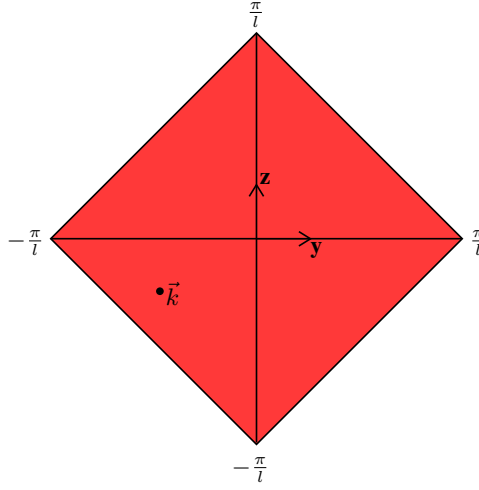


Figure 3.14: The Brillouin zone of the finite metallic layer.

where the superscripted signs denote the sign used in ϵ . The amplitudes o_p and w_p are generally given by

$$o_p = -\lambda Y \sinh(N\psi) \frac{(-1)^p \sinh(\xi(p - (N + 1)))}{\sinh((N + 1)\xi)} + Y \sinh(\psi(p - (N + 1)))$$

$$w_p = -\lambda Y \sinh(N\psi) \frac{(-1)^p \sinh(\xi(p - (N + 1)))}{\sinh((N + 1)\xi)} - Y \sinh(\psi(p - (N + 1))),$$

with the normalisation

$$\lambda^2 \frac{\sinh^2(N\psi)}{\sinh^2((N + 1)\xi)} \left(\frac{\sinh((N + 1)\xi)}{\sinh \xi} \cosh((N + 2)\xi) - \cosh(2(N + 1)\xi) - N \right)$$

$$+ \left(\frac{\sinh((N + 1)\psi)}{\sinh \psi} \cosh((N + 2)\psi) - \cosh(2(N + 1)\psi) - N \right) = \frac{1}{Y^2}.$$

Here, the operators $\mathbf{a}_{m\vec{k},p}$ and $\mathbf{b}_{m\vec{k},p}$ for any spin value m (\uparrow or \downarrow) are planar sublattice electron waves given by

$$\mathbf{a}_{m\vec{k},p} = \frac{1}{2G + 2} \sum_{\vec{a} \in \mathbb{A}_p} e^{i\vec{k} \cdot \vec{a}} \mathbf{c}_{m\vec{a}},$$

$$\mathbf{b}_{m\vec{k},p} = \frac{1}{2G + 2} \sum_{\vec{b} \in \mathbb{B}_p} e^{i\vec{k} \cdot \vec{b}} \mathbf{c}_{m\vec{b}},$$

in which the operators $\mathbf{c}_{m\vec{r}}$ annihilate spin- m electrons at each lattice site \vec{r} .

For certain values of ω , special threshold electrons appear, whose amplitudes o_p and w_p differ from the ones above. If ω satisfies

$$\frac{N+1}{N} \frac{\sin((N+1) \arccos(1-\omega))}{\sin(N \arccos(1-\omega))} = \lambda^2,$$

bulk threshold electrons of energy quantum $\epsilon = \pm(2-\omega)$ appear, with amplitudes

$$o_p = X(p - (N+1))(-1)^p - \lambda X N \frac{\sin((p - (N+1)) \arccos(1-\omega))}{\sin((N+1) \arccos(1-\omega))},$$

$$w_p = X(p - (N+1))(-1)^p + \lambda X N \frac{\sin((p - (N+1)) \arccos(1-\omega))}{\sin((N+1) \arccos(1-\omega))}$$

and normalisation

$$\frac{\lambda^2 N^2}{\sin^2((N+1) \arccos(1-\omega))} \left(N + \cos(2(N+1) \arccos(1-\omega)) \right. \\ \left. - \frac{\sin((N+1) \arccos(1-\omega))}{\sin \arccos(1-\omega)} \cos((N+2) \arccos(1-\omega)) \right) \\ + \frac{N(N+1)(2N+1)}{3} = \frac{1}{X^2}.$$

If ω satisfies

$$\frac{N+1}{N} \frac{\sinh((N+1) \operatorname{arcosh}(1+\omega))}{\sinh(N \operatorname{arcosh}(1+\omega))} = \lambda^2,$$

surface threshold electrons of energy quantum $\epsilon = \pm(\omega+2)$ appear, with amplitudes

$$o_p = -\lambda Y N \frac{(-1)^p \sinh((p - (N+1)) \operatorname{arcosh}(1+\omega))}{\sinh((N+1) \operatorname{arcosh}(1+\omega))} + Y(p - (N+1)),$$

$$w_p = -\lambda Y N \frac{(-1)^p \sinh((p - (N+1)) \operatorname{arcosh}(1+\omega))}{\sinh((N+1) \operatorname{arcosh}(1+\omega))} - Y(p - (N+1))$$

and normalisation

$$- \frac{\lambda^2 N^2}{\sinh^2((N+1) \operatorname{arcosh}(1+\omega))} \left(N + \cosh(2(N+1) \operatorname{arcosh}(1+\omega)) \right. \\ \left. - \frac{\sinh((N+1) \operatorname{arcosh}(1+\omega))}{\sinh \operatorname{arcosh}(1+\omega)} \cosh((N+2) \operatorname{arcosh}(1+\omega)) \right) \\ + \frac{N(N+1)(2N+1)}{3} = \frac{1}{Y^2}.$$

Finally, if $\omega = 0$ and $\lambda = \frac{N+1}{N}$, double threshold electrons of energy quantum $\epsilon = \pm 2$ appear with amplitudes

$$o_p = Y(p - (N+1))(1 - (-1)^p),$$

$$w_p = -Y(p - (N+1))(1 + (-1)^p)$$

and normalisation

$$\frac{2N(N+1)(2N+1)}{3} = \frac{1}{Y^2}.$$

There are N solutions to the frequencies ξ and ψ , and hence N electron groups, for each planar wave vector \vec{k} in the Brillouin zone. All these electrons have energy quanta that lie within the bulk/mixed continuum shown in figure 3.15, except possibly two surface electron branches which appear if

$$\lambda > \frac{N+1}{N}.$$

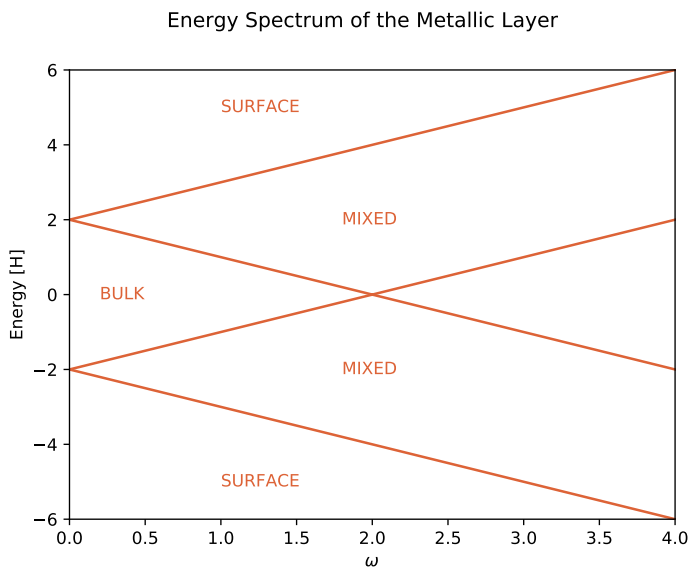


Figure 3.15: The energy spectrum of the finite metallic layer.

Chapter 4

Junction

Chapters 2 and 3 looked thoroughly at the energy eigenstates of the antiferromagnetic insulator layer and the metallic conductor layer separately. In this chapter, we combine the knowledge from these chapters to finally look at the junction between the two layers and the spin transport across. In the first section, we describe the model for the interaction across the junction.

4.1 Model

To model the interaction across the junction, we use an antiferromagnetic Heisenberg model that couples each static spin on the surface of the antiferromagnetic layer to the closest itinerant electron spins on the surface of the metallic layer. The junction Hamiltonian is then

$$\mathbf{H} = \frac{I}{\hbar^2} \sum_{\substack{\vec{a} \in \Lambda_1 \\ m, m'}} \vec{\mathbf{s}}_{\vec{a}} \cdot \vec{\sigma}_{mm'} \mathbf{c}_{m\vec{a}}^\dagger \mathbf{c}_{m'\vec{a}} + \frac{I}{\hbar^2} \sum_{\substack{\vec{b} \in \mathbb{B}_1 \\ m, m'}} \vec{\mathbf{s}}_{\vec{b}} \cdot \vec{\sigma}_{mm'} \mathbf{c}_{m\vec{b}}^\dagger \mathbf{c}_{m'\vec{b}}. \quad (4.1)$$

Here, I is the spin exchange parameter across the junction introduced in section 3.1, $\vec{\mathbf{s}}_{\vec{r}}$ are the spin operators on each antiferromagnetic site $\vec{r} \in \mathbb{T}$ and $\mathbf{c}_{m\vec{r}}$ are the operators annihilating an electron with spin m (\uparrow or \downarrow) on each metallic site $\vec{r} \in \mathbb{M}$. The matrix vector $\boxed{\vec{\sigma}}$ is the well-known vector of Pauli matrices,

$$\begin{aligned} \boxed{\sigma_x} &= \frac{\hbar}{2} \begin{bmatrix} 0 & 1 \\ 1 & 0 \end{bmatrix}, \\ \boxed{\sigma_y} &= \frac{\hbar}{2} \begin{bmatrix} 0 & -i \\ i & 0 \end{bmatrix}, \\ \boxed{\sigma_z} &= \frac{\hbar}{2} \begin{bmatrix} 1 & 0 \\ 0 & -1 \end{bmatrix}, \end{aligned} \quad (4.2)$$

in which the upper rows and left columns correspond to index \uparrow and vice versa.

Note that in (4.1), we have taken advantage of the fact that we used the same symbols \mathbb{A}_1 and \mathbb{B}_1 to denote the two sublattices of the surface plane in both the antiferromagnetic and the metallic layer. Strictly speaking this is an abuse of notation, but the meaning should be clear: The spin operator $\vec{s}_{\vec{a}}$ sits in the up sublattice of the antiferromagnetic surface plane, while the electron operator $c_{m\vec{a}}$ works on the neighbouring site in the up sublattice of the metallic surface plane.

Writing out the dot product in the first term of the Hamiltonian (4.1) and using the approximate Holstein-Primakoff transformation (2.12) from section 2.3, it reduces to

$$\frac{Is}{2} \sum_{\vec{a} \in \mathbb{A}_1} \left(c_{\uparrow\vec{a}}^\dagger c_{\uparrow\vec{a}} - c_{\downarrow\vec{a}}^\dagger c_{\downarrow\vec{a}} \right) + I \sqrt{\frac{s}{2}} \sum_{\vec{a} \in \mathbb{A}_1} \left(\mathbf{a}_{\vec{a}} c_{\downarrow\vec{a}}^\dagger c_{\uparrow\vec{a}} + \mathbf{a}_{\vec{a}}^\dagger c_{\uparrow\vec{a}}^\dagger c_{\downarrow\vec{a}} \right).$$

Similarly the second term of the Hamiltonian reduces to

$$\frac{Is}{2} \sum_{\vec{a} \in \mathbb{B}_1} \left(c_{\downarrow\vec{a}}^\dagger c_{\downarrow\vec{a}} - c_{\uparrow\vec{a}}^\dagger c_{\uparrow\vec{a}} \right) + I \sqrt{\frac{s}{2}} \sum_{\vec{b} \in \mathbb{B}_1} \left(\mathbf{b}_{\vec{b}}^\dagger c_{\downarrow\vec{b}}^\dagger c_{\uparrow\vec{b}} + \mathbf{b}_{\vec{b}} c_{\uparrow\vec{b}}^\dagger c_{\downarrow\vec{b}} \right).$$

The pure electronic terms above correspond to the interaction across the junction to the zeroth order in the magnonic operators. They were already included in the metallic model back in section 3.1. The perturbation to the Hamiltonian of the entire system (antiferromagnetic layer and metallic layer) stemming from the interaction across the junction is then

$$\delta\mathbf{H} = I \sqrt{\frac{s}{2}} \left(\sum_{\vec{a} \in \mathbb{A}_1} \left(\mathbf{a}_{\vec{a}} c_{\downarrow\vec{a}}^\dagger c_{\uparrow\vec{a}} + \mathbf{a}_{\vec{a}}^\dagger c_{\uparrow\vec{a}}^\dagger c_{\downarrow\vec{a}} \right) + \sum_{\vec{b} \in \mathbb{B}_1} \left(\mathbf{b}_{\vec{b}}^\dagger c_{\downarrow\vec{b}}^\dagger c_{\uparrow\vec{b}} + \mathbf{b}_{\vec{b}} c_{\uparrow\vec{b}}^\dagger c_{\downarrow\vec{b}} \right) \right) \quad (4.3)$$

This can be regarded as a perturbation because the number of Holstein-Primakoff bosons, and hence each bosonic operator \mathbf{a}_\bullet and \mathbf{b}_\bullet , is assumed small.

4.2 Transformations

The perturbation (4.3) should be transformed into an expression with the magnonic operators α_\bullet and β_\bullet from chapter 2 and the electronic operators γ_\bullet^\pm from chapter 3, since these operators describe the energy eigenstates of the two layers in the absence of any perturbation, which are the eigenstates used in Fermi's golden rule later on. To this end we first use the Fourier back transformations (2.28) and (3.5) to transform the perturbation further. Since the antiferromagnetic and metallic layers are assumed to have the same lattice parameter l , the same planar lattice size G and hence the same planar wave lattice \vec{k} given in (2.24), the useful sums (2.26) and (2.27) apply. After some algebra the perturbation turns into

$$\delta\mathbf{H} = \frac{I \sqrt{\frac{s}{2}}}{2G + 2} \sum_{\vec{k}, \vec{k}'} \left(\mathbf{a}_{\vec{k}' - \vec{k}, 1} \mathbf{a}_{\downarrow\vec{k}', 1}^\dagger \mathbf{a}_{\uparrow\vec{k}, 1} + \mathbf{a}_{\vec{k} - \vec{k}', 1}^\dagger \mathbf{a}_{\uparrow\vec{k}', 1}^\dagger \mathbf{a}_{\downarrow\vec{k}, 1} + \right. \\ \left. \mathbf{b}_{\vec{k}' - \vec{k}, 1} \mathbf{b}_{\uparrow\vec{k}', 1}^\dagger \mathbf{b}_{\downarrow\vec{k}, 1} + \mathbf{b}_{\vec{k} - \vec{k}', 1}^\dagger \mathbf{b}_{\downarrow\vec{k}', 1}^\dagger \mathbf{b}_{\uparrow\vec{k}, 1} \right). \quad (4.4)$$

At this stage the expression is a little confusing because of multiple use of the letters **a** and **b**. However, antiferromagnetic operator waves and metallic operator waves can be distinguished by the appearance of spin values (\uparrow or \downarrow) in the indices.

Next up are the Bogoliubov transformation from section 2.6 and the unitary transformation from section 3.3. Using the inverse given in (2.72), the Bogoliubov back transformation (2.56) for the antiferromagnetic operator waves becomes

$$\begin{bmatrix} \bar{\mathbf{a}}_{\vec{k}} \\ \bar{\mathbf{b}}_{-\vec{k}}^\dagger \end{bmatrix} = \begin{bmatrix} \boxed{u(\vec{k})}^\dagger & -\boxed{v(\vec{k})}^\dagger \\ -\boxed{v(\vec{k})}^\dagger & \boxed{u(\vec{k})}^\dagger \end{bmatrix} \begin{bmatrix} \bar{\alpha}_{\vec{k}} \\ \bar{\beta}_{\vec{k}} \end{bmatrix}, \quad (4.5)$$

where we have added back the planar wave vector \vec{k} that was omitted at the end of section 2.4. The amplitude matrices $\boxed{u(\vec{k})}$ and $\boxed{v(\vec{k})}$ depend on \vec{k} through ω . The above equation applies to all planar wave vectors \vec{k} within the Brillouin zone. Writing it out, we get the back transformations

$$\begin{aligned} \mathbf{a}_{\vec{k},p} &= u_{np}(\vec{k})\alpha_{\vec{k},n} - v_{np}(\vec{k})\beta_{\vec{k},n}^\dagger, \\ \mathbf{b}_{-\vec{k},p}^\dagger &= u_{np}(\vec{k})\beta_{\vec{k},n}^\dagger - v_{np}(\vec{k})\alpha_{\vec{k},n} \end{aligned} \quad (4.6)$$

for all plane indices p between 1 and N and all planar wave vectors \vec{k} within the Brillouin zone. In this equation, the Einstein summation convention is used, so there is a sum over all the magnonic eigenstates.

The unitary back transformation for the metallic operator waves is

$$\begin{bmatrix} \bar{\mathbf{a}}_{\uparrow\vec{k}} \\ \bar{\mathbf{b}}_{\uparrow\vec{k}}^\dagger \end{bmatrix} = \begin{bmatrix} \boxed{o(\vec{k})}^\dagger & \boxed{w(\vec{k})}^\dagger \\ \boxed{w(\vec{k})}^\dagger & -\boxed{o(\vec{k})}^\dagger \end{bmatrix} \begin{bmatrix} \bar{\gamma}_{\uparrow\vec{k}}^+ \\ \bar{\gamma}_{\uparrow\vec{k}}^- \end{bmatrix}, \quad (4.7)$$

in which the split (3.18) was used to separate positive and negative energy electrons. Here again, we added back the spin up value \uparrow and the planar wave vector \vec{k} that were omitted in section 3.3. Writing it out, we get the back transformation

$$\begin{aligned} \mathbf{a}_{\uparrow\vec{k},p} &= o_{np}(\vec{k})\gamma_{\uparrow\vec{k},n}^+ + w_{np}(\vec{k})\gamma_{\uparrow\vec{k},n}^-, \\ \mathbf{b}_{\uparrow\vec{k},p}^\dagger &= w_{np}(\vec{k})\gamma_{\uparrow\vec{k},n}^+ - o_{np}(\vec{k})\gamma_{\uparrow\vec{k},n}^-, \end{aligned} \quad (4.8)$$

for spin-up operators, and using the sublattice swap/spin flip symmetry discussed in section 3.3 on (4.7) we get

$$\begin{aligned} \mathbf{a}_{\downarrow\vec{k},p} &= w_{np}(\vec{k})\gamma_{\downarrow\vec{k},n}^+ - o_{np}(\vec{k})\gamma_{\downarrow\vec{k},n}^-, \\ \mathbf{b}_{\downarrow\vec{k},p}^\dagger &= o_{np}(\vec{k})\gamma_{\downarrow\vec{k},n}^+ + w_{np}(\vec{k})\gamma_{\downarrow\vec{k},n}^- \end{aligned} \quad (4.9)$$

for spin-down operators. Both these back transformations hold for all plane indices p between 1 and N and all planar wave vectors \vec{k} within the Brillouin zone, and the Einstein summation convention is used in both.

Entering the back transformations (4.6), (4.8) and (4.9) as well as their adjoints into the perturbation (4.4) and refactoring the resulting expression, we end up with

$$\begin{aligned}
 \delta\mathbf{H} = & \frac{I\sqrt{\frac{s}{2}}}{2G+2} \sum_{m,\vec{k},n,\vec{k}',n'} \ddagger \left(\left(\Sigma_m(\vec{k}', n', \vec{k}, n) \gamma_{\uparrow\vec{k}',n'}^{+\dagger} \gamma_{\downarrow\vec{k},n}^+ - \Sigma_m(\vec{k}, n, \vec{k}', n') \gamma_{\uparrow\vec{k}',n'}^{-\dagger} \gamma_{\downarrow\vec{k},n}^- \right. \right. \\
 & - \Gamma_m(\vec{k}', n', \vec{k}, n) \gamma_{\uparrow\vec{k}',n'}^{+\dagger} \gamma_{\downarrow\vec{k},n}^- + \Xi_m(\vec{k}', n', \vec{k}, n) \gamma_{\uparrow\vec{k}',n'}^{-\dagger} \gamma_{\downarrow\vec{k},n}^+ \left. \right) \alpha_{\vec{k}-\vec{k}',m}^\dagger \\
 & + \left(\Sigma_m(\vec{k}, n, \vec{k}', n') \gamma_{\uparrow\vec{k}',n'}^{+\dagger} \gamma_{\downarrow\vec{k},n}^+ - \Sigma_m(\vec{k}', n', \vec{k}, n) \gamma_{\uparrow\vec{k}',n'}^{-\dagger} \gamma_{\downarrow\vec{k},n}^- \right. \\
 & \left. \left. + \Xi_m(\vec{k}', n', \vec{k}, n) \gamma_{\uparrow\vec{k}',n'}^{+\dagger} \gamma_{\downarrow\vec{k},n}^- - \Gamma_m(\vec{k}', n', \vec{k}, n) \gamma_{\uparrow\vec{k}',n'}^{-\dagger} \gamma_{\downarrow\vec{k},n}^+ \right) \beta_{\vec{k}-\vec{k}',m} \right), \quad (4.10)
 \end{aligned}$$

where the three amplitude functions

$$\begin{aligned}
 \Sigma_m(\vec{k}', n', \vec{k}, n) &= u_{m1}(\vec{k} - \vec{k}') o_{n'1}(\vec{k}') w_{n1}(\vec{k}) - v_{m1}(\vec{k} - \vec{k}') w_{n'1}(\vec{k}') o_{n1}(\vec{k}) \\
 \Gamma_m(\vec{k}', n', \vec{k}, n) &= u_{m1}(\vec{k} - \vec{k}') o_{n'1}(\vec{k}') o_{n1}(\vec{k}) + v_{m1}(\vec{k} - \vec{k}') w_{n'1}(\vec{k}') w_{n1}(\vec{k}) \\
 \Xi_m(\vec{k}', n', \vec{k}, n) &= u_{m1}(\vec{k} - \vec{k}') w_{n'1}(\vec{k}') w_{n1}(\vec{k}) + v_{m1}(\vec{k} - \vec{k}') o_{n'1}(\vec{k}') o_{n1}(\vec{k}) \quad (4.11)
 \end{aligned}$$

were defined. In (4.10), the double dagger indicates that the operator within the brackets should be summed with its adjoint operator, as defined in the notation section.

The equation (4.10) and the definitions (4.11) may look overwhelming at first glance, but they are actually quite structured. Each term transfers spin between the antiferromagnetic layer and the metallic layer by flipping the spin of an electron and creating or annihilating an appropriate magnon. The planar momentum of the magnon corresponds to the difference in the planar momentum of the electron before and after the spin flip, so that the total planar momentum is conserved (within the Brillouin zone). The amplitude function Σ_\bullet is involved with the spin flip of an electron whose energy stays the same side of zero, while the amplitude functions Γ_\bullet and Ξ_\bullet are involved with the spin flip of an electron whose energy crosses from one side of zero to the other.

4.3 Fermi's golden rule

To get an expression for the spin transport across the junction, we use Fermi's golden rule for a time-independent perturbation. This rule says that the transition probability from an initial energy eigenstate $|i\rangle$ to the final energy eigenstate $|f\rangle$ after a time t with a small perturbation $\delta\mathbf{H}$ is

$$P_{i \rightarrow f}(t) = \frac{2\pi}{\hbar} |\langle f | \delta\mathbf{H} | i \rangle|^2 \delta_t(E_f - E_i)t \quad (4.12)$$

where E_i and E_f are the energies of $|i\rangle$ and $|f\rangle$ respectively, and the function δ_t is a function that approaches the Dirac delta function after a long time t .

For our system, the transition probability in (4.12) is zero in most cases. Looking at the perturbation $\delta\mathbf{H}$ given in (4.10), the inner product $\langle f | \delta\mathbf{H} | i \rangle$ is only nonzero for final states $|f\rangle$ that have exactly one magnon more or one magnon less than the initial state

$|i\rangle$). Furthermore, even if the magnon number fulfils this, the final state must also have an electron configuration that matches the initial state after one of the corresponding electron spin flips. Finally, even when all these criteria are met, the final and initial states must have the same energy because of the delta function. In total then, only very specific transitions are allowed.

Summing (4.12) over all final states $|f\rangle$ which have one α -magnon more than the initial state, we get the total probability for one α -magnon to appear. Only the first part of the perturbation (4.3), the part that involves creation operators $\alpha_{\bullet}^{\dagger}$, survives. Denoting this part with $\delta\mathbf{H}_{+\alpha}$, this probability becomes

$$P_{+\alpha}(t) = \frac{2\pi}{\hbar} \sum_f \langle f | \delta\mathbf{H}_{+\alpha} | i \rangle \langle i | \delta\mathbf{H}_{+\alpha}^{\dagger} | f \rangle \delta(E_f - E_i) t.$$

The sum can now actually be taken over *all* energy eigenstates $|f\rangle$, because the operator $\delta\mathbf{H}_{+\alpha}$ anyway annihilates all the eigenstates which do not have exactly one α -magnon more than $|i\rangle$.

The energy difference $E_f - E_i$ varies with each term in $\delta\mathbf{H}_{+\alpha}$. But since all magnons have positive energy quanta, the energy difference from the electron spin flip must be negative in order for the total energy to be conserved. Because of this, the terms in $\delta\mathbf{H}_{+\alpha}$ involving Γ_{\bullet} can be neglected – these terms annihilate a negative-energy electron and create a positive-energy electron, so the spin flip energy difference is always positive, which means that they will all be zeroed by the delta function. Similar arguments hold for $\delta\mathbf{H}_{+\beta}$, defined as the part of $\delta\mathbf{H}$ that involves the creation of a β -magnon, and also for their adjoints $\delta\mathbf{H}_{+\alpha}^{\dagger}$ and $\delta\mathbf{H}_{+\beta}^{\dagger}$, in which the Γ_{\bullet} terms annihilate positive-energy electrons and create negative-energy electrons, which is incompatible with the annihilation of a magnon.

Neglecting then all Γ_{\bullet} terms, absorbing the delta functions into $\delta\mathbf{H}_{+\alpha}$ and finally also assuming a mixed initial state with density operator ρ instead of the pure initial state $|i\rangle$, the probability for an α -magnon to appear becomes

$$P_{+\alpha}(t) = \frac{2\pi}{\hbar} \text{tr} \left(\delta\mathbf{H}_{+\alpha} \rho \delta\mathbf{H}_{+\alpha}^{\dagger} \right) t, \quad (4.13)$$

with

$$\begin{aligned} \delta\mathbf{H}_{+\alpha} = & \frac{I\sqrt{\frac{s}{2}}}{2G+2} \sum_{m, \vec{k}, n, \vec{k}', n'} \left(\Sigma_m(\vec{k}', n', \vec{k}, n) \delta(\varepsilon_m(\vec{k} - \vec{k}') + \epsilon_{n'}(\vec{k}') - \epsilon_n(\vec{k})) \gamma_{\uparrow\vec{k}', n'}^{+\dagger} \gamma_{\downarrow\vec{k}, n}^{+} \right. \\ & - \Sigma_m(\vec{k}, n, \vec{k}', n') \delta(\varepsilon_m(\vec{k} - \vec{k}') - \epsilon_{n'}(\vec{k}') + \epsilon_n(\vec{k})) \gamma_{\uparrow\vec{k}', n'}^{-\dagger} \gamma_{\downarrow\vec{k}, n}^{-} \\ & \left. + \Xi_m(\vec{k}', n', \vec{k}, n) \delta(\varepsilon_m(\vec{k} - \vec{k}') - \epsilon_{n'}(\vec{k}') - \epsilon_n(\vec{k})) \gamma_{\uparrow\vec{k}', n'}^{-\dagger} \gamma_{\downarrow\vec{k}, n}^{+} \right) \alpha_{\vec{k}-\vec{k}', m}^{\dagger}. \end{aligned} \quad (4.14)$$

The probability for an α -magnon to disappear is

$$P_{-\alpha}(t) = \frac{2\pi}{\hbar} \text{tr} \left(\delta\mathbf{H}_{-\alpha} \rho \delta\mathbf{H}_{-\alpha}^{\dagger} \right) t, \quad (4.15)$$

with

$$\begin{aligned}
 \delta\mathbf{H}_{-\alpha} = \frac{I\sqrt{\frac{s}{2}}}{2G+2} \sum_{m,\vec{k},n,\vec{k}',n'} & \left(\Sigma_m(\vec{k},n,\vec{k}',n')\delta(-\varepsilon_m(\vec{k}'-\vec{k})+\varepsilon_{n'}(\vec{k}')-\varepsilon_n(\vec{k}))\gamma_{\downarrow\vec{k}',n'}^{+\dagger}\gamma_{\uparrow\vec{k},n}^+ \right. \\
 & - \Sigma_m(\vec{k}',n',\vec{k},n)\delta(-\varepsilon_m(\vec{k}'-\vec{k})-\varepsilon_{n'}(\vec{k}')+\varepsilon_n(\vec{k}))\gamma_{\downarrow\vec{k}',n'}^{-\dagger}\gamma_{\uparrow\vec{k},n}^- \\
 & \left. + \Xi_m(\vec{k}',n',\vec{k},n)\delta(-\varepsilon_m(\vec{k}'-\vec{k})+\varepsilon_{n'}(\vec{k}')+\varepsilon_n(\vec{k}))\gamma_{\downarrow\vec{k}',n'}^{+\dagger}\gamma_{\uparrow\vec{k},n}^- \right) \alpha_{\vec{k}'-\vec{k},m}.
 \end{aligned} \tag{4.16}$$

The *transport rate* of α -magnons across the junction is then

$$T_\alpha = \frac{2\pi}{\hbar} \left(\text{tr} \left(\delta\mathbf{H}_{+\alpha} \rho \delta\mathbf{H}_{+\alpha}^\dagger \right) - \text{tr} \left(\delta\mathbf{H}_{-\alpha} \rho \delta\mathbf{H}_{-\alpha}^\dagger \right) \right). \tag{4.17}$$

This rate quantifies the creation of α -magnons at the antiferromagnetic side of the junction through corresponding spin flips on the metallic side. Since α -magnons consist of down-tilts on the antiferromagnetic up-lattice $\mathbb{A}_T \in \mathbb{T}$ as well as down-tilts on the antiferromagnetic down-lattice $\mathbb{B}_T \in \mathbb{T}$, the rate T_α also quantifies the spin-down transport across the junction and into the antiferromagnetic layer.

The reasoning above also applies to β -magnons. The total transport rate of β -magnons is then

$$T_\beta = \frac{2\pi}{\hbar} \left(\text{tr} \left(\delta\mathbf{H}_{+\beta} \rho \delta\mathbf{H}_{+\beta}^\dagger \right) - \text{tr} \left(\delta\mathbf{H}_{-\beta} \rho \delta\mathbf{H}_{-\beta}^\dagger \right) \right), \tag{4.18}$$

with

$$\begin{aligned}
 \delta\mathbf{H}_{+\beta} = \frac{I\sqrt{\frac{s}{2}}}{2G+2} \sum_{m,\vec{k},n,\vec{k}',n'} & \left(\Sigma_m(\vec{k}',n',\vec{k},n)\delta(\varepsilon_m(\vec{k}'-\vec{k})+\varepsilon_{n'}(\vec{k}')-\varepsilon_n(\vec{k}))\gamma_{\downarrow\vec{k}',n'}^{+\dagger}\gamma_{\uparrow\vec{k},n}^+ \right. \\
 & - \Sigma_m(\vec{k},n,\vec{k}',n')\delta(\varepsilon_m(\vec{k}'-\vec{k})-\varepsilon_{n'}(\vec{k}')+\varepsilon_n(\vec{k}))\gamma_{\downarrow\vec{k}',n'}^{-\dagger}\gamma_{\uparrow\vec{k},n}^- \\
 & \left. + \Xi_m(\vec{k}',n',\vec{k},n)\delta(\varepsilon_m(\vec{k}'-\vec{k})-\varepsilon_{n'}(\vec{k}')-\varepsilon_n(\vec{k}))\gamma_{\downarrow\vec{k}',n'}^{-\dagger}\gamma_{\uparrow\vec{k},n}^+ \right) \beta_{\vec{k}'-\vec{k},m}^\dagger.
 \end{aligned} \tag{4.19}$$

and

$$\begin{aligned}
 \delta\mathbf{H}_{-\beta} = \frac{I\sqrt{\frac{s}{2}}}{2G+2} \sum_{m,\vec{k},n,\vec{k}',n'} & \left(\Sigma_m(\vec{k},n,\vec{k}',n')\delta(-\varepsilon_m(\vec{k}-\vec{k}')+\varepsilon_{n'}(\vec{k}')-\varepsilon_n(\vec{k}))\gamma_{\uparrow\vec{k}',n'}^{+\dagger}\gamma_{\downarrow\vec{k},n}^+ \right. \\
 & - \Sigma_m(\vec{k}',n',\vec{k},n)\delta(-\varepsilon_m(\vec{k}-\vec{k}')-\varepsilon_{n'}(\vec{k}')+\varepsilon_n(\vec{k}))\gamma_{\downarrow\vec{k}',n'}^{-\dagger}\gamma_{\uparrow\vec{k},n}^- \\
 & \left. + \Xi_m(\vec{k}',n',\vec{k},n)\delta(-\varepsilon_m(\vec{k}-\vec{k}')+\varepsilon_{n'}(\vec{k}')+\varepsilon_n(\vec{k}))\gamma_{\uparrow\vec{k}',n'}^{+\dagger}\gamma_{\downarrow\vec{k},n}^- \right) \beta_{\vec{k}-\vec{k}',m}^\dagger.
 \end{aligned} \tag{4.20}$$

Since β -magnons consist of up-tilts on the antiferromagnetic down-lattice $\mathbb{B}_T \in \mathbb{T}$ as well as up-tilts on the antiferromagnetic up-lattice $\mathbb{A}_T \in \mathbb{T}$, the rate T_β also quantifies the spin-up transport across the junction and into the antiferromagnetic layer. The expressions (4.17) and (4.18) correspond to equation (9) in Fjærbu et al. [2017].

4.4 Spin transport

The spin transport rate expressions given in (4.17) and (4.18) conclude our work on the junction. Note that these rates indeed depend on the magnonic surface amplitudes $u_{\bullet 1}$ and $v_{\bullet 1}$ discussed in 2.15 through the amplitude functions Σ_{\bullet} and Ξ_{\bullet} . We see that a magnonic surface amplitude appears in every term in (4.11). Then, if the m th magnon (for the given planar momentum) has vanishing surface amplitudes u_{m1} and v_{m1} , the corresponding amplitude functions Σ_m and Ξ_m will also be suppressed, and so such magnons could arguably be neglected from the calculation altogether. In this sense, only the magnons with significant surface amplitudes will contribute to the spin transport. The plots in section 2.15 then seem to suggest that for low values of ω (and hence large planar wave vectors \vec{k} near the edge of the Brillouin zone), only the surface magnons contribute to spin transport across the junction, which could possibly allow the transport rate expressions to be simplified. This topic is left for future investigation.

We finish this chapter with a visualisation of the spin transport across the junction. As explained in sections 4.2 and 4.3, every term in $\delta\mathbf{H}_{+\alpha}$, $\delta\mathbf{H}_{-\alpha}$, $\delta\mathbf{H}_{+\beta}$ or $\delta\mathbf{H}_{-\beta}$ corresponds to a *transport channel*, in which an electron flips its spin to create or annihilate a magnon, possibly transferring some planar momentum in the process. However, many transport channels are "passive", because they are suppressed by the delta function due to difference in energy before and after the flip.

The "active" transport channels across the junction can be visualised using the antiferromagnetic and metallic energy spectrum plots from sections 2.13 and 3.11. If the involved electronic states are plotted as points in the metallic energy spectrum and the involved magnonic state is plotted as a point in the antiferromagnetic spectrum, the vertical distance between the electron points must correspond to the vertical distance between the magnon point and the x-axis. In figure 4.1, this is illustrated for a bilayer system consisting of a 6-plane antiferromagnetic layer and a 6-plane metallic layer.

Note that the planar momentum of the involved magnon state must correspond to the difference in the planar momenta of the electronic states, so only certain combinations of ω values are allowed. This puts some additional horizontal constraints on the visualisation, which must be controlled by drawing level curves for the three ω values in the Brillouin zone and ensuring that there exist planar wave vectors \vec{k} and \vec{k}' which can produce them. From figure 2.7, we see that the all the level curves of ω are closed curves which resemble something between a circle and a square.

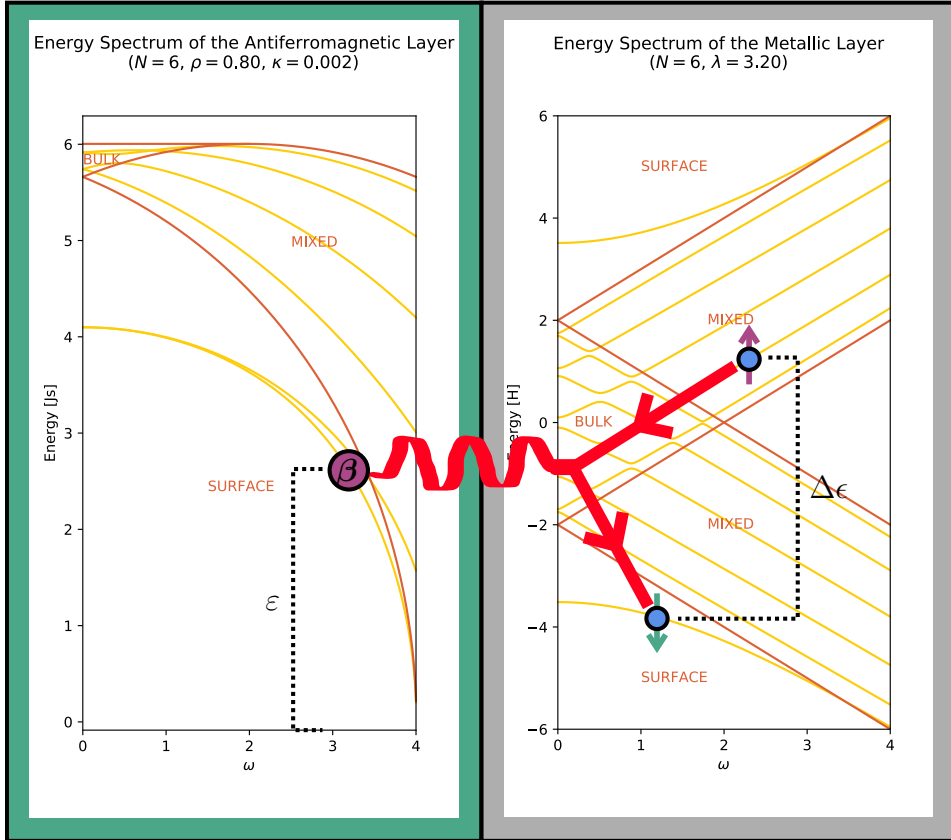


Figure 4.1: An example of a possibly active spin transport channel in the junction between a 6-plane antiferromagnetic layer and a 6-plane metallic layer with the given parameters. A positive-energy spin-up mixed electron flips its spin to become a negative-energy spin-down surface electron, transferring spin-up into the antiferromagnetic layer through the creation of a symmetric surface β -magnon. The energy lost by flipping the electron is the same as the energy gained from creating the magnon, $\varepsilon = \Delta\varepsilon$. Note that for this channel to actually be active, the ω values of the three particles must also satisfy conservation of planar momentum within the Brillouin zone.

4.5 Summary

The key results for the spin transport across the antiferromagnetic insulator–metallic conductor junction are concisely summed up here. For more details, please consult the rest of the chapter.

Considering the junction between two finite antiferromagnetic and metallic layers as described in the summary sections 2.16 and 3.13, the interaction Hamiltonian

$$\mathbf{H} = \frac{I}{\hbar^2} \sum_{\substack{\vec{a} \in \Lambda_1 \\ m, m'}} \vec{s}_{\vec{a}} \cdot \vec{\sigma}_{mm'} \mathbf{c}_{m\vec{a}}^\dagger \mathbf{c}_{m'\vec{a}} + \frac{I}{\hbar^2} \sum_{\substack{\vec{b} \in \mathbb{B}_1 \\ m, m'}} \vec{s}_{\vec{b}} \cdot \vec{\sigma}_{mm'} \mathbf{c}_{m\vec{b}}^\dagger \mathbf{c}_{m'\vec{b}}$$

leads to the transport rates

$$T_\alpha = \frac{2\pi}{\hbar} \left(\text{tr} \left(\delta \mathbf{H}_{+\alpha} \rho \delta \mathbf{H}_{+\alpha}^\dagger \right) - \text{tr} \left(\delta \mathbf{H}_{-\alpha} \rho \delta \mathbf{H}_{-\alpha}^\dagger \right) \right),$$

$$T_\beta = \frac{2\pi}{\hbar} \left(\text{tr} \left(\delta \mathbf{H}_{+\beta} \rho \delta \mathbf{H}_{+\beta}^\dagger \right) - \text{tr} \left(\delta \mathbf{H}_{-\beta} \rho \delta \mathbf{H}_{-\beta}^\dagger \right) \right),$$

quantifying the creation of α - and β -magnons respectively. (Equivalently, they quantify the spin-down and spin-up transport into the antiferromagnetic layer respectively.) Here ρ is the density operator of the bilayer system and

$$\begin{aligned} \delta \mathbf{H}_{+\alpha} &= \frac{I\sqrt{\frac{s}{2}}}{2G+2} \sum_{m, \vec{k}, n, \vec{k}', n'} \left(\Sigma_m(\vec{k}', n', \vec{k}, n) \delta(\varepsilon_m(\vec{k} - \vec{k}') + \epsilon_{n'}(\vec{k}') - \epsilon_n(\vec{k})) \gamma_{\uparrow \vec{k}', n'}^{+\dagger} \gamma_{\downarrow \vec{k}, n}^+ \right. \\ &\quad - \Sigma_m(\vec{k}, n, \vec{k}', n') \delta(\varepsilon_m(\vec{k} - \vec{k}') - \epsilon_{n'}(\vec{k}') + \epsilon_n(\vec{k})) \gamma_{\uparrow \vec{k}', n'}^{-\dagger} \gamma_{\downarrow \vec{k}, n}^- \\ &\quad \left. + \Xi_m(\vec{k}', n', \vec{k}, n) \delta(\varepsilon_m(\vec{k} - \vec{k}') - \epsilon_{n'}(\vec{k}') - \epsilon_n(\vec{k})) \gamma_{\uparrow \vec{k}', n'}^{-\dagger} \gamma_{\downarrow \vec{k}, n}^+ \right) \alpha_{\vec{k} - \vec{k}', m}^\dagger, \\ \delta \mathbf{H}_{-\alpha} &= \frac{I\sqrt{\frac{s}{2}}}{2G+2} \sum_{m, \vec{k}, n, \vec{k}', n'} \left(\Sigma_m(\vec{k}, n, \vec{k}', n') \delta(-\varepsilon_m(\vec{k}' - \vec{k}) + \epsilon_{n'}(\vec{k}') - \epsilon_n(\vec{k})) \gamma_{\downarrow \vec{k}', n'}^{+\dagger} \gamma_{\uparrow \vec{k}, n}^+ \right. \\ &\quad - \Sigma_m(\vec{k}', n', \vec{k}, n) \delta(-\varepsilon_m(\vec{k}' - \vec{k}) - \epsilon_{n'}(\vec{k}') + \epsilon_n(\vec{k})) \gamma_{\downarrow \vec{k}', n'}^{-\dagger} \gamma_{\uparrow \vec{k}, n}^- \\ &\quad \left. + \Xi_m(\vec{k}', n', \vec{k}, n) \delta(-\varepsilon_m(\vec{k}' - \vec{k}) + \epsilon_{n'}(\vec{k}') + \epsilon_n(\vec{k})) \gamma_{\downarrow \vec{k}', n'}^{+\dagger} \gamma_{\uparrow \vec{k}, n}^- \right) \alpha_{\vec{k}' - \vec{k}, m}^\dagger, \\ \delta \mathbf{H}_{+\beta} &= \frac{I\sqrt{\frac{s}{2}}}{2G+2} \sum_{m, \vec{k}, n, \vec{k}', n'} \left(\Sigma_m(\vec{k}', n', \vec{k}, n) \delta(\varepsilon_m(\vec{k}' - \vec{k}) + \epsilon_{n'}(\vec{k}') - \epsilon_n(\vec{k})) \gamma_{\downarrow \vec{k}', n'}^{+\dagger} \gamma_{\uparrow \vec{k}, n}^+ \right. \\ &\quad - \Sigma_m(\vec{k}, n, \vec{k}', n') \delta(\varepsilon_m(\vec{k}' - \vec{k}) - \epsilon_{n'}(\vec{k}') + \epsilon_n(\vec{k})) \gamma_{\downarrow \vec{k}', n'}^{-\dagger} \gamma_{\uparrow \vec{k}, n}^- \\ &\quad \left. + \Xi_m(\vec{k}', n', \vec{k}, n) \delta(\varepsilon_m(\vec{k}' - \vec{k}) - \epsilon_{n'}(\vec{k}') - \epsilon_n(\vec{k})) \gamma_{\downarrow \vec{k}', n'}^{-\dagger} \gamma_{\uparrow \vec{k}, n}^+ \right) \beta_{\vec{k}' - \vec{k}, m}^\dagger, \\ \delta \mathbf{H}_{-\beta} &= \frac{I\sqrt{\frac{s}{2}}}{2G+2} \sum_{m, \vec{k}, n, \vec{k}', n'} \left(\Sigma_m(\vec{k}, n, \vec{k}', n') \delta(-\varepsilon_m(\vec{k} - \vec{k}') + \epsilon_{n'}(\vec{k}') - \epsilon_n(\vec{k})) \gamma_{\uparrow \vec{k}', n'}^{+\dagger} \gamma_{\downarrow \vec{k}, n}^+ \right. \\ &\quad - \Sigma_m(\vec{k}', n', \vec{k}, n) \delta(-\varepsilon_m(\vec{k} - \vec{k}') - \epsilon_{n'}(\vec{k}') + \epsilon_n(\vec{k})) \gamma_{\uparrow \vec{k}', n'}^{-\dagger} \gamma_{\downarrow \vec{k}, n}^- \\ &\quad \left. + \Xi_m(\vec{k}', n', \vec{k}, n) \delta(-\varepsilon_m(\vec{k} - \vec{k}') + \epsilon_{n'}(\vec{k}') + \epsilon_n(\vec{k})) \gamma_{\uparrow \vec{k}', n'}^{+\dagger} \gamma_{\downarrow \vec{k}, n}^- \right) \beta_{\vec{k} - \vec{k}', m}^\dagger, \end{aligned}$$

with the transport amplitude functions

$$\begin{aligned}\Sigma_m(\vec{k}', n', \vec{k}, n) &= u_{m1}(\vec{k} - \vec{k}') o_{n'1}(\vec{k}') w_{n1}(\vec{k}) - v_{m1}(\vec{k} - \vec{k}') w_{n'1}(\vec{k}') o_{n1}(\vec{k}), \\ \Xi_m(\vec{k}', n', \vec{k}, n) &= u_{m1}(\vec{k} - \vec{k}') w_{n'1}(\vec{k}') w_{n1}(\vec{k}) + v_{m1}(\vec{k} - \vec{k}') o_{n'1}(\vec{k}') o_{n1}(\vec{k}).\end{aligned}$$

Conclusion

Throughout this thesis, the energy eigenstates of a finite-depth antiferromagnetic insulator layer with a distinct surface spin exchange and the energy eigenstates of a finite-depth metallic conductor layer were calculated and examined in chapters 2 and 3, towards a perturbation-based calculation of the spin transport across the bilayer junction in chapter 4. In this concluding chapter, we first sum up the main results, before we look at some prospects for future work based on these results.

5.1 Main results

The main results of the thesis are the expressions and equations determining the energy quanta and eigenstates of the finite antiferromagnetic and metallic layers, summed up in sections 2.16 and 3.13, as well as the spin transport rate expressions summed up in section 4.5. Also, the numerical script included in the appendix should be considered part of the main results, as it is an actual implementation of both the numerical and the analytical methods worked out throughout the chapters 2 and 3. In the following we recap these main results in a brief and qualitative fashion to give a concluding overview.

Both the finite antiferromagnetic insulator layer and the finite metallic conductor layer were shown to have non-trivial energy eigenstates, for which a system of equations has to be solved numerically in order to get approximate energy quanta and amplitudes. (An exception is the special case of a *non-interacting* finite metallic layer, which *can* be solved explicitly.) This is in contrast to the semi-infinite metallic layer treated in Fjærbu et al. [2017], which could be solved explicitly even for a finite interaction.

Some of the main results from Wolfram and De Wames [1969] were reproduced, more specifically the threshold surface spin exchange ratio for a magnonic surface branch to appear below the bulk continuum in the semi-infinite antiferromagnetic layer. A simple condition for electronic surface branches to appear outside the bulk continuum in the finite metallic layer was also derived, as well as conditions for surface electrons and threshold electrons to appear for a given planar wave vector \vec{k} .

Finally, transport rate expressions for spin-up and spin-down transport across the junction between the antiferromagnetic and metallic layers were calculated. These are exact all the way down to the assumptions justifying the use of the approximate Holstein-Primakoff transformation and Fermi's golden rule.

The accuracy of the transport rate expressions greatly enhances the versatility of our results. Indeed, the general transport rate expressions derived can be used to investigate the effect of the distinct surface spin exchange, but they could also be specialised to a number of other scenarios. Furthermore, the fact that our results apply to finite-depth layers could also be useful. Such finite layers, just some atoms across, are physically realisable with modern technology, and hence they are interesting to examine with the prospect of nanoscale spintronic devices. As far as the author knows, no finite-depth layer calculations for this particular model have been done earlier.

In short, the summary sections 2.16, 3.13 and 4.5 can be consulted by others to act as a baseline for a variety of future work on both finite-depth and infinite-depth antiferromagnetic insulator-metallic conductor bilayer systems. We consider some of these prospects in the next and final section.

5.2 Outlook

The obvious application of the results from this thesis is to find approximate expressions for the spin transport across the junction in the spirit of Fjærbu et al. [2017]. As described back in section 1.2, several limits and assumptions are made by Fjærbu, Rohling and Brataas to make the system simpler. Following a similar procedure, one could get thermal expressions for the spin transport rates and finally use these to investigate the actual effect of the distinct surface spin exchange on the spin transport across the junction.

Among the topics touched upon, but not fully explored, in this thesis, is the relation between the antiferromagnetic surface spin exchange and magnonic surface amplitudes, which was discussed briefly in section 2.15. An extension of our ansatz to include optical magnon branches above the antiferromagnetic bulk continuum could also be in order. Such magnons were described in Wolfram and De Wames [1969] and were shown in figure 2.34 to be present also in our finite-depth case. With the provided approach and results of chapter 2, both these topics lie ready to be examined further.

Intrigued by the research on enhanced spin transport through antiferromagnetic insulator interlayers discussed in section 1.1 (Wang et al. [2014], Moriyama et al. [2015], Wang et al. [2015], Hahn et al. [2014]), a last possible application of our results is to consider trilayer systems with an antiferromagnetic insulator interlayer, to investigate whether the resulting equations are able to explain the phenomenon. In Takei et al. [2015], such a trilayer system is explored using LLG equations and spin Hall phenomenology at the antiferromagnetic insulator-metallic conductor interface. Of course, the results from this thesis are readily applicable for a proper, quantum-mechanical operator treatment for comparison.

Bibliography

- Sebastian Anthony. Transistors will stop shrinking in 2021, but Moore's law will live on, Jul 2016. URL <https://arstechnica.com/gadgets/2016/07/itrs-roadmap-2021-moores-law/>. Accessed 2018-05-22.
- S. A. Wolf, D. D. Awschalom, R. A. Buhrman, J. M. Daughton, S. von Molnár, M. L. Roukes, A. Y. Chtchelkanova, and D. M. Treger. Spintronics: A spin-based electronics vision for the future. *Science*, 294(5546):1488–1495, 2001. ISSN 0036-8075. doi: 10.1126/science.1065389. URL <http://science.sciencemag.org/content/294/5546/1488>.
- Y. Kajiwara, K. Harii, S. Takahashi, J. Ohe, K. Uchida, M. Mizuguchi, H. Umezawa, H. Kawai, K. Ando, K. Takanashi, S. Maekawa, and E. Saitoh. Transmission of electrical signals by spin-wave interconversion in a magnetic insulator. 464:262–6, 03 2010. doi: 10.1038/nature08876. URL <https://doi.org/10.1038/nature08876>.
- Eirik L. Fjærbu, Niklas Rohling, and Arne Brataas. Electrically driven Bose-Einstein condensation of magnons in antiferromagnets. *Phys. Rev. B*, 95:144408, Apr 2017. doi: 10.1103/PhysRevB.95.144408. URL <https://link.aps.org/doi/10.1103/PhysRevB.95.144408>.
- S. O. Demokritov, V. E. Demidov, O. Dzyapko, G. A. Melkov, A. Serga, B. Hillebrands, and A. N. Slavin. Bose-Einstein condensation of quasi-equilibrium magnons at room temperature under pumping. *Nature*, 443:430–3, 10 2006. doi: 10.1038/nature05117. URL <https://doi.org/10.1038/nature05117>.
- V. E. Demidov, O. Dzyapko, S. O. Demokritov, G. A. Melkov, and A. N. Slavin. Observation of spontaneous coherence in Bose-Einstein condensate of magnons. *Phys. Rev. Lett.*, 100:047205, Jan 2008. doi: 10.1103/PhysRevLett.100.047205. URL <https://link.aps.org/doi/10.1103/PhysRevLett.100.047205>.
- P. Nowik-Boltyk, O. Dzyapko, V. E. Demidov, N. Berloff, and S. O. Demokritov. Spatially non-uniform ground state and quantized vortices in a two-component Bose-Einstein condensate of magnons. 2:482, Jun 2012.

-
- Chen Sun, Thomas Nattermann, and Valery L. Pokrovsky. Unconventional superfluidity in yttrium iron garnet films. *Phys. Rev. Lett.*, 116:257205, Jun 2016. doi: 10.1103/PhysRevLett.116.257205. URL <https://link.aps.org/doi/10.1103/PhysRevLett.116.257205>.
- Yu. M. Bunkov, E. M. Alakshin, R. R. Gazizulin, A. V. Klochkov, V. V. Kuzmin, T. R. Safin, and M. S. Tagirov. Discovery of the classical Bose-Einstein condensation of magnons in solid antiferromagnets. *JETP Letters*, 94(1):68, Sep 2011. ISSN 1090-6487. doi: 10.1134/S0021364011130066. URL <https://doi.org/10.1134/S0021364011130066>.
- Yu. M. Bunkov, E. M. Alakshin, R. R. Gazizulin, A. V. Klochkov, V. V. Kuzmin, V. S. L'vov, and M. S. Tagirov. High- T_c spin superfluidity in antiferromagnets. *Phys. Rev. Lett.*, 108:177002, Apr 2012. doi: 10.1103/PhysRevLett.108.177002. URL <https://link.aps.org/doi/10.1103/PhysRevLett.108.177002>.
- L. Berger. Emission of spin waves by a magnetic multilayer traversed by a current. *Phys. Rev. B*, 54:9353–9358, Oct 1996. doi: 10.1103/PhysRevB.54.9353. URL <https://link.aps.org/doi/10.1103/PhysRevB.54.9353>.
- Ran Cheng, Jiang Xiao, Qian Niu, and Arne Brataas. Spin pumping and spin-transfer torques in antiferromagnets. *Phys. Rev. Lett.*, 113:057601, Jul 2014. doi: 10.1103/PhysRevLett.113.057601. URL <https://link.aps.org/doi/10.1103/PhysRevLett.113.057601>.
- J. C. Slonczewski. Current-driven excitation of magnetic multilayers. *Journal of Magnetism and Magnetic Materials*, 159(1):L1 – L7, 1996. ISSN 0304-8853. doi: [https://doi.org/10.1016/0304-8853\(96\)00062-5](https://doi.org/10.1016/0304-8853(96)00062-5). URL <http://www.sciencedirect.com/science/article/pii/0304885396000625>.
- Arne Brataas, Andrew D. Kent, and Hideo Ohno. Current-induced torques in magnetic materials. *Nature Materials*, 11(5):372–381, 5 2012. ISSN 1476-1122. doi: 10.1038/nmat3311. URL <https://doi.org/10.1038/nmat3311>.
- Yaroslav Tserkovnyak, Arne Brataas, Gerrit E. W. Bauer, and Bertrand I. Halperin. Non-local magnetization dynamics in ferromagnetic heterostructures. *Rev. Mod. Phys.*, 77:1375–1421, Dec 2005. doi: 10.1103/RevModPhys.77.1375. URL <https://link.aps.org/doi/10.1103/RevModPhys.77.1375>.
- Scott A. Bender, Rembert A. Duine, and Yaroslav Tserkovnyak. Electronic pumping of quasiequilibrium Bose-Einstein-condensed magnons. *Phys. Rev. Lett.*, 108:246601, Jun 2012. doi: 10.1103/PhysRevLett.108.246601. URL <https://link.aps.org/doi/10.1103/PhysRevLett.108.246601>.
- Scott A. Bender, Rembert A. Duine, Arne Brataas, and Yaroslav Tserkovnyak. Dynamic phase diagram of dc-pumped magnon condensates. *Phys. Rev. B*, 90:094409, Sep 2014. doi: 10.1103/PhysRevB.90.094409. URL <https://link.aps.org/doi/10.1103/PhysRevB.90.094409>.
-

Michel Dyakonov and V. I. Perel. Possibility of orienting electron spins with current. 13: 467, 05 1971.

J. E. Hirsch. Spin Hall effect. *Phys. Rev. Lett.*, 83:1834–1837, Aug 1999. doi: 10.1103/PhysRevLett.83.1834. URL <https://link.aps.org/doi/10.1103/PhysRevLett.83.1834>.

Luqiao Liu, Takahiro Moriyama, D. C. Ralph, and R. A. Buhrman. Spin-torque ferromagnetic resonance induced by the spin Hall effect. *Phys. Rev. Lett.*, 106:036601, Jan 2011. doi: 10.1103/PhysRevLett.106.036601. URL <https://link.aps.org/doi/10.1103/PhysRevLett.106.036601>.

C. W. Sandweg, Y. Kajiwara, A. V. Chumak, A. A. Serga, V. I. Vasyuchka, M. B. Jungfleisch, E. Saitoh, and B. Hillebrands. Spin pumping by parametrically excited exchange magnons. *Phys. Rev. Lett.*, 106:216601, May 2011. doi: 10.1103/PhysRevLett.106.216601. URL <https://link.aps.org/doi/10.1103/PhysRevLett.106.216601>.

Takuya Satoh, Sung-Jin Cho, Ryugo Iida, Tsutomu Shimura, Kazuo Kuroda, Hiroaki Ueda, Yutaka Ueda, B. A. Ivanov, Franco Nori, and Manfred Fiebig. Spin oscillations in antiferromagnetic NiO triggered by circularly polarized light. *Phys. Rev. Lett.*, 105:077402, Aug 2010. doi: 10.1103/PhysRevLett.105.077402. URL <https://link.aps.org/doi/10.1103/PhysRevLett.105.077402>.

Helen V. Gomonay and Vadim M. Loktev. Spin transfer and current-induced switching in antiferromagnets. *Phys. Rev. B*, 81:144427, Apr 2010. doi: 10.1103/PhysRevB.81.144427. URL <https://link.aps.org/doi/10.1103/PhysRevB.81.144427>.

Ran Cheng, Di Xiao, and Arne Brataas. Terahertz antiferromagnetic spin Hall nano-oscillator. *Phys. Rev. Lett.*, 116:207603, May 2016. doi: 10.1103/PhysRevLett.116.207603. URL <https://link.aps.org/doi/10.1103/PhysRevLett.116.207603>.

Hailong Wang, Chunhui Du, P. C. Hammel, and Fengyuan Yang. Antiferromagnonic spin transport from $\text{Y}_3\text{Fe}_5\text{O}_{12}$ into NiO. *Phys. Rev. Lett.*, 113:097202, Aug 2014. doi: 10.1103/PhysRevLett.113.097202. URL <https://link.aps.org/doi/10.1103/PhysRevLett.113.097202>.

Hailong Wang, Chunhui Du, P. C. Hammel, and Fengyuan Yang. Spin transport in antiferromagnetic insulators mediated by magnetic correlations. *Phys. Rev. B*, 91:220410, Jun 2015. doi: 10.1103/PhysRevB.91.220410. URL <https://link.aps.org/doi/10.1103/PhysRevB.91.220410>.

Takahiro Moriyama, So Takei, Masaki Nagata, Yoko Yoshimura, Noriko Matsuzaki, Takahito Terashima, Yaroslav Tserkovnyak, and Teruo Ono. Anti-damping spin transfer torque through epitaxial nickel oxide. *Applied Physics Letters*, 106(16):162406, 2015. doi: 10.1063/1.4918990. URL <https://doi.org/10.1063/1.4918990>.

-
- Christian Hahn, Grgoire de Loubens, Vladimir V. Naletov, Jamal Ben Youssef, Olivier Klein, and Michel Viret. Conduction of spin currents through insulating antiferromagnetic oxides. *EPL (Europhysics Letters)*, 108(5):57005, 2014. URL <http://stacks.iop.org/0295-5075/108/i=5/a=57005>.
- Yaroslav Tserkovnyak, Arne Brataas, and Gerrit E. W. Bauer. Enhanced Gilbert damping in thin ferromagnetic films. *Phys. Rev. Lett.*, 88:117601, Feb 2002. doi: 10.1103/PhysRevLett.88.117601. URL <https://link.aps.org/doi/10.1103/PhysRevLett.88.117601>.
- S. Mizukami, Y. Ando, and T. Miyazaki. Effect of spin diffusion on Gilbert damping for a very thin permalloy layer in Cu/permalloy/Cu/Pt films. *Phys. Rev. B*, 66:104413, Sep 2002. doi: 10.1103/PhysRevB.66.104413. URL <https://link.aps.org/doi/10.1103/PhysRevB.66.104413>.
- M. W. Daniels, W. Guo, G. M. Stocks, D. Xiao, and J. Xiao. Spin-transfer torque induced spin waves in antiferromagnetic insulators. *New Journal of Physics*, 17(10):103039, Oct 2015. doi: 10.1088/1367-2630/17/10/103039. URL <https://doi.org/10.1088/1367-2630/17/10/103039>.
- C. G. Windsor and R. W. H. Stevenson. Spin waves in RbMnF_3 . *Proceedings of the Physical Society*, 87(2):501, 1966. URL <http://stacks.iop.org/0370-1328/87/i=2/a=319>.
- J. C. López Ortiz, G. A. Fonseca Guerra, F. L. A. Machado, and S. M. Rezende. Magnetic anisotropy of antiferromagnetic RbMnF_3 . *Phys. Rev. B*, 90:054402, Aug 2014. doi: 10.1103/PhysRevB.90.054402. URL <https://link.aps.org/doi/10.1103/PhysRevB.90.054402>.
- T. Wolfram and R. E. De Wames. Surface spin waves for the simple cubic antiferromagnet. *Phys. Rev.*, 185:762–769, Sep 1969. doi: 10.1103/PhysRev.185.762. URL <https://link.aps.org/doi/10.1103/PhysRev.185.762>.
- So Takei, Takahiro Moriyama, Teruo Ono, and Yaroslav Tserkovnyak. Antiferromagnet-mediated spin transfer between a metal and a ferromagnet. *Phys. Rev. B*, 92:020409, Jul 2015. doi: 10.1103/PhysRevB.92.020409. URL <https://link.aps.org/doi/10.1103/PhysRevB.92.020409>.

Appendix A: Source Code

```
1 import time
2 import numpy as np
3 import scipy.optimize as sp
4 from matplotlib import pyplot as pp
5 from matplotlib import cm
6 from matplotlib.ticker import MaxNLocator
7 from mpl_toolkits.mplot3d import Axes3D
8 from matplotlib import patches as pat
9
10 ## START
11
12 tic = time.clock()
13
14 ## MAGNET SOLVER
15
16 class MagnetSolver():
17
18     # CLASS CONSTANTS:
19
20     # Number of values for continuous functions in 1D plots:
21     plotnum = 1000
22     #Number of values in each direction for continuous functions in 3D plots:
23     plotnum3 = 100
24
25     # Infinitesimal threshold:
26     inft = 0.000001
27
28     # CLASS METHODS:
29
30
31     def calcOmega(self,mu,nu):
32         # Calculates the wave parameter for given planar wave vector index fractions mu and nu.
33         # Here, mu and nu must be between -0.5 and 0.5, including 0.5.
34
35         return 4*np.cos(mu*np.pi)*np.cos(nu*np.pi)
36
37
38     def plotOmega(self):
39         # Plots the wave parameter for the possible values of mu and nu.
40
41         plotnum3 = self.plotnum3
42         vals = np.linspace(-0.5,0.5,self.plotnum3)
43         [mus, nus] = np.meshgrid(vals,vals)
44         omegas = np.zeros([plotnum3,plotnum3])
45         for i in range(plotnum3):
46             for j in range(plotnum3):
47                 omegas[i,j] = self.calcOmega(mus[i,j],nus[i,j])
48         fig = pp.figure('Omega')
49         fig.suptitle('Possible Wave Parameter Values')
50         ax = fig.gca(projection='3d')
51         surf = ax.plot_surface(mus,nus,omegas,cmap=cm.copper)
52         ax.set_xlabel(r'$\mu$')
53         ax.set_ylabel(r'$\nu$')
54         ax.set_zlabel(r'$\omega$')
55         fig.colorbar(surf)
56
57
58     def calcNumMagnons(self):
59         # Solves the eigenequation numerically and rescales the eigenvectors to fulfil the canonicity condition.
60
61         N = self.N
62         inft = self.inft
63
64         # Finds the energy quanta and the Bogoliubov matrices:
65         [eps, BT] = np.linalg.eig(self.AN)
66         B = np.conj(np.transpose(BT))
67
68         # Sorts the energy quanta and magnons from lowest to highest magnitude:
69         sorted = np.argsort(eps)
70         sorted = sorted[::-1]
71         eps = eps[sorted]
72         B = B[sorted]
73         sorted = np.argsort(eps[:N])
74         eps[:N] = eps[sorted]
75         B[:N,:] = B[sorted,:]
76
77         # Symmetrises and normalises the magnons:
78         for i in range(N):
79             if (i%2 == 0) and ((eps[i]-eps[i+1])**2 < inft**2):
80                 B[i,:] = self.symmetriseMagnon(B[i,:],1)
81                 B[N+i,:] = self.symmetriseMagnon(B[N+i,:],1)
```

```

82         B[i+1,:] = self.symmetriseMagnon(B[i+1,:],-1)
83         B[N+1+1,:] = self.symmetriseMagnon(B[N+1+1,:],-1)
84         P = np.sum(B[1,:N]**2-B[1,N]**2)
85         B[1,:] /= np.sqrt(P)
86         B[N+1,:] /= np.sqrt(P)
87         if (B[1,0] < 0):
88             B[1,:] *= -1
89         if (B[N+1,N] < 0):
90             B[N+1,:] *= -1
91     # Here, the sign is chosen so that the first creation amplitude is positive.
92
93     # Constructs a matrix of magnons for storage:
94     numMagnons = np.zeros([N,2*N+1])
95     numMagnons[:,2*N] = B[:,N:]
96     numMagnons[:,2*N] = eps[:N]
97     # Here, the energy quantum is stored to the right of the amplitude vectors.
98
99     # Stores the energy quanta and matrices:
100    self.eps = eps
101    self.B = B
102    self.BT = np.conj(np.transpose(B))
103    self.numMagnons = numMagnons
104
105    def symmetriseMagnon(self,magnon,par):
106        u = magnon[:N]
107        v = magnon[N:]
108        rmagnon = np.zeros(2*N)
109        rmagnon[:N] = u[::-1]
110        rmagnon[N:] = v[::-1]
111        smagnon = magnon+par*rmagnon
112        return smagnon
113
114    def plotMagnons(self,magnons,plotlist,type=''):
115        # Plots a given list of magnons of the antiferromagnet.
116
117        N = self.N
118        rho = self.rho
119        kappa = self.kappa
120        omega = self.omega
121
122        # Finds the number of magnons to be plotted (max 6):
123        num = len(plotlist)
124
125        # Finds the maximal and minimal amplitude values to be plotted and sets upper and lower limits for the y-axis:
126        ulim = np.max(magnons[:,2*N])+0.2
127        llim = np.min(magnons[:,2*N])-0.2
128
129        # Creates a figure or a figure of subplots based on the number of magnons to be plotted:
130        if (num == 1):
131            fig = pp.figure(type+'Magnons')
132            fig.suptitle(type+'Magnons of the Antiferromagnetic Layer\n'+r'($N = %d$, $\rho = %.2f$, $\kappa = %.3f$, $\omega = %.2f$)'%(N,rho,kappa,omega))
133        else:
134            [fig,axes] = pp.subplots((num+1)//2,2,num=type+'Magnons',sharex=True,sharey=True)
135            fig.suptitle(type+'Magnons of the Antiferromagnetic Layer\n'+r'($N = %d$, $\rho = %.2f$, $\kappa = %.3f$, $\omega = %.2f$)'%(N,rho,kappa,omega))
136
137        # Extracts the amplitude vectors and energy quantum for each magnon and plots it:
138        for p in range(num):
139            i = plotlist[p]-1
140            magnon = magnons[i,2*N]
141            energy = magnons[i,2*N]
142            if (num == 1):
143                ax = fig.gca()
144            elif (num == 2):
145                ax = axes[p%2]
146            else:
147                ax = axes[p//2,p%2]
148            ax.xaxis.set_major_locator(MaxNLocator(integer=True))
149            ax.plot([1,N],[0,0],color='#888888',linestyle='solid')
150            ax.plot([1,1],[llim,ulim],color='#888888',linestyle='dashed')
151            ax.plot([N,N],[llim,ulim],color='#888888',linestyle='dashed')
152            ax.plot([(N+1)/2,(N+1)/2],[llim,ulim],color='#888888',linestyle='dashed')
153            ax.plot(np.arange(1,self.N+1),magnon[:N],'-o',color='#00b80c')
154            ax.plot(np.arange(1,self.N+1),magnon[N:],'-o',color='#ff0a0d')
155            ax.set_title(r'Magnon Group %d ($E = %.4fJs$)'%(i+1,energy), fontsize=10)
156            if (num == 1):
157                ax.set_ylabel('Amplitude')
158                ax.set_xlabel('Plane index')
159            else:
160                if (p%2 == 0):
161                    ax.set_ylabel('Amplitude')
162                if (p//2 == (num-1)//2) or ((num%2 != 0) and (p == num-2)):
163                    ax.set_xlabel('Plane index')
164            ax.set_ylim([llim,ulim])
165            ax.set_xlim([0,N+1])
166        # Removes any extra empty plot:
167        if (num > 2) and (num%2 != 0):
168            fig.delaxes(axes[num//2,num%2])
169        fig.tight_layout(rect=[0, 0, 1, 0.92])

```

```

170
171
172 def controlSandwichMatrix(self):
173     # Calculates and plots the canonicity condition for control.
174
175     NEG = self.NEG
176     B = self.B
177     BT = self.BT
178
179     S = BT.dot(NEG).dot(B)
180     fig = pp.figure('Antiferromagnetic Canonicity Condition')
181     pp.suptitle('Canonicity Condition  $S \hat{=} N B \dagger$ ')
182     pp.imshow(S)
183     pp.colorbar()
184
185
186 def controlEnergyMatrix(self):
187     # Calculates and plots the energy matrix E for control.
188     NEG = self.NEG
189     B = self.B
190     BT = self.BT
191     A = self.A
192
193     E = NEG.dot(B).dot(NEG).dot(A).dot(NEG).dot(BT).dot(NEG)
194     fig = pp.figure('Antiferromagnetic Energy Matrix')
195     pp.suptitle('Energy Matrix  $E \hat{=} N B N A N B \dagger$ ')
196     pp.imshow(E)
197     pp.colorbar()
198
199
200 def controlBogoliubovMatrix(self):
201     # Plots the Bogoliubov matrix B for control.
202     B = self.B
203
204     fig = pp.figure('Antiferromagnetic Bogoliubov Matrix')
205     pp.suptitle('Bogoliubov Matrix  $B \hat{=} S$ ')
206     pp.imshow(B)
207     pp.colorbar()
208
209
210 def calcTheta(self, phi, type):
211     # Calculates the frequency parameter theta for the given phi and type.
212
213     omega = self.omega
214
215     if (type == 'Surface'):
216         return np.arccosh(np.cosh(phi)+omega)
217     elif (type == 'Bulk'):
218         return np.arccos(np.cos(phi)+omega)
219     elif (type == 'Mixed'):
220         return np.arccosh(np.cos(phi)+omega)
221
222
223 def calcEnergyQuantum(self, phi, type):
224     # Calculates the energy quantum for the given phi and type.
225
226     omega = self.omega
227     kappa = self.kappa
228     epsmax = self.epsmax
229
230     if (type == 'Surface'):
231         return np.sqrt(epsmax**2-(omega+2*np.cosh(phi))**2)
232     elif (type == 'Bulk') or (type == 'Mixed'):
233         return np.sqrt(epsmax**2-(omega+2*np.cos(phi))**2)
234
235
236 def calcRatioR(self, phi, eps, type):
237     # Calculates the ratio R = -V/U = W/X for the given phi and epsilon, and the given type.
238
239     omega = self.omega
240     epsmax = self.epsmax
241
242     theta = self.calcTheta(phi, type)
243
244     if (type == 'Surface'):
245         return (omega+2*np.cosh(phi))/(epsmax+eps)
246     elif (type == 'Bulk') or (type == 'Mixed'):
247         return (omega+2*np.cos(phi))/(epsmax+eps)
248
249
250 def calcCondition(self, phi, parity, type):
251     # Calculates the condition function for the given phi, and the given parity and type.
252
253     N = self.N
254     omega = self.omega
255     kappa = self.kappa
256     zeta = self.zeta
257     eta = self.eta
258     epsmax = self.epsmax
259

```

```

260 theta = self.calcTheta(phi, type)
261
262 if (type == 'Surface'):
263     fac = (omega+2*np.cosh(phi))
264     if (parity == 'Symmetric'):
265         cond = 0
266         cond += fac*np.sinh((N+1)*theta/2)*np.cosh((N+1)*phi/2)
267         cond += (epsmax*zeta-fac*eta)*np.sinh((N+1)*theta/2)*np.cosh((N-1)*phi/2)
268         cond += (epsmax*zeta+fac*eta)*np.sinh((N-1)*theta/2)*np.cosh((N+1)*phi/2)
269         cond += fac*(zeta**2-eta**2)*np.sinh((N-1)*theta/2)*np.cosh((N-1)*phi/2)
270         return cond
271     elif (parity == 'Antisymmetric'):
272         cond = 0
273         cond += fac*np.cosh((N+1)*theta/2)*np.sinh((N+1)*phi/2)
274         cond += (epsmax*zeta-fac*eta)*np.cosh((N+1)*theta/2)*np.sinh((N-1)*phi/2)
275         cond += (epsmax*zeta+fac*eta)*np.cosh((N-1)*theta/2)*np.sinh((N+1)*phi/2)
276         cond += fac*(zeta**2-eta**2)*np.cosh((N-1)*theta/2)*np.sinh((N-1)*phi/2)
277         return cond
278     elif (type == 'Bulk'):
279         fac = (omega+2*np.cos(phi))
280         if (parity == 'Symmetric'):
281             cond = 0
282             cond += fac*np.sin((N+1)*theta/2)*np.cos((N+1)*phi/2)
283             cond += (epsmax*zeta-fac*eta)*np.sin((N+1)*theta/2)*np.cos((N-1)*phi/2)
284             cond += (epsmax*zeta+fac*eta)*np.sin((N-1)*theta/2)*np.cos((N+1)*phi/2)
285             cond += fac*(zeta**2-eta**2)*np.sin((N-1)*theta/2)*np.cos((N-1)*phi/2)
286             return cond
287         elif (parity == 'Antisymmetric'):
288             cond = 0
289             cond += fac*np.cos((N+1)*theta/2)*np.sin((N+1)*phi/2)
290             cond += (epsmax*zeta-fac*eta)*np.cos((N+1)*theta/2)*np.sin((N-1)*phi/2)
291             cond += (epsmax*zeta+fac*eta)*np.cos((N-1)*theta/2)*np.sin((N+1)*phi/2)
292             cond += fac*(zeta**2-eta**2)*np.cos((N-1)*theta/2)*np.sin((N-1)*phi/2)
293             return cond
294         elif (type == 'Mixed'):
295             fac = (omega+2*np.cos(phi))
296             if (parity == 'Symmetric'):
297                 cond = 0
298                 cond += fac*np.sinh((N+1)*theta/2)*np.cos((N+1)*phi/2)
299                 cond += (epsmax*zeta-fac*eta)*np.sinh((N+1)*theta/2)*np.cos((N-1)*phi/2)
300                 cond += (epsmax*zeta+fac*eta)*np.sinh((N-1)*theta/2)*np.cos((N+1)*phi/2)
301                 cond += fac*(zeta**2-eta**2)*np.sinh((N-1)*theta/2)*np.cos((N-1)*phi/2)
302                 return cond
303             elif (parity == 'Antisymmetric'):
304                 cond = 0
305                 cond += fac*np.cosh((N+1)*theta/2)*np.sin((N+1)*phi/2)
306                 cond += (epsmax*zeta-fac*eta)*np.cosh((N+1)*theta/2)*np.sin((N-1)*phi/2)
307                 cond += (epsmax*zeta+fac*eta)*np.cosh((N-1)*theta/2)*np.sin((N+1)*phi/2)
308                 cond += fac*(zeta**2-eta**2)*np.cosh((N-1)*theta/2)*np.sin((N-1)*phi/2)
309                 return cond
310
311
312 def calcRatio0(self, phi, theta, R, parity, type):
313     # Calculates the ratio O = X/U for the given phi, theta and R, and for the given parity and type.
314
315     N = self.N
316     rho = self.rho
317     zeta = self.zeta
318     eta = self.eta
319     inft = self.inft
320
321     if (type == 'Surface'):
322         if (parity == 'Symmetric'):
323             return (np.sinh((N+1)*theta/2)+(zeta*R+eta)*np.sinh((N-1)*theta/2))/(np.cosh((N+1)*phi/2)+(zeta*R-eta)*
324 ← np.cosh((N-1)*phi/2))
325         elif (parity == 'Antisymmetric'):
326             return (np.cosh((N+1)*theta/2)+(zeta*R+eta)*np.cosh((N-1)*theta/2))/(np.sinh((N+1)*phi/2)+(zeta*R-eta)*
327 ← np.sinh((N-1)*phi/2))
328         elif (type == 'Bulk'):
329             if (parity == 'Symmetric'):
330                 if (rho == 5/4) and ((4*np.cos((N+1)/2*np.arccos(-omega/2))-omega*np.cos((N-1)/2*np.arccos(-omega/2)))
331 ← **2 < inft):
332                     return 0
333                 else:
334                     return (np.sin((N+1)*theta/2)+(zeta*R+eta)*np.sin((N-1)*theta/2))/(np.cos((N+1)*phi/2)+(zeta*R-eta)
335 ← np.cos((N-1)*phi/2))
336             elif (parity == 'Antisymmetric'):
337                 if (rho == 5/4) and ((4*np.sin((N+1)/2*np.arccos(-omega/2))-omega*np.sin((N-1)/2*np.arccos(-omega/2)))
338 ← **2 < inft):
339                     return 0
340                 else:
341                     return (np.cos((N+1)*theta/2)+(zeta*R+eta)*np.cos((N-1)*theta/2))/(np.sin((N+1)*phi/2)+(zeta*R-eta)
342 ← np.sin((N-1)*phi/2))
343         elif (type == 'Mixed'):
344             if (parity == 'Symmetric'):
345                 return (np.sinh((N+1)*theta/2)+(zeta*R+eta)*np.sinh((N-1)*theta/2))/(np.cos((N+1)*phi/2)+(zeta*R-eta)*
346 ← np.cos((N-1)*phi/2))
347             elif (parity == 'Antisymmetric'):
348                 return (np.cosh((N+1)*theta/2)+(zeta*R+eta)*np.cosh((N-1)*theta/2))/(np.sin((N+1)*phi/2)+(zeta*R-eta)*
349 ← np.sin((N-1)*phi/2))

```

```

342
343
344 def calcNormAmplitude(self, phi, theta, R, O, parity, type):
345     # Calculates the normalised amplitude U for the given phi, theta, R and O, and for the given parity and type.
346
347     N = self.N
348
349     if (type == 'Surface'):
350         par = np.sinh(N*theta)/np.sinh(theta)+O**2*np.sinh(N*phi)/np.sinh(phi)
351         if (parity == 'Symmetric'):
352             par += 4*O*((1+R**2)/(1-R**2))*(np.sinh((N+1)/2*theta)*np.cosh((N-1)/2*phi)+np.sinh((N-1)/2*theta)*np.
↪ cosh((N+1)/2*phi))/(np.cosh(theta)+np.cosh(phi))
353             par -= N*(1-O**2)
354             return np.sqrt(2/((1-R**2)*par))
355         elif (parity == 'Antisymmetric'):
356             par += 4*O*((1+R**2)/(1-R**2))*(np.cosh((N+1)/2*theta)*np.sinh((N-1)/2*phi)+np.cosh((N-1)/2*theta)*np.
↪ sinh((N+1)/2*phi))/(np.cosh(theta)+np.cosh(phi))
357             par += N*(1-O**2)
358             return np.sqrt(2/((1-R**2)*par))
359     elif (type == 'Bulk'):
360         par = np.sin(N*theta)/np.sin(theta)-O**2*np.sin(N*phi)/np.sin(phi)
361         if (parity == 'Symmetric'):
362             par += 4*O*((1+R**2)/(1-R**2))*(np.sinh((N+1)/2*theta)*np.cos((N-1)/2*phi)+np.sin((N-1)/2*theta)*np.cos
↪ ((N+1)/2*phi))/(np.cos(theta)+np.cos(phi))
363             par -= N*(1+O**2)
364             return np.sqrt(-2/((1-R**2)*par))
365         elif (parity == 'Antisymmetric'):
366             par += 4*O*((1+R**2)/(1-R**2))*(np.cosh((N+1)/2*theta)*np.sin((N-1)/2*phi)+np.cos((N-1)/2*theta)*np.sin
↪ ((N+1)/2*phi))/(np.cos(theta)+np.cos(phi))
367             par += N*(1+O**2)
368             return np.sqrt(2/((1-R**2)*par))
369     elif (type == 'Mixed'):
370         par = np.sinh(N*theta)/np.sinh(theta)
371         if (parity == 'Symmetric'):
372             par += O**2*np.sin(N*phi)/np.sin(phi)
373             par += 4*O*((1+R**2)/(1-R**2))*(np.sinh((N+1)/2*theta)*np.cos((N-1)/2*phi)+np.sinh((N-1)/2*theta)*np.
↪ cos((N+1)/2*phi))/(np.cosh(theta)+np.cos(phi))
374             par -= N*(1-O**2)
375         elif (parity == 'Antisymmetric'):
376             par += O**2*np.sin(N*phi)/np.sin(phi)
377             par += 4*O*((1+R**2)/(1-R**2))*(np.cosh((N+1)/2*theta)*np.sin((N-1)/2*phi)+np.cosh((N-1)/2*theta)*np.
↪ sin((N+1)/2*phi))/(np.cosh(theta)+np.cos(phi))
378             par += N*(1+O**2)
379             return np.sqrt(2/((1-R**2)*par))
380
381
382 def calcCreationAmplitude(self, p, theta, phi, U, R, O, parity, type):
383     # Calculates the creation amplitude u(p) for the given parameters theta, phi, R and O, and for the given parity
↪ and type.
384
385     pm = self.pm
386
387     if (type == 'Surface'):
388         if (parity == 'Symmetric'):
389             return U*(-1)**p*np.sinh(theta*(p-pm))+O*U*np.cosh(phi*(p-pm))
390         elif (parity == 'Antisymmetric'):
391             return U*(-1)**p*np.cosh(theta*(p-pm))+O*U*np.sinh(phi*(p-pm))
392     elif (type == 'Bulk'):
393         if (parity == 'Symmetric'):
394             return U*(-1)**p*np.sin(theta*(p-pm))+O*U*np.cos(phi*(p-pm))
395         elif (parity == 'Antisymmetric'):
396             return U*(-1)**p*np.cos(theta*(p-pm))+O*U*np.sin(phi*(p-pm))
397     elif (type == 'Mixed'):
398         if (parity == 'Symmetric'):
399             return U*(-1)**p*np.sinh(theta*(p-pm))+O*U*np.cos(phi*(p-pm))
400         elif (parity == 'Antisymmetric'):
401             return U*(-1)**p*np.cosh(theta*(p-pm))+O*U*np.sin(phi*(p-pm))
402
403
404 def calcAnnihilationAmplitude(self, p, theta, phi, U, R, O, parity, type):
405     # Calculates the annihilation amplitude v(p) for the given parameters theta, phi, R and O, and for the given
↪ parity and type.
406
407     pm = self.pm
408
409     if (type == 'Surface'):
410         if (parity == 'Symmetric'):
411             return -R*U*(-1)**p*np.sinh(theta*(p-pm))+R*O*U*np.cosh(phi*(p-pm))
412         elif (parity == 'Antisymmetric'):
413             return -R*U*(-1)**p*np.cosh(theta*(p-pm))+R*O*U*np.sinh(phi*(p-pm))
414     elif (type == 'Bulk'):
415         if (parity == 'Symmetric'):
416             return -R*U*(-1)**p*np.sin(theta*(p-pm))+R*O*U*np.cos(phi*(p-pm))
417         elif (parity == 'Antisymmetric'):
418             return -R*U*(-1)**p*np.cos(theta*(p-pm))+R*O*U*np.sin(phi*(p-pm))
419     elif (type == 'Mixed'):
420         if (parity == 'Symmetric'):
421             return -R*U*(-1)**p*np.sinh(theta*(p-pm))+R*O*U*np.cos(phi*(p-pm))
422         elif (parity == 'Antisymmetric'):
423             return -R*U*(-1)**p*np.cosh(theta*(p-pm))+R*O*U*np.sin(phi*(p-pm))

```

```

424
425
426 def findMagnons(self, parity, type, plotCond=False):
427     # Finds and plots all magnons of the given parity and type.
428     # The last boolean parameter decides whether to plot the condition function on the range of interest or not.
429
430     N = self.N
431     rho = self.rho
432     kappa = self.kappa
433     omega = self.omega
434     zeta = self.zeta
435     epsmax = self.epsmax
436     plotnum = self.plotnum
437     infit = self.infit
438
439     # Sets the range of interest for phi:
440     if (type == 'Surface'):
441         phistart = 0.0
442         phistop = np.arccosh((epsmax-omega)/2)
443     elif (type == 'Bulk'):
444         if (omega > 2) or ((omega-2)**2 < infit):
445             print('No '+parity+' Bulk Magnons exist for this value of omega.')
446             return
447         phistart = np.arccos(1-omega)
448         phistop = np.arccos(-omega/2)
449     elif (type == 'Mixed'):
450         if (omega**2 < infit):
451             print('No '+parity+' Mixed Magnons exist for this value of omega.')
452             return
453         phistart = 0.0
454         if (omega > 2):
455             phistop = np.pi
456         else:
457             phistop = np.arccos(1-omega)
458
459     # Calculates the condition function on the range of interest and counts the number of roots:
460     rootcount = 0
461     roots = np.repeat(-1.0, N)
462     phis = np.linspace(phistart, phistop, plotnum)
463     conds = np.zeros(plotnum)
464     for i in range(plotnum):
465         conds[i] = self.calcCondition(phis[i], parity, type)
466         if (i == 0) and (conds[i]**2 < infit):
467             if (type == 'Surface'):
468                 continue
469             elif (type == 'Bulk'):
470                 if (parity == 'Symmetric'):
471                     continue
472                 elif (omega == 0) and (parity == 'Antisymmetric'):
473                     continue
474             elif (type == 'Mixed'):
475                 if (parity == 'Antisymmetric'):
476                     continue
477             roots[rootcount] = phis[i]
478             rootcount += 1
479         elif (i == plotnum-1) and (conds[i]**2 < infit):
480             if (type == 'Surface'):
481                 continue
482             elif (type == 'Bulk'):
483                 if (rho == 5/4) and (parity == 'Symmetric') and ((4*np.cos((N+1)/2*np.arccos(-omega/2))-omega*np.
484     ↪ cos((N-1)/2*np.arccos(-omega/2))**2 < infit):
485                     print('Symmetric max threshold solution found!')
486                 elif (rho == 5/4) and (parity == 'Antisymmetric') and ((4*np.sin((N+1)/2*np.arccos(-omega/2))-omega
487     ↪ *np.sin((N-1)/2*np.arccos(-omega/2))**2 < infit):
488                     print('Antisymmetric max threshold solution found!')
489                 else:
490                     continue
491             elif (type == 'Mixed'):
492                 if (omega < 2):
493                     continue
494                 elif (omega >= 2) and (parity == 'Symmetric'):
495                     continue
496             roots[rootcount] = phis[i]
497             rootcount += 1
498         elif (i > 0) and (conds[i-1]*conds[i] < 0):
499             roots[rootcount] = phis[i]
500             rootcount += 1
501
502     # Prints the amount of roots found and escapes if none were found:
503     if (rootcount == 0):
504         print('Found no '+parity+' '+type+' Magnons.')
505         if (plotCond == True):
506             fig = pp.figure('Antiferromagnetic '+parity+' '+type+' Condition Function')
507             fig.suptitle('Antiferromagnetic '+parity+' '+type+' Condition Function\n'+r'(SN = %d$, S\rho = %.2f$, %
508     ↪ \kappa = %.3f$, %\omega = %.2f$)'%(N, rho, kappa, omega))
509             pp.plot(phis, conds, color='#338454', linestyle='solid')
510             pp.xlabel(r'$\varphi$')
511         return
512     elif (rootcount == 1):
513         print('Found %d'%(rootcount)+parity+' '+type+' Magnon.')

```

```

511     else:
512         print('Found %d '%(rootcount)+parity+' '+type+' Magnons.')
513
514     # Discards all empty slots of the root vector:
515     roots = roots[roots>=0]
516
517     # Solves each root properly with Newton's method:
518     for n in range(rootcount):
519         roots[n] = sp.newton(self.calcCondition, roots[n], args=(parity, type), maxiter=100000)
520
521     # Plots the condition function on the range of interest:
522     if (plotCond == True):
523         fig = pp.figure('Antiferromagnetic '+parity+' '+type+' Condition Function')
524         fig.suptitle('Antiferromagnetic '+parity+' '+type+' Condition Function\n'+r'($N = %d$, $\rho = %.2f$, $\kappa = %.3f$, $\omega = %.2f$)'%(N, rho, kappa, omega))
525         pp.plot(phis, conds, color='#338454', linestyle='solid')
526         pp.scatter(roots, 0*roots, color='#338454')
527         pp.xlabel(r'$\varphi$')
528
529     # Constructs the matrix of magnons:
530     magnons = np.zeros([rootcount, 2*N+6])
531     for n in range(rootcount):
532         phi = roots[n]
533         theta = self.calcTheta(phi, type)
534         eps = self.calcEnergyQuantum(phi, type)
535         R = self.calcRatioR(phi, eps, type)
536         O = self.calcRatioO(phi, theta, R, parity, type)
537         U = self.calcNormAmplitude(phi, theta, R, O, parity, type)
538         for i in range(N):
539             p = i+1
540             magnons[n, i] = self.calcCreationAmplitude(p, theta, phi, U, R, O, parity, type)
541             magnons[n, N+i] = self.calcAnnihilationAmplitude(p, theta, phi, U, R, O, parity, type)
542             if (magnons[n, 0] < 0):
543                 magnons[n, :2*N] *= -1
544             magnons[n, 2*N:] = [eps, theta, phi, U, R, O]
545     # Here, the frequency parameters, the amplitude U and the ratios R and O are stored to the right of the
546     # amplitudes as well.
547
548     # Plots all the magnons:
549     all = np.arange(1, rootcount+1)
550     self.plotMagnons(magnons, all, parity+' '+type+' ')
551
552     # Returns magnon matrix:
553     return magnons
554
555 def calcAnaMagnons(self, plotCond=False):
556     # Calculates all the magnons "analytically" and stores them in respective magnon matrices.
557
558     self.SS = self.findMagnons('Symmetric', 'Surface', plotCond)
559     self.AS = self.findMagnons('Antisymmetric', 'Surface', plotCond)
560     self.SM = self.findMagnons('Symmetric', 'Mixed', plotCond)
561     self.AM = self.findMagnons('Antisymmetric', 'Mixed', plotCond)
562     self.SB = self.findMagnons('Symmetric', 'Bulk', plotCond)
563     self.AB = self.findMagnons('Antisymmetric', 'Bulk', plotCond)
564
565 def controlBulkConditions(self, magnons):
566     # Calculates and prints the bulk conditions for control.
567
568     N = self.N
569     omega = self.omega
570     kappa = self.kappa
571
572     num = len(magnons[:, 0])
573     for i in range(num):
574         energy = magnons[i, 2*N]
575         magnon = magnons[i, :2*N]
576         print('Magnon %d, first bulk control: %.2f'%(i+1, (6+2*kappa-energy)*magnon[1]-magnon[N]-omega*magnon[N+1]-
577             magnon[N+2]))
578         print('Magnon %d, second bulk control: %.2f'%(i+1, (6+2*kappa+energy)*magnon[N+1]-magnon[0]-omega*magnon[1]-
579             magnon[2]))
580
581 def controlSurfaceConditions(self, magnons):
582     # Calculates and prints the surface conditions for control.
583
584     N = self.N
585     omega = self.omega
586     rho = self.rho
587     kappa = self.kappa
588
589     num = len(magnons[:, 0])
590     for i in range(num):
591         energy = magnons[i, 2*N]
592         magnon = magnons[i, :2*N]
593         print('Magnon %d, first surface control: %.2f'%(i+1, (4*rho+1+2*kappa-energy)*magnon[0]-omega*rho*magnon[N]-
594             magnon[N+1]))
595         print('Magnon %d, second surface control: %.2f'%(i+1, (4*rho+1+2*kappa+energy)*magnon[N]-omega*rho*magnon
596             [0]-magnon[1]))

```

```

595
596 # CLASS CONSTRUCTOR:
597 def __init__(self, N, rho=0.8, kappa=0.002, omega=4.0):
598
599     # Stores parameters:
600     self.N = N
601     self.pm = (N+1)/2
602     self.rho = rho
603     self.kappa = kappa
604     self.omega = omega
605     self.eta = omega*(rho-1)
606     self.zeta = 4*rho-5
607
608     # Plot list of all magnons:
609     self.all = np.arange(1,N+1)
610
611     # Constructs matrices:
612     c = np.repeat(omega,N)
613     c[0] = c[N-1] = omega*rho
614     c2 = np.repeat(1,N-1)
615     C = np.diagflat(c)+np.diagflat(c2,1)+np.diagflat(c2,-1)
616     dI = 4*rho+1+2*kappa
617     dB = 6+2*kappa
618     d = np.repeat(dB,N)
619     d[0] = d[N-1] = dI
620     D = np.diagflat(d)
621     A = np.zeros([2*N,2*N])
622     A[:,N:] = D
623     A[:,N:] = C
624     A[N, :] = C
625     A[N, :] = D
626     NEG = np.zeros([2*N,2*N])
627     NEG[:,N:] = np.identity(N)
628     NEG[N, :] = -np.identity(N)
629     AN = A.dot(NEG)
630
631     # Stores matrices:
632     self.C = C
633     self.epsmax = dB
634     self.D = D
635     self.A = A
636     self.NEG = NEG
637     self.AN = AN
638
639 ## METAL SOLVER
640
641 class MetalSolver():
642
643     # CLASS CONSTANTS:
644
645     # Number of values for continuous functions in 1D plots:
646     plotnum = 1000
647     #Number of values in each direction for continuous functions in 3D plots:
648     plotnum3 = 100
649
650     # Infinitesimal threshold:
651     inft = 0.000001
652
653     # CLASS METHODS:
654
655     def calcOmega(self, mu, nu):
656         # Calculates the wave parameter for given planar wave vector index fractions mu and nu.
657         # Here, mu and nu must be between -0.5 and 0.5.
658
659         return 4*np.cos(mu*np.pi)*np.cos(nu*np.pi)
660
661     def calcNumElectrons(self):
662         # Solves the eigenequation numerically and rescales the eigenvectors to fulfil the canonicity condition.
663
664         N = self.N
665
666         # Finds the energy quanta and the Boym matrices:
667         [eps, BT] = np.linalg.eig(self.A)
668         B = np.conj(np.transpose(BT))
669
670         # Sorts the energy quanta and electrons from lowest to highest:
671         sorted = np.argsort(eps)
672         sorted = sorted[::-1]
673         eps = eps[sorted]
674         B = B[sorted]
675         sorted = np.argsort(eps[:N])
676         eps[:N] = eps[sorted]
677         B[:N] = B[sorted]
678
679         # Normalises the electrons:
680         for i in range(N):
681             P = np.sum(B[i, :]**2)

```

```

685         B[i,:] /= np.sqrt(P)
686         B[N+1,:] /= np.sqrt(P)
687         if (B[i,0] < 0):
688             B[i,:] *= -1
689         if (B[N+1,N] > 0):
690             B[N+1,:] *= -1
691     # Here, the sign is chosen so that the first main amplitude is positive.
692
693     # Constructs a matrix of electrons for storage:
694     numElectrons = np.zeros((N,2*N+1))
695     numElectrons[:,2*N] = B[:N]
696     numElectrons[:,2*N+1] = eps[:N]
697     # Here, the energy quantum is stored to the right of the amplitude vectors.
698
699     # Stores the energy quanta and matrices:
700     self.eps = eps
701     self.B = B
702     self.BT = np.conj(np.transpose(B))
703     self.numElectrons = numElectrons
704
705
706 def plotElectrons(self, electrons, plotlist, type=''):
707     # Plots a given list of electrons of the metal.
708
709     N = self.N
710     lam = self.lam
711     omega = self.omega
712
713     # Finds the number of electrons to be plotted:
714     num = len(plotlist)
715
716     # Finds the maximal and minimal amplitude values to be plotted and sets upper and lower limits for the y-axis:
717     ulim = np.max(electrons[:,2*N])*1.2
718     llim = np.min(electrons[:,2*N])*1.2
719
720     # Creates a figure or a figure of subplots based on the number of electrons to be plotted:
721     if (num == 1):
722         fig = pp.figure(type+'Electrons')
723         fig.suptitle(type+'Electrons of the Metallic Layer\n'+r'(SN = %d$, $\lambda$ = %.2f$, $\omega$ = %.2f$)'%(N,
724         ↪ lam, omega))
725     else:
726         [fig, axes] = pp.subplots((num+1)//2, 2, num=type+'Electrons', sharex=True, sharey=True)
727         fig.suptitle(type+'Electrons of the Metallic Layer\n'+r'(SN = %d$, $\lambda$ = %.2f$, $\omega$ = %.2f$)'%(N,
728         ↪ lam, omega))
729
730     # Extracts the amplitude vectors and energy quantum for each electron and plots it:
731     for p in range(num):
732         i = plotlist[p]-1
733         electron = electrons[i,2*N]
734         energy = electrons[i,2*N+1]
735         if (num == 1):
736             ax = fig.gca()
737         elif (num == 2):
738             ax = axes[p%2]
739         else:
740             ax = axes[p//2, p%2]
741         ax.xaxis.set_major_locator(MaxNLocator(integer=True))
742         ax.plot([1,N],[0,0], color='#888888', linestyle='solid')
743         ax.plot([1,1],[llim,ulim], color='#888888', linestyle='dashed')
744         ax.plot([N,N],[llim,ulim], color='#888888', linestyle='dashed')
745         ax.plot([(N+1)/2, (N+1)/2],[llim,ulim], color='#888888', linestyle='dashed')
746         ax.plot(np.arange(1,self.N+1), electron[:N], '-o', color='#00b80c')
747         ax.plot(np.arange(1,self.N+1), electron[N:], '-o', color='#ff0000')
748         ax.set_title(r'Electron Group %d ($E = %.4f$)'%(i+1, energy), fontsize=10)
749         if (num == 1):
750             ax.set_ylabel('Amplitude')
751             ax.set_xlabel('Plane index')
752         else:
753             if (p%2 == 0):
754                 ax.set_ylabel('Amplitude')
755                 if (p//2 == (num-1)//2) or ((num%2 != 0) and (p == num-2)):
756                     ax.set_xlabel('Plane index')
757             ax.set_ylim([llim,ulim])
758             ax.set_xlim([0,N+1])
759     # Removes any extra empty plot:
760     if (num > 2) and (num%2 != 0):
761         fig.delaxes(axes[num//2, num%2])
762     fig.tight_layout(rect=[0, 0, 1, 0.92])
763
764 def controlSandwichMatrix(self):
765     # Calculates and plots the canonicality condition for control.
766
767     B = self.B
768     BT = self.BT
769
770     S = BT.dot(B)
771     fig = pp.Figure('Metallic Canonicality Condition')
772     pp.suptitle('Canonicity Condition $B^\dagger B$')
773     pp.imshow(S)

```

```

773     pp.colorbar()
774
775
776     def controlEnergyMatrix(self):
777         # Calculates and plots the energy matrix E for control.
778         B = self.B
779         BT = self.BT
780         A = self.A
781
782         E = B.dot(A).dot(BT)
783         fig = pp.figure('Metallic Energy Matrix')
784         pp.suptitle('Energy Matrix $E = B A B^\dagger$')
785         pp.imshow(E)
786         pp.colorbar()
787
788
789     def controlUnitaryMatrix(self):
790         # Plots the unitary matrix B for control.
791         B = self.B
792
793         fig = pp.figure('Metallic Unitary Matrix')
794         pp.suptitle('Unitary Matrix $B$')
795         pp.imshow(B)
796         pp.colorbar()
797
798
799     def calcXi(self, psi, type):
800         # Calculates the frequency parameter xi for the given psi and type.
801
802         omega = self.omega
803
804         if (type == 'Surface'):
805             return np.arccosh(np.cosh(psi)+omega)
806         elif (type == 'Bulk'):
807             return np.arccos(np.cos(psi)+omega)
808         elif (type == 'Mixed'):
809             return np.arccosh(np.cos(psi)+omega)
810         elif (type == 'Surface Threshold'):
811             return np.arccosh(1+omega)
812         elif (type == 'Bulk Threshold'):
813             return 0.0
814         elif (type == 'Double Threshold'):
815             return 0.0
816
817
818     def calcEnergyQuantum(self, psi, type):
819         # Calculates the energy quantum for the given psi and type.
820
821         omega = self.omega
822
823         if (type == 'Surface'):
824             return (omega+2*np.cosh(psi))
825         elif (type == 'Bulk') or (type == 'Mixed'):
826             return (omega+2*np.cos(psi))
827         elif (type == 'Surface Threshold'):
828             return omega+2
829         elif (type == 'Bulk Threshold'):
830             return 2-omega
831         elif (type == 'Double Threshold'):
832             return 2
833
834
835     def calcCondition(self, psi, type):
836         # Calculates the condition function for the given psi and the given type.
837
838         N = self.N
839         lam = self.lam
840         xi = self.calcXi(psi, type)
841
842         if (type == 'Surface'):
843             cond = 0
844             cond += np.sinh((N+1)*xi)*np.sinh((N+1)*psi)
845             cond -= lam**2*np.sinh(N*xi)*np.sinh(N*psi)
846             return cond
847         elif (type == 'Bulk'):
848             cond = 0
849             cond += np.sin((N+1)*xi)*np.sin((N+1)*psi)
850             cond -= lam**2*np.sin(N*xi)*np.sin(N*psi)
851             return cond
852         elif (type == 'Mixed'):
853             cond = 0
854             cond += np.sinh((N+1)*xi)*np.sin((N+1)*psi)
855             cond -= lam**2*np.sinh(N*xi)*np.sin(N*psi)
856             return cond
857
858
859     def calcNormAmplitude(self, xi, psi, type):
860         # Calculates the normalised amplitude Y (X) for the given xi and psi and the given type.
861
862         N = self.N

```

```

863     lam = self.lam
864
865     if (type == 'Surface'):
866         return np.sqrt(1/(lam**2*(np.sinh(N*psi)/np.sinh((N+1)*xi))*2*(np.sinh((N+1)*xi)/np.sin(xi))*np.cosh((N
← +2)*xi)-np.cosh(2*(N+1)*xi)-N)+(np.sinh((N+1)*psi)/np.sinh(psi))*np.cosh((N+2)*psi)-np.cosh(2*(N+1)*psi)-N))
← )
867     elif (type == 'Bulk'):
868         return np.sqrt(-1/(lam**2*(np.sin(N*psi)/np.sin((N+1)*xi))*2*(np.sin((N+1)*xi)/np.sin(xi))*np.cos((N+2)*
← xi)-np.cos(2*(N+1)*xi)-N)+(np.sin((N+1)*psi)/np.sin(psi))*np.cos((N+2)*psi)-np.cos(2*(N+1)*psi)-N))
869     elif (type == 'Mixed'):
870         return np.sqrt(1/(lam**2*(np.sin(N*psi)/np.sinh((N+1)*xi))*2*(np.sinh((N+1)*xi)/np.sin(xi))*np.cosh((N
← +2)*xi)-np.cosh(2*(N+1)*xi)-N)-(np.sin((N+1)*psi)/np.sin(psi))*np.cos((N+2)*psi)-np.cos(2*(N+1)*psi)-N))
871     elif (type == 'Surface Threshold'):
872         return np.sqrt(1/((N*(N+1)*(2*N+1))/3-lam**2*N**2*(N+np.cosh(2*(N+1)*xi)-(np.sinh((N+1)*xi)/np.sinh(xi))*np
← .cosh((N+2)*xi))/(np.sinh((N+1)*xi)**2))
873     elif (type == 'Bulk Threshold'):
874         return np.sqrt(1/((N*(N+1)*(2*N+1))/3+lam**2*N**2*(N+np.cos(2*(N+1)*psi)-(np.sin((N+1)*psi)/np.sin(psi))*np
← .cos((N+2)*psi))/(np.sin((N+1)*psi)**2))
875     elif (type == 'Double Threshold'):
876         return np.sqrt(3/(2*N*(N+1)*(2*N+1)))
877
878 def calcUpAmplitude(self, p, xi, psi, XY, type):
879     # Calculates the up amplitude u(p) for the given parameters xi and psi and the given type.
880
881     N = self.N
882     lam = self.lam
883
884     if (type == 'Surface'):
885         return -lam*XY*(-1)**p*np.sinh(N*psi)*np.sinh(xi*(p-(N+1)))/np.sinh((N+1)*xi)+XY*np.sinh(psi*(p-(N+1)))
886     elif (type == 'Bulk'):
887         return -lam*XY*(-1)**p*np.sin(N*psi)*np.sin(xi*(p-(N+1)))/np.sin((N+1)*xi)+XY*np.sin(psi*(p-(N+1)))
888     elif (type == 'Mixed'):
889         return -lam*XY*(-1)**p*np.sin(N*psi)*np.sinh(xi*(p-(N+1)))/np.sinh((N+1)*xi)+XY*np.sin(psi*(p-(N+1)))
890     elif (type == 'Surface Threshold'):
891         return -lam*XY*N*(-1)**p*np.sinh((p-(N+1))*xi)/np.sinh((N+1)*xi)+XY*(p-(N+1))
892     elif (type == 'Bulk Threshold'):
893         return XY*(p-(N+1))*(-1)**p-lam*XY*N*np.sin((p-(N+1))*psi)/np.sin((N+1)*psi)
894     elif (type == 'Double Threshold'):
895         return -XY*(-1)**p-1*(p-(N+1))
896
897
898 def calcDownAmplitude(self, p, xi, psi, XY, type):
899     # Calculates the annihilation amplitude v(p) for the given parameters xi and psi and the given type.
900
901     N = self.N
902     lam = self.lam
903
904     if (type == 'Surface'):
905         return -lam*XY*(-1)**p*np.sinh(N*psi)*np.sinh(xi*(p-(N+1)))/np.sinh((N+1)*xi)-XY*np.sinh(psi*(p-(N+1)))
906     elif (type == 'Bulk'):
907         return -lam*XY*(-1)**p*np.sin(N*psi)*np.sin(xi*(p-(N+1)))/np.sin((N+1)*xi)-XY*np.sin(psi*(p-(N+1)))
908     elif (type == 'Mixed'):
909         return -lam*XY*(-1)**p*np.sin(N*psi)*np.sinh(xi*(p-(N+1)))/np.sinh((N+1)*xi)-XY*np.sin(psi*(p-(N+1)))
910     elif (type == 'Surface Threshold'):
911         return -lam*XY*N*(-1)**p*np.sinh((p-(N+1))*xi)/np.sinh((N+1)*xi)-XY*(p-(N+1))
912     elif (type == 'Bulk Threshold'):
913         return XY*(p-(N+1))*(-1)**p+lam*XY*N*np.sin((p-(N+1))*psi)/np.sin((N+1)*psi)
914     elif (type == 'Double Threshold'):
915         return -XY*(-1)**p+1*(p-(N+1))
916
917
918 def normaliseElectron(self, electron):
919     # Normalises the given electron vector and returns the normalised electron.
920
921     N = self.N
922
923     P = np.sum(electron[:2*N]**2)
924     if (P == 0):
925         nelectron = electron*0
926     else:
927         nelectron = electron/np.sqrt(P)
928     if (nelectron[0] < 0):
929         nelectron *= -1
930     return nelectron
931
932 def findElectrons(self, type, plotCond=False):
933     # Finds and plots all electrons of the given type.
934     # The last boolean parameter decides whether to plot the condition function on the range of interest or not.
935
936     N = self.N
937     omega = self.omega
938     lam = self.lam
939     lamB = self.lamB
940     lamS = self.lamS
941     plotnum = self.plotnum
942     inft = self.inft
943
944     # If the wanted type is surface, bulk or mixed electrons, plot the condition function and root it:
945     if (type == 'Surface') or (type == 'Bulk') or (type == 'Mixed'):
946         # Sets the range of interest for psi:

```

```

947     if (type == 'Surface'):
948         if (lam <= lamS):
949             print('No Surface Electrons exist for this value of omega.')
950             return
951         psistart = 0.0
952         psistop = 1.0
953     elif (type == 'Bulk'):
954         if (omega > 2) or ((omega-2)**2 < inf):
955             print('No Bulk Electrons exist for this value of omega.')
956             return
957         psistart = np.arccos(1-omega)
958         psistop = np.arccos(-omega/2)
959     elif (type == 'Mixed'):
960         if (omega**2 < inf):
961             print('No Mixed Electrons exist for this value of omega.')
962             return
963         psistart = 0.0
964         if (omega > 2):
965             psistop = np.pi
966         else:
967             psistop = np.arccos(1-omega)
968
969     # Calculates the condition function on the range of interest and counts the number of roots:
970     rootcount = 0
971     roots = np.repeat(-100.0,N)
972     psis = np.linspace(psistart,psistop,plotnum)
973     conds = np.zeros(plotnum)
974     for i in range(plotnum):
975         conds[i] = self.calcCondition(psis[i],type)
976         if (i > 0) and (conds[i-1]*conds[i] <= 0):
977             if (i == 1) or (i == plotnum-1):
978                 continue
979             else:
980                 roots[rootcount] = psis[i]
981                 rootcount += 1
982
983     # Prints the amount of roots found and escapes if none were found:
984     if (rootcount == 0):
985         print('Found no '+type+' Electrons.')
986         if (plotCond == True):
987             fig = pp.figure('Metallic '+type+' Condition Function')
988             fig.suptitle('Metallic '+type+' Condition Function\n'+r'($N = %d$, $\lambda = %.2f$, $\omega = %.2f$'
989             ← )'% (N,lam,omega))
990             pp.plot(psis,conds,color='#369fff',linestyle='solid')
991             pp.xlabel(r'$\psi_i$')
992             return
993     elif (rootcount == 1):
994         print('Found %d '%(rootcount)+type+' Electron.')
995     else:
996         print('Found %d '%(rootcount)+type+' Electrons.')
997
998     # Discards all empty slots of the root vector:
999     roots = roots[roots>-100]
1000
1001     # Solves each root properly with Newton's method:
1002     for n in range(rootcount):
1003         roots[n] = sp.newton(self.calcCondition,roots[n],args=(type,),maxiter=100000)
1004
1005     # Reverses the root vector in the case of bulk and mixed electrons:
1006     if (type == 'Bulk') or (type == 'Mixed'):
1007         roots = roots[::-1]
1008
1009     # Plots the condition function on the range of interest:
1010     if (plotCond == True):
1011         fig = pp.figure('Metallic '+type+' Condition Function')
1012         fig.suptitle('Metallic '+type+' Condition Function\n'+r'($N = %d$, $\lambda = %.2f$, $\omega = %.2f$'
1013         ← )'% (N,lam,omega))
1014         pp.plot(psis,conds,color='#369fff',linestyle='solid')
1015         pp.scatter(roots,0*roots,color='#369fff')
1016         pp.xlabel(r'$\psi_i$')
1017
1018     # If the wanted type is threshold electrons, check that the conditions are fulfilled:
1019     if (type == 'Surface Threshold'):
1020         if ((lam-lamS)**2 > inf or ((omega**2 < inf) and ((lam-(N+1)/N)**2 < inf))):
1021             print('No Surface Threshold Electrons exist for these values of lambda and omega.')
1022             return
1023         else:
1024             rootcount = 1
1025             roots = np.zeros(1)
1026             print('Found 1 Surface Threshold Electron.')
1027     if (type == 'Bulk Threshold'):
1028         if ((lam-lamB)**2 > inf or ((omega**2 < inf) and ((lam-(N+1)/N)**2 < inf))):
1029             print('No Bulk Threshold Electrons exist for these values of lambda and omega.')
1030             return
1031         else:
1032             rootcount = 1
1033             roots = np.array([np.arccos(1-omega)])
1034             print('Found 1 Bulk Threshold Electron.')
1035     if (type == 'Double Threshold'):
1036         if (omega**2 > inf) or ((lam-(N+1)/N)**2 > inf):

```

```

1035         print('No Double Threshold Electrons exist for these values of lambda and omega.')
1036         return
1037     else:
1038         rootcount = 1
1039         roots = np.zeros(1)
1040         print('Found 1 Double Threshold Electron.')
1041
1042     # Constructs the matrix of electrons:
1043     electrons = np.zeros([rootcount,2*N+3])
1044     for n in range(rootcount):
1045         psi = roots[n]
1046         xi = self.calcXi(psi,type)
1047         eps = self.calcEnergyQuantum(psi,type)
1048         XY = self.calcNormAmplitude(xi,psi,type)
1049         for i in range(N):
1050             p = i+1
1051             electrons[n,i] = self.calcUpAmplitude(p,xi,psi,XY,type)
1052             electrons[n,N+i] = self.calcDownAmplitude(p,xi,psi,XY,type)
1053             # electrons[n,:2*N] = self.normaliseElectron(electrons[n,:2*N])
1054             if (electrons[n,0] < 0):
1055                 electrons[n,:2*N] *= -1
1056             electrons[n,2*N:] = [eps,xi,psi]
1057         # Here, the frequency parameters xi and psi are stored to the right of the amplitudes as well.
1058
1059     # Plots all the electrons:
1060     all = np.arange(1,rootcount+1)
1061     self.plotElectrons(electrons,all,type+' ')
1062
1063     # Returns electron matrix:
1064     return electrons
1065
1066
1067 def calcAnaElectrons(self,plotCond=False):
1068     # Calculates all the electrons "analytically" and stores them in respective electron matrices.
1069
1070     self.S = self.findElectrons('Surface',plotCond)
1071     self.M = self.findElectrons('Mixed',plotCond)
1072     self.B = self.findElectrons('Bulk',plotCond)
1073     self.STE = self.findElectrons('Surface Threshold',plotCond)
1074     self.BTE = self.findElectrons('Bulk Threshold',plotCond)
1075     self.DTE = self.findElectrons('Double Threshold',plotCond)
1076
1077
1078 # CLASS CONSTRUCTOR:
1079 def __init__(self, N, lam=0.8, omega=4.0):
1080
1081     inft = self.inft
1082
1083     # Stores parameters:
1084     self.N = N
1085     self.lam = lam
1086     self.omega = omega
1087
1088     # Prints and stores lambda threshold values:
1089     if (omega**2 < inft):
1090         lamB = (N+1)/N
1091         self.lamB = lamB
1092     elif (omega < 2):
1093         psiB = np.arccos(1-omega)
1094         lamB2 = ((N+1)/N)*(np.sin((N+1)*psiB)/np.sin(N*psiB))
1095         if (lamB2 >= 0):
1096             lamB = np.sqrt(lamB2)
1097             self.lamB = lamB
1098         else:
1099             self.lamB = -1.0
1100     else:
1101         self.lamB = -1.0
1102     if (omega**2 < inft):
1103         lamS = (N+1)/N
1104         self.lamS = lamS
1105     else:
1106         xiS = np.arccosh(1+omega)
1107         lamS = np.sqrt(((N+1)/N)*(np.sinh((N+1)*xiS)/np.sinh(N*xiS)))
1108         self.lamS = lamS
1109
1110     # Plot list of all electrons:
1111     self.all = np.arange(1,N+1)
1112
1113     # Constructs matrices:
1114     c = np.repeat(-omega,N)
1115     c2 = np.repeat(-1,N-1)
1116     C = np.diagflat(c)+np.diagflat(c2,1)+np.diagflat(c2,-1)
1117     D = np.zeros([N,N])
1118     D[0,0] = lam
1119     A = np.zeros([2*N,2*N])
1120     A[:N,:N] = D
1121     A[:N,N:] = C
1122     A[N,:N] = C
1123     A[N,N:] = -D
1124

```

```

1125         # Stores matrices:
1126         self.C = C
1127         self.D = D
1128         self.A = A
1129
1130
1131     ## OTHER FUNCTIONS
1132
1133     def plotFrequencies(title, plotValues=False, plots=1, titles='', phis=[0.0], omegas=[0.0]):
1134         # Plots a number of frequency charts with the given phi and omega values indicated.
1135         res = 1000
1136         freqs = np.linspace(0, np.pi, res)
1137         coshes = np.zeros(res)
1138         coses = np.zeros(res)
1139         for i in range(res):
1140             coshes[i] = np.cosh(freqs[i])
1141             coses[i] = np.cos(freqs[i])
1142         if (plots == 1):
1143             fig = pp.figure(title)
1144         else:
1145             [fig, axes] = pp.subplots(plots, 1, num=title, sharex=True, sharey=True)
1146         for p in range(plots):
1147             if (plots == 1):
1148                 ax = fig.gca()
1149             else:
1150                 ax = axes[p]
1151             phi = phis[p]
1152             omega = omegas[p]
1153             ax.set_xlim([-0.2, np.pi+0.2])
1154             ax.set_ylim([-1.5, 5.5])
1155             ax.plot(freqs, coshes, color='#000000', linestyle='solid', zorder=1)
1156             ax.plot(freqs, coses, color='#ff0000', linestyle='solid', zorder=2)
1157             if (plotValues == True):
1158                 ax.set_title(titles[p], size=10)
1159                 if (phis[p] < 0):
1160                     phicos = np.cosh(-phi)
1161                     ax.scatter(-phi, phicos, color='#000000', zorder=3)
1162                     ax.text(-phi+0.04, phicos-0.2, r'\varphi$', size=12, verticalalignment='center', zorder=4)
1163                 else:
1164                     phicos = np.cos(phi)
1165                     ax.scatter(phi, phicos, color='#ff0000', zorder=3)
1166                     ax.text(phi+0.04, phicos-0.2, r'\varphi$', size=12, verticalalignment='center', zorder=4)
1167                 thetacos = phicos+omega
1168                 if (thetacos > 1):
1169                     theta = np.arccosh(thetacos)
1170                     ax.scatter(theta, thetacos, color='#000000', zorder=5)
1171                 else:
1172                     theta = np.arccos(thetacos)
1173                     ax.scatter(theta, thetacos, color='#ff0000', zorder=5)
1174                 ax.add_patch(pat.Rectangle([-0.3, phicos], np.pi+0.6, omega, color='#f48000', alpha=0.3, zorder=0))
1175                 ax.text(theta+0.04, thetacos-0.2, r'\vartheta$', size=12, verticalalignment='center', zorder=6)
1176                 ax.text(np.pi-0.2, phicos+omega/2, r'\omega$', size=12, verticalalignment='center', zorder=7)
1177             fig.tight_layout()
1178
1179
1180     def plotMagSpectrum(N, rho=0.8, kappa=0.002):
1181         # Plots the antiferromagnetic energy spectrum over all possible values of omega for the given values of N, rho and
1182         # ← kappa.
1183         res = 1000
1184         omegas = np.linspace(0, 4, res)
1185         energies = np.zeros([N, res])
1186         zeta = 4+rho-5
1187         epsmax = 6+2*kappa
1188         epsbulks = np.zeros(res)
1189         epssurfs = np.zeros(res)
1190         epslims = np.zeros(res)
1191         for i in range(res):
1192             mag = MagnetSolver(N, rho, kappa, omegas[i])
1193             epsbulks[i] = np.sqrt(epsmax**2 - (omegas[i]-2)**2)
1194             epssurfs[i] = np.sqrt(epsmax**2 - (omegas[i]+2)**2)
1195             mag.calcNumMagnons()
1196             energies[:, i] = mag.eps[:N]
1197         fig = pp.figure('Antiferromagnetic Energy Spectrum')
1198         ax = fig.gca()
1199         fig.suptitle('Energy Spectrum of the Antiferromagnetic Layer\n'+r'($N = %d$, $\rho = %.2f$, $\kappa = %.3f$)'%(N,
1200         ← rho, kappa))
1201         pp.xlabel(r'$\omega$')
1202         pp.ylabel('Energy [Js]')
1203         ax.set_xlim([0, 4])
1204         for n in range(N):
1205             ax.plot(omegas, energies[n, :], color='#fdce0b', linestyle='solid')
1206         ax.plot([0, 2], [epsmax, epsmax], color='#dd6337', linestyle='solid')
1207         ax.plot(omegas, epsbulks, color='#dd6337', linestyle='solid')
1208         ax.plot(omegas, epssurfs, color='#dd6337', linestyle='solid')
1209         sxpos = 1.5
1210         sypos = epssurfs[int(sxpos*res/4)]/2
1211         mxpos = 2.5
1212         mypos = (epssurfs[int(mxpos*res/4)]+epssurfs[int(mxpos*res/4)])/2
1213         bxpos = 0.0
1214         bypos = (epssurfs[int(bxpos*res/4)]+epsmax)/2

```

```

1213 ax.text(sxpos, sypos, 'SURFACE', size=10, color='dd6337', verticalalignment='center')
1214 ax.text(mxpos, mypos, 'MIXED', size=10, color='dd6337', verticalalignment='center')
1215 ax.text(bxpos, bypos, 'BULK', size=10, color='dd6337', verticalalignment='center')
1216
1217
1218 def plotMagSurfTruncCondition(rhos):
1219     # Plots the surface truncation condition for the semi-infinite antiferromagnetic layer for the given values of rho.
1220     res = 1000
1221     omegas = np.linspace(0, 4, res)
1222     num = len(rhos)
1223     conds = np.zeros((num, res))
1224     for n in range(num):
1225         zeta = 4*rhos[n]-5
1226         for i in range(res):
1227             eta = omegas[i]*(rhos[n]-1)
1228             conds[n, i] = (omegas[i]+2)*(1-eta)*(np.exp(np.arccosh(1+omegas[i]))+eta)+zeta**2)+6*zeta*(np.exp(np.
1229                 ↪ arccosh(1+omegas[i]))+1)
1230 fig = pp.figure('Surface Truncation Conditions')
1231 ax = fig.gca()
1232 fig.suptitle('Surface Truncation Condition of the Semi-Infinite Antiferromagnetic Layer')
1233 pp.xlabel(r'$\omega$')
1234 ax.set_xlim([0, 4])
1235 pp.plot([0, 4], [0, 0], color='000000')
1236 for n in range(num):
1237     pp.plot(omegas, conds[n, :], color='808284')
1238     ipos = int(2.1*res/4)
1239     ax.text(omegas[ipos], conds[n, ipos]-0.5, r'$\rho = %.3f$'%(rhos[n]), size=10, verticalalignment='center')
1240
1241 def plotMagSurfAmps(N, kappa=0.002, omega=4.0, plotList=[1, 2, 3]):
1242     # Plots the three lowest-energy magnonic surface amplitudes over rho values between 0 and 1 for the given values of
1243     ↪ N, kappa and omega.
1244     res = 100
1245     rhos = np.linspace(0, 1.0, res)
1246     camps = np.zeros([3, res])
1247     aamps = np.zeros([3, res])
1248     for n in range(3):
1249         for i in range(res):
1250             m = plotList[n]
1251             mag = MagnetSolver(N, rhos[i], kappa, omega)
1252             mag.calcNumMagnons()
1253             camps[n, i] = mag.numMagnons[m-1, 0]
1254             aamps[n, i] = mag.numMagnons[m-1, N]
1255 [fig, axes] = pp.subplots(1, 3, num='Antiferromagnetic Surface Amplitudes (Magnon Groups %d, %d and %d)'%(plotList[0],
1256     ↪ plotList[1], plotList[2]), sharex=True, sharey=True)
1257 fig.suptitle('Antiferromagnetic Surface Amplitudes\n'+r'($N = %d$, $\kappa = %.3f$, $\omega = %.2f$)'%(N, kappa,
1258     ↪ omega))
1259 for n in range(3):
1260     axes[n].set_title('Magnon Group %d'%(plotList[n]), fontsize=10)
1261     axes[n].set_xlabel(r'$\rho$')
1262     axes[n].plot(rhos, camps[n, :], '-', color='00b80c')
1263     axes[n].plot(rhos, aamps[n, :], '-', color='ff0a1d')
1264 fig.tight_layout(rect=[0, 0, 1, 0.92])
1265
1266 def plotMetSpectrum(N, lam=0.8, whole=False):
1267     # Plots the metallic energy spectrum over all possible values of omega for the given values of N and lambda.
1268     res = 1000
1269     omegas = np.linspace(0, 4, res)
1270     energies = np.zeros([N, res])
1271     for i in range(res):
1272         met = MetalSolver(N, lam, omegas[i])
1273         met.calcNumElectrons()
1274         energies[:, i] = met.eps[:N]
1275 fig = pp.figure('Metallic Energy Spectrum')
1276 ax = fig.gca()
1277 fig.suptitle('Energy Spectrum of the Metallic Layer\n'+r'($N = %d$, $\lambda = %.2f$)'%(N, lam))
1278 pp.xlabel(r'$\omega$')
1279 pp.ylabel('Energy [H]')
1280 ax.set_xlim([0, 4])
1281 ax.set_ylim([0, 6])
1282 for n in range(N):
1283     ax.plot(omegas, energies[n, :], color='fdce0b', linestyle='solid')
1284     if (whole == True):
1285         ax.plot(omegas, -energies[n, :], color='fdce0b', linestyle='solid')
1286 ax.plot([0, 2], [2, 0], color='dd6337', linestyle='solid')
1287 ax.plot([2, 4], [0, 2], color='dd6337', linestyle='solid')
1288 ax.plot([0, 4], [2, 6], color='dd6337', linestyle='solid')
1289 sxpos = 1.0
1290 sypos = 5.0
1291 mxpos = 1.8
1292 mypos = 2.0
1293 bxpos = 0.2
1294 bypos = (2-bxpos)/2
1295 ax.text(sxpos, sypos, 'SURFACE', size=10, color='dd6337', verticalalignment='center')
1296 ax.text(mxpos, mypos, 'MIXED', size=10, color='dd6337', verticalalignment='center')
1297 # Plots the whole spectrum (not only the positive half) if specified:
1298 if (whole == True):
1299     ax.set_ylim([-6, 6])
1300     ax.plot([0, 2], [-2, 0], color='dd6337', linestyle='solid')

```

```

1299     ax.plot ([2,4], [0,-2], color='#dd6337', linestyle='solid')
1300     ax.plot ([0,4], [-2,-6], color='#dd6337', linestyle='solid')
1301     ax.text (sxpos, -sypos, 'SURFACE', size=10, color='#dd6337', verticalalignment='center')
1302     ax.text (mxpos, -mypos, 'MIXED', size=10, color='#dd6337', verticalalignment='center')
1303     ax.text (bxpos, 0, 'BULK', size=10, color='#dd6337', verticalalignment='center')
1304     else:
1305         ax.plot ([0,2], [0,0], color='#dd6337', linestyle='solid')
1306         ax.text (bxpos, bypos, 'BULK', size=10, color='#dd6337', verticalalignment='center')
1307
1308
1309
1310     ## EXECUTIONS
1311
1312     # (Here, many different executions were made to get the different plots of the thesis.)
1313
1314     N = 6
1315     omega = 3.98
1316
1317     rho = 0.8
1318     kappa = 0.002
1319
1320     plotMagSpectrum(N, rho, kappa)
1321     # plotMagSurfAmps (N, kappa, omega, [1, 2, 3])
1322     # mag = MagnetSolver (N, rho, kappa, omega)
1323     # mag.calcNumMagnons ()
1324     # mag.plotMagnons (mag.numMagnons, [1, 2, 3, 4, 5, 6], 'Low Energy ')
1325     # mag.plotMagnons (mag.numMagnons, [7, 8, 9, 10, 11, 12], 'High Energy ')
1326     # mag.calcAnaMagnons ()
1327
1328
1329     # plotFrequencies ('Magnon Types', True, 3, ['Surface Magnons', 'Bulk Magnons', 'Mixed Magnons
1330     ↔ '], [-1.3, 2.6, 1.3], [1.6, 1.6, 1.6])
1331     # plotMagSurfTruncCondition ([1.105, 1.13, 1.209])
1332
1333     lam = 3.2
1334
1335     plotMetSpectrum (N, lam, True)
1336     # met = MetalSolver (N, lam, omega)
1337     # met.calcNumElectrons ()
1338     # met.plotElectrons (met.numElectrons, [1, 2, 3, 4, 5, 6])
1339     # met.calcAnaElectrons (False)
1340
1341     ## STOP
1342
1343     toc = time.clock ()
1344
1345     # Prints the calculation time of the execution:
1346     print ('Calculation time: %.3f seconds.' % (toc-tic))
1347
1348     ## SHOWTIME
1349
1350     pp.show ()

```